Imperial College London

Charge Generation and Recombination in Organic Photovoltaics

by

Michelle Southworth Vezie

A thesis presented for the degree of
Doctor of Philosophy

Imperial College London
Department of Physics
February 2017
Supervisor: Prof. J. Nelson

Declaration of Originality

I declare that the work presented herein, unless otherwise noted, is my own work, undertaken between October 2012 and February 2017 in the Experimental Sold State group in the Physics department of Imperial College, supervised by Prof. Jenny Nelson. The preface to each chapter notes any collaborations which have contributed to the results presented. Any published work is appropriately referenced and the appropriate permissions obtained.

Copyright Declaration

The copyright of this thesis rests with the author and is made available under a Creative Commons Attribution Non-Commercial No Derivatives licence. Researchers are free to copy, distribute or transmit the thesis on the condition that they attribute it, that they do not use it for commercial purposes and that they do not alter, transform or build upon it. For any reuse or redistribution, researchers must make clear to others the licence terms of this work.

Abstract

At the most basic level, a photovoltaic needs to convert solar power to electrical power. Therefore, the processes which result in electrons reaching the external circuit must out-compete the losses. I address this balance in organic photovoltaics, using a range of experimental techniques and test systems.

In Chapter 4, I consider the fundamental limits to solar cell efficiency using detailed balance. I use the voltage loss due to non-radiative recombination as a metric to quantify how close a set of polymer:fullerene blend devices approach the radiative limit, using an indacenodithiophene-co-benzothiadiazole (C_2C_6-IDTBT) polymer. In particular, I examine the effect of C_2C_6-IDTBT fractionation on the non-radiative recombination, and find that devices made from high molecular weight (MW) polymer exhibit reduced non-radiative recombination losses relative to the non-fractionated polymer.

I also probe the effect of polymer MW in Chapters 5 and 6, using a different polymer, a thienothiophene-diketopyrrolopyrrole (DPP-TT-T). In Chapter 5, I find that devices made from high MW DPP-TT-T out-perform devices made from low MW DPP-TT-T, particularly the short-circuit current. While I find some differences in electronic quality, the most striking difference between the polymer fractions is the light absorption: high MW DPP-TT-T absorbs light more strongly than low MW DPP-TT-T. Furthermore, the extinction coefficient maximum of high MW DPP-TT-T is about 50% greater than any conjugated polymer we had measured previously.

In Chapter 6, I explore the causes of this high optical absorption. We find that calculated persistence length can be a good predictor of optical absorption strength: polymers with high calculated persistence length, or high linearity, exhibit stronger absorption. We also find that high MW DPP-TT-T has a greater proportion of linear chain segments than low MW DPP-TT-T, and that this is the likely cause of the greater extinction coefficient.

Chapter 7 treats the mechanism of charge separation by using two modified fullerenes with different electron affinities to probe the energetic offset required

between the polymer and the acceptor for efficient free charge generation from polymer excitons. We find that, when there is very little energetic offset, the polymer excitons are unable to dissociate, and subsequent charge generation is inefficient. However, when the energetic offset between the polymer and acceptor LUMO levels is increased, the efficiency of polymer exciton dissociation is increased and there is significant charge generation.

Overall therefore, I have examined how charge generation, from light absorption to subsequent free charge generation, and recombination, particularly non-geminate recombination in the bulk, affect solar cell performance.

Acknowledgements

I feel very lucky to have had the privilege of spending over four years researching solar cells under the supervision of Jenny Nelson. I am so grateful that Jenny took me on, when I had no experience in doing research in solar, and very little otherwise. I have learnt so much from you and am inspired by your example. I am so thankful that you have allowed me freedom both in my research and away from it as you supported me to pursue my sport without question.

Thanks to Thomas Kirchartz for being willing to take the time to teach me about device physics. I learned a lot about which questions to ask from you. And thank you Sachetan Tuladhar for teaching me everything I know about how to make devices, and for introducing me to Nepalese food. Most of this thesis would not exist were it not for Mariano Campoy-Quiles; I have truly enjoyed working with you and have learnt so much from you.

All of my work has been at the mercy of synthetic chemists, and I feel lucky to have had such capable collaborators. Many thanks to Iain McCulloch, right from that first coffee and subsequent introduction to Jenny; almost every polymer I've ever worked with can trace its lineage in some way back to you. Particular mention of course goes to Iain Meager, who made DPP-TT-T, my main preoccupation throughout my PhD. I thank Shahid Ashraf who made the best-performing devices I've ever measured. Also thanks to Hugo Bronstein: in addition to making the IDTBTs, and supervising the INDT and DPP oligomer syntheses, your enthusiasm is infectious and I have loved talking science with you. Thanks to Anastasia Leventis, who made the DPP oligomers and introduced me to heat guns; I'm looking forward to finding out what's going on with the oligomers. Also thanks to Bob Schroeder who made BTT-DPP, and Abby Casey for GeDCN.

Many thanks to Sophia Hayes and Sheridan Few, who completed the core team for trying to get to the bottom of the DPPs. I have really enjoyed working with you both, and am looking forward to what else we find. Sheridan, thank you so much for your careful work, and discovering the snakes and bananas. I've enjoyed our conversations, from persistence length to the wider world! I aspire to your idealism. And Sophia, thank you for keeping me involved, also for sharing your wisdom on life alongside science.

Thanks to everyone who has helped with the LUMO project, from Thomas Kirchartz who had the idea to work with ketolactam in the first place, and Alex Sieval at Solenne BV who provided it, to Stoichko Dimitrov who got me started with BTT-DPP and then GeDCN, through to Hugo Bronstein who thought that

the INDTs might be interesting. Many thanks to Anna Jungbluth, and to Andrew Telford for supervising her; I have never done such efficient science! This would not have been possible if you hadn't been willing to spend your summer measuring hundreds of pixels with uninspiring efficiencies; I'm glad we got somewhere in the end! Thanks to Artem Bakulin for helping me find the weaknesses in my work and being willing to help me plug the holes, with the help of Tom Hopper. And thanks to Tracey Clarke who came on board, I'm glad our paths crossed again!

I thank Derya Baran for our fruitful collaboration on the IDTBTs, and further discussions later. I thank Carlos Silva for many helpful discussions, and for the introduction to Sophia, as well as the opportunity to visit Montreal. Thanks to Eleanora Vella for being such a good host, and for introducing me to ultrafast spectroscopy. I thank Ali Nedoma for giving me my first experience of a synchrotron, and for being a kindred foodie spirit. And thanks to everyone I've encountered through the CPE, I've really enjoyed being able to talk shop with people from such varied academic backgrounds.

I feel especially lucky to have been a member of the JN group. I've learnt so much about science and life from you, with special mentions for Davide Moia, Jason Röhr, Xingyuan Shi, Chris Emmott, Andrew Telford, Anne Guilbert and Alise Virbule. Also thanks to James Semple and Jose Videira who were there from the first wine and cheese evening. Thanks to all the inhabitants of H1101 over the last 4.5 years who have tolerated my occasional verbosity, especially those already mentioned and Milan Bratko, Katharina Zeissler, Tyler Roschuk (honorary member!), Themis Sidiropoulos, Michael Nielsen, Drew Pearce, Beth Rice, Phil Calado and Viktoryia Shautsova. I feel so lucky I have been able to make some good friends during my PhD, I hope we stay in touch.

I am grateful to have had the use of various facilities and rigs. Thanks to Thomas Kirchartz and Jizhong Yao for building the EL and EQE rigs, and especially to Jizhong for training me on them. Thanks to Florent Deledalle and his predecessors in James Durrant's group who built the charge extraction and transient photovoltage rig, and to Flo especially for spending many hours training me in the art of TPV. And thanks to Scot for useful discussions, and for introducing me to parkrun! Thanks to Stefan Maier's group for letting me use your ellipsometer. Many thanks to Xuhua Wang who has kept the glove box lab running, and to Steve Cussell and Sofia Bekou for running the cleanroom. Thanks to Steve and Dave Bowler for working so hard in the workshop, and to Carolyn Dale, Juraci Didone, Bhavna Patel, Anna Lal, Wenda Sadila and Alicia Tulloch for running the cluster office. Special thanks to Carolyn and Juraci who have been steadfast; I'm sure I don't know the half of what you do for the group, so thank you!

Many thanks to the EPSRC for funding my doctoral award, as well as the projects which allowed me to travel to conferences. Thanks to the StableNextSol COST centre for funding an enlightening trip to ICMAB, and SuperSolar for funding my travel to ICSM. I also thank Sport Imperial for their generous support, which helped me to pursue rowing alongside my PhD. And thanks to everyone at ICBC who helped me strive towards my goals and was a friend on and off the

water.

Thanks to my examiners, René Janssen and Paul Stavrinou for taking the time to read and examine this thesis, and for making my viva a surprisingly pleasant experience. Thanks also to James Durrant for examining my Early and Late Stage Assessments.

I have been lucky enough to have encountered inspiring teachers and mentors along the way. Thanks to Ezi Papakastopoulos and Kate Lee particularly for fostering my excitement in Chemistry and Physics at school. Thanks to Channing Robertson for getting me hooked into chemical engineering, and to Stacey Bent for mentoring me. Thanks too for Tom Jaramillo, David Abram, Claire Adjiman and Frances Pereira for giving me my first experiences of research.

Last but certainly not least, I would not be who I am today without the support of my family. Thanks to my parents and grandparents who have always valued education: to my mum, for pressing me to achieve the last 2%; to my dad, for thinking my work is alchemy; to my sisters, for putting me in my place; to my grandparents who are no longer with us, I am sorry I couldn't share this with you; to Grandmary, I'm glad I could. And heartfelt thanks to Matthew Taylor, for your patience and willingness to ride the waves with me.

List of Publications

M. S. Vezie, S. Few, I. Meager, G. Pieridou, B. Dörling, R. S. Ashraf, A. R. Goñi, H. Bronstein, I. McCulloch, S. C. Hayes, M. Campoy-Quiles, and J. Nelson. "Exploring the origin of high optical absorption in conjugated polymers". *Nature Materials* **15** (2016), pp. 746–753

D. Baran*, M. S. Vezie*, N. Gasparini, F. Deledalle, J. Yao, B. C. Schroeder, H. Bronstein, T. Ameri, T. Kirchartz, I. McCulloch, J. Nelson, and C. J Brabec. "Role of Polymer Fractionation in Energetic Losses and Charge Carrier Lifetimes of Polymer: Fullerene Solar Cells" *The Journal of Physical Chemistry C* **119** (2015), pp. 19668–19673
* These authors contributed equally

J. Yao, T. Kirchartz, M. S. Vezie, M. A. Faist, W. Gong, Z. He, H. Wu, J. Troughton, T. Watson, D. Bryant, and J. Nelson. "Quantifying losses in open-circuit voltage in solution- processable solar cells". *Physical review applied* **4** (2015): 014020

F. Deledalle, T. Kirchartz, M. S. Vezie, M. Campoy-Quiles, P. S. Tuladhar, J. Nelson, and J. R. Durrant. "Understanding the Effect of Unintentional Doping on Transport Optimization and Analysis in Efficient Organic Bulk- Heterojunction Solar Cells". *Physical Review X* **5** (2015): 011032

I. Meager, R. S. Ashraf, S. Mollinger, B. C. Schroeder, H. Bronstein, D. Beatrup, M. S. Vezie, T. Kirchartz, A. Salleo, J. Nelson, and I. McCulloch. "Photocurrent Enhancement from Diketopyrrolopyrrole Polymer Solar Cells through Alkyl-Chain Branching Point Manipulation". *Journal of the American Chemical Society* **135** (2013), pp. 11537–40

Other Publications

E. Vella, H. Li, P. Grégoire, S. M. Tuladhar, M. S. Vezie, S. Few, C. M. Bazán, J. Nelson, C. Silva-Acuña, E. R. Bittner. "Ultrafast decoherence dynamics govern photocarrier generation efficiencies in polymer solar cells". *Scientific Reports* **6** 29437

R. Dattani, J. H. Bannock, Z. Fei, R. C. I. MacKenzie, A. A. Y. Guilbert, M. S. Vezie, J. Nelson, J. C. de Mello, M. Heeney, J. T. Cabral, and A. J. Nedoma. "A general mechanism for controlling thin film structures in all-conjugated block copolymer: fullerene blends". *Journal of Materials Chemistry A* **2** (2014), pp. 14711–14719.

List of Conference Contributions

"Charge generation in organic photovoltaics" *SPIE Optics + Photonics* San Diego, USA. September 2016, talk

"Charge generation in polymer:fullerene photovoltaic systems" *International Conference on Science and Technology of Synthetic Metals* Guangzhou, China. June 2016, talk

"Understanding enhanced light absorption in conjugated polymers" *International Conference on Amorphous and Nanocrystalline Semiconductors* Aachen, Germany. September 2015, talk

"Understanding enhanced light absorption in a conjugated polymer" *International Conference on Hybrid and Organic Photovoltaics* Rome, Italy. May 2015, talk

"The effect of polymer molecular weight on the loss pathways in indacenodithiophene:fullerene solar cells" *E-MRS Spring Meeting* Lille, France. May 2015, talk

Contents

Abstract iv

Acknowledgements vii

List of Publications ix

List of Figures xvii

List of Tables xxiii

1 Motivation 1

1.1 Why solar? . . . 1

1.2 Why organic photovoltaics? . . . 2

1.3 Current state and context . . . 3

2 Background Theory 9

2.1 Bonding and the origin of π-conjugation . . . 9

2.2 Semiconducting Polymers . . . 12

2.3 Electromagnetic Interactions . . . 13

2.3.1 Interaction of light with solids . . . 13

2.3.2 Interaction of light with conjugated polymers . . . 22

2.4 Disorder in OPV devices . . . 23

2.4.1 Polymer structural disorder . . . 23

2.4.2 Polymer:fullerene bulk heterojunctions . . . 27

2.4.3 Energetic disorder . . . 30

2.4.4 Doping . . . 31

2.5 Solar cell operation . . . 32

2.5.1 Device model . . . 32

2.5.2 Charge separation . . . 39

2.5.3 Charge collection . . . 44

2.6 Limits to efficiency . . . 49

2.7 Light propagation in a solar cell 54

3 Experimental Techniques 61

3.1 Device and film fabrication 61

3.2 Steady-state device characterisation 66

3.2.1 Current-Voltage 66

3.2.2 Capacitance-Voltage 66

3.2.3 Quantum efficiency 70

3.3 Charge Extraction and Transient Photovoltage 73

3.4 Steady-state spectroscopy 80

3.4.1 Ultraviolet-visible spectroscopy 80

3.4.2 Ellipsometry 82

3.4.3 Photoluminescence 89

3.4.4 Electroluminescence and voltage losses 89

4 Understanding voltage losses in indacenodithiophene-based solar cells 91

4.1 Abstract 91

4.2 Introduction 92

4.3 Results 96

4.3.1 Capacitance-voltage 96

4.3.2 UV-Vis 97

4.3.3 Voltage losses 99

4.3.4 Charge carrier dynamics 105

4.4 Discussion 110

4.5 Conclusion 112

4.6 Experimental Details 113

5 Understanding enhanced photocurrent in polymer:fullerene solar cells 115

5.1 Abstract 115

5.2 Introduction 116

5.3 Results 120

5.3.1 Solar cell performance 120

5.3.2 Capacitance-Voltage 122

5.3.3 Charge carrier dynamics 123

5.3.4 Electroluminescence 129

5.3.5 External quantum efficiency and voltage losses 131

5.3.6 Ellipsometry . . . 134
5.3.7 Ultraviolet-visible spectroscopy . . . 138
5.3.8 Transfer matrix modelling and current collection . . . 142
5.4 Discussion . . . 147
5.5 Conclusion . . . 152
5.6 Experimental Details . . . 152

6 Understanding absorption in conjugated polymers 155
6.1 Abstract . . . 155
6.2 Introduction . . . 156
6.3 Results . . . 158
6.3.1 Calculations . . . 158
6.3.2 Test of persistence length-absorption relationship in polymers 170
6.3.3 Probing the origin of molecular weight dependence of absorption in DPP-TT-T . . . 172
6.3.4 Case study: diketopyrrolopyrrole-based oligomers . . . 180
6.4 Discussion . . . 182
6.4.1 Design considerations . . . 185
6.5 Conclusion . . . 186
6.6 Experimental Details . . . 187

7 Understanding the LUMO-LUMO offset required for charge generation 193
7.1 Abstract . . . 193
7.2 Introduction . . . 194
7.2.1 Research question . . . 198
7.2.2 Research approach: investigating another polymer with possible excitation wavelength dependence of charge generation 200
7.3 Results . . . 202
7.3.1 Ultraviolet-visible spectroscopy . . . 202
7.3.2 Ellipsometry . . . 204
7.3.3 Current-voltage and external quantum efficiency . . . 214
7.3.4 Reflectivity . . . 216
7.3.5 Internal quantum efficiency . . . 218
7.3.6 Electroluminescence and voltage losses . . . 221
7.3.7 Summary of device data and motivation for further measurements . . . 228
7.3.8 Pump-push photocurrent . . . 229

7.3.9 Transient absorption spectroscopy 231
7.3.10 Photoluminescence 235
7.4 Discussion 237
7.5 Conclusion 242
7.6 Experimental Details 242

8 Conclusions and further work **245**
8.1 Conclusions 245
8.2 Suggestions for further work 247

List of Figures

1.1 Global solar resource map 2
1.2 Certified power conversion efficiencies of research-scale photovoltaics 4

2.1 s and p atomic orbitals 10
2.2 Formation of molecular orbitals from atomic orbitals 11
2.3 Two resonant structures of polyacetylene 12
2.4 The possible processes when light hits a solid 14
2.5 Illustration of absorption and emission in a molecule 19
2.6 Interactions of light with a two level system 21
2.7 Gaussian distribution of molecular weights 25
2.8 Effect of polymer molecular weight on morphology 27
2.9 Arrangement of molecules in a typical polymer:fullerene bulk heterojunction 28
2.10 Chemical structures of the fullerenes used in this thesis 29
2.11 Density of states in an OPV solar cell 31
2.12 Equivalent circuit diagram of a solar cell 33
2.13 Alignment of Fermi energies for a metal-semiconductor-metal sandwich structure 34
2.14 Schematic of a current-voltage (J-V) curve 36
2.15 AM1.5 solar spectrum 36
2.16 Effect of the depletion region on the device band diagram 38
2.17 Diagram showing the states involved in charge separation 40
2.18 Steps involved in Shockley-Read-Hall recombination 47
2.19 Reflection and refraction of light at an interface 54
2.20 The definition of s- and p- polarisation 55
2.21 Schematic of the transfer matrix method 56
2.22 Effect of phase difference on the polarisation of light 58

3.1 Typical device architectures 62
3.2 Schematic of bladecoating and spincoating 63

3.3 Layout of a standard device substrate 65
3.4 Typical transmittance of a spectrosil substrate 66
3.5 Charge density profile in a device as a function of voltage 68
3.6 Example capacitance-voltage data 69
3.7 Experimental set-up of in-house high dynamic range EQE system . 71
3.8 Example of the step and glue process for EQE spectra 71
3.9 The principles of the charge extraction experiment 74
3.10 The principles of the transient photovoltage experiment 77
3.11 Two possible configurations of ultraviolet-visible spectrometer . . . 81
3.12 Schematic of a typical ellipsometer 84
3.13 Flowchart of the fitting protocol used to analyse ellipsometry data. 87

4.1 Chemical structure of IDTBT 93
4.2 Gel permeation chromatography of IDTBT batches 94
4.3 Current-voltage curves of devices with two different molecular weight IDTBT batches 95
4.4 Apparent doping concentration of IDTBT-based devices 97
4.5 Ultraviolet-visible absorption spectra of IDTBT polymers 98
4.6 Current-voltage curves of devices with two different molecular weight IDTBT batches 100
4.7 Electroluminescence spectra of IDTBT:$PC_{70}BM$ blend devices . . . 101
4.8 Device voltage as a function of injection current density for IDTBT devices 101
4.9 Electroluminescence spectra of IDTBT:$PC_{70}BM$ blend devices at different injection currents 102
4.10 External quantum efficiency of IDTBT:$PC_{70}BM$ blend devices . . . 102
4.11 Voltage losses as a function of EL injection current density 104
4.12 Current-voltage curves of IDTBT devices used in transient photovoltage and charge extraction. 106
4.13 Transient photovoltage and charge extraction data of IDTBT devices 108
4.14 Measured and calculated open-circuit voltage as a function of light intensity for IDTBT devices 109
4.15 Charge carrier lifetime and mobility data as a function of charge density of IDTBT devices 110
4.16 Mobility-lifetime product as a function of charge density of IDTBT devices 111

5.1 Chemical structure of DPP-TT-T 116

5.2 Current density-voltage characteristics of DPP-TT-T C1, C2 and C3 solar cells . . . 117
5.3 Gel permeation chromatography traces of DPP-TT-T polymers . . 120
5.4 Solar cell current density-voltage characteristics of low and high molecular weight C1 and C3 . . . 121
5.5 Mott-Schottky analysis of C1, C2 and C3 devices . . . 123
5.6 *J-V* curves of the devices used in the transient experiments . . . 125
5.7 Measured transient photovoltage and charge extraction data of C1 and C3 DPP-TT-T devices . . . 126
5.8 Measured and calculated open-circuit voltage as a function of light intensity . . . 127
5.9 Charge dynamics parameters as a function of charge density of DPP-TT-T devices . . . 128
5.10 Electroluminescence spectra of C1 and C3 DPP-TT-T . . . 129
5.11 Normalised DPP-TT-T electroluminescence spectra for different injection currents . . . 130
5.12 External quantum efficiency spectra of C1 and C3 DP-TT-T devices 131
5.13 Full combined EQE spectra using directly measured EQE and converted EL spectra. . . . 132
5.14 Radiative open-circuit voltage and non-radiative voltage loss . . . 133
5.15 Molecular weight dependence of C1 and C3 refractive index . . . 135
5.16 Thickness effect on C1 and C3 refractive index . . . 136
5.17 Fits of DPP-TT-T experimental ellipsometric angles . . . 137
5.18 Decadic molar extinction coefficient of C3 as a function of molecular weight . . . 138
5.19 Solvent dependence of C1 and C3 solution absorption . . . 139
5.20 Concentration dependence of C1 and C3 solution absorption . . . 140
5.21 Temperature dependence of C1 and C3 solution absorption . . . 141
5.22 EQE data used for the IQE estimation of DPP-TT-T devices, and corresponding *J-V* curves. . . . 143
5.23 EQE fits from the estimation of IQE . . . 145
5.24 Charge recombination lifetime and mobility as a function of light intensity. . . . 148
5.25 Simple model of photocurrent external quantum efficiency as a function of thickness . . . 151

6.1 Extinction coefficient κ spectra and maximum value of κ for a range of conjugated polymers . . . 157

6.2 The definitions of θ_{mon} and θ_{ring} . . . 159
6.3 Calculated oscillator strength spectra for oligothiophene and oligo-DPP-TT-T . . . 163
6.4 Calculated oscillator strength, normalised by the number of π-electrons . . . 166
6.5 Modelled ε_2 spectra calculated from eq. (2.28) . . . 167
6.6 Illustration of the influence of oligomer conformation on the overall transition dipole moment . . . 168
6.7 Calculated persistence length for a range of polymer structures . . . 169
6.8 C8-IDTBT and DPP3T chemical structures . . . 171
6.9 Solution ultraviolet-visible absorption spectra of DPP3T and C8-IDTBT . . . 171
6.10 Complex refractive index data for C8-IDTBT films and DPP3T . . . 172
6.11 Schematic of Raman scattering . . . 174
6.12 Resonance Raman spectra of C3-99 and C3-16 polymers . . . 175
6.13 Resonance Raman intensity analysis (RRIA) of CF solutions of high- and low-MW C3 polymer, with one transition . . . 176
6.14 Resonance Raman intensity analysis (RRIA) of ODCB solutions of high- and low-MW C3 polymer, with one transition . . . 177
6.15 Resonance Raman intensity analysis (RRIA) of solutions of high- and low-MW C3 polymer . . . 178
6.16 Resonance Raman intensity analysis (RRIA) of solutions of high- and low-MW C3 polymer . . . 179
6.17 Schematic showing the proposed effect of molecular weight on DPP polymer conformation . . . 180
6.18 Chemical structures of DPP oligomers . . . 181
6.19 Solution UV-Vis absorption spectra of DPP oligomers and two different molecular weight DPP-TPT polymer . . . 182
6.20 Calculated and experimental summed oscillator strength per π-system electron . . . 184
6.21 Thickness dependence of the complex refractive index for C8-IDTBT films . . . 188

7.1 Chemical structures of BTT-DPP and INDT-S . . . 195
7.2 BTT-DPP:$PC_{70}BM$ blend quantum efficiency data from a previous study . . . 196
7.3 BTT-DPP blend spectroscopy data from a previous study. . . . 197
7.4 Proposed energy level diagram from a previous study . . . 198

7.5 Chemical structure of ketolactam 199
7.6 Schematic of the effect of using KL instead of PCBM 200
7.7 INDT-S blend EQE, from previous study. 201
7.8 Absorption spectra of BTT-DPP, ketolactam and $PC_{70}BM$ and blends 203
7.9 Absorption spectra of INDT-S, ketolactam and PCBM and blends . 204
7.10 Complex refractive index spectra of BTT-DPP polymer and blend films. 206
7.11 Vertical fullerene concentration profile of BTT-DPP blends 207
7.12 Complex refractive index spectra of INDT-S polymer and blend films. 208
7.13 Experimental and fit ellipsometric angles Ψ and Δ of INDT-S . . . 209
7.14 Comparison of extinction coefficients derived from ellipsometry and ultraviolet-visible spectroscopy 211
7.15 Experimental and fit ellipsometric angles Ψ and Δ of INDT-S blend films 212
7.16 Complex refractive index spectra of the device interlayers 213
7.17 Current density-voltage and external quantum efficiency graphs of BTT-DPP-based devices 215
7.18 Current density-voltage and external quantum efficiency graphs of INDT-S-based devices 216
7.19 Reflectance spectra of full device stacks based on BTT-DPP and INDT-S 217
7.20 Calculated parasitic absorption spectra of BTT-DPP and INDT-S device stacks. 219
7.21 Calculated internal quantum efficiency of BTT-DPP and INDT-S devices. 220
7.22 Current density-voltage and external quantum efficiency graphs of BTT-DPP-based devices 222
7.23 Electroluminescence of BTT-DPP devices 222
7.24 Electroluminescence as a function of injection current of BTT-DPP devices 223
7.25 Non-radiative voltage losses of BTT-DPP devices 224
7.26 Electroluminescence of INDT-S devices 225
7.27 Normalised electroluminescence of INDT-S devices at different injection currents 226
7.28 High-range external quantum efficiency spectra of INDT-S devices . 226
7.29 Non-radiative voltage losses of INDT-S devices 227
7.30 Pump-push photocurrent of INDT-S blend devices 231

7.31 Picosecond transient absorption spectroscopy of INDT-S polymer and blend films. 233
7.32 ps-TAS data of INDT-S polymer and blend films 234
7.33 µs-TAS data of INDT-S blend films 234
7.34 INDT-S polymer and blend photoluminescence 236
7.35 Proposed model to explain INDT-S experimental results 241

List of Tables

2.1 Rates involved in Shockley-Read-Hall recombination 46

3.1 The filters used during a high-range EQE measurement 71
3.2 The number of π-electrons counted per polymer subunit. 83
3.3 Parameters used to model spectrosil 87
3.4 Parameters used to model silicon 88
3.5 Parameters used to model the native SiO_2 on a silicon substrate . . 88

4.1 Molecular weights of IDTBT fractions 93
4.2 IDTBT solar cell performance across multiple batches. 95
4.3 Solar cell performance parameters of best-performing IDTBT devices 96
4.4 Solar cell performance parameters of IDTBT devices used in voltage loss analysis 100
4.5 Non-radiative voltage losses of IDTBT:$PC_{70}BM$ devices 103
4.6 Solar cell performance parameters of IDTBT devices used in transient photovoltage and charge extraction 106
4.7 Transient photovoltage and differential charging fit parameters . . . 107
4.8 Fabrication batch parameters of IDTBT devices 114

5.1 Solar cell performance parameters of DPP-TT-T devices shown in Figure 5.2 118
5.2 Statistics of devices based on C1, C2 and C3. 118
5.3 Molecular weights of each DPP-TT-T batch 119
5.4 C1 and C3 solar cell parameters 121
5.5 Statistics of C1 and C3 devices 122
5.6 Solar cell performance parameters of C1 and C3 blend devices at time of transient experiments 124
5.7 Fit parameters from transient photovoltage and differential charging data analysis 125
5.8 DPP-TT-T J_{sc} values from J-V and EQE data 144

5.9 Measured and fit film thicknesses for IQE estimation 144
5.10 Assessment of the breakdown of short-circuit current increase of DPP-TT-T C1 devices 146
5.11 Assessment of the breakdown of short-circuit current increase of DPP-TT-T C3 devices 146

6.1 Names and chemical structures of oligomers studied 159
6.1 (cont.) Names and chemical structures of oligomers studied. 160
6.1 (cont.) Names and chemical structures of oligomers studied. 161
6.2 Optimised geometry for planar oligomers in all-*trans* and all-*cis* conformations 161
6.2 (cont.) Optimised geometry for planar oligomers of $60 < N_\pi < 85$, and associated monomer length and θ_{mon}. 162
6.3 The number of π-electrons counted per polymer subunit. 165
6.4 Molecular weights of C8-IDTBT and DPP3T polymer fractions . . 189
6.5 Materials and maximum extinction coefficients from the literature . 189
6.5 (cont.) Materials and maximum extinction coefficients from the literature 190
6.5 (cont.) Materials and maximum extinction coefficients from the literature 191

7.1 PCBM and KL cyclic voltammetry results 199
7.2 Parameters used to model INDT-S ellipsometry 210
7.3 Parameters used to model INDT-S blend films 214
7.4 *J*-*V* parameters of BTT-DPP devices 215
7.5 *J*-*V* parameters of INDT-S devices 216
7.6 Ratio of polymer absorption at pump wavelengths in the pump-push photocurrent experiment. 229

Chapter 1

Motivation

1.1 Why solar?

The world's population is approaching 7.5 billion and rising at a rate of about 1% per year [1]. Furthermore, about one in five people do not have access to reliable electricity [2]. Demand for electricity in 2012 was 21.6 trillion kilowatthours (kWh), and predicted to rise to 36.5 trillion kWh by 2040, driven mostly by demand in developing countries [3]. Electricity is relatively easy to decarbonise, which is another driver to increase the role of electricity in the energy system; an example of this is the rising prevalence of electric vehicles [4].

Historically, the majority of the world's energy consumption has been supplied by fossil fuels which are burned to release carbon dioxide, a greenhouse gas (GHG), into the atmosphere. The resultant global warming has slowly become an issue of international political significance, with the signing of the COP 21 agreement in Paris marking a landmark international consensus for governments to address their greenhouse gas outputs. Furthermore, fossil fuels are an inherently unsustainable resource with global reserves being steadily depleted.

Therefore there has been an ever-increasing emphasis on low-carbon energy technologies; that is, energy technologies which overall result in zero carbon dioxide emissions. It has been estimated that the global annual solar potential, or the potential amount of solar energy which could be used by humans, is approximately 440 PWh - 13.9 EWh per year [5]. Therefore harnessing the sun's energy is an obvious way to tackle the energy crisis. Recent developments have seen the cost of the most prevalent solar cells, those made from silicon, reach grid parity in some countries and markets. The uptake of solar is greatly influenced by factors such as governmental policy; for example, subsidies such as feed-in tariffs and net metering incentivise individual homeowners to install solar panels. This all

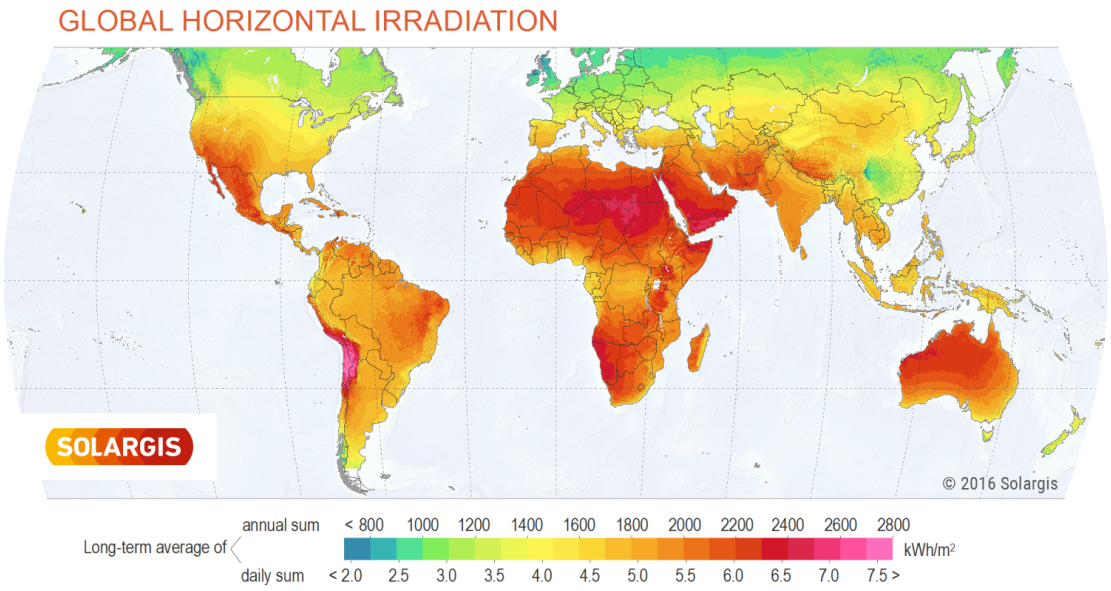


Figure 1.1: Global solar resource map, showing the global horizontal irradiance (GHI), defined as the total amount of solar energy incident on a horizontal surface. Map reproduced with permission from Solargis [7].

has resulted in accelerating global solar installation, with installed solar electric capacity reaching 227 GW in 2015 [6].

The electrification of the developing world, much of which receives a high annual solar flux (see Figure 1.1), is also a powerful driver for the development of solar technologies. Solar cells are modular and thus are scaleable; they are suitable for individual households as well as for utility-scale power production. This modularity also means that it is suitable for areas without enough infrastructure to support, for example, traditional fossil fuel generated electricity distribution. A simple example is the replacement of kerosene lamps with solar lanterns, which provide immediate financial and health benefits [6, 8].

1.2 Why organic photovoltaics?

The above discussion focussed on the case of silicon photovoltaics, which are rigid and heavy and therefore not suited to every application. Furthermore, the manufacture of crystalline silicon involves temperatures of 1800 °C, and is therefore very energy intensive. So there has been a shift towards development of thin-film solar technologies, where active layers are often mere microns thick so are therefore much lighter and can be flexible. These thin-film technologies can be categorised according to whether the absorbing layer is inorganic, organic, or a hybrid of the two.

The advantage of organic photovoltaics (OPV) over the other technologies lies in considering another aspect of the environmental impact of solar cell production: the abundance of the raw materials [9]. Many inorganic and hybrid solar cells use heavy elements such as cadmium, which has an earth crust abundance of approximately 0.1- 0.2 ppm [10]. Furthermore, these heavy elements are toxic and so raise concerns about the overall life cycle environmental impact. Therefore it is difficult to defend these technologies as the basis of a large increase in global solar energy production.

OPV, on the other hand, relies on earth-abundant and non-toxic elements, such as carbon, oxygen, nitrogen and sulphur, to constitute the absorbing layer of the solar cell. The materials used in OPV can be small molecules or polymers, or a mixture of the two. The inherent flexibility and plasticity of polymers means that plastics are very robust, and have therefore attracted much of the focus of the OPV community. In order to capitalise on these advantages, a large proportion of the research in OPV has been on solution-processed devices; the ability to coat the absorber on flexible substrates facilitates roll-to-roll printing or coating processes [11], in which an ink of the material(s) dissolved in a solvent is coated onto flexible substrates in a continuous manner. This ability therefore opens up the possibility of the production of large area solar cells with low energy input.

While OPV may not replace silicon solar cells in utility-scale solar power plants, there is certainly an opportunity for applications which are not otherwise possible. For example, with OPV the integration of solar cells into flexible electronics is possible. Another key application is building-integrated solar [12]; here the inherent tunability of organic molecules provides another advantage: while inorganic materials are limited by the properties of the constituent elements, there are potentially infinite possibilities for organic design, meaning that the bandgap, for example, can be tuned to the particular application. An example of this is the possibility for semi-transparent solar cells for greenhouses [13].

The work in this thesis focusses on solution-processed organic photovoltaic systems, and unless stated otherwise the devices have been fabricated using the scaleable bladecoating technique to ensure that the results are as relevant as possible for future development towards commercialisation.

1.3 Current state and context

The field of organic photovoltaics has seen huge development in recent years. Figure 1.2 shows how the record efficiencies of each main class of photovoltaics

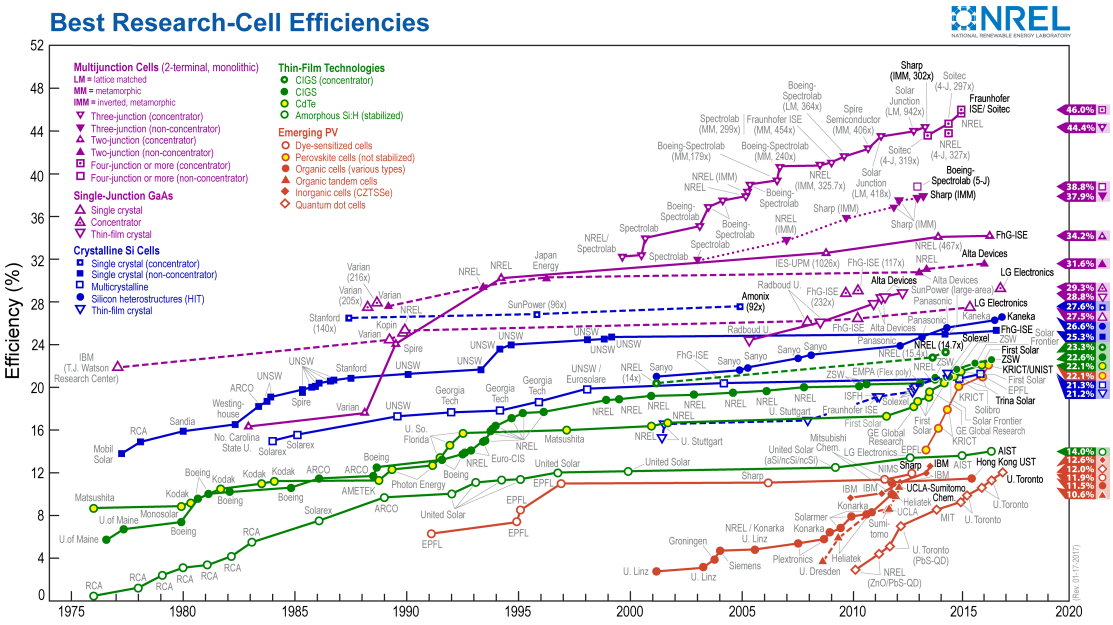


Figure 1.2: Certified record power conversion efficiencies of research-scale photovoltaics, classified by technology type. OPV is shown in red filled circles. The efficiencies shown were measured under standard testing conditions: global reference spectrum irradiance and 25 °C. This plot is courtesy of the National Renewable Energy Laboratory, Golden, Colorado USA [14]

has progressed in the last forty years [14]; the figure shows that OPV has been steadily approaching the efficiency of amorphous silicon solar cells, one of the oldest thin-film technologies.

The original workhorse of OPV was a blend of the conjugated homopolymer, poly(3-hexylthiophene) (P3HT), with a fullerene, [6,6]-phenyl-C_{61}-butyric acid methyl ester (PCBM); Sections 2.1 and 2.2 introduce the class of conjugated polymers. P3HT has a simple synthetic route which requires the polymerisation of thiophene, a commercially available chemical. However the bandgap of P3HT is too large to be optimal for the solar spectrum in a simple blend with PCBM and so lower bandgap materials have been targeted. The principal strategy is to design so-called push-pull, or donor-acceptor, copolymer monomer units, with two or more subunits with different electron affinities [15]. This approach is effective at lowering the bandgap of the material, but the increased length and complexity of the monomer results in a more complicated and expensive synthesis.

The proliferation of new materials has resulted in many different device structures breaking power conversion efficiencies of 10% [16–18]; historically most of the synthetic effort has been on designing new polymers, although recently this focus has shifted towards new acceptors too [19], as well as all-polymer blend solar cells [20, 21] and small-molecule solar cells [22–24]. The research in this thesis was

all done on devices using polymer:fullerene blends as the absorber material, and so this category is the focus of this discussion.

Although much progress has been made, there is still a long way to go for OPV to become a mainstream technology. While the record power conversion efficiencies are now over 10%, these are often for relatively small-scale devices, and scaling up to sizes appropriate for commercialisation usually results in a decrease of efficiency. One of the main issues in terms of targeting roll-to-roll solution processing is the film thickness: usually OPV devices are optimised for thicknesses below 100 nm, corresponding to the first interference maximum [25, 26]. Uniform films of such low thicknesses are difficult to achieve using conventional printing technologies, and result in a much stricter thickness tolerance. Below the first interference maximum, the short-circuit current is strongly dependent on thickness, whereas above this maximum, the dependence is much weaker. Furthermore, inhomogeneities in the film coating can result in pinholes, resulting in the device being shorted. However, increasing the film thickness requires better carrier collection, which shall be discussed in Section 2.5.3. The work I present in Chapters 4 and 5 addresses the effect of charge collection on device performance. While charge collection is still a limiting factor, another tactic with respect to increasing the available photocurrent from the device is to increase the optical absorption properties of the absorber. In Sections 2.3 and 2.7 I summarise the theory behind understanding light absorption and propagation in solar cells, while in Chapter 6, I investigate the optical absorption of polymers, with the aim of proposing design considerations to increase the extinction of the active layer.

Another limiting factor on OPV efficiencies to date is the large energy losses needed for efficient charge generation, relative to other solar cell technologies [27, 28]. This is an inherent cost of the type II bulk heterojunction formed from blending the polymer and fullerene, which appears to be necessary for efficient charge generation; I shall expand on this is Section 2.5.2. Furthermore the disorder inherent in these materials can contribute to the energy losses; I will discuss the sources of disorder in Section 2.4, and the limits to efficiency in Section 2.6. This background then informs the work done in Chapters 4 and 7, which explore the energy losses from the perspective of voltage losses, and from the energetics of charge separation, respectively.

Other aspects of OPV which need addressing, specifically from a commercialisation perspective, are the long-term stability and the cost of devices. Encapsulated OPV devices have been shown to have approximately 2-3 years operational stability [29], although this is dependent on the climate [30]; for reference, silicon

solar cells are typically covered under warranty for 25 years. The precise mechanism of OPV degradation can be system-dependent. Some common sources of degradation are (photo-)chemical degradation, for example from oxygen diffusing into the device or from photochemical reactions of the materials themselves, or physical degradation, for example from inter-diffusion of the organic materials [31]. Meanwhile, assessing the cost of devices must take into account the raw materials as well as the balance of systems [32, 33]. From this perspective, the prevalence of polymers with increasing complexity is problematic, as is the use of fullerenes. Fortunately the advent of non-fullerene acceptors is addressing this latter problem. In addition, the interlayers of OPV devices are often made from expensive materials, and many cannot be solution-processed. As a result, novel interlayers and electrodes have been the subject of research [34]. However these topics are outside the remit of this thesis and I will not be discussing them further.

OPV record efficiencies are often difficult to reproduce because it is difficult to define the system. There are many factors which affect reproducibility. Firstly, polymers, in contrast with small molecules, do not have a precisely defined molecular weight, but instead each batch has its own molecular weight distribution, which is a function of the polymerisation conditions. And the molecular weight distribution can profoundly affect the bulk properties of the material, both physical and optoelectriconic [35]. Therefore it can be difficult to draw conclusions about chemical structures themselves, since different batches may easily behave very differently.

Secondly, often the microstructure of the blend film is not at thermodynamic equilibrium, but is instead kinetically trapped [36]. This means that it can be strongly affected by factors such as the casting solvent and the temperature. And again the microstructure can have a profound impact on the film properties, since the domain sizes of the blend components, as well as the interface between them and the microstructure of individual domains themselves can be altered. This factor is also important when considering the long-term stability of OPV devices, since exposure to sustained solar radiation can heat up the solar cell significantly, with solar cells in some locations regularly reaching 85 °C [37], which can result in a possible change in morphology and of device performance. It is also possible that heat can change the chemical structures of the blend components although this is less likely.

Finally, OPV devices are composed of many layers of different materials, in addition to the active blend layer. Therefore the nature of the interfaces between these composite layers is another important factor which is often not well con-

trolled. In devices which are completely solution-processed, coating successive layers requires orthogonal solvents, which is sometimes difficult to achieve completely, or the chosen orthogonal solvent can have poor wetting characteristics on the underlying film. Therefore it can be difficult to achieve well-defined interfaces. Often the back electrode is an evaporated metal, and so the parameters of the evaporation can affect the quality of the electrode interface, especially considering that organic materials are very soft. The quality of the interface can affect electrical properties of the overall device, such as the series resistance and the degree of surface recombination, and so it is important to adequately control [38].

The above points therefore illustrate why it is important to accurately report all aspects of device fabrication, and to spend time understanding individual systems in detail, as opposed to focussing entirely on materials development. It is also clear that simple design rules are inherently difficult to define.

The work in this thesis uses a wide range of experimental techniques to systematically probe the factors which can affect device performance in order to ascertain the pertinent factors in a given system; see Chapter 3 for the methods I have used. The goal is that, by carefully investigating a set of devices, it maybe be possible to narrow down differences in device performance to a particular factor, and to then use this observation to inform further improvements. In general, I have been focussed on understanding differences in device performance in terms of the competition between charge generation and recombination. To this end, Chapter 4 investigates differences in non-radiative recombination, and therefore collection, in a set of devices made from polymers of different molecular weights. Meanwhile, Chapter 5 identifies differences in optical absorption and collection as the source of differences in performance of devices made from a different polymer, also with different molecular weights. Then Chapter 6 investigates optical absorption further, attempting to identify aspects of the molecular design which can affect absorption. On a different tack, but also related to charge generation, Chapter 7 investigates specifically the states formed immediately after light absorption, and the effect of the energetics of the blend components on the efficiency of free charge generation.

Chapter 2

Background Theory

Prelude

This chapter deals with the underlying theory involved in the operation of organic photovoltaics. Firstly, I go over the fundamentals of bond formation, specifically in semiconducting polymers. Bonding informs electronic structure which then determines the interaction of the material with light, which is the topic of Section 2.3. Meanwhile the macrostructure of the active materials in organic photovoltaic blends has a critical impact on how devices function, so this is dealt with in Section 2.4. I outline the specifics of how solar cell devices convert solar power to electrical power in Section 2.5, starting from a macroscopic treatment of the device physics in Section 2.5.1, and then moving to the microscopic picture of how free charges are generated (Section 2.5.2) and then transported to the contacts (Section 2.5.3). In Section 2.6 I consider the theoretical efficiency limits of solar cells, while the final topic I address in this chapter bis light propagation through a device in Section 2.7.

2.1 Bonding and the origin of π-conjugation

The first step towards understanding the behaviour of the materials used in organic photovoltaics is to understand their chemical structure, and the atoms and bonds which constitute them. Conjugated polymers are a sub-class of polymer which are semiconducting. The origin of this semiconducting behaviour is in the bonding structure of the polymers and will be introduced in this section.

Second-row atoms such as carbon, nitrogen, sulphur and oxygen have four atomic orbitals that are either available for bonding or are already filled: one s orbital and three p orbitals. s orbitals are spherically symmetric, whereas p or-

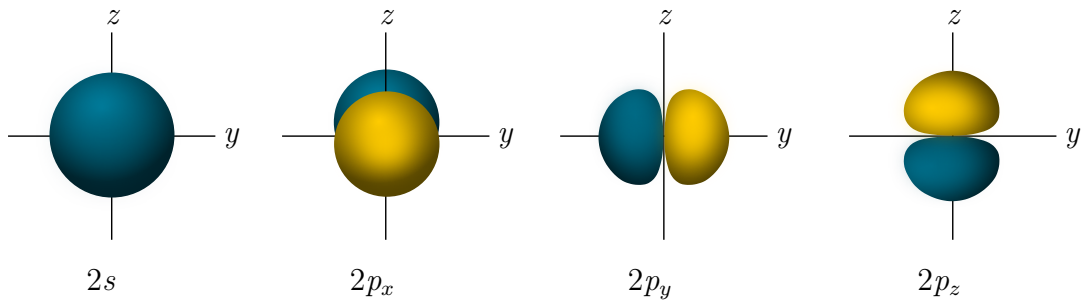


Figure 2.1: s and p atomic orbitals for the case of $n = 2$, the bonding orbitals of carbon, nitrogen and oxygen. s orbitals are spherically symmetric, and the $2s$ orbital has one node. $2p$ orbitals each have a nodal plane.

bitals are oriented along the x, y and z axes; the $2s$ and $2p$ orbitals are shown in Figure 2.1. A covalent bond forms when the atomic orbitals of the two atoms hybridise and form molecular orbitals. For the case of bonding with the four s and p orbitals, they can be hybridised in three different ways: to form four equal bonds (sp^3 hybridisation), three equal bonds plus one unhybridised p orbital (sp^2 hybridisation) or two equal bonds plus two unhybridised p orbitals (sp hybridisation). The hybridised bonding orbitals lie pointing along the direction of the bond, so form a direct overlap. This results in a strong interaction which forms the molecular orbitals, called σ bonds; the in-phase interaction forms the bonding σ orbital, and the out-of-phase interaction forms the antibonding σ^* orbital.

Meanwhile, the unhybridised p orbitals, in the case of sp^2 hybridisation lie perpendicular to the bonding plane, resulting in a weaker side-on interaction that gives rise to a π bonding orbital and corresponding π^* antibonding orbital. The weaker interaction means that the energy difference between the π and π^* orbitals is smaller than between the σ and σ^* orbitals, see Figure 2.2 for an illustration. The directionality of the bonds also results in another important distinction: namely that σ bonds are localised between the bonding nuclei, whereas the electron density in π bonds is above and below the sp^2 plane. Therefore an individual π bond is more available to interact with any neighbouring π systems; this can lead to longer range delocalisation within chains or networks of π-bonds or unhybridised p orbitals which is called conjugation, and forms the basis of electrical conduction in conjugated polymers.

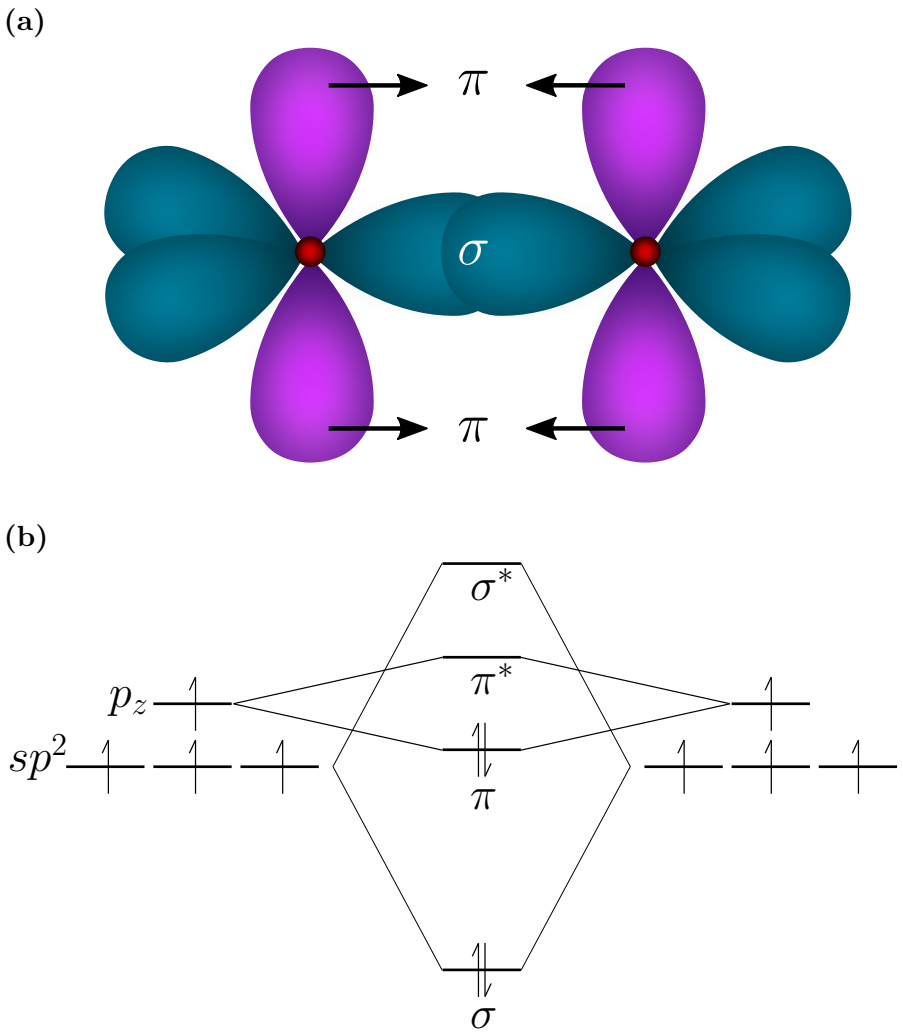


Figure 2.2: Diagram showing the formation of molecular orbitals from atomic orbitals, including the difference between σ and π bonds. (a) The formation of a σ and a π bond between two identical sp^2-hybridised molecules. (b) Energy diagram showing the formation of bonding and anti-bonding molecular orbitals, for the case of two identical sp^2-hybridised molecules. As in (a), both molecules contribute one sp^2 electron and one p electron. Anti-bonding orbitals are indicated by an asterix.

2.2 Semiconducting Polymers

By definition, a polymer is a very long chain of a repeated smaller unit, called the monomer. Its characteristics are determined by, but distinct from, the chemical structure of the monomer. A conjugated, or semiconducting, polymer is one in which there is continuous π delocalisation, or conjugation, along the polymer chain. The simplest example of a conjugated polymer is polyacetylene (Figure 2.3).

As can be seen from Figure 2.3, since the polymer can be considered infinite, there are two equivalent resonant structures available; due to degeneracy, if the carbon nuclei were fixed in position such that they were evenly spaced along the chain, there would be a continuous set of energy levels, half of which would be filled (i.e. bonding) and half of which would be empty (i.e. anti-bonding). The material would therefore behave like a one-dimensional metal because there would not be a band gap. However, if the distribution is distorted slightly, so that each carbon centre is slightly closer to one neighbour and slightly further away from the other, the loss in symmetry allows for a stronger overlap and interaction between the molecular orbitals associated with carbon centres that are now closer together. Conversely, the interaction between the carbon centres that are further apart is weakened, and the energy levels are no longer continuous, giving rise to an energy gap in the middle of the distribution. This phenomenon is called the Peierls distortion, and is responsible for the semiconducting behaviour of these materials. The frontier bonding orbital is called the highest occupied molecular orbital (HOMO) while the frontier antibonding orbital is called the lowest unoccupied molecular orbital (LUMO).

The Peierls distortion also brings to light the strong coupling between the spatial arrangement of the atoms and the electronic wavefunctions. This effect in turn allows semiconducting polymers to be able to accommodate charges more readily: the energy of an additional charge carrier can be lessened by the spatial arrangement of the atoms adjusting to best accommodate that charge. This species is called a polaron, encompassing the electronic and phonon modes. A similar species is an exciton, which is a neutral excitation formed either by the material absorbing a photon, or through electron injection (and corresponding hole

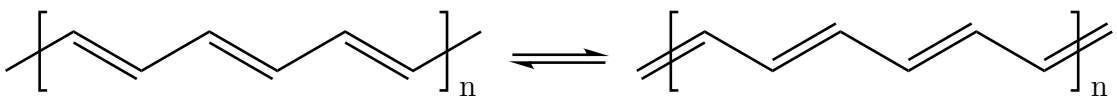


Figure 2.3: Two resonant structures of polyacetylene, resulting in electron delocalisation along the π system.

removal) from contacts with appropriate workfunctions. The bandgap of a material can be affected by its conformation; the interaction of conjugated polymers with light will be considered further in Section 2.3.2.

The simplest case of a polymer is when the monomer is a single moiety, such as a thiophene ring; this kind of polymer is called a homopolymer. However the properties of polymers can be more finely tuned by designing more complicated structures. The most common strategy used in polymers for organic photovoltaics are co-polymers, whereby the monomer unit is composed of at least two moieties. Commonly for OPV a combination of electron-rich and electron-poor subunits are chosen, which results in a narrowing of the polymer bandgap; these polymers are referred to as donor-acceptor co-polymers.

2.3 Electromagnetic Interactions

Interactions with light form the basis of solar cell function. In this section, I first treat the interaction of light with a general solid, from a classical and then a quantum perspective. Since the principal light-absorbing species in the organic photovoltaics I study in this thesis are the polymers, I then briefly discuss the particular traits of light absorption by conjugated polymers.

2.3.1 Interaction of light with solids

When light impinges on a solid, five processes could occur: the light could be reflected, transmitted, absorbed, scattered, or stimulate emission; see Figure 2.4. The probability of these happening depends on the properties of the material; the degree of reflection, transmission and absorption is determined by the complex refractive index $\tilde{n} = n + i\kappa$. Scattering is caused by inhomogeneities in the film or at the interfaces, and is generally negligible in OPV films. Stimulated emission is only appreciable if there is a large excited state population, which is not the case for the regimes encountered in OPV so is also regarded as negligible.

An incoming electric field $\mathbf{E}$, propagating along the $\mathbf{r}$ direction can be described as $\mathbf{E}(\mathbf{r}, t) = \mathbf{E}_0[\exp i(\mathbf{k} \cdot \mathbf{r} - \omega t) + \exp i(\mathbf{k} \cdot \mathbf{r} + \omega t)]$, where $\mathbf{E}_0$ is the wave amplitude, $\mathbf{k}$ is the wave vector and ω is the angular frequency. The refractive index describes the reduction of the wavelength in the medium with respect to vacuum, so in the medium $|\mathbf{k}| = 2\pi\tilde{n}/\lambda = \tilde{n}\omega/c$. By substituting this and the definition $\tilde{n} = n + i\kappa$ into the expression for $\mathbf{E}$, and considering a plane wave travelling in the z direction,

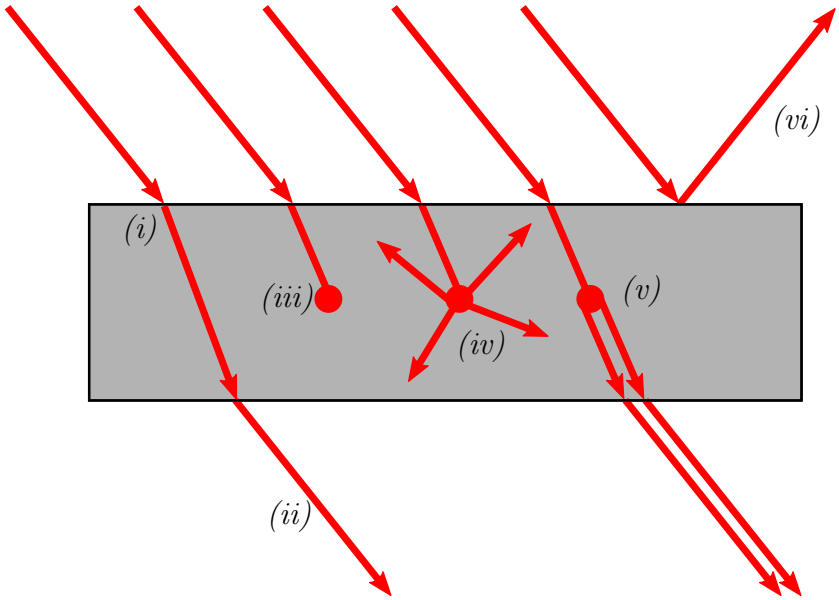


Figure 2.4: The possible processes when light hits a solid: (i) refraction, (ii) transmission, (iii) absorption, (iv) scattering, (v) stimulated emission, (vi) reflection.

we arrive at:

$$\mathbf{E} = \mathbf{E}_0 \exp\left(-\frac{\kappa\omega z}{c}\right)\left[\exp i\left(\frac{n\omega z}{c} - \omega t\right) + \exp i\left(\frac{n\omega z}{c} + \omega t\right)\right] \tag{2.1}$$

The intensity of light is proportional to the square of the electric field, so the intensity I decays in a medium exponentially with decay constant $2\kappa\omega/c$. The absorption coefficient α is defined using the Beer-Lambert law $I = I_0 \exp(-\alpha z)$, so we have the relation:

$$\alpha = \frac{2\kappa\omega}{c} = \frac{4\pi\kappa}{\lambda} \tag{2.2}$$

This relation is useful because it is possible experimentally to determine either κ and α, so it is useful to be able to convert between the two. Another important quantity is the complex dielectric function $\varepsilon = \varepsilon_1 + i\varepsilon_2$, where $\tilde{n}$ and ε are related through $\varepsilon = \tilde{n}^2$. Therefore the following relations can be derived:

$$\varepsilon_1 = n^2 - \kappa^2 \tag{2.3}$$

$$\varepsilon_2 = 2n\kappa \tag{2.4}$$

In order to understand how to determine ε theoretically, it is necessary first to understand the fundamentals of the process of absorption. If the interaction of light with a system is considered a first-order perturbation from the stationary state, time-dependent perturbation theory can be used to understand the effect.

The time-dependent Schrödinger equation is:

$$\hat{\boldsymbol{H}}\Psi = i\hbar\frac{\partial\Psi}{\partial t} \tag{2.5}$$

To relate optical properties to the electronic wavefunctions, here I assume a two-level system, such that the total wavefunction can be expressed, using $\omega_n = E_n/\hbar$:

$$\Psi(\mathbf{r},t) = a_1(t)\psi_1(\mathbf{r})\exp(-i\omega_1 t) + a_2(t)\psi_2(\mathbf{r})\exp(-i\omega_2 t) \tag{2.6}$$

The first-order perturbation Hamiltonian is $\hat{\boldsymbol{H}}(\mathbf{r},t) = \hat{\boldsymbol{H}}_0(\mathbf{r}) + \hat{\boldsymbol{H}}'(\mathbf{r},t)$. Expanding out eq. (2.5):

$$a_1\hat{\boldsymbol{H}}_0\Psi_1 + a_2\hat{\boldsymbol{H}}_0\Psi_2 + a_1\hat{\boldsymbol{H}}'\Psi_1 + a_2\hat{\boldsymbol{H}}'\Psi_2 = i\hbar\left(\frac{\mathrm{d}a_1}{\mathrm{d}t}\Psi_1 + a_1\frac{\partial\Psi_1}{\partial t} + \frac{\mathrm{d}a_2}{\mathrm{d}t}\Psi_2 + a_1\frac{\partial\Psi_1}{\partial t}\right) \tag{2.7}$$

Cancelling out terms using eq. (2.5) evaluated for the stationary case $\hat{\boldsymbol{H}}_0$:

$$a_1\hat{\boldsymbol{H}}'\Psi_1 + a_2\hat{\boldsymbol{H}}'\Psi_2 = i\hbar\left(\frac{\mathrm{d}a_1}{\mathrm{d}t}\Psi_1 + \frac{\mathrm{d}a_2}{\mathrm{d}t}\Psi_2\right) \tag{2.8}$$

Multiplying from the left by ψ_2^*, integrating over all space, and switching to bra-ket notation:

$$\begin{aligned} a_1\langle 2|\hat{\boldsymbol{H}}'|1\rangle\exp(-i\omega_1 t) + a_2\langle 2|\hat{\boldsymbol{H}}'|2\rangle\exp(-i\omega_2 t) \\ = i\hbar\left(\frac{\mathrm{d}a_1}{\mathrm{d}t}\langle 2|1\rangle\exp(-i\omega_1 t) + \frac{\mathrm{d}a_2}{\mathrm{d}t}\langle 2|2\rangle\exp(-i\omega_2 t)\right) \end{aligned} \tag{2.9}$$

Since the wavefunctions form a normalised and orthogonal basis set, $\langle n|n\rangle = 1$, and $\langle n|m\rangle = 0$. In addition, the system is assumed to be initially in state 1, and the perturbation is sufficiently small that we can assume $a_2 \approx 0$. Eliminating terms in eq. (2.9), and rearranging to solve for $\mathrm{d}a_2/\mathrm{d}t$:

$$\frac{\mathrm{d}a_2}{\mathrm{d}t} = \frac{a_1(t)}{i\hbar}\exp(i\omega_{12}t)\langle 2|\hat{\boldsymbol{H}}'|1\rangle \tag{2.10}$$

where ω_{12} is defined by $\omega_{12} = \omega_2 - \omega_1$. Now I assume that the perturbation $\hat{\boldsymbol{H}}'(\mathbf{r},t)$ can be separated into a component which is oscillating in time, and a component that is stationary with respect to time. $\hat{\boldsymbol{H}}'(\mathbf{r},t) = \hat{\boldsymbol{H}}''(\mathbf{r})\,[\exp(i\omega t) + \exp(-i\omega t)]$. Then, integrating from $t = 0$ to $t = t$, assuming that the perturbation is small

and therefore $a_1 \approx 1$:

$$a_2 = -\frac{\langle 2|\hat{\boldsymbol{H}}''|1\rangle}{\hbar}\left(\frac{\exp\left(i\left(\omega_{12}+\omega\right)t\right)-1}{\omega_{12}+\omega}+\frac{\exp\left(i\left(\omega_{12}-\omega\right)t\right)-1}{\omega_{12}-\omega}\right) \tag{2.11}$$

It is evident from eq. (2.11) that the function $a_2(\omega)$ is dominated by the fraction with $\omega_{12}-\omega$ for $\omega_{12} \approx \omega$. So I calculate the probability of finding the system in state 2 after a time t by taking $P_{1\to 2} = a_2^* a_2$:

$$P_{1\to 2} = \frac{|\langle 2|\hat{\boldsymbol{H}}''|1\rangle|^2}{\hbar^2}\left(\frac{2-\exp(i(\omega_{12}-\omega)t)-\exp(-i(\omega_{12}-\omega)t)}{(\omega_{12}-\omega)^2}\right) \tag{2.12}$$

$$= \frac{4|\langle 2|\hat{\boldsymbol{H}}''|1\rangle|^2}{\hbar^2}\frac{\sin^2((\omega_{12}-\omega)t/2)}{(\omega_{12}-\omega)^2} \tag{2.13}$$

where I use the relation $\sin^2\alpha = (2-\mathrm{e}^{2\alpha}-\mathrm{e}^{-2\alpha})/4$. Furthermore we can assume that the system is subjected to a broadband frequency distribution $g(\omega_{12})$, which we assume to be nearly constant over the range of frequencies where the integrand is significant, so we must integrate eq. (2.12) over ω; the definite integral $\int_{-\infty}^{\infty}(\sin^2 x/x^2)\mathrm{d}x = \pi$ is used.

$$P_{1\to 2} = \frac{2\pi|\langle 2|\hat{\boldsymbol{H}}''|1\rangle|^2}{\hbar^2}g(\omega_{12})t \tag{2.14}$$

The transition rate W is found by differentiating eq. (2.14) with respect to time, while also converting to energy units:

$$W_{1\to 2} = \frac{2\pi}{\hbar}|\langle 2|\hat{\boldsymbol{H}}''|1\rangle|^2 g(\hbar\omega_{12}) \tag{2.15}$$

Equation (2.15) is referred to as Fermi's Golden Rule, and can be used to describe the transition rate due to electromagnetic radiation [39–42]. In this context, the momentum of the particle is increased by $e\mathbf{A}$ by the electric field, where $\mathbf{A}$ is the vector potential of the applied field, $\mathbf{A} = \mathbf{A}_0[\exp(i(\mathbf{k}\cdot\mathbf{r}-\omega t))+\exp(-i(\mathbf{k}\cdot\mathbf{r}-\omega t))]$. Since the atomic spacing is small relative to the wavelength of the light, we can use a Taylor expansion to simplify this expression: $\mathbf{A} \approx \mathbf{A}_0[\exp(-i\omega t)+\exp(i\omega t)](1+\mathbf{k}\cdot\mathbf{r}+\cdots) \approx \mathbf{A}_0[\exp(-i\omega t)+\exp(i\omega t)]$. So the Hamiltonian for the system is:

$$\hat{\boldsymbol{H}} = \frac{(\mathbf{p}+e\mathbf{A})^2}{2m_0} \tag{2.16}$$

$$= \frac{\mathbf{p}^2}{2m_0}+\frac{e\mathbf{p}\cdot\mathbf{A}_0[\exp(-i\omega t)+\exp(i\omega t)]}{m_0}+\frac{(e\mathbf{A})^2}{2m_0} \tag{2.17}$$

Because we have assumed the perturbation is small, we can disregard the $\mathbf{A}^2$ term,

and $\hat{\boldsymbol{H}}_{\mathbf{0}} = \mathbf{p}^2/2m_0$, where m_0 is the electron mass, so

$$\hat{\boldsymbol{H}}' = \frac{e\mathbf{p}\cdot\mathbf{A}_0[\exp(-i\omega t)+\exp(i\omega t)]}{m_0} \tag{2.18}$$

Assuming no static applied field, $\mathbf{E} = -\partial\mathbf{A}/\partial t = i\omega\mathbf{A} = \mathbf{E}_0[\exp(-i\omega t)+\exp(i\omega t)]$. So:

$$\hat{\boldsymbol{H}}' = \frac{e}{i\omega m_0}\mathbf{p}\cdot\mathbf{E}_0[\exp(-i\omega t)+\exp(i\omega t)] \tag{2.19}$$

The commutator relationship $[\hat{\boldsymbol{H}}, \hat{\boldsymbol{r}}] = \hat{\boldsymbol{H}}\hat{\boldsymbol{r}} - \hat{\boldsymbol{r}}\hat{\boldsymbol{H}} = (\hbar/im)\hat{\boldsymbol{p}}$ can be used to write the momentum operator in terms of energy and the position operator. Since the Hamiltonian is Hermitian, and $\langle 2|\hat{\boldsymbol{p}}|1\rangle = (im_0/\hbar)\langle 2|\hat{\boldsymbol{H}}\hat{\boldsymbol{r}} - \hat{\boldsymbol{r}}\hat{\boldsymbol{H}}|1\rangle$, we can arrive at:

$$\langle 2|\hat{\boldsymbol{p}}|1\rangle = \frac{im_0}{\hbar}(E_2 - E_1)\langle 2|\hat{\boldsymbol{r}}|1\rangle \tag{2.20}$$

Substituting this expression into eq. (2.19) yields:

$$\hat{\boldsymbol{H}}' = \frac{e}{\omega\hbar}(E_2 - E_1)\mathbf{r}\cdot\mathbf{E}_{\mathbf{0}}[\exp(-i\omega t)+\exp(i\omega t)] \tag{2.21}$$

For a transition from state 1 to state 2, as we've previously established, the resonant frequency of the function is $\omega_{12} = (E_2 - E_1)/\hbar$; thus the transition can be described by:

$$\langle 2|\hat{\boldsymbol{H}}''|1\rangle = e|\mathbf{E}_0|\langle 2|\mathbf{r}\cdot\mathbf{e}_0|1\rangle \tag{2.22}$$

where $\mathbf{e}_0$ is the unit vector in the direction of $\mathbf{E_0}$, and the quantity $e\langle 2|\mathbf{r}\cdot\mathbf{e}_0|1\rangle$ is called the transition dipole matrix element d_{12}. The name derives from the classical description of light absorption, in which an atom which absorbs or emits a photon must temporarily possess an electric dipole that oscillates at the photon frequency. It is evident from this expression that the strength of a transition is determined by the spatial overlap between the final and initial states. Furthermore, the symmetry of the $\psi_2^*\mathbf{r}\cdot\mathbf{e}_0\psi_1$ function determines whether the transition is allowed. Equation (2.22) can then be used in eq. (2.15) to determine the transition rate of a particle in an electromagnetic field:

$$W_{1\to 2} = \frac{2\pi}{\hbar}d_{12}^2|\mathbf{E_0}|^2 g(\hbar\omega_{12}) \tag{2.23}$$

Now it is possible to relate this quantity to the absorption coefficient α and the dielectric function [42]. As alluded to previously, the absorption coefficient is defined by:

$$\frac{\mathrm{d}I}{\mathrm{d}z} = -\alpha I \tag{2.24}$$

where I is the intensity of light propagating in the z-direction. From the conservation of energy:

$$-\frac{\mathrm{d}I}{\mathrm{d}z} = \frac{\mathrm{d}U}{\mathrm{d}t} = NW_{12}\hbar\omega_{12} \tag{2.25}$$

where U is the energy density of the radiation, which is depleted by the material; N is the volume density of atoms which can transition. Using the definition of the intensity of an electromagnetic field $I = nc\varepsilon_0|E_0|^2/2$, where n is the real part of the refractive index, and eqs. (2.24) and (2.25), the absorption coefficient can be written:

$$\alpha = \frac{2NW_{12}\hbar\omega_{12}}{nc\varepsilon_0|E_0|^2} \tag{2.26}$$

Substituting the expression for W_{12}, and using eqs. (2.2) and (2.4) to interrelate α and ε, such that $\varepsilon_2 = \alpha nc/\omega_{12}$, we have:

$$\varepsilon_2 = \frac{4\pi N\mu_{12}^2}{3\varepsilon_0} g(\hbar\omega_{12})\delta(\omega - \omega_{12}) \tag{2.27}$$

where μ_{12} is the transition dipole moment of the transition. The dipole moment operator $\hat{\boldsymbol{\mu}}$ is multiplication by $-e\mathbf{r}$, summed across all electrons in the molecule, which results in the transition dipole moment $\mu_{ij} = e\langle f|\hat{\boldsymbol{r}}|i\rangle$. In arriving at eq. (2.27), I have averaged over all orientations, thus introducing a factor of 1/3, and replacing d_{12}^2 with μ_{12}^2. If we now consider a material with a series of possible $i \to j$ transitions, we have:

$$\varepsilon_2(\omega) = \frac{2\pi Ne^2}{\varepsilon_0 m_0} \sum_{ij} \frac{f_{ij}}{\omega} \delta(\omega - \omega_{ij}) \tag{2.28}$$

where f is the oscillator strength, which is a dimensionless number and in turn is defined:

$$f_{ij} = \frac{2}{3}\frac{m_0}{\hbar e^2}\omega_{12}\mu_{ij}^2 \tag{2.29}$$

An important property of the oscillator strength is expressed in the Thomas-Reiche-Kuhn sum rule [43]:

$$\sum_j f_{ij} = N_e \tag{2.30}$$

where N_e is the number of electrons in the system, and the oscillator strength is summed from state i to all other possible states j. The significance of the relationships between f, ε and α is that they allow for the calculation of experimentally-determined quantities.

So far we have only considered the full wavefunction of the system, including the electrons and the nuclei. Due to the very different masses of these components,

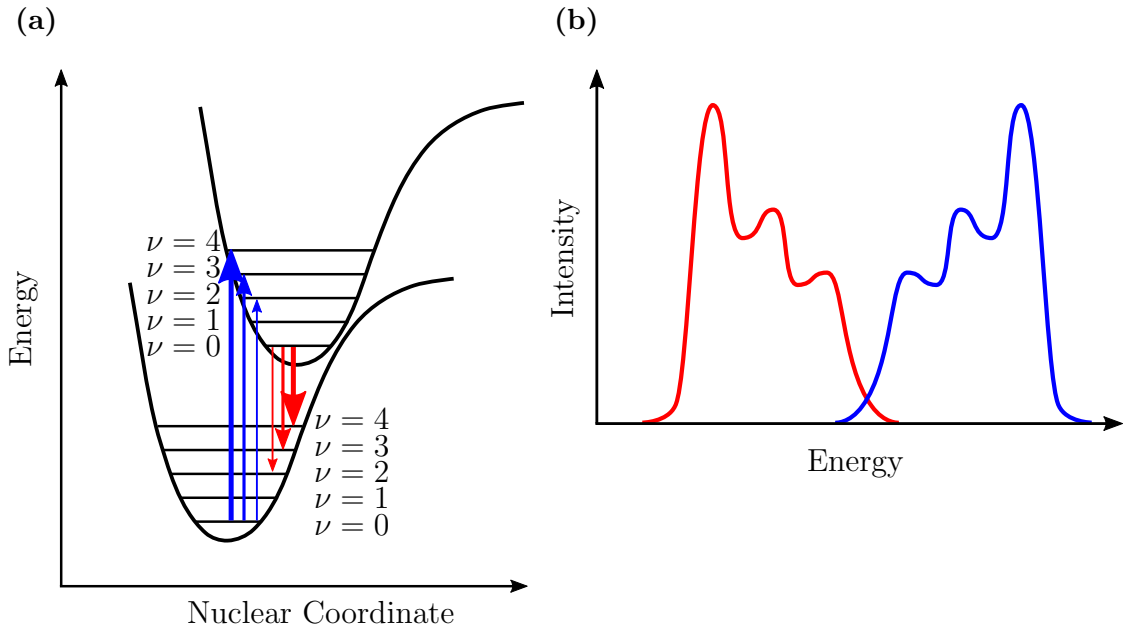


Figure 2.5: Illustration of absorption and emission in a molecule. (a) A schematic showing vertical electronic transitions between ground and excited state potential energy surfaces (represented by simple curves). Also shown are the available vibrational levels, indicated by integer values of ν. Excitation from the ground state is shown by red arrows, while emission from the excited state is shown by blue arrows. In both processes, the relative strengths of the transitions are indicated by the weights of the arrows; the strongest transitions have the greatest wavefunction overlap. (b) A schematic showing the absorption (red) and emission (blue) profiles resulting from the vertical transitions. In an ideal case, absorption and emission spectra are mirror images, with the shift between maxima giving the Stokes shift.

and hence different time-scales of motion, we can express the overall wavefunction as the product of the constituent electronic and nuclear wavefunctions; this is called the Born-Oppenheimer approximation. Therefore the total wavefunction of the molecule can be expressed as $\Psi = \Psi_{\text{elec}}\Psi_{\text{nuc}}\Psi_{\text{spin}}$. The rotational degrees of freedom need not be considered here since we are focussing on condensed phases.

Before going further, it is useful to define the concept of a potential energy surface (PES). Considering first the simplest example, a diatomic molecule: the potential energy of each atom has a minimum at a certain distance relative to the other, which corresponds to the bond length. If the atoms are closer, they experience strong repulsion, and if they are further apart, the electronic overlap is lessened resulting in decreased net stabilisation and a higher potential energy; at the infinite limit, the atoms are dissociated and are no longer affected by each other. This feature of bonded atoms is general, and can be applied to larger molecules or collections of molecules; in these situations, there are more degrees of freedom, so instead of a simple one-dimensional potential curve, the potential energy is multi-dimensional. This potential is termed the potential energy surface, and is affected by the electronic state of the molecule.

In addition to electronic states, vibrations are also quantised, such that each electronic state has a vibrational manifold of allowed vibrational states. These states can be understood in analogy with standing waves of a string, or a particle in an infinite well. Each allowed vibrational state has an integer number of nodes (see Figure 2.5a).

The Franck Condon principle is the application of the Born-Oppenheimer approximation to photon absorption and emission. As Figure 2.5 shows, an instantaneous electronic transition between two states can be represented as a vertical transition in coordinate space, or in the PES; this means that the nuclear coordinates only change after the electronic transition has occurred. Since the lowest vibrational states of the two electronic states are not necessarily the same nuclear configuration, upon photon absorption, the molecule is in a higher vibrational state, and only subsequently is able to relax into the ground state. Emission is precisely the opposite process, comprising a vertical transition from the lowest vibrational state of the excited state to a higher vibrational transition of the ground state, followed by relaxation to the lowest vibrational state.

The strength of the transition is determined by the magnitude of the transition dipole moment and the population of the initial state, so the absorption and emission spectra have different shapes. The strongest absorption is from the lowest vibrational state of the electronic ground state to the vibrational manifold of the

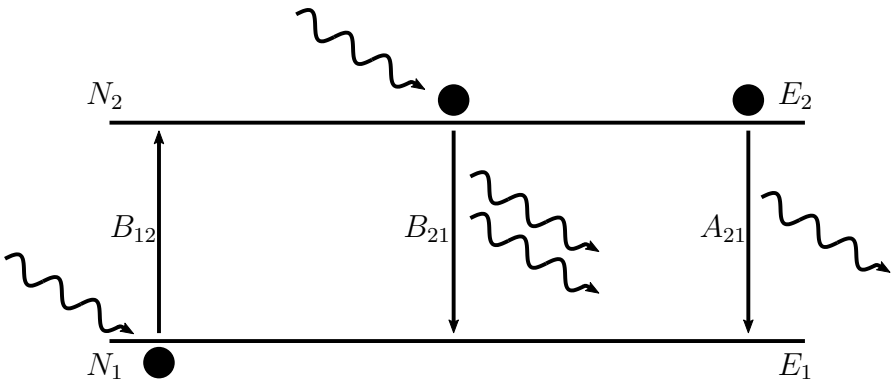


Figure 2.6: A schematic of the possible interactions of light with a two level system, with levels at E_1 and E_2, having occupancies of N_1 and N_2 respectively. The rate coefficient of absorption is B_{12}, spontaneous emission is A_{21} and stimulated emission is B_{21}.

electronic excited state. Conversely, the strongest emission is from the lowest vibrational state of the electronic excited state to the vibrational manifold of the electronic ground state. This results in absorption and emission spectra often appearing to be mirror images of each other. The difference in wavelength between the maxima of the absorption and emission spectra is called the Stokes shift, and can give information about the system and its environment. Relaxation processes which can contribute to a Stokes shift include thermalisation of the electron (hole) to the edge of the conduction (valence) bands, vibrational relaxation, excitation localisation, exciton formation, exciton migration and structural relaxation.

A final general consideration with regards to interactions of materials with light is the interrelationship between absorption and emission rates. Figure 2.6 shows a two level system with the possible processes and their governing rates. An incoming photon can either be absorbed by a molecule in the ground state, promoting it to the excited state (B_{12}), or it can be absorbed by a molecule in the excited state, stimulating emission of two photons in phase (B_{21}). Finally a molecule in the excited state can spontaneously decay to the ground state, emitting a photon (A_{21}). For a system in thermal equilibrium, the rate of excitations must be equal to the rate of relaxations.

$$B_{12}N_1u(\nu) = A_{21}N_2 + B_{21}N_2u(\nu) \tag{2.31}$$

In eq. (2.31), A represents the spontaneous process, while B terms involve absorption from the environmental blackbody radiation, $u(\nu)$, given by eq. (2.32),

where $h\nu = E_2 - E_1$.

$$u(\nu) = \frac{8\pi h\nu^3}{c^3} \frac{1}{\exp\left(h\nu/k_B T\right) - 1} \tag{2.32}$$

The state occupancies are governed by Boltzmann statistics, thus:

$$\frac{N_2}{N_2} = \frac{g_2}{g_1} \exp\left(-\frac{h\nu}{k_B T}\right) \tag{2.33}$$

where g_n is the degeneracy of the nth state. From these expressions it is possible to derive interrelationships between the rate constants, which are a further reminder of the reciprocity between the absorption and emission processes:

$$g_1 B_{12} = g_2 B_{21} \tag{2.34}$$

$$A_{21} = \frac{8\pi h\nu^3}{c^3} B_{21} \tag{2.35}$$

2.3.2 Interaction of light with conjugated polymers

The above discussion is general, but there are some idiosyncrasies for the particular case of conjugated polymers which must be considered. Firstly, as mentioned previously, in molecular materials there is a strong connection between electronic and vibrational processes, which leads to excitations being localised. In addition the electron and hole are relatively tightly bound because of the low dielectric constant of most conjugated polymers; this electron-hole entity is called an exciton, and tends to decay on the order of ∼ns.

A polymer is essentially infinite, but the excitation does not extend along the whole chain and so the chromophore, the photoactive sub-entity, must be understood. A chromophore can be defined as the coherence length of the exciton centre-of-mass wavefunction [44, 45]. In one-dimensional systems, such as polymers, any disorder localises wavefunctions; the density of states has a tail which extends into the bandgap (more on this in Section 2.4), and these states are more localised than the higher-lying states. Increased disorder results in more localisation and therefore a decreased chromophore size, as well as increased inhomogeneous broadening. Meanwhile, it can be shown that the more planar a polymer chain, the more extended the chromophore, the greater the exciton bandwidth and lower the transition energy.

2.4 Disorder in OPV devices

As alluded to in Section 2.3, conjugated polymers, and blends based on them, are inherently disordered systems. Disorder can be classified into structural, sometimes called configurational, and energetic disorder: structural disorder is specifically variations in the arrangement of the molecules, while energetic disorder corresponds to variations in the energy levels of the molecules. This section therefore describes firstly the causes of structural disorder in a polymer-only film, and then that in a polymer:fullerene blend film. Then I discuss the causes of energetic disorder, which can include the presence of structural disorder. And finally I touch on the related subject of doping.

2.4.1 Polymer structural disorder

Polymers in general can adopt a wide range of conformations in a film, from rigid rods to random coils, dependent on processing as well as the polymer chemical structure and molecular weight distribution [46, 47]. In other words, the local atomic environment along the polymer chain is affected by nanoscale (polymer chemical structure), microscale (molecular weight distribution) and macroscale (e.g. phase segregation) factors.

There are two principal components of the chemical structure of a typical conjugated polymer: the polymer backbone and the aliphatic side-chains. The conjugated segments of the polymers tend to be planar due to the stabilising effect of the π system in the polymer backbone, which also promotes chain rigidity. Especially if the polymer backbone also has a high torsional potential tending to planarise the backbone, and is therefore stiff, conjugated polymers can have a high degree of microstructural order because neighbouring backbones can stack.

The ability of the polymers to stack is also affected by the side-chains. Conjugated polymers are typically synthesised with alkyl side-chains which promote solubility without changing the optoelectronic properties. These are typically around six to ten carbons long for polymers used in solar cells, and can be linear or branched. Branched side chains result in more soluble polymers for fewer total sp^3 carbons so are often used [48–50]. Good solubility of the polymer is important for both processing and synthesis, allowing a higher degree of polymerisation before the polymer ceases to be soluble and stops the reaction. In addition, the relative solubility of the polymer and fullerene in the casting solvent can strongly affect the blend morphology, and this can be tuned with the polymer side-chain length [51]. However since the side-chains are aliphatic, they are insulating and

do not contribute to the optoelectronic properties of the material, so their volume should be minimised. The texture, or the preferential orientation of the polymer relative to the substrate, can also be affected by the side-chains, possibly impacting the device performance [52].

In addition, the position of the side-chains on the polymer backbone can promote or hinder crystallinity. An example of the effect of this is the comparison between regioregular and regiorandom polymers [53]. Regioregularity arises from the polymerisation of only one isomer of the monomer, in a regular way such that each monomer is bonded 'head-to-tail' to its neighbours. If this isomerism is not controlled, a regiorandom polymer is synthesised, where steric hindrance of the side-chains may result in the backbone twisting. Such effects have consequences for chain-packing and therefore properties such as charge transport.

Unlike small molecules, polymers do not have a precisely defined molecular weight, since they can be composed of any number of consecutive monomers. The term polydisperse describes a polymer sample which contains a range of chain lengths. The opposite, monodisperse chains, where all the polymer chains have the same number of monomer units, is impossible to achieve by the common synthesis methods used to make conjugated polymers for OPV: Suzuki or Stille coupling, both of which are condensation reactions. Polydispersity arises from the statistics of condensation reactions, as well as out of heterogeneities in the reaction vessel; for example, slight variations in temperature may lead the reaction to occur faster in one region of the vessel than somewhere else. Therefore the degree of polydispersity can vary greatly between different synthesis reaction schemes and different reaction geometries; for example a way to decrease polydispersity is to conduct the reaction in a droplet microreactor [54], where the reaction takes place in a series of small droplets whose conditions can be much better controlled than those of a large volume.

The distribution of chain lengths of a given polymer sample, and therefore its molecular weight, is often log-normally distributed, see Figure 2.7. It is common to define two separate average molecular weight values to describe the sample: the first, M_n, is the number-average molecular weight, which is simply the arithmetic mean of the of the molecular weights of all the polymer molecules (eq. (2.36)), while the second is the weight-average molecular weight, M_w (eq. (2.37)). The weight-average value is useful because the larger molecules have more of an influence on properties such as viscosity than smaller molecules, and the weighted average takes this into consideration. The polydispersity index, or PDI, is defined as the ratio of the two molecular weight averages (eq. (2.38)), and is equal to or greater

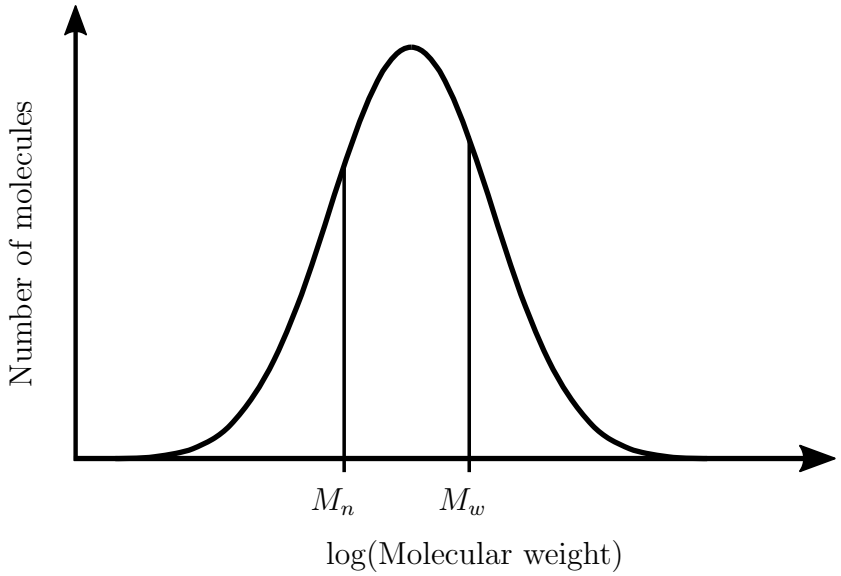


Figure 2.7: A diagram showing a typical Gaussian distribution of molecular weights, marked with the corresponding M_n and M_n values.

than 1; a monodisperse sample has identical M_n and M_w, so has a PDI of 1.

$$M_n = \frac{\sum_i N_i M_i}{\sum_i N_i} \tag{2.36}$$

$$M_w = \frac{\sum_i N_i M_i^2}{\sum_i N_i M_i} \tag{2.37}$$

$$\text{PDI} = \frac{M_w}{M_n} \tag{2.38}$$

Molecular weight distributions of polymer samples are often measured using size exclusion chromotography (SEC), also known as gel permeation chromatography (GPC). The polymer is dissolved in a solvent and passed through a column: smaller molecules are able to penetrate pores in the column more easily than larger molecules, so take longer to pass through the column. In this way the sample is spatially separated according to molecular size. The solvent is passed through the column at a constant speed, and the concentration of polymer exiting the column as a function of time is measured using a UV probe. The measurement must be calibrated against samples of known molecular weights; typically polystyrene is used. However this can introduce systematic errors since polystyrene tends to adopt a more coiled conformation in solution to conjugated polymers, resulting in conjugated polymer molecular weights being overestimated by up to approximately a factor of 2 [55].

Most properties of a polymer are affected by its molecular weight, at least

in some regimes [56]. Many of the polymers studied in OPV are classified as semi-crystalline, meaning that (parts of) the polymer chains can crystallise. A collection of low molecular weight semi-crystalline polymer chains is more likely to align fully extended, forming crystallites as shown in Figure 2.8. As the molecular weight increases, however, this becomes impossible under standard conditions due to entropic considerations, and instead the polymer film texture becomes that of lamellar crystallites surrounded by amorphous and entangled polymer. In this latter case, a single polymer chain may be part of multiple crystallites. Therefore as the molecular weight is increased past a critical point, the overall film texture is not strongly affected because only sections of each molecule are involved in the crystalline regions, with the rest being incorporated into the amorphous regions [57]. Meanwhile a polymer which cannot crystallise instead forms a more homogeneous amorphous entangled morphology. This invariability in microstructure for high MW polymers then results in macroscopic properties of the film often not being strongly affected by small changes in processing. The precise relationship of a particular parameter to molecular weight of course depends on the property. For instance, the mobility of the workhorse conjugated polymer P3HT in the bulk was found to decrease for high molecular weight polymer samples [58], because the homogenous extended crystalline structure was most conducive to bulk transport of charges across the film. On the other hand, another study found that the field-effect transistor mobility, which measures the mobility through a very thin layer, saturates at high molecular weights [57]. Another example is that in low MW regimes, properties such as melting temperature are strongly related to the polymer MW [57].

Ultimately therefore, since different molecular weight polymers can access different morphologies, which in turn affects the local atomic environment along the polymer chain, the molecular weight can have a strong effect on the structural disorder of a film. A related consequence of variations in molecular weight is the corresponding variations in concentrations of polymer chain end-groups, which can themselves change the packing.

Finally, the processing conditions can have a strong effect on the final polymer conformation. For example, the choice of casting solvent can greatly affect the polymer conformation in solution, which in turn affects the conformation upon casting [59]. A good solvent exhibits favourable interactions between the solvent molecules and the polymer, meaning that the polymer chains expand so as to maximise the number of these favourable interactions. Meanwhile a bad solvent does not exhibit favourable interactions and so the polymer will tend to contract

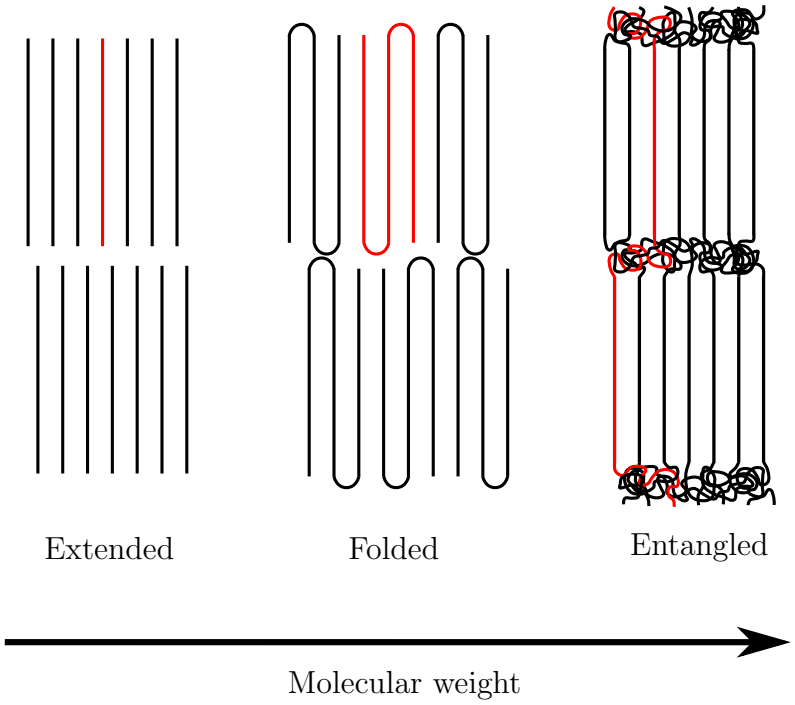


Figure 2.8: Effect of polymer molecular weight on morphology. Shorter chains can more readily form extended crystalline structures, but beyond a critical point, the chains entangle and a semi-crystalline morphology develops. A single chain is highlighted in each morphology type.

as the polymer-polymer interactions are more favourable than the polymer-solvent interactions. Furthermore the temperature of the solvent affects both the solvation of the polymer, by affecting the entropic term, and the speed at which the solvent evaporates upon casting [60]. The slower the solvent evaporates, the more time the polymer has to form its equilibrium conformation; fast solvent evaporation results in the polymer conformation being frozen in the solvated arrangement. For this reason, some solvent additives can affect the polymer conformation by introducing a two-phase drying [61] if the additive boiling point is higher than the solvent boiling point. Similarly, post-treatments such as thermal or solvent-vapour annealing alter the film microstructure after casting by allowing the polymer chains more time to equilibrate [62].

2.4.2 Polymer:fullerene bulk heterojunctions

As has been mentioned already, the active material in most organic photovoltaic devices is a blend of a polymer with a small molecule such as a fullerene. The materials are co-dissolved in the casting solution, and the microstructure formed in the film depends on the mutual miscibility of the blend components. The purpose of the blend is to support charge separation and transport (more in Sections 2.5.2

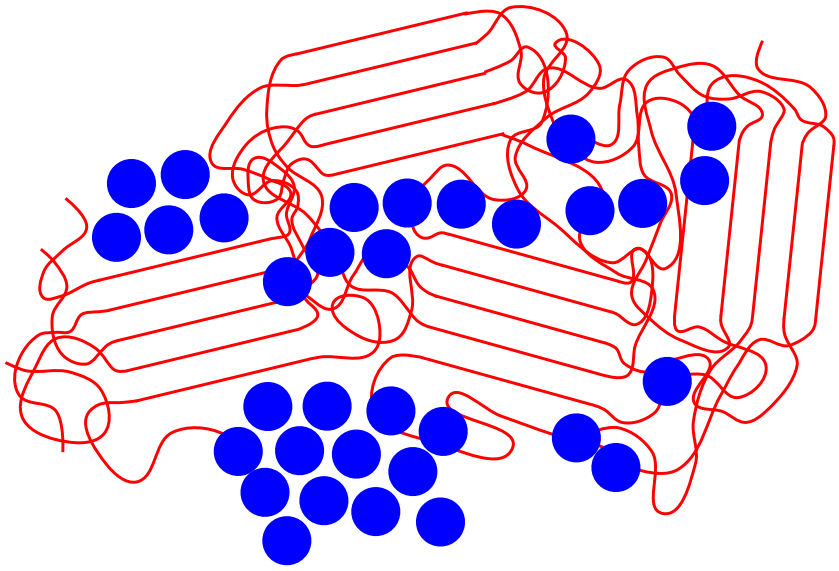


Figure 2.9: Schematic of the arrangement of molecules in a typical polymer:fullerene bulk heterojunction. The polymer is shown in red and the fullerene in blue. A bulk heterojunction has many different phases, including crystalline polymer, amorphous polymer, aggregated or crystalline fullerene and mixed polymer-fullerene.

and 2.5.3), and so well-controlled phase separation is important. The goal is to have enough interface to promote charge separation, but enough percolation for charge transport, so the composition and length scales of the phases formed are both very important [63–65]. This kind of microstructure is called a bulk heterojunction (BHJ); see Figure 2.9 for a schematic.

As can be seen from Figure 2.9, there are a few different kinds of phases present in a typical polymer:fullerene BHJ: a polymer-rich phase, a fullerene-rich phase, and a mixed phase [66]. Furthermore there are both crystalline and amorphous polymer regions, as well as aggregated and disperse fullerene regions, representing a range of structural environments which add to the structural disorder. In addition, the microstructure after solution processing is typically kinetically trapped, and not at thermodynamic equilibrium. And so, depending on the glass transition temperature of the polymer, that is, the temperature required for the polymer to be able to flow, the blend microstructure can be sensitive to temperature even after processing. A possible variation on BHJs is to use cross-linking moieties or block co-polymers to afford greater control over the microstructure formation [67, 68].

In Section 2.4.1, I focused on the effect of the polymer on the disorder in a polymer:fullerene film, but the other component of the blend can have a strong effect too. Here I focus on fullerenes because they were the acceptor used in every blend I studied. Specifically I have predominantly used $PC_{60}BM$ and $PC_{70}BM$, al-

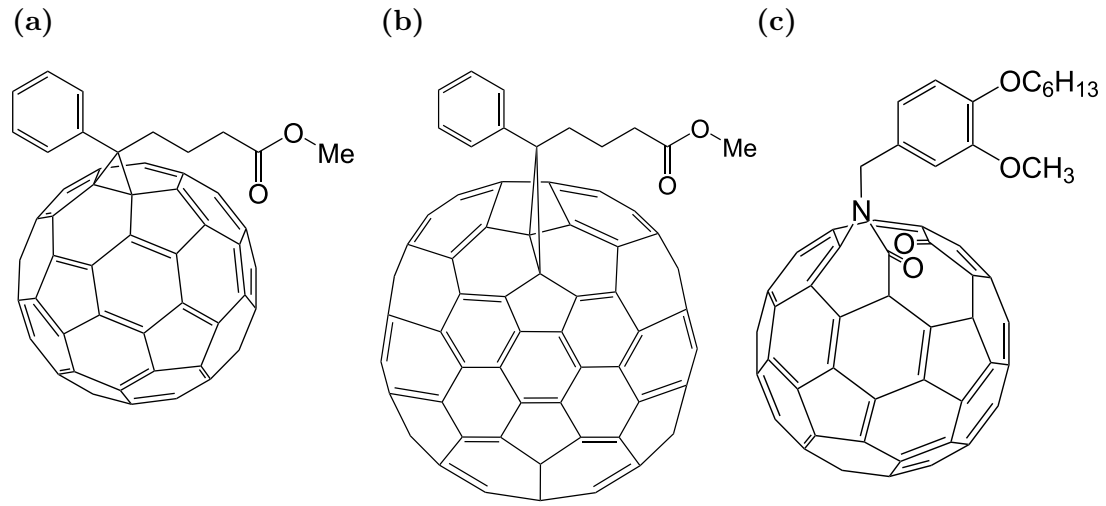


Figure 2.10: Chemical structures of the fullerenes used in this thesis. (a) Phenyl-C_{61}-butyric acid methyl ester (PCBM), (b) Phenyl-C_{71}-butyric acid methyl ester ($PC_{70}BM$), (c) ketolactam (KL, *N*-3-(2-methyloxy, 3-hexyloxy)benzyl ketolatam)

though in Chapter 7 I also use a ketolactam fullerene (full name *N*-3-(2-methyloxy, 3-hexyloxy)benzyl ketolatam); structures of all three fullerenes are shown in Figure 2.10.

Fullerenes can form aggregates or crystallites, or be dispersed in the polymer. Furthermore, since the molecule itself is asymmetrical, the relative orientation of fullerenes with respect to each other, and to the polymer, represents another source of structural disorder. In addition, at interfaces with the polymer, the fullerene can dock at different points along the polymer chain. The favourability of polymer-fullerene interactions along the polymer chain can be affected by steric hindrance, for example from side-chains, or by varying electrostatics along the chain [69].

In addition to variations in the local microstructure, the blend microstructure can vary through the film. The most common example of this is a vertical concentration profile, which is caused by imbalances in the interactions between the individual components and either the substrate or air interfaces [70]. Vertical segregation, as this effect is called, can have a strong effect on the device performance. For example if the hole-transporting component segregates to the device anode, it can enhance performance by forming an effective electron-blocking layer; however if it segregates to the cathode, surface recombination can be promoted, resulting in worse device performance. Another consideration is that a lack of hole-transporting material far from the anode means that any holes generated in this region, which have to traverse the whole device thickness, do not have access

to a good percolation pathway. These examples highlight the effect that structural disorder can have on processes such as charge transport, as inhomogeneities in the molecular distribution through the film change which states are available to a charge.

2.4.3 Energetic disorder

Thus far I have discussed the many ways in which structural disorder is introduced into both polymer and polymer:fullerene films. Different atomic arrangements within molecules result in different local energetic environments, since the energetics of a particular atom will be affected by the electronic environment around it, which in turn is affected by, for example, the local orientation of neighbouring atoms and bonds. The distribution of available energetic states in the system overall can be represented by the density of states (DoS) function, which is defined as the number of states available at each energy. The shape of the DoS has an impact on the device performance, and so it is important to understand.

To illustrate this concept, I consider as an example, the local conformation of a polymer; whether or not a particular part of the chain is in a crystalline or amorphous phase affects the local density of states: strong associations between crystallised polymer chains can stabilise the system, and can allow charge delocalisation and therefore higher charge mobility in this region. However in terms of the overall energetic landscape of the film, crystalline regions can also act as traps since the free charges are stabilised relative to the surroundings [71]. This therefore illustrates how the DoS of polymer and blend films can often be described by tails into the bandgap of the material, as some regions are stabilised relative to others. Figure 2.11 shows the case for an exponential tail DoS, which is a common model used to describe organic films.

Furthermore, in a blend, the various phases present result in different energetic and electronic environments. This can be beneficial, since different phases can stabilise different charges (see Sections 2.5.2 and 2.5.3). Energetic disorder can also be introduced by factors such as isomerism, which can result in variation of energetic levels.

The energy of an electronic state is also affected by electrostatic interactions with surrounding charges and dipoles. The addition of a charge to an environment can also induce dipoles in surrounding molecules. Therefore charges and variation in the effective net charge can introduce differences in energy between otherwise similar molecular configurations. Electrostatic forces are long-range, and so can have a large effect on the energetic disorder of a material [72, 73].

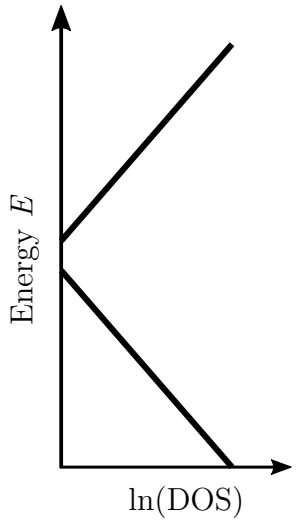


Figure 2.11: A schematic of a typical density of states in an OPV solar cell.

2.4.4 Doping

In addition to disorder caused by the blend components themselves, films can be doped, either intentionally or unintentionally. By definition, a dopant is characterised by a mid-bandgap state which can either accept or donate electrons from/to the host material, resulting in an imbalance in mobile charge carrier densities. Intentionally doping organic films requires the addition of an extra molecular species; therefore there are additional factors to consider, such as the dopant's effect on the blend morphology. When used, intentional dopants are usually included to enhance the film conductivity [74], for example by accepting an electron from the host thus increasing the hole concentration [75]. Therefore doped materials can play an important role as charge transporting layers in organic light emitting diodes and solar cells [76].

The synthesis methods to make conjugated polymers can sometimes introduce impurities that are sometimes quite difficult to remove; two of the most popular synthesis reactions are Stille and Suzuki coupling, both of which are catalysed by palladium [77–79]. Since organic molecules are generally sensitive to excessive heating and otherwise harsh conditions, usual purification methods such as distillation are not possible. Furthermore, polymers do not fully crystallise, and palladium is known to bind to conjugated polymers, so neither crystallisation nor filtration methods work [80]. This is an issue because even low amounts of palladium impurities have been observed to act as short circuits in thin polymer films, severely impacting on their efficacy as devices [81]. Fortunately, there have been reports in the literature of palladium-scavenging molecules that are soluble in organic solvents [80, 82, 83] to address this issue. There has also been some effort

to develop metal-free synthesis routes [84].

Another unintentional dopant is oxygen, which can be incorporated into the blend upon air exposure, and can oxidise the blend components, affecting the density of states. This effect can be more pronounced if oxygen exposure is concurrent with light exposure, resulting in photo-oxidation processes [85]. The effect of doping generally on charge density in the device and the device operation will be discussed in Section 2.5.1.

2.5 Solar cell operation

2.5.1 Device model

In order for a solar cell to convert solar power into electrical power, multiple steps need to occur. If we follow an electron, the first step is light absorption resulting in promotion of an electron into the LUMO, leaving a hole in the HOMO. These two coulombically-bound charged entities must then separate into free charges. The electron then must find its way to the cathode, while the hole must get to the anode; along the way both will be scattered due to the thermal motion of other molecules in the material. This scattering results in a macroscopic series resistance. Meanwhile, if an electron encounters another hole, it can recombine, thus losing the potential energy stored in the separated charges. Therefore on average charges must be generated and collected before they recombine. Additionally, any pinholes in the material can provide an alternative lower-resistance pathway for the generated charges, resulting in a loss in current available to the external circuit; this is called the shunt resistance.

The above process can be translated into an equivalent circuit diagram, which is a model of a solar cell using electrically equivalent components. This equivalent circuit is shown in Figure 2.12, and comprises the photogenerated current, I_l, the series resistance R_s, shunt resistance R_sh, and output voltage V. The current I in a solar cell can be described in terms of these variables, giving the characteristic equation:

$$\begin{aligned} I &= -I_\mathrm{l} + I_\mathrm{d} + I_\mathrm{sh} \\ &= -I_\mathrm{l} + I_0 \left[\exp\left(\frac{q(V + IR_\mathrm{s})}{nkT} \right) - 1 \right] + \frac{V + IR_\mathrm{s}}{R_\mathrm{sh}} \end{aligned} \tag{2.39}$$

where I_l is the photo-generated current, I_d is the diode current, and I_sh is the shunt current.

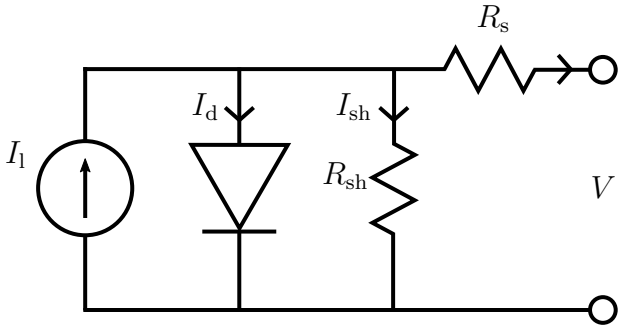


Figure 2.12: Equivalent circuit diagram of a solar cell. I_l is the light-generated current, I_d is the dark diode current, R_{sh} is the shunt resistance in parallel to the diode, and R_s is the series resistance.

The driving force, which drives the electrons and holes to their respective contacts, is achieved through appropriate choice of electrodes in organic photovoltaics. We can consider a simple single-layer solar cell, with two electrodes, which forms a metal-semiconductor-metal sandwich structure. The Fermi energy E_F describes the chemical potential of each material; for metals this is the same as the work-function of the material in isolation, whereas for intrinsic semiconductors before contact is made to another material, the Fermi energy lies in the middle of the bandgap. When the materials are first brought into contact, as in Figure 2.13a, the bands of the semiconductor are flat, and at the interfaces the relative band levels are pinned. But the device is not at equilibrium because the chemical potential of the electrons in the cathode are greater than those in the semiconductor, which are greater than those in the anode. Therefore as a result of these differences in chemical potential, electrons flow until the Fermi energies align and the system is at equilibrium [86]; the end result is shown in Figure 2.13b. As is evident from the diagram, there is now a gradient in the bands of the semiconductor layer which results in an electric field.

The band diagrams in Figures 2.13a, 2.13b and 2.13d are shown for the case of the system in the dark. The convention to define the bias across the device is such that the bias is positive if the cathode potential is raised relative to the anode. In a diode, for the case of zero and negative bias, no current can flow because, as you can see in Figures 2.13b and 2.13c, there is no way for electrons to traverse the semiconductor due to the opposing field.

The system can be pushed out of equilibrium by applying a voltage, as already mentioned, and/or shining light on the device. In this case, we can consider a quasi-equilibrium, where the concentration of charges is higher than at thermal equilibrium; this is represented by a splitting of the Fermi energy level into quasi-Fermi levels (Figures 2.13c and 2.13d): one for electrons ($E_{F,e}$) and one for holes

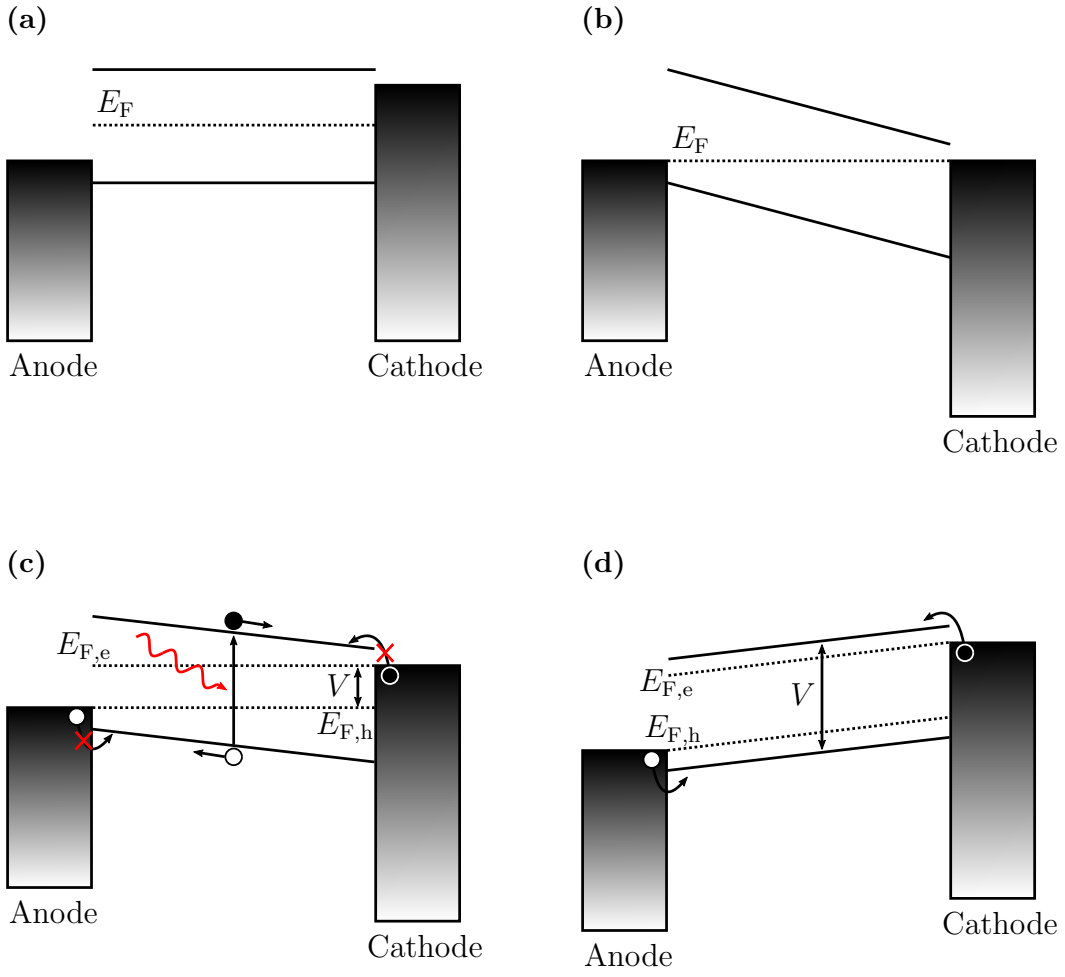


Figure 2.13: Diagram showing the alignment of Fermi energies for a metal-semiconductor-metal sandwich structure. (a) Layers of a device before alignment of Fermi energies. The cathode is the metal with the lower workfunction, and the semiconductor is assumed to be intrinsic so its Fermi level is mid-gap. (b) A device at equilibrium, where the chemical potential, or Fermi energy, has aligned throughout the device. The semiconductor HOMO and LUMO levels are pinned at the metal interfaces, resulting in an electric field gradient. (c) A device at a low applied voltage, which results in a splitting of the Fermi energy into quasi-Fermi energies for electrons and holes, $E_{F,e/h}$. Carriers from the electrodes cannot cross the device due to the opposing electric field, resulting in approximately zero dark current. However, photogenerated charges in the semiconductor can be collected at the electrodes due to the driving force from the electric field. (d) A device at a high applied voltage, which has resulted in the electric field changing direction. Under these conditions, charges from the electrodes can move through the device. In (c) and (d), electrons are represented by black-filled circles while holes are represented by white-filled circles.

($E_{\mathrm{F,h}}$). Figure 2.13d shows the situation at high applied voltage, such that the electric field becomes steep enough that electrons can tunnel from the cathode into the semiconductor, and then be swept towards the anode, resulting in current.

On the other hand, in the light, charges are photogenerated in the bulk of the semiconductor material. In a solar cell at negative and small positive biases, there is a net electric field driving the electrons to the cathode (Figure 2.13c). This results in negative photocurrent which to a first approximation can be considered independent of applied voltage. At larger positive biases, the diode current starts to dominate, and eventually the current is positive again. The voltage at which there is no net current flowing is called the open-circuit voltage, and this is light-dependent. The fourth quadrant of the current-voltage, or J-V curve, is when the solar cell is generating net power, and is the quadrant of most interest in solar research.

Figure 2.14 shows a schematic of a current density-voltage curve of a solar cell, showing the open-circuit voltage V_{oc} and the short-circuit current J_{sc}. Also shown is the maximum power point (MPP), where the gradient of the J-V curve is greatest. The MPP defines the fill factor FF such that:

$$FF = \frac{J_{\mathrm{MPP}} V_{\mathrm{MPP}}}{J_{\mathrm{sc}} V_{\mathrm{oc}}} \tag{2.40}$$

where $(J_{\mathrm{MPP}}, V_{\mathrm{MPP}})$ are the current and voltage values at the MPP.

The efficiency most often quoted when comparing solar cells is the power conversion efficiency (PCE): this is defined as the electrical power generated divided by the incident solar power. Equation 2.42 gives the efficiency, η in terms of the open-circuit voltage, V_{oc}, the short-circuit current J_{sc} and the fill factor FF. Typically in experimental testing, the temperature is set to 25 °C and P_{in} is set to the approximate solar spectrum on the Earth's surface at mid-latitudes, which is called AM1.5, for an air mass coefficient of 1.5 (see Figure 2.15 for the spectrum). Under AM1.5 conditions, the solar flux is 100 $\mathrm{mW\,cm^{-2}}$.

$$\mathrm{FF} = \frac{J_{\mathrm{MPP}} V_{\mathrm{MPP}}}{J_{\mathrm{sc}} V_{\mathrm{oc}}} \tag{2.41}$$

$$\eta = \frac{V_{\mathrm{oc}} J_{\mathrm{sc}} FF}{P_{\mathrm{in}}} \tag{2.42}$$

Thus far I have simplified the metal-semiconductor interfaces by keeping the semiconductor bands flat. In reality however, charges are likely to be injected into the semiconductor upon contact due to a mismatch in Fermi energies. This results in an interfacial charge, which causes band-bending close to the interface.

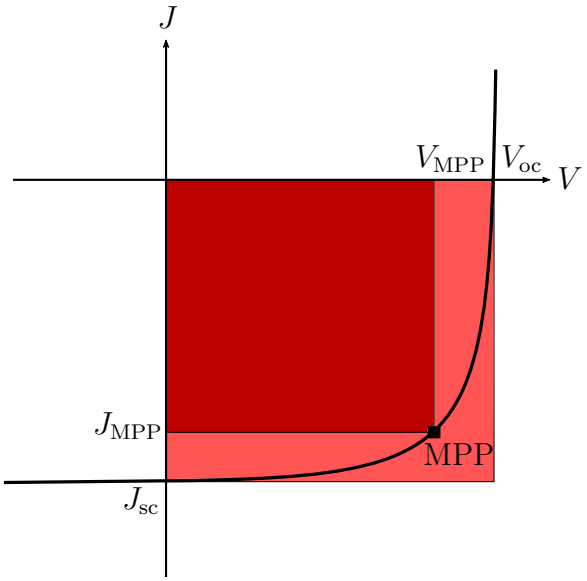


Figure 2.14: Schematic of a current-voltage (J-V) curve, showing the open-circuit voltage and the short-circuit current. The maximum power point (MPP) is shown, which defines the maximum power current (J_{MPP}) and maximum power voltage (V_{MPP}). The fill factor is defined according to eq. (2.41), and is the ratio of the areas of the light and dark red squares.

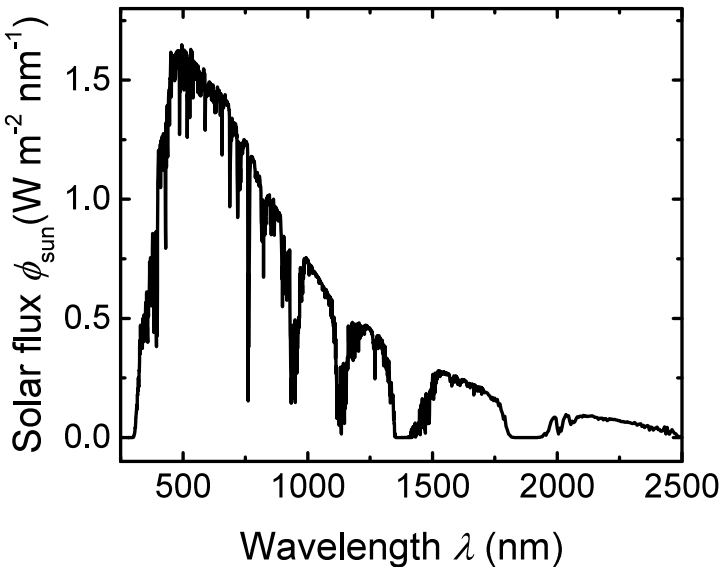


Figure 2.15: The AM1.5 direct solar spectrum used as the standard illumination power when evaluating solar cell efficiency. The integrated power is 100 mW cm^{-2}.

Another cause of band-bending in a device is any doping in the semiconductor; so far the semiconductor has been treated as an intrinsic material. Since doping introduces an imbalance in the mobile carrier concentrations at equilibrium, it normally results in band bending. In this discussion I will discuss the example of *p*-type doping, since this is the most usual type of doping in the materials used for polymer photovoltaic cells. In the bulk of a *p*-type device there are many more mobile holes and stationary negatively charged acceptor species, whose concentration is denoted N_{A}, than in the intrinsic material. Upon contact with a low workfunction cathode, these holes can diffuse towards the cathode, where they recombine with the electrons from the electrode. This results therefore in a region by the electrode of few mobile carriers, but an overall negative charge due to the stationary dopants. Therefore, there is a non-uniform electric field through the device, and a depletion region forms as seen in Figure 2.16. We can understand this phenomenon analytically by recalling the Poisson equation:

$$\Delta\varphi = \frac{d^2\varphi}{dx^2} = -\frac{\rho}{\varepsilon_r\varepsilon_0} \tag{2.43}$$

where φ is the electrostatic potential, ρ is the charge density, ε_r is the relative permittivity and ε_0 is the vacuum permittivity. The depletion approximation assumes that in the depletion region, there are no free carriers, and instead the only charge is due to N_{A}, resulting in $\mathrm{d}^2\varphi/\mathrm{d}x^2 = qN_A/\varepsilon$. Therefore, by integrating twice and using the boundary conditions $\mathrm{d}\varphi/\mathrm{d}x(x = 0) = 0$, and $\varphi(w) - \varphi(0) = V_{\mathrm{bi}} - V$, where w is the width of the depletion region, and x is measured from the cathode towards the anode, the following relation is derived:

$$w = \sqrt{\frac{2(V_{\mathrm{bi}} - V)\varepsilon_r\varepsilon_0}{qN_{\mathrm{A}}}} \tag{2.44}$$

Since there is no net charge except in the depletion region, the capacitance of the device is therefore given by the parallel plate relation:

$$C = \frac{\varepsilon_r\varepsilon_0 A}{d} \tag{2.45}$$

where A is the electrode area, and d is the thickness of the region with an electric field, which is equal to w so long as the semiconductor thickness exceeds d. Hence, the thickness of the depletion region, and therefore the doping density, can be probed by measuring the capacitance; this will be discussed in Section 3.2.2.

From the band diagram in Figure 2.16, it is clear that if the depletion region

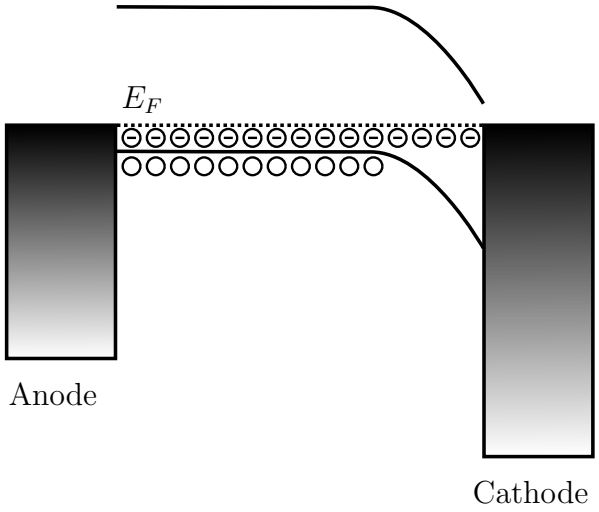


Figure 2.16: The depletion region at the cathode and its effect on the device band diagram. In this case the device is *p*-doped, resulting in an excess of mobile holes and stationary negative charges. A mobile charge-free region forms by the cathode, called the depletion region, which is the only part of the device with a net electric field. The bands by the anode, by contrast, are flat.

width from doping is less than the total device thickness, the resulting band bending will affect charge collection in the device. At short circuit in the light, only the charges photogenerated in the depletion region will be collected efficiently; charges generated in the flat-band region are only able to diffuse to the contacts - there is no electric field to provide a driving force. Figure 2.16 shows the case of *p*-type doping; also pertinent for understanding the effect of doping on the current density-voltage curve is the direction of illumination. Considering first the case of *p*-type doping with illumination from the cathode side, since increasing the thickness merely increases the thickness of the flat-band region, which does not generate charge, the *J*-*V* curve is unlikely to vary much with total film thickness, with the most likely change being a reduction of FF as collection might be hindered. If however, on the other hand, the illumination is impinging from the anode side, increasing the film thickness means that less light will reach the space charge region at the back contact, so fewer charges will be generated and the J_{sc} will decrease. The fill factor, on the other hand, is not necessarily affected because the field in the depletion region is invariant so the charges that are generated there can be collected efficiently so long as the charges are able to diffuse through the flat-band region.

These observations are in direct contrast to the case where the device is intrinsic and therefore the bands can be approximated as being linear across the whole device. In this case, as the thickness increases, the gradient of the bands, and

therefore the potential driving force, decreases across the whole device. This effect, coupled with the greater series resistance of the thicker device, means that both J_{sc} and FF decrease together as the thickness increases. These considerations are all discussed theoretically by Kirchartz et al. [87] and experimentally by Deledalle et al. [26] and Dibb et al. [88].

Thus far the semiconductor has been generally described within the framework of inorganic semiconductors. As has already been discussed in Section 2.4.2, the active layer of organic photovoltaics is generally made from a polymer:fullerene blend. Since the polymer generally transports the holes while the fullerene transports the electrons, it is appropriate to define an effective medium, which has a conduction band corresponding to the fullerene LUMO, and a valence band corresponding to the polymer HOMO. This is called the effective medium approximation and simplifies the modelling and discussion of band diagrams in OPV.

2.5.2 Charge separation

The process of light absorption was covered in Section 2.3, and so this section covers the process of charge separation once a photon has been absorbed. For the sake of simplicity, this discussion will focus on the case of a polymer:fullerene blend where the polymer is the light absorbing material and electron donor, and the fullerene is the electron acceptor.

There is a good deal of discussion in the literature as to the precise mechanism of free charge generation. The principal species involved, excitons and electron or hole polarons, were introduced in Section 2.2; excitons (polarons) are neutral (charged) quasiparticles, formed as a result of the host molecule changing its conformation to stabilise the species. Overall, the generation of free polarons involves the separation of the optically-generated exciton into electron and hole polarons (see Figure 2.17 for a schematic); in bulk heterojunction OPV the polymer typically has the greater absorption in the visible, therefore an electron must be transferred from the polymer to the fullerene, leaving a hole behind on the polymer. The mechanism involved relies heavily on the energetics of the species, and different mechanisms imply different timescales.

The first consideration is the nature of the exciton. Excitons in organic blends should generally be considered within the Frenkel exciton framework, meaning that the exciton is strongly localised; this is in contrast to Wannier excitons which are found in inorganic semiconductors, and are delocalised across many sites in a lattice. The origin of the difference in exciton nature between organic and inorganic semiconductors is the lower dielectric constant in the former, resulting

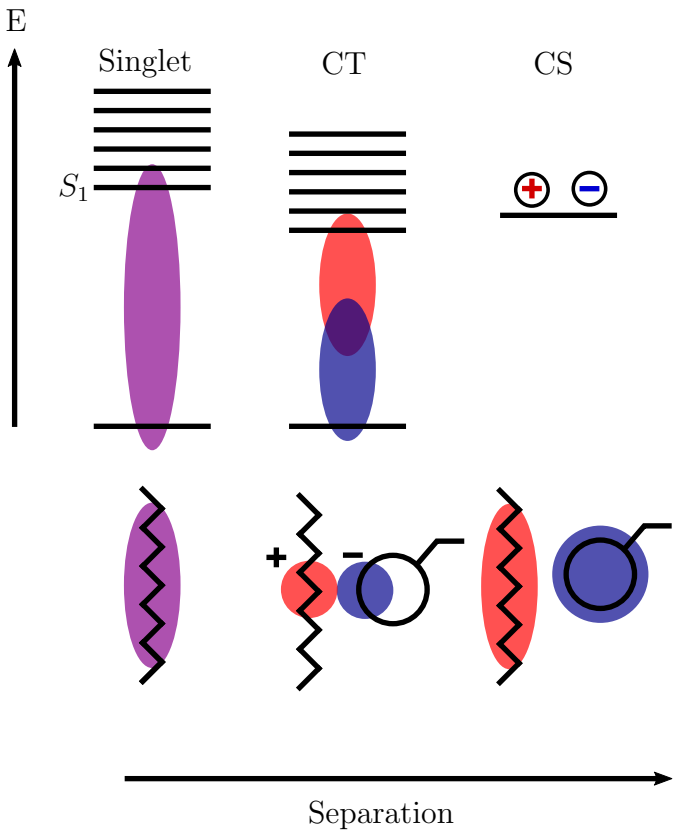


Figure 2.17: Diagram showing the states involved in charge separation, for photon absorption by the polymer and subsequent electron transfer to the fullerene. A singlet (far left, purple) is formed when a photon is absorbed by the polymer. A charge transfer (CT) state can be formed at a polymer-fullerene interface, whereby there is a net negative charge on the fullerene and a net positive charge on the polymer, but the electron and hole are still strongly coupled and can radiatively recombine. Charge separation (CS) is then possible, whereby the charges are fully located on the respective species, and the charges are free to move.

in less screening of the charges, as well as the confinement of the excitation to a smaller volume by the molecular nature of the material. The electron and hole are attracted to each other by a Coulombic interaction, which when the charges are treated as point charges is given by:

$$E_{\mathrm{B}} = \frac{q^2}{4\pi\varepsilon_r\varepsilon_0 r} \tag{2.46}$$

where E_{B} is the binding energy, q is the elementary charge and r is the distance between the electron and hole. This interaction results in exciton binding energies having reported values of $0.1 - 0.5$ eV [89]; for comparison, at 298 K, $kT = 0.026$ eV. Excitons in OPV are either located on one species, such as the polymer, or on two species across an interface; the latter is called a charge transfer (CT) exciton.

The expression for E_{B} highlights an important factor: the spatial separation between the electron and hole. The degree of localisation of an exciton (or a polaron) is dependent on the interplay of a number of factors. Light absorption generates an ensemble of excited states, some of which may initially be delocalised and mobile prior to forming a bound exciton; thermal relaxation of this 'hot' state into a bound exciton takes place on the order of picoseconds [90].

Delocalisation of an exciton may be enhanced by greater coupling between neighbouring sites. A higher degree of order, whether that be planarity of a conjugated polymer chain, or crystallisation or aggregation in polymer and/or fullerene domains, can therefore allow the exciton to delocalise and promote exciton dissociation [91, 92]. Exciton dissociation can also occur at interfaces between crystalline and amorphous parts. The degree of intrachain and interchain coherence of a polymeric exciton can be modulated by the polymeric molecular weight [93]. Exciton-phonon coupling is also possible, which competes with intersite coupling and localises the exciton since the nuclear coordinates can rearrange to minimise its free energy. A competing theory of exciton localisation was proposed by Barford, Tozer and Marcus, who proposed that excitons in conjugated polymers localise due to disorder, instead of exciton-phonon coupling [44, 45, 94]. There is evidently much work to be done to iron out the theoretical differences in the literature, which can be made difficult when two distinct theoretical frameworks predict very similar behaviour.

As already mentioned, since an electron must be transferred to the fullerene for the charges to be long-lived, this transfer must occur either via ultrafast processes before the exciton is localised, or if an exciton has already localised on the polymer it must diffuse to an interface. Excitons can move by energy transfer via the

mediation of dipole-dipole interactions, which are long-range; this is called the Förster mechanism, or Förster resonance energy transfer (FRET). The energy transfer rate is dependent on the oscillator strength of the sites, since the process is mediated by a virtual photon, so is significant for diffusion of singlet excitons. An alternative mechanism involves electron exchange, which requires overlap of the electronic wavefunctions; this is called the Dexter mechanism and is short-range [95]. Exciton diffusion can take tens of picoseconds per step, so the process overall results in quite slow charge generation, on the order of pico- to nanoseconds [96]. It should be noted that diffusion is heavily morphology-dependent, which results in a wide range of diffusion coefficients and lengths reported [97].

However, in many cases free charges are observed at very fast timescales, before 100 fs [65, 98, 99]. At these timescales, the possible resonance of the photoexcited species with charge separated states becomes relevant [100]. There have been some arguments that this is why fullerene aggregation is often observed to be crucial for charge separation, because a higher density of higher-energy states, which can be resonant with the photogenerated exciton, become accessible [100, 101]. In addition, it has been proposed that the role of disorder and noise in the coupling between neighbouring states can be significant; Bittner and colleagues [102, 103] have proposed that phonon fluctuations, for example from the zero-point motion of the molecular lattice and/or thermal noise, facilitate direct resonant tunnelling to charge separated states; an experimental study has suggested the possibility of coherent charge transfer via the vibrational modes [104]. The regime in which resonant tunnelling can be expected to play a role is when the coupling between the initial photoexciton and higher-lying states is of the same order as the energy difference between the states. Furthermore the authors argue that increasing the energy offset between the donor and acceptor results in a greater density of charge separated states in resonance with the primary photoexcitation. A similar proposal was put forward by Aragó and Troisi, who proposed that dynamic disorder due to thermal fluctuations can result in fluctuations in excitonic coupling between neighbouring sites [105]. For the case of excitonic coupling having a similar magnitude as electron-phonon coupling, exciton transport can be coherent and much faster than the case of exciton coupling being smaller than electron-phonon coupling.

The density of states at the polymer-fullerene interface has been shown to be very important for OPV operation [106–109]. Generally in efficient blends, the fullerene has a deeper LUMO level, which provides a driving force for electron transfer from the polymer to the fullerene; an alternate description of the same

picture is that the lowest energy states of a polymer:fullerene pair can be CT states with the electron located on the fullerene and the hole on the polymer [110]. A different possible interaction at the interface is energy transfer of the polymer exciton to the fullerene by the FRET mechanism, followed by charge separation [111–114].

It has been shown that a fully relaxed CT state sometimes cannot dissociate, instead requiring promotion into a higher state in the CT state manifold, which tends to be more delocalised. Higher CT states may be accessed upon initial formation of the CT state. Bakulin et al. performed a pump-push experiment whereby they excited a sample with a pump pulse of visible light, followed by an IR push pulse; the change in photocurrent as a result of the push pulse was recorded [115]. They proposed that the IR push excites a relaxed CT_0 state to a more delocalised state higher in the CT state manifold, and that this state can charge separate resulting in photocurrent; the hypothesis is that these excited CT states are the same as those formed immediately after CT state formation, before relaxation into the ground state. This study therefore raises the possibility that CT states can represent a loss mechanism, if they are too tightly bound to dissociate spontaneously; this observation is in agreement with some other studies [100].

In contrast to the work of Bakulin et al., there is also evidence that directly excited CT states can generate charge as efficiently as CT states generated through dissociation of an exciton [116], and that the generated photocurrent is not increased by photoexcitation into states above the ground CT state [117, 118]. Furthermore another study has suggested that the morphology of the blend, and specifically the degree of fullerene crystallisation, strongly affects the delocalisation and subsequent separation efficiency of the CT state [119]. However, these studies typically access states which are optically active, by either photoexciting the system, or observing electroluminescence, and so it is still possible that the observed states are not necessarily the lowest energy states of the system.

To summarise, charge separation is critically dependent on the energetic landscape of the material, and the critical steps occur at very short timescales [120]. Upon initial excitation, the ability of the exciton to sample delocalised states appears to be crucial for eventual charge separation to occur. Ideally this exciton is generated at or very close to an interface, such that the electron (hole) can transfer to the fullerene (polymer). For this transfer to take place, an energy offset between the two blend components is necessary such that the lowest energy state is a charge transfer state. If the exciton relaxes before achieving charge separation,

it can be possible to re-excite the system up the exciton energetic manifold, which can then result in charge separation.

2.5.3 Charge collection

This section follows on from above and discusses the collection of free charges, i.e. polarons, at the electrodes. The degree of charge collection is determined by the competition between charge extraction, which in turn is affected by the carrier mobility, and recombination [121, 122]. Integral to the treatments of mobility and recombination is the disordered nature of the materials.

Charge mobility in particular involves a wide range of length scales, from molecular to device levels, and is typically low in organic materials, with the highest values reported approaching 10 $cm^2\,V^{-1}\,s^{-1}$ [123–125]. However the reported mobility values can vary by multiple orders of magnitude, according to the materials and the method used [57, 126, 127].

At the molecular level, polaron transport involves the transfer of charge from species to species across the film. This process is therefore heavily affected by factors such as the molecular packing, the structural and energetic disorder [128], as well as dynamic disorder [129]. The molecular packing can affect the spatial wavefunction overlap between adjoining species which can in turn affect charge mobility [130]. Structural disorder describes variation in how the molecules are arranged; as described already in Section 2.4, structural disorder generally affects the energetic disorder, which describes variation in local energetic levels. Dynamic disorder meanwhile takes into account fluctuations in the intermolecular coupling due to vibrational modes [131]. Computer simulations of materials can help to resolve the pertinent factors in a given system [129, 131, 132].

In general, as already discussed, the various sources of disorder overall result in a tail in the density of states which extends into the band gap. The shape of the density of states directly affects the ability of charges to move through the film. For instance, at short times after photo-excitation, the photo-generated species have excess energy and take time to thermalise down the density of states, resulting in enhanced mobility relative to the fully thermalised quasi-equilibrium case [133]. In addition, the tail in the density of states results in a charge-density dependent carrier mobility, as at higher concentrations the deeper trap states get filled [134]. The lower the charge's energy, the more likely it is to be trapped; for example, linear regions of polymer chains tend to have a deeper density of states relative to a folded section, meaning that the charges may become trapped in the linear regions [135].

Moving to the macroscopic level, it is extremely desirable, but elusive, to be able to relate polymer structure to carrier mobility. Historically, highly crystalline materials, such as P3HT, were targeted; however more recently nominally amorphous polymers have shown very high mobilities [124, 136]. Upon inspection, however, while these high-performing materials showed little diffraction patterns in X-ray diffraction, for example, suggesting a lack of long-range order, they did exhibit short-range order [137]. Highly linear chains enable charges to travel further in short times, through the delocalisation of the wavefunctions [138, 139]. However, highly crystalline regions can act as traps as already mentioned [135, 140]. Delocalisation is generally not sufficient for transport across a film, and so some strong interchain coupling is required to facilitate charges hopping between chains. Therefore a balance between fast transport along polymer chains and minimising the effects of disorder, resulting in shallow trap states, is crucial, and this balance is achieved by the recent plethora of high-mobility conjugated polymers [136].

In general, charge transport through a device may be described as the sum of diffusion and drift components. For the case of electron transport this can be written:

$$J_n = q\left(D_n\frac{\mathrm{d}n}{\mathrm{d}x} + \mu_n F n\right) \tag{2.47}$$

where n is the electron density, D_n is the electron diffusion coefficient, μ_n is the electron mobility, and F is the electric field. The dominating process in OPV generally depends on the electric field: at short-circuit for example, when there is often a strong electric field throughout the device, the drift current dominates. However, at the built-in voltage V_{bi} when there is no field in the device, diffusion dominates.

Recombination in an OPV device is most likely to occur between a trapped electron (hole) and a free hole (electron), since more of either carrier are trapped than free, and the mobile carrier is free to find the trapped carrier, which by definition is stationary. This scheme of recombination is called Shockley-Read-Hall (SRH) recombination, and has been shown to well-reproduce OPV device data [141, 142]. Figure 2.18 is a schematic showing the processes involved in SRH recombination, illustrating the various rate coefficients involved. The rates of hole and electron capture and emission, for the case of recombination via the conduction band tail, are displayed in Table 2.1; N_{t} is the trap concentration, f is the electron occupation probability, and $e_{n,p}$ are the electron and hole emission rate coefficients respectively.

By considering the conditions of thermal equilibrium and steady state, the rate

Table 2.1: Rates involved in Shockley-Read-Hall recombination, for the case of recombination via conduction band tails. n and p are the electron and hole concentrations, β_n^0 is the capture rate coefficient for a free electron into a trap, and β_p^- is the capture rate coefficient for a free hole into an electron-occupied trap, N_t is the trap concentration, $e_{n,p}$ are the electron and hole emission rates, and f is the trap electron occupation probability.

Process		Rate
Electron capture	r_1	$n\beta_n^0 N_\mathrm{t}(1-f)$
Electron emission	r_2	$e_n N_\mathrm{t} f$
Hole capture	r_3	$p\beta_p^- N_\mathrm{t} f$
Hole emission	r_4	$e_p N_\mathrm{t}(1-f)$

of SRH recombination per unit volume, for the case of recombination between a trapped electron in the conduction band and a free hole in the valence band (R_cbt) can be derived and is given by eq. (2.48), where N_cbt is the density of conduction band tail states per unit energy, η_r is the recombination rate, $E_\mathrm{c,v}$ are the conduction and valence band energies respectively, N_c0 is the tail state density at the mobility edge, E_uc is the Urbach energy for the conduction band tails, n_i is the intrinsic carrier density, and $N_\mathrm{c,v}$ are the conduction and valence band density of states, excluding the tail states. The rate of recombination is therefore dependent on the charge density, as follows:

$$\begin{aligned} R_\mathrm{cbt} &= \int_{E_\mathrm{v}}^{E_\mathrm{c}} N_\mathrm{cbt}(E)\eta_\mathrm{r}(E)\mathrm{d}E \\ &= \int_{E_\mathrm{v}}^{E_\mathrm{c}} N_\mathrm{c0}\exp\left(\frac{E-E_\mathrm{c}}{E_\mathrm{uc}}\right) \\ &\qquad \frac{np-n_i^2}{(n+N_\mathrm{c}\exp[(E-E_\mathrm{c})/kT])/\beta_p^- + (p+N_\mathrm{v}\exp[(E_\mathrm{v}-E)/kT])/\beta_n^0}\mathrm{d}E \end{aligned} \tag{2.48}$$

where β_p^- and β_n^0 are the rate coefficients for charge capture, defined in Table 2.1.

SRH recombination describes recombination in the bulk of a device, but charges can also recombine at the electrodes, which is termed surface recombination and occurs when there is a concentration of holes (electrons) at the electron- (hole-) selective contact. For example, the surface recombination current at the cathode is given by $J_\mathrm{cath} = qS_p p$, where S_p is the surface recombination velocity for holes. The surface recombination rate is also proportional to $\exp(\varphi_\mathrm{cath}/kT)$, where

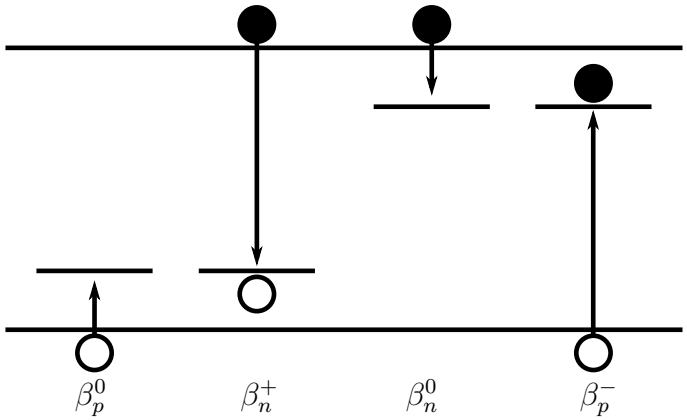


Figure 2.18: Scheme showing the various steps involved in Shockley-Read-Hall recombination, for the case of both conduction and valence band traps. Electrons are shown by filled circles while holes are shown by empty circles. β_p^0, β_n^+, β_n^0 and β_p^- are the capture rate coefficients.

φ_{cath} is the contact barrier between the cathode and the conduction band [143]. These relations therefore illustrate the importance of electrode selection, as well as interlayers.

The mobility and the charge carrier lifetime together strongly affect the current collected from the device. Since both are carrier-density dependent, it is not typically possible to simply assign a single value, and drift-diffusion modelling is generally required to quantitatively model a current-voltage characteristic. However for the purposes of a qualitative understanding, we can assign single values. Then it is possible to construct a model to determine an analytical equation for the short-circuit current density and corresponding external quantum efficiency. We assume that the device has both a uniform field $F = (V_{\text{bi}} - V)/d$ and uniform charge generation $\overline{G}$. Since we are considering the situation at short-circuit current, as we have already seen we assume that the current is dominated by the drift current, $J_n = e\mu_n F n$, where we are solely considering the electron density n. We also set up the system such that the electrons are collected at the contact at $x = 0$, and the device has a thickness of d.

We are assuming steady-state conditions, so the continuity equation in one dimension is given by:

$$\frac{1}{q}\frac{\mathrm{d}J_n}{\mathrm{d}x} + \overline{G} - R = 0 \tag{2.49}$$

where R is the recombination rate, which is given by $R = n/\tau_n$. To determine the expression for $\overline{G}$, we neglect interference effects and reflection, such that the light intensity I follows Beer-Lambert:

$$I = I_0\,(1 - r)\exp(-\alpha x) \tag{2.50}$$

where r is the reflection coefficient, I_0 is the incident light intensity, and α is the absorption coefficient. In this discussion, the generation terms are implicitly functions of photon energy E. The rate of loss of intensity through the device thickness is proportional to the generation rate, such that:

$$\begin{aligned} -\frac{\mathrm{d}I}{\mathrm{d}x} &= G(x)\,E \\ &= I_0\,(1-r)\,\alpha \exp(-\alpha x) \end{aligned} \tag{2.51}$$

Note that here I have used $G(x)$, the position-dependent generation term. When internal reflections are taken into account, the generation tends to be less position-dependent. Therefore, the average generation through the device, $\overline{G}$ is given by:

$$\begin{aligned} \overline{G} &= \frac{1}{d}\int_0^d G(x)\,\mathrm{d}x \\ &= \frac{1}{d}\,\frac{I_0\,(1-r)}{E}\int_0^d \alpha\,\exp(-\alpha x)\,\mathrm{d}x \\ &= \frac{1}{d}\,\frac{I_0\,(1-r)}{E}\big[1-\exp(-\alpha d)\big] \end{aligned} \tag{2.52}$$

Returning to the continuity equation, we have:

$$\mu\,F\,\frac{\mathrm{d}n}{\mathrm{d}x} - \frac{n}{\tau} = -\overline{G} \tag{2.53}$$

This is a first-order inhomogeneous differential equation, which can be solved to give:

$$n = C\exp\left(\frac{x}{\mu\,\tau F}\right) + \overline{G}\,\tau \tag{2.54}$$

where C is the constant of integration. Substituting this expression into the expression for the drift current J_n, and using the boundary condition $J_n(d) = 0$ we determine that:

$$C = -\overline{G}\,\tau\exp\left(\frac{d}{\mu\,\tau F}\right) \tag{2.55}$$

Including the full expression for $\overline{G}$, defining the drift length $L_{\mathrm{dr}} = \mu\tau F$, and evaluating at $x = 0$, we arrive at the Hecht equation [87, 144]:

$$J_n = q\,L_{\mathrm{dr}}\,\frac{1}{d}\,\frac{I_0\,(1-r)}{E}\,[1-\exp(-\alpha\,d)]\left[1-\exp\left(-\frac{d}{L_{\mathrm{dr}}}\right)\right] \tag{2.56}$$

The external quantum efficiency can be evaluated by dividing eq. (2.56) by the

number of photons entering the device, and by the elementary charge, thus:

$$\mathrm{EQE}(E) = \frac{L_{\mathrm{dr}}}{d}\left[1 - \exp(-\alpha(E)\, d)\right]\left[1 - \exp\left(-\frac{d}{L_{\mathrm{dr}}}\right)\right] \tag{2.57}$$

For the limit where $L_{\mathrm{dr}} \gg d$, the expression $[L_{\mathrm{dr}}(1 - \exp(-d/L_{\mathrm{dr}}))/d]$ tends towards unity. Therefore EQE is limited only by the optical depth, αd, and thus will approach unity as d is increased. On the other hand, for the limit where $L_{\mathrm{dr}} \ll d$, the same expression tends towards L_{dr}/d, such that the expression for EQE asymptotes to zero with increasing d. For intermediate values of L_{dr}, the expression for EQE as a function of d has a maximum which represents the optimum compromise between the collection and the optical depth.

To summarise, the expressions above represent a very simplified case, considering only electrons, uniform field, uniform generation, and no interference or reflection off a back contact. Nevertheless they highlight that the mobility-lifetime product $\mu\tau$, and hence the drift length L_{dr} can have a large effect on charge collection, and provide a starting point for considering the limitations of working devices.

2.6 Limits to efficiency

In order to assess solar cell efficiency, it is helpful to consider the maximum possible efficiency available from a hypothetical device. Shockley and Queisser developed what is called the radiative efficiency limit [145], which is based on the principle that any medium which absorbs light must also emit light, as stated by Kirchoff's law. This principle is called detailed balance, and means that the maximum possible efficiency is achieved if the only allowed recombination is radiative. Non-radiative recombination, the competing process, occurs, for example, by interaction with defects in the material or by thermalisation by the release of phonons. These processes serve to decrease the lifetime of the electron-hole pair; the maximum possible lifetime is that of the radiative recombination process. The Shockley-Quiesser (SQ) limit was developed for a single-junction solar cell at thermal equilibrium, where the maximum efficiency is achieved when the solar cell has a step absorption spectrum $\alpha(E) = H(E - E_{\mathrm{g}})$ where H is the Heaviside function, i.e. no photons are absorbed at energies less than the band gap energy E_{g}, and all photons are absorbed above the band gap. In this discussion I will consider the case of normal incidence on a flat solar cell, and ideal diode behaviour. A useful way to focus on energy losses is to quantify the voltage loss, since efficiency is a

more complicated metric, so I will focus on the limits to V_{oc}[146].

Planck's law describes the thermal radiation of a blackbody at temperature T. Würfel extended this to the case of a semiconductor under applied bias V [147], assuming an ideal diode with flat quasi-Fermi levels, such that the emitted spectral photon flux density $\phi(V, E)$ is given by:

$$\phi(V, E) = \frac{2\pi E^2}{h^3 c^2} \frac{\alpha(E)}{\exp[(E - qV)/kT] - 1} \tag{2.58}$$

where E is the photon energy, h is the Planck constant, and c is the speed of light in a vacuum. For the case of small applied voltage relative to the emitted photon energy, such that $E - qV \gg kT$, this can simplify to:

$$\begin{aligned} \phi(V, E) &\approx \frac{2\pi E^2}{h^3 c^2} \alpha(E) \exp\left(\frac{qV - E}{kT}\right) \\ &= \alpha(E)\phi_{\mathrm{bb}} \exp\left(\frac{qV}{kT}\right) \\ \text{where } \phi_{\mathrm{bb}} &= \frac{2\pi E^2}{h^3 c^2} \exp\left(-\frac{E}{kT}\right) \end{aligned} \tag{2.59}$$

ϕ_{bb} is the photon flux spectrum of a blackbody at temperature T, emitting from a flat surface. So eq. (2.59) describes the radiation of an ideal blackbody under applied bias. In the radiative limit, only radiative recombination can occur, thus a recombination current J_{rec} can be defined by $J_{\mathrm{rec}} = q\Phi$, where Φ is the total photon flux. Therefore in the SQ limit,

$$\begin{aligned} J_{\mathrm{rec,SQ}} &= q\,\Phi_{\mathrm{SQ}} \\ &= q \int_0^\infty \phi(V, E)\, \mathrm{d}E \\ &\approx q \int_{E_{\mathrm{g}}}^\infty \phi_{\mathrm{bb}} \exp\left(\frac{qV}{kT}\right) \mathrm{d}E \end{aligned} \tag{2.60}$$

If we consider thermal equilibrium, the applied voltage and the total current are both zero. In this situation, the rate of absorption must be equal to the rate of emission, so the photocurrent $J_{\mathrm{bb,SQ}}$ is equal to the recombination current. Under applied bias voltage in the dark, the photocurrent is unchanged so the total current

is:

$$\begin{aligned} J_{\mathrm{SQ}} &= J_{\mathrm{rec,SQ}} - J_{\mathrm{bb,SQ}} \\ &= q\left(\Phi(V,E) - \Phi(0,E)\right) \\ &= q\int_{E_{\mathrm{g}}}^{\infty} \phi_{\mathrm{bb}}\,\mathrm{d}E\left[\exp\left(\frac{qV}{kT}\right) - 1\right] \end{aligned} \tag{2.61}$$

From eq. (2.61) we can see that for the case of negative applied bias, J_{SQ} approaches a constant value, called the dark saturation current $J_{0,\mathrm{SQ}}$:

$$J_{0,\mathrm{SQ}} = q\int_{E_{\mathrm{g}}}^{\infty} \phi_{\mathrm{bb}}\,\mathrm{d}E \tag{2.62}$$

If we now consider the case under illumination, we must include the short-circuit current density $J_{\mathrm{sc,SQ}}$, thus:

$$J_{\mathrm{SQ}} = J_{0,\mathrm{SQ}}\left[\exp\left(\frac{qV}{kT}\right) - 1\right] - J_{\mathrm{sc,SQ}} \tag{2.63}$$

The same step-function absorption applies, so the solar spectral photon flux incident on the solar cell (i.e. AM1.5), ϕ_{sun}, results in $J_{\mathrm{sc,SQ}}$ given by:

$$J_{\mathrm{sc,SQ}} = q\int_{E_{\mathrm{g}}}^{\infty} \phi_{\mathrm{sun}}\,\mathrm{d}E \tag{2.64}$$

The open-circuit voltage $V_{\mathrm{oc,SQ}}$ is determined by setting J_{SQ} in eq. (2.63) to zero and solving for V:

$$V_{\mathrm{oc,SQ}} = \frac{kT}{q}\ln\left(\frac{J_{\mathrm{sc,SQ}}}{J_{0,\mathrm{SQ}}} + 1\right) \tag{2.65}$$

The difference between the $qV_{\mathrm{oc,SQ}}$ and the optical bandgap is a direct consequence of reciprocity and radiative recombination and corresponds to an energy loss of around 250 meV for a band gap of 1.18 eV under one sun illumination [27].

This discussion can be extended to more realistic scenarios by considering an absorption spectrum which is not a step-function. Moreover, the process of electrical transport can be considered as part of the detailed balance. Rau applied the detailed balance formulation developed by Würfel to describe semiconductors in devices such as light emitting diodes and solar cells [148]. Rau's theory considers the complementary pair of processes of light absorption followed by charge carrier collection, and carrier injection followed by light emission. The maximum open-circuit voltage in this limit is the radiative open-circuit voltage $V_{\mathrm{oc,rad}}$.

If we extend the current density expressions above to incorporate $\alpha(E)$, as well

as carrier collection Q, which is defined by $Q = \alpha F_c$, where F_c is the probability that a generated electron-hole pair will separate and contribute q to the device current. In the SQ limit, $F_c = 1$, and $\alpha(E) = 0$ for photon energy $E < E_g$, and 1 for $E \geq E_g$, where E_g is the band gap of the material. When averaged over the cell area, Q corresponds to the external quantum efficiency (EQE) defined as the number of electrons collected per photon of a particular wavelength incident on the cell's surface. Therefore the short-circuit current density of the device under solar illumination is:

$$J_{sc} = q \int_0^\infty \text{EQE}\ \phi_{sun}\ \mathrm{d}E \tag{2.66}$$

where we assume that non-radiative recombination is insignificant at short-circuit, allowing us to use the value of J_{sc} from the current density-voltage curve. Similarly, the radiative limit dark saturation current density $J_{0,rad}$ can be written:

$$J_{0,rad} = q \int_0^\infty \text{EQE}\ \phi_{bb}\ \mathrm{d}E \tag{2.67}$$

and the radiative open-circuit voltage $V_{oc,rad}$ is:

$$V_{oc,rad} = \frac{kT}{q} \ln\left(\frac{J_{sc}}{J_{0,rad}} + 1\right) \tag{2.68}$$

The difference between $V_{oc,rad}$ and the previously derived $V_{oc,SQ}$ is a consequence of a finite absorption profile which is not a step-function; so we can call it $\Delta V_{oc,abs}$. We can understand this voltage loss further by considering the interrelationship between the quantum efficiency and the electroluminescence (EL), i.e. the excess photon emission under applied bias relative to the emission at thermal equilibrium, by going back to eq. (2.59):

$$\phi_{EL}(V, E) = \text{EQE}(E)\ \phi_{bb} \left[\exp\left(\frac{qV}{kT}\right) - 1\right] \tag{2.69}$$

This final relation is important because it allows for the indirect determination of EQE from the EL spectrum. Due to the type II heterojunction required for charge separation (see Section 2.5.2), the lowest radiative state in an OPV device is usually a charge transfer state at the donor-acceptor interface, and thus is lower in energy than either the polymer or fullerene singlet states [107]. This is significant because at 300 K, the blackbody radiation spectrum increases exponentially towards low energies, thus the radiative limit dark saturation current $J_{0,rad}$ is strongly affected by low energy contributions to the EQE spectrum. And from eq. (2.68), the greater $J_{0,rad}$, the lesser $V_{oc,rad}$, thus illustrating the voltage

cost in OPV devices of radiation from low-energy states.

Finally, in a similar vein, we can assess the difference between the radiative open-circuit voltage and the actual device open-circuit voltage, which is the loss due to non-radiative recombination. In order to do this, we first consider the quantum efficiency of radiation, which we term the light-emitting diode (LED) quantum efficiency $Q_{\mathrm{LED}} = q\Phi/J_{\mathrm{inj}}$, where Φ is the radiation flux ϕ_{EL} integrated over energy, and J_{inj} is the injected current. Considering the case at V_{oc}, and taking the natural logarithm:

$$\ln Q_{\mathrm{LED}}(V_{\mathrm{oc}}) = \ln\left[\frac{q\int \mathrm{EQE}\,\phi_{\mathrm{bb}}\,\mathrm{d}E\,[\exp(qV_{\mathrm{oc}}/kT)-1]}{J_{\mathrm{inj}}}\right] \tag{2.70}$$

Since we are considering V_{oc}, the net current density is zero, and assuming that J_{sc} is equivalent to the photocurrent at V_{oc}, then we have $J(V_{\mathrm{oc}}) = J_{\mathrm{inj}} - J_{\mathrm{sc}} = 0$. Also substituting eq. (2.67), and using $J_{\mathrm{sc}} \gg J_{0,\mathrm{rad}}$ as well as $kT \ll qV_{\mathrm{oc}}$, we have:

$$\begin{aligned}\ln Q_{\mathrm{LED}}(V_{\mathrm{oc}}) &\approx \frac{qV_{\mathrm{oc}}}{kT} + \ln\left[\frac{J_{0,\mathrm{rad}}}{J_{\mathrm{sc}}}\right] \\ &\approx \frac{qV_{\mathrm{oc}}}{kT} - \frac{qV_{\mathrm{oc,rad}}}{kT}\end{aligned} \tag{2.71}$$

$$\therefore \Delta V_{\mathrm{oc,nr}} \equiv V_{\mathrm{oc,rad}} - V_{\mathrm{oc}} \approx -\frac{kT}{q}\ln Q_{\mathrm{LED}} \tag{2.72}$$

This final relation therefore directly links the voltage loss due to non-radiative recombination $\Delta V_{\mathrm{oc,nr}}$ with the LED quantum efficiency, which in organic solar cells is typically approximately between 10^{-9} and 10^{-6} [109, 149], corresponding to a loss of approximately 0.36 V for the case of $Q_{\mathrm{LED}} = 10^{-6}$. By considering the causes of non-radiative recombination we can start to attempt to minimise this significant energy loss. For example, a higher charge transfer state lifetime would decrease the voltage losses because in OPV the lifetime is dominated by non-radiative recombination [150]. In addition, minimising the concentration of potential recombination centres, such as impurities, could be beneficial. A further dynamic consideration is that low charge carrier mobility means that the effect of non-radiative recombination is further enhanced because the carriers cannot be collected as quickly. The work I present in Chapter 4 uses this methodology to probe possible differences in the degree of non-radiative recombination observed.

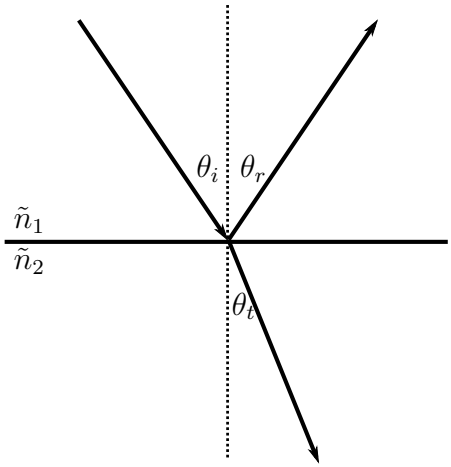


Figure 2.19: Reflection and refraction of light at an interface of two materials with refractive indices $\tilde{n}_1$ and $\tilde{n}_2$. θ_i is the angle of incidence, θ_r is the angle of reflection, and θ_t is the angle of refraction.

2.7 Light propagation in a solar cell

Thus far our discussion of electromagnetic waves and interactions with matter have focussed on bulk properties. However a solar cell is a multi-layer structure and therefore it is important to be able to describe the interaction of light with interfaces, which is the focus of this section.

As we have already seen in Section 2.3, the electric field of an electromagnetic wave propagating in the z direction may be described as $E(z,t) = E_0 \exp\left[i(kz - \omega t + \delta)\right]$, where we have introduced the initial phase δ. Similarly, the associated magnetic field B, which propagates in the same direction as E but in the perpendicular plane if the light is polarised, can be described by $B(z,t) = B_0 \exp\left[i(kz - \omega t + \delta)\right]$. The magnitude of E and B are related through $E = cB$, where c is the speed of light in a vacuum.

When light travels from a medium of refractive index $\tilde{n}_1$ to a medium of refractive index $\tilde{n}_2$ at an oblique angle, some light is reflected, and some propagates in the second medium, but is refracted and propagates at a different angle (see Figure 2.19). It is trivial to show that the angles of incidence and reflection are equal, that is $\theta_i = \theta_r$, and that the angles of incidence and refraction are related through Snell's law:

$$\tilde{n}_i \sin\theta_i = \tilde{n}_t \sin\theta_t \tag{2.73}$$

It is possible to define two kinds of polarisation of light respective to the interface: so-called *s*- and *p*- polarisation. *p*-polarisation refers to light polarised such that the electric fields of the incident and reflected light oscillate in the same plane, which is called the plane of incidence. *s*-polarisation is orthogonal to

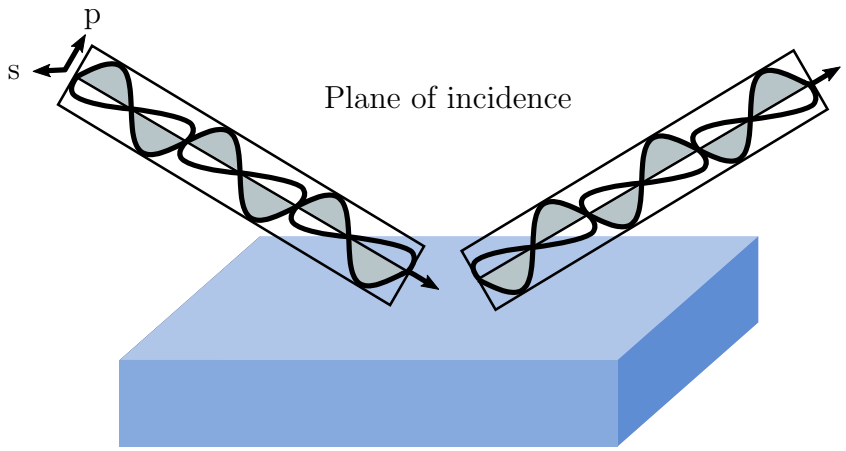


Figure 2.20: The definition of *s*- and *p*- polarisation. The plane of incidence is the plane which is defined by the incoming and reflected propagation directions, and is indicated by the rectangles. Light polarised in this plane is called *p*-polarised, which is shaded above, and light polarised in the orthogonal direction is called *s*-polarised. Figure adapted from [151].

p-polarisation (see Figure 2.20).

At the interface, the components of **E** and **B** parallel to the interface must be continuous. This boundary condition allows us to determine the transmission and reflection coefficients: t_p, r_p and t_s, r_s for *p*- and *s*-polarised light respectively. Equations (2.74) to (2.77) are called the Fresnel equations.

$$r_p \equiv \frac{E_{rp}}{E_{ip}} = \frac{\tilde{n_t}\cos\theta_i - \tilde{n_i}\cos\theta_t}{\tilde{n_t}\cos\theta_i + \tilde{n_i}\cos\theta_t} \tag{2.74}$$

$$t_p \equiv \frac{E_{tp}}{E_{ip}} = \frac{2\tilde{n_i}\cos\theta_i}{\tilde{n_t}\cos\theta_i + \tilde{n_i}\cos\theta_t} \tag{2.75}$$

$$r_s \equiv \frac{E_{rs}}{E_{is}} = \frac{\tilde{n_i}\cos\theta_i - \tilde{n_t}\cos\theta_t}{\tilde{n_i}\cos\theta_i + \tilde{n_t}\cos\theta_t} \tag{2.76}$$

$$t_s \equiv \frac{E_{ts}}{E_{is}} = \frac{2\tilde{n_i}\cos\theta_i}{\tilde{n_i}\cos\theta_i + \tilde{n_t}\cos\theta_t} \tag{2.77}$$

These coefficients in turn allow us to calculate reflectance and transmittance, $R_{s,p}$ and $T_{s,p}$. Since the angles of incidence and reflection are identical, reflectance is simple to define in terms of the intensities of the incident and reflected beams; eq. (2.78) is the relation for R_s, and similarly $R_p = |r_p|^2$. For transmittance, however, because the angles of the incident and refracted beams are different, it is necessary to take the cross-sectional area of the beam into consideration. This

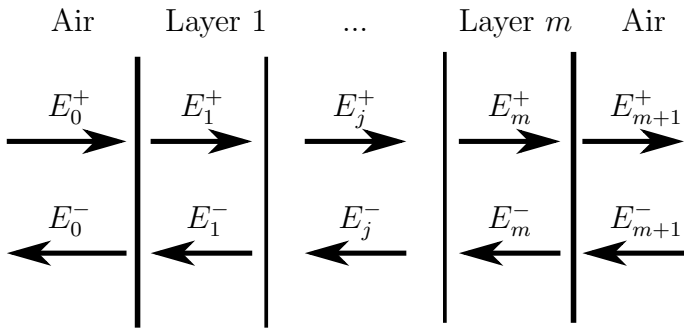


Figure 2.21: A schematic of the transfer matrix method, showing a stack of m layers, with light incident from the left. The forward and backward propagating electric fields are indicated in each layer.

results in eq. (2.79) describing T_s, with the analogous expression holding for T_p.

$$R_s \equiv \frac{I_{rs}}{I_{is}} = \left|\frac{E_{rs}}{E_{is}}\right|^2 = |r_s|^2 \tag{2.78}$$

$$T_s \equiv \frac{I_{ts}\cos\theta_t}{I_{is}\cos\theta_i} = \frac{\tilde{n}_t\cos\theta_t}{\tilde{n}_i\cos\theta_i}\left|\frac{E_{ts}}{E_{is}}\right|^2 = \frac{\tilde{n}_t\cos\theta_t}{\tilde{n}_i\cos\theta_i}|t_s|^2 \tag{2.79}$$

The above discussion has been for one interface, but these expressions can be applied to multilayer structures. The transfer matrix method has been developed [152–154] as a simple way to calculate the reflection and transmission of a multilayer stack, as well as to calculate the electric field within layers. A schematic illustrating the concept is shown in Figure 2.21; I will simplify the discussion by assuming normal incidence (so any polarisation is equivalent) although of course the angular component can be included. Light is assumed to be incident from the left, and the ambient is labelled layer 0.

At each interface light is transmitted and reflected; we can consider an interface between layer j and layer k. The reflection and transmission amplitude coefficients for the jk interface are r_{jk} and t_{jk}. It is trivial from eq. (2.74) or eq. (2.76) to show that $r_{kj} = -r_{jk}$. Furthermore, by multiplying out the expressions, it is simple to show that $t_{jk}t_{kj} + r_{jk}^2 = 1$. So we can consider expressions for the two fields propagating away from the interface, that is:

$$\begin{aligned}\mathbf{E}_k^+ &= t_{jk}\mathbf{E}_j^+ + r_{kj}\mathbf{E}_k^- \\ \mathbf{E}_j^- &= t_{kj}\mathbf{E}_k^- + r_{jk}\mathbf{E}_j^+\end{aligned} \tag{2.80}$$

We can rearrange to obtain expressions for $\mathbf{E}_j^{+,-}$ in terms of $\mathbf{E}_k^{+,-}$ and thus define

$\boldsymbol{I}$ such that:

$$\begin{bmatrix} \mathbf{E}_j^+ \\ \mathbf{E}_j^- \end{bmatrix} = \boldsymbol{I} \begin{bmatrix} \mathbf{E}_k^+ \\ \mathbf{E}_k^- \end{bmatrix} = \frac{1}{t_{jk}} \begin{bmatrix} 1 & r_{jk} \\ r_{jk} & 1 \end{bmatrix} \begin{bmatrix} \mathbf{E}_k^+ \\ \mathbf{E}_k^- \end{bmatrix} \tag{2.81}$$

The other building-block matrix we must define describes the propagation of both forward and backward fields within a layer, $\boldsymbol{L}$:

$$\begin{bmatrix} \mathbf{E}_j^+ \\ \mathbf{E}_j^- \end{bmatrix} = \boldsymbol{L} \begin{bmatrix} \mathbf{E}_k^+ \\ \mathbf{E}_k^- \end{bmatrix} = \begin{bmatrix} \exp(-i2\pi\tilde{n}d_j/\lambda) & 0 \\ 0 & \exp(-i2\pi\tilde{n}d_j/\lambda) \end{bmatrix} \begin{bmatrix} \mathbf{E}_k^+ \\ \mathbf{E}_k^- \end{bmatrix} \tag{2.82}$$

Then we can define an overall transfer matrix $\boldsymbol{S}$ such that:

$$\begin{bmatrix} \mathbf{E}_0^+ \\ \mathbf{E}_0^- \end{bmatrix} = \boldsymbol{S} \begin{bmatrix} \mathbf{E}_{m+1}^+ \\ \mathbf{E}_{m+1}^- \end{bmatrix} \tag{2.83}$$

It is evident that $\boldsymbol{S}$ is composed of $\boldsymbol{I}$ and $\boldsymbol{L}$:

$$\boldsymbol{S} = \begin{bmatrix} S_{11} & S_{12} \\ S_{21} & S_{22} \end{bmatrix} = \left(\prod_{v=1}^{m} \boldsymbol{I}_{(v-1)v} \boldsymbol{L}_v \right) \boldsymbol{I}_{m(m+1)} \tag{2.84}$$

For the case where light is incident on the ambient side, and reflected from the back side, as in the case of OPV devices, $\mathbf{E}_{m+1}^- = 0$. So $\mathbf{E}_0^+ = S_{11}\mathbf{E}_{m+1}^+$ and $\mathbf{E}_0^- = S_{21}\mathbf{E}_{m+1}^+$, and the reflection and transmission coefficients of the whole stack are:

$$\begin{aligned} r &= \frac{\mathbf{E}_0^-}{\mathbf{E}_0^+} = \frac{S_{21}}{S_{11}} \\ t &= \frac{\mathbf{E}_{m+1}^+}{\mathbf{E}_0^+} = \frac{1}{S_{11}} \end{aligned} \tag{2.85}$$

In order to calculate the electric field in layer j of the device, the overall scattering matrix can be divided into parts:

$$\begin{aligned} \boldsymbol{S} &= \boldsymbol{S'_j} \boldsymbol{L_j} \boldsymbol{S''_j} \\ \text{where } \boldsymbol{S'_j} &= \left(\prod_{v=1}^{j-1} \boldsymbol{I_{(v-1)v}} \boldsymbol{L_v} \right) \boldsymbol{I_{(j-1)j}} \\ \boldsymbol{S''_j} &= \left(\prod_{v=j+1}^{m} \boldsymbol{I_{(v-1)v}} \boldsymbol{L_v} \right) \boldsymbol{I_{(m(m+1)}} \end{aligned} \tag{2.86}$$

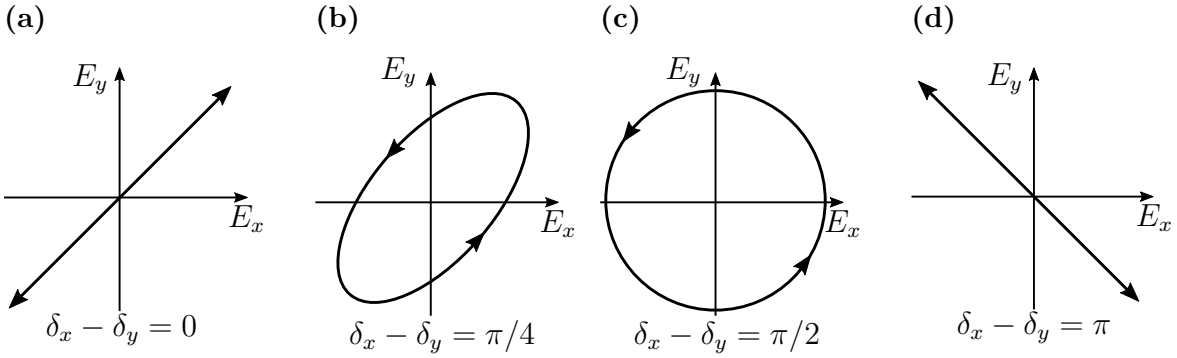


Figure 2.22: Schematic showing the effect of phase difference $\delta_x - \delta y$ on the polarisation of light. For simplicity, in these diagrams $E_{x0} = E_{y0}$. Figure adapted from [151].

Using the same naming convention of eq. (2.84), the electric field within layer j can be derived as:

$$\begin{aligned}\mathbf{E}_j(x) &= \mathbf{E}_j^+(x) + \mathbf{E}_j^-(x) \\ &= \frac{S''_{11}\exp(-i2\pi\tilde{n}(d_j - x)/\lambda) + S''_{21}\exp(i2\pi\tilde{n}(d_j - x)/\lambda)}{S'_{11}S''_{11}\exp(-i2\pi\tilde{n}d_j/\lambda) + S'_{12}S''_{21}\exp(i2\pi\tilde{n}d_j/\lambda)}\ \mathbf{E}_0^+ \end{aligned} \tag{2.87}$$

The above formalism is called transfer matrix modelling (TMM); the McGehee group at Stanford University has developed an open-source Matlab code [155] which calculates the reflection and absorption per layer in a full device stack, as well as the electric field in each layer. This then allows calculation of the maximum available short-circuit current from a given device stack, and will be used later in this thesis.

So far only linear (s and p) polarisation has been considered, but polarisation can be defined more broadly. A general electric field $\mathbf{E}(z,t)$ propagating in the z direction can be resolved into x and y components such that $\mathbf{E}(z,t) = \Big[E_{x,0}\exp\big(i(kz - \omega t + \delta_x)\big)\Big]\mathbf{x} + \Big[E_{y,0}\exp\big(i\,(kz - \omega t + \delta_y)\,\big)\Big]\mathbf{y}$, where $\mathbf{x}$ and $\mathbf{y}$ are unit vectors in the x and y directions respectively.

The polarisation can be defined simply by considering the relative phase difference $\delta_x - \delta_y$. If $\delta_x - \delta_y = 0$ or π, then the light is linearly polarised, as shown in Figures 2.22a and 2.22d. However if this is not the case, the light is elliptically polarised (Figure 2.22b). A special case of elliptical polarisation is circular polarisation, when $E_{x0} = E_{y0}$ and $\delta_x - \delta y = \pi/2$ or $3\pi/2$ (Figure 2.22c). Of course light can also be unpolarised, in which case the oscillatory direction is completely random.

Optical systems can be made up of many different components, and so, as

for the case of TMM above, it is useful to define matrices which describe each component or operation. The Jones vector is a useful way to keep track of the resolved components of polarised light, where $\mathbf{E}(z,t)$ can be described:

$$\mathbf{E}(z,t) = \begin{bmatrix} E_{x0}\exp(i\delta_x) \\ E_{y0}\exp(i\delta_y) \end{bmatrix} \exp(i(kz-\omega t)) \tag{2.88}$$

Commonly only the relative changes are pertinent, in which case eq. (2.88) would be normalised by intensity. Jones vectors are useful for describing polarised light, but cannot describe unpolarised light. Another similar scheme, called the Stokes parameters or Stokes vector, can be used instead; the definitions are shown in eq. (2.89).

$$\begin{aligned} S_0 &= I_x + I_y \\ S_1 &= I_x - I_y \\ S_2 &= I_{+45} - I_{-45} \\ S_3 &= I_{\mathrm{R}} - I_{\mathrm{L}} \end{aligned} \tag{2.89}$$

where I_x, I_y, I_{+45} and I_{-45} are the intensities in the linear directions of x, y, $+45^\circ$ and -45° respectively. I_{R} and I_{L} are the intensities of right- and left- circular polarisation. Therefore the Stokes parameters S_{1-3} describe the relative polarisation in those three directions. The experimental technique of ellipsometry (Section 3.4.2) uses changes in the polarisation of light to probe the refractive index and thickness of thin films.

Chapter 3

Experimental Techniques

3.1 Device and film fabrication

This section describes the fabrication of devices and films used in this thesis; unless stated, the methods described in this section were used to make the samples for all the work in this thesis. I will start with describing the process for devices for electrical measurements, and then describe the process for films for optical measurements.

Figure 3.1 shows typical device architectures used: the term 'conventional' refers to a device with a top-cathode, whereas 'inverted' refers to a top-anode architecture. Both architectures were used in this work. In both cases, the active layer is sandwiched between a cathode and an anode, with the possible inclusion of an electron-transport layer on the cathode side, and/or a hole-transport layer on the anode side.

All films were made by solution processing in the ambient in a Class 1000 cleanroom, while electrodes were evaporated in an MBraun 200B glove box. Two distinct coating techniques were used for the solution-processed layers: spin coating and blade coating. Spin coating is the workhorse technique of solution-processed plastic electronics, and involves pipetting a solution onto a substrate which is held in place on a chuck by vacuum; see Figure 3.2a. As the name suggests, the film is formed by the chuck spinning at a pre-determined speed; the acceleration is also controlled. The slower the spin speed, the thicker the film.

Blade coating, on the other hand, is less often used in the literature, but has the advantages of being an inherently scalable technique which uses less than 50% of the solution volume required for spin coating. A diagram of the apparatus is shown in Figure 3.2b. The model I used in this work is a Zehntner ZAA2300. The blade is free-standing, and there are multiple sizes available for differently

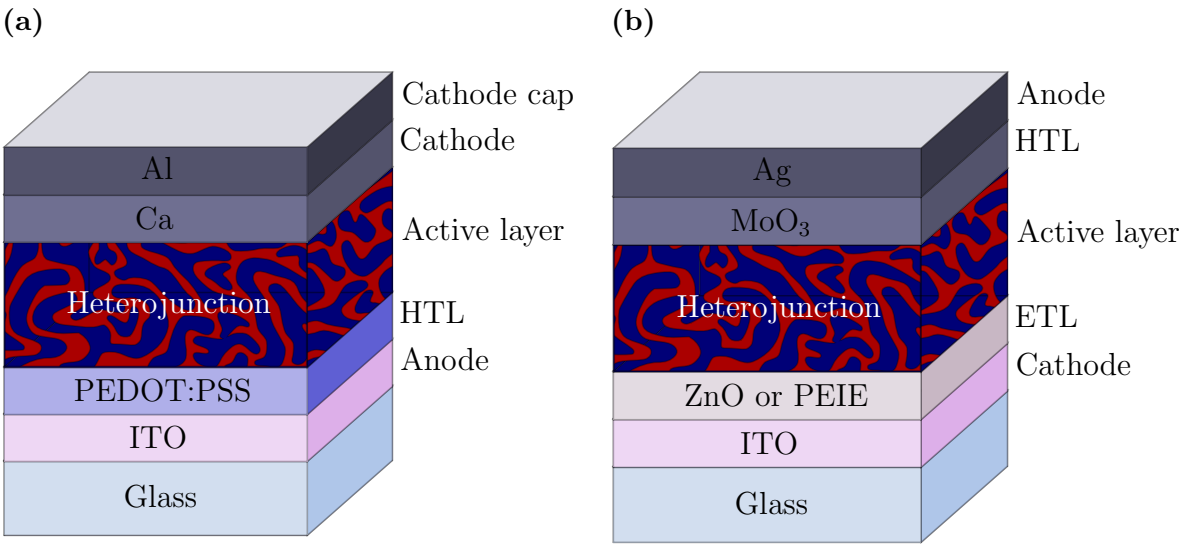


Figure 3.1: Typical device architectures used in this thesis (a) conventional architecture, (b) inverted architecture. In both cases solar illumination is from the bottom; ETL is the electron transporting layer, and HTL is the hole transporting layer.

sized substrates. The height of the blade above the bed can be finely adjusted, allowing for substrates of different thicknesses, as well as providing an additional factor to control the film thickness. The blade is pushed along the bed by a metal bar that is attached to the bed of the machine; the coating speed can be adjusted from 1 mm s^{-1} to 99 mm s^{-1}, and is the main parameter for controlling film thickness. Increasing the coating speed increases the film thickness, with the caveat being that thicker films tend to be less homogeneous. Especially in the case of relatively small substrates where the films need to be uniform right to the substrate edge, dummy slides are used either side of substrate to eliminate the inhomogeneity where the solution is pipetted at the top and the spill-back of excess liquid at the bottom. There are no issues in increasing the substrate size; apart from possibly slightly more solution being required, no change is needed to the method. A final advantage to this film-coating method is that the bed temperature can be controlled. The option to heat substrates allows for more control over the morphology of the films, since the rate of solvent evaporation can be changed. In addition, the wettability of the substrates can be increased by increasing the temperature; this is especially helpful for making polymer-only films which can sometimes present wetting issues.

All devices were made using pre-patterned indium tin oxide (ITO) on a glass substrate, purchased from PsioTec. Unless stated otherwise, the substrates are 12 mm × 12 mm, with a single strip of ITO. Prior to coating the first film, the

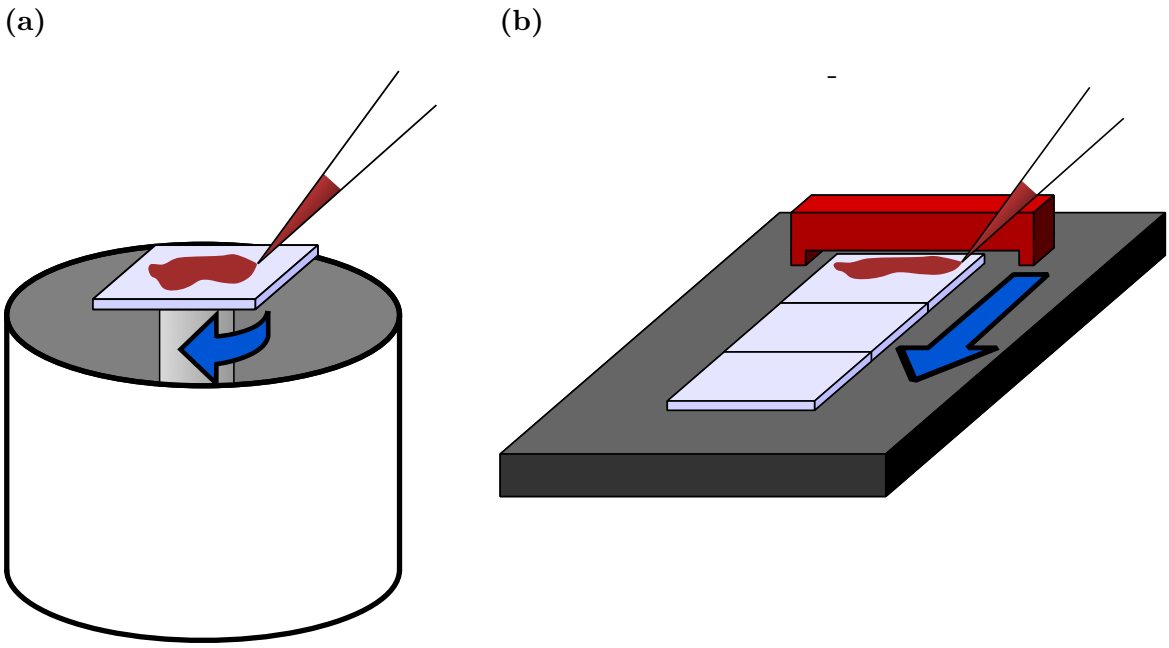


Figure 3.2: Diagrams of the two coating techniques used in this thesis. (a) Spincoating (b) Blade coating, with two dummy slides being used either side of the sample.

substrates must first be ultrasonicated in acetone for fifteen minutes to remove the resist, and then ultrasonicated in isopropanol for a further fifteen minutes. They are then dried and subsequently treated with a plasma asher for five minutes at 100 W in order to remove any remaining organic residues, as well as to increase the surface energy to improve wetting. Immediately after treating, I coat the first layer; this is typically poly(3,4-ethylenedioxythiophene) polystyrene sulfonate (PEDOT:PSS) in conventional devices or either ZnO or polyethylenimine (PEIE) [156] in inverted devices. Then I coat the organic layer, taking care to use an orthogonal solvent. Finally I evaporate the top electrode in a glove box. The specific coating parameters for the common interlayers are below.

PEDOT:PSS

We purchase PEDOT:PSS from Heraeus, formulated in water; specifically we use the Clevios^{TM} P VP AI 4083 formulation, which has a solids content of 1.3-1.7%, and a PEDOT:PSS weight ratio of 1:6. I filter this solution using a 0.45 µm filter. The film can be coated using either the spincoating or bladecoating technique. To spincoat, I use the filtered solution as is, and for a standard 12 mm × 12 mm substrate I use 40 µl. The spin speed is 2500 rpm for 1 minute, with an acceleration of $10,000$ rpm s^{-1}. On the other hand, to blade coat, I mix the filtered solution with isopropanol with a 1:3 mixture. I set the blade height to 150 µm, and the

bed temperature is 50 °C. I apply two consecutive coats at 7 $\mathrm{mm\,s^{-1}}$, each with a solution volume of 15 µl. For both techniques, after coating the film, I anneal the substrate on a hotplate at 140 °C for twenty minutes to eliminate any water left in the film. The above processes both result in film thicknesses of about 10-15 nm.

Zinc Oxide

Zinc oxide films must be spincoated. The day before coating, I prepare the precursor solution of zinc acetate, using 219.5 mg zinc acetate dehydrate, 2 ml 2-methoxyethanol and 60.4 µl ethanolamine (all purchased from Sigma Aldrich). I set this solution to stir vigorously overnight at room temperature. To coat the film, I spincoat 40 µl of solution at a speed of 4000 rpm, with an acceleration of $10,000$ rpm $\mathrm{s^{-1}}$. I then anneal the substrate at 150°C for 10 minutes.

PEIE

We purchase polyethylenimine, 80% ethoxylated (molecular weight $70,000\ \mathrm{g\,mol^{-1}}$), dissolved in water to a concentration of 35-40 wt.% from Sigma Aldrich. I further dilute this solution with 2-methoxyethanol to a weight concentration of 0.4%. I made PEIE films by spincoating, using 40 µl of solution, with a spin speed of 5000 rpm and acceleration of 1000 rpm $\mathrm{s^{-1}}$, for one minute. After coating, I anneal the film at 100°C for ten minutes.

Once all the solution-processed layers have been coated, the substrates are then transferred to the glove box, which maintains oxygen and water concentrations of less than 0.1 ppm. The evaporator is contained within the glovebox and includes an Inficon quartz crystal system to monitor electrode thickness. Unless stated otherwise, the device area is 4.5 $\mathrm{mm^2}$, which is defined by the overlap between the ITO strip and the electrodes, as shown in Figure 3.3; there are six separate pixels per substrate, and sixteen separate substrates can be evaporated at one time. Once I load the substrates and evaporation sources, I pump the chamber down to $\leq 10^{-6}$ bar. The top electrode for inverted devices is typically molybdenum oxide (10 nm) / silver (100 nm), whereas for conventional devices typically I evaporate calcium (10 nm) / aluminium (100 nm). Both materials can be evaporated consecutively with no need to vent the chamber. Typically I target an evaporation rate of $0.1 - 0.2$ $\mathrm{Å\,s^{-1}}$ at the beginning of each layer, which can be increased after about 5-10 nm has been evaporated.

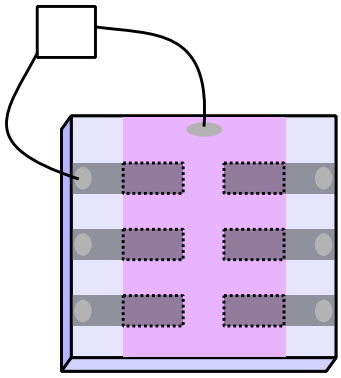


Figure 3.3: Layout of a standard substrate with six 4.5 mm^2 devices. The bottom ITO strip is shown as well as the top evaporated electrodes to illustrate the overlap which defines the device area and is outlined by dashes. When measuring a device, the ITO forms a common contact as illustrated.

Films for optical measurements are typically made on spectrosil or silicon. I purchase spectrosil from UQG Optics; its transmission is shown in Figure 3.4. Silicon is purchased from IDB Technologies, and is N<100> type with a native oxide and polished on one side. The wafers as-bought are 10 cm diameter, and I then cut them to the size required. Both spectrosil and silicon substrates are cleaned in the same manner as ITO substrates, before coating the required layer(s).

Often it is necessary to know the film thickness, for which I used profilometry on either a Tencor Alphastep or Bruker DektakXT. Profilometry involves scratching the film, taking care to remove all the coated material but leaving the substrate unharmed. During measurement I drag the profilometer tip across the scratch to obtain the vertical profile, giving the film thickness. It is necessary to make many measurements at different points on the film to ensure any inhomogeneities are accounted for.

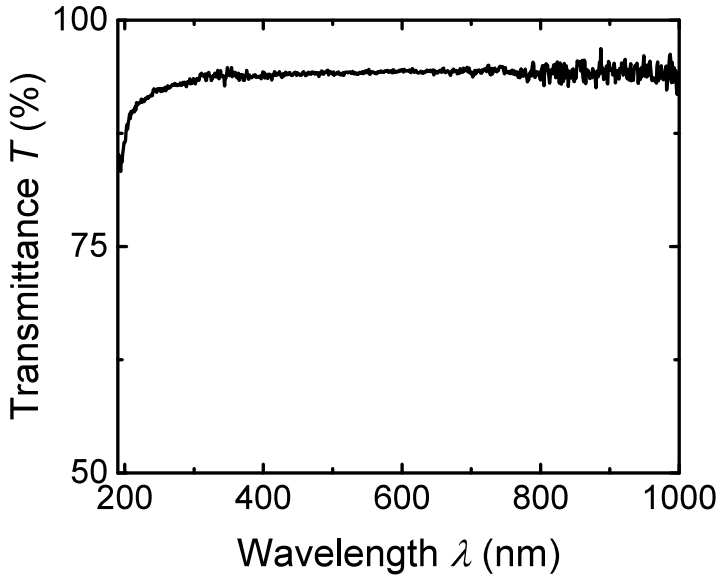


Figure 3.4: Typical transmittance of a spectrosil substrate, used for optical measurements.

3.2 Steady-state device characterisation

3.2.1 Current-Voltage

I measure the current-voltage (J-V) curves using a Keithley 236 source measure unit and a 300W Xenon lamp from Newport, which is fitted with an AM1.5 filter, and therefore provides 100 $\mathrm{mW\,cm^{-2}}$ AM1.5 radiation (one sun). I turn on the lamp at least twenty minutes prior to measurement to warm up. I mount the substrate to be tested in an airtight sample chamber, which maintains the nitrogen atmosphere from the glove box. I position the chamber in the centre of the beam, at a distance determined by calibrating with a silicon photodiode with known current at one sun conditions. The current is scanned from -1.2 V to $+1.2$ V. In addition to a scan under illumination, I also measure dark J-Vs.

3.2.2 Capacitance-Voltage

As mentioned before, doping changes the electrostatics of a device and the behaviour of the device as a function of voltage due to the formation of a depletion region. Therefore the capacitance as a function of voltage is a way to probe the doping density as outlined in this section.

Expanding on the definition of capacitance in eq. (2.45) from Section 2.5.1, the

differential capacitance is defined:

$$C = \frac{\mathrm{d}Q}{\mathrm{d}V} \tag{3.1}$$

The response of capacitance to applied voltage can be understood by tracking the number of carriers in the device as the voltage is varied. First we consider an undoped device in the dark. At 0 V, the situation is as seen in Figure 3.5a, black lines. In order for the device to be in equilibrium, there must be one constant Fermi level through the device. Therefore electrons have flowed into the device from the cathode, which has a higher Fermi level (or a lower workfunction) while holes have flowed into the device from the anode, which has a lower Fermi level (or a higher workfunction). Therefore there is a significant concentration of holes by the anode, and a complementary concentration of electrons by the cathode; however the total net charge in the device is zero.

Meanwhile, if the device is p-type, there is an excess of mobile holes and stationary negative charges, resulting in a depletion region of width w being formed (band diagram shown previously in Figure 2.16). This results in no net electric field towards the anode and a strong electric field towards the cathode, and the charge carrier concentration is as shown by the red lines in Figure 3.5a.

When a positive voltage is applied, the potential of the cathode is raised relative to that of the anode, and there is a splitting of the constant Fermi level into two quasi-Fermi levels: one for electrons and one for holes. The degree of splitting is determined by the applied voltage. The effect of this is to flatten the slope of the bands between the electrodes, meaning that electrons entering the device from the cathode experience less of a barrier in getting through the device, and vice versa for holes. Therefore, the gradient of $\log n, p$ vs w is shallower (Figure 3.5b, black lines), indicating that more electrons make it through the device to the anode, and vice versa. Also, the total number of free carriers in the device is higher than the zero applied bias case.

The concentration of carriers in a doped device at small positive voltages is similar to the case of zero applied voltage, except that the thickness of the depletion layer is reduced.

When a large forward bias is applied, the device reaches a flat-band situation where, as seen in Figure 3.5c, the local concentration of holes and electrons through the centre bulk of the device is equal, resulting in no local net charge, regardless of the doping level in the device.

Relating these changes in carrier concentration to the total charge brings us to

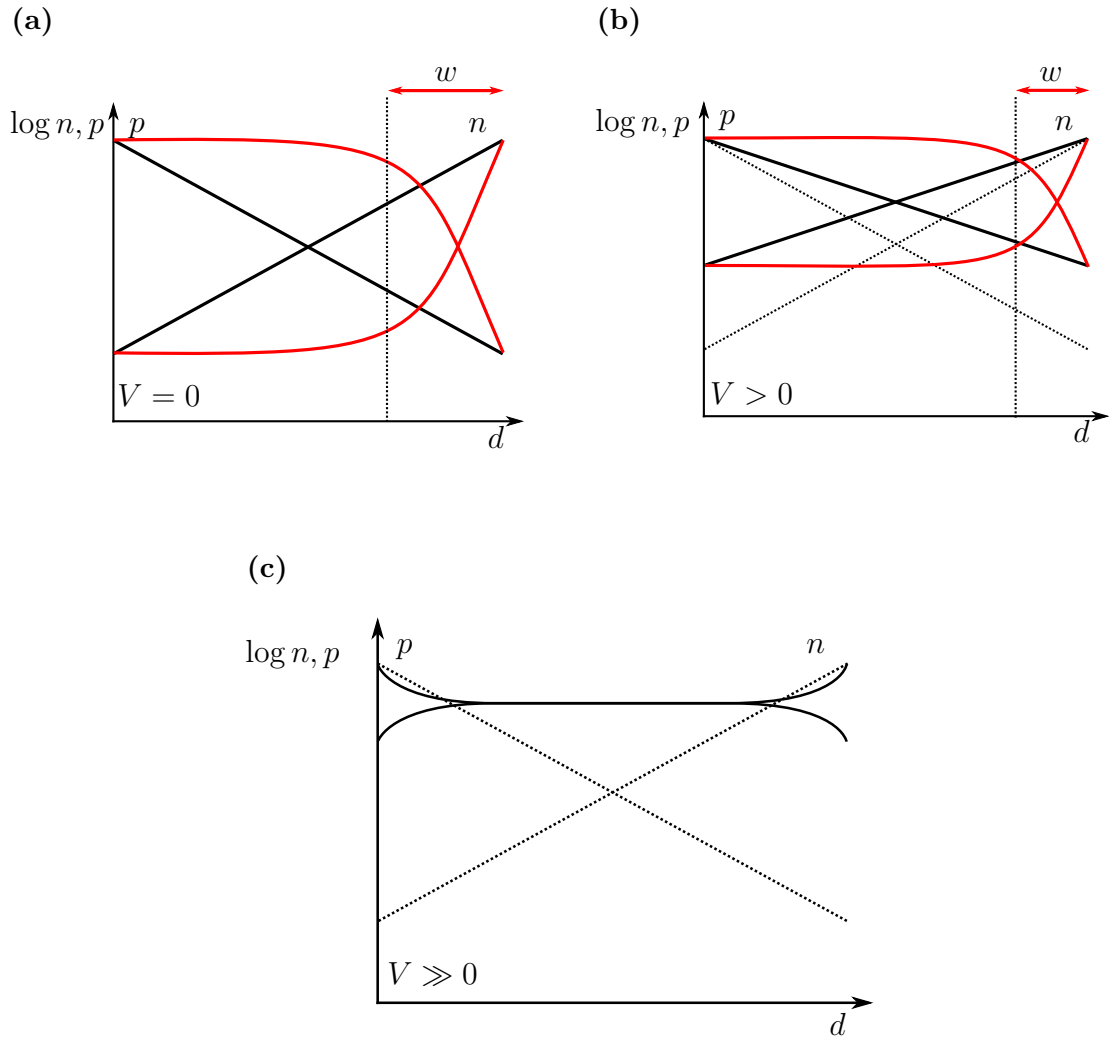


Figure 3.5: Charge density profile in a device for the case of (a) zero applied bias, (b) small positive bias, (c) large positive bias, such that the device reaches flat-band conditions. In (a) and (b), black lines correspond to an undoped device, whereas red lines correspond to a doped device. The resulting depletion depth w is shown. In (b) and (c), the case for an undoped device at zero applied bias is shown by dashed black lines. The anode side is at $d = 0$ while the cathode is towards positive d.

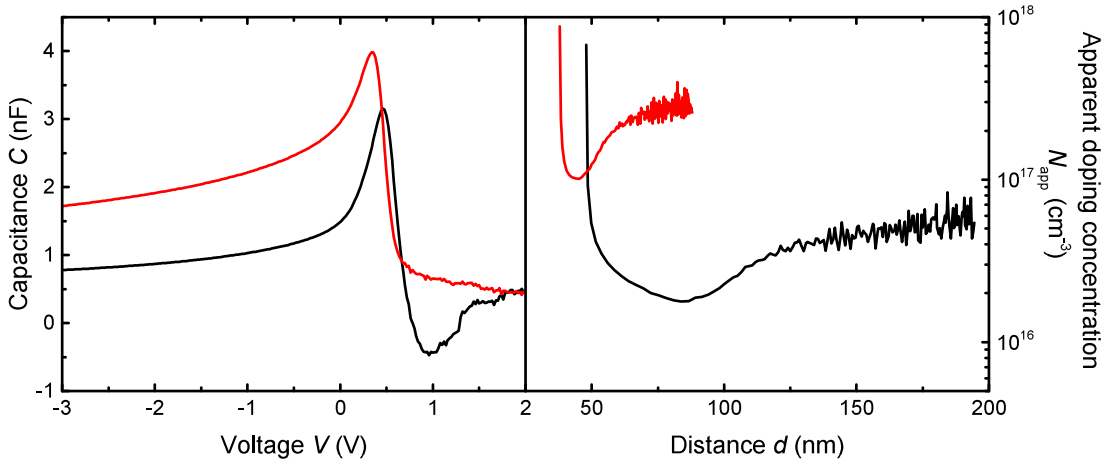


Figure 3.6: Example capacitance-voltage data (left panel) and resulting apparent doping profile (right panel). The capacitance is determined by the rate of change of charge. At reverse bias, there is little total charge density through the device, but as the voltage increases towards the built-in voltage, the charge density increases, resulting in increased capacitance. The maximum of the C-V curve corresponds to flat-band conditions, when the charge density in the device is maximal. Black lines correspond to a device with low doping ($N_{\text{app}} \approx 2 \times 10^{16}$ cm^{-1}) while red lines correspond to a device with high doping ($N_{\text{app}} \approx 10^{17}$ cm^{-1}); the values are taken from the minimum of the N_{app}-d curve.

understand the change in capacitance through eq. (3.1) since $Q = q(p - n)$. The resulting dependence of capacitance on applied voltage for typical devices with different doping levels is shown in Figure 3.6.

In a doped device, as opposed to an undoped device, band bending will mean that the measurement will probe the depletion width if this is less than the total film thickness. By rearranging eqs. (2.44) and (2.45), it is evident that the apparent doping density, N_{app}, is proportional to the reciprocal of the gradient of $1/C^2$ plotted against voltage. This can be plotted against the distance x through the device, as calculated using the static dielectric constant and the capacitance, using eqs. (2.45) and (3.2).

$$N_{\text{app}}(x) = -\frac{2}{q\varepsilon A^2}\left(\frac{\mathrm{d}C(x)^{-2}}{\mathrm{d}V}\right)^{-1} \tag{3.2}$$

However, for these measurements to be valid, the devices must be thick enough so that the experimentalist can be sure that the measurement is detecting the depletion width and is not limited by the whole film thickness [157]. Kirchartz did a range of simulations using a drift-diffusion model to calculate the level of doping that would be measured in films of varying thicknesses, if the input level

of doping was zero. He found that in thicker films there was less variance in N_{min}, the minimum apparent level of doping; in addition, the measured doping concentration decreased with increasing thickness, saturating to the correct value at high thicknesses (on the order of 500 nm). The higher the doping, the stronger the effect on depletion width so the thinner the device could be, but in general in this thesis I made devices that were as thick as possible, and the measured doping densities were compared to the figures in [157] to ensure the numbers were not artefacts.

Capacitance-voltage measurements were performed on a Schlumberger SI 1260 impedance analyser, at 1, 10 and 100 kHz. The voltage interval was [-3 V; +2 V], with steps of 20 mV. The device architecture was the same as that used for solar cells, with the only difference being the active layer thickness. The sample was held in nitrogen atmosphere in the dark during the measurement.

3.2.3 Quantum efficiency

Quantum efficiency describes the number of electrons generated per incoming photon (external quantum efficiency, EQE) or absorbed photon (internal quantum efficiency, IQE). EQE is more straightforward to determine, since it only relies on knowledge of the light source spectrum. IQE however requires both the EQE and the absorption spectrum of the active layer itself, which is more difficult to determine because it can be affected by interference and interfacial effects.

I measured the EQE spectra in this thesis on an in-house set-up, comprising of a Newport 300 W Xenon lamp, a CVI Instruments Digikrom 240 monochromator, Bentham 218 variable frequency optical chopper and Stanford Research Systems SR830 DSP lock-in amplifier; see Figure 3.7. This set-up has the advantage of being able to measure a high dynamic range, such that the quantum efficiency of the charge transfer state can be measured (see Section 3.4.4). I use a silicon photodiode with a known quantum efficiency response to calibrate the system, and the available wavelength range is 300 nm to 1100 nm. I use appropriate Thorlabs long-pass filters at longer wavelengths to reduce the noise since the signal tends to be low in this region. Therefore if the low signal, long wavelength range is of interest, I perform the measurement in steps, with different filters for different ranges of wavelength, ensuring overlap regions so that the data can be spliced together accurately later; Figure 3.8 shows an example set of data, and Table 3.1 lists the filter configurations.

The samples are typically standard solar cell devices, which I measure in a sample chamber under nitrogen atmosphere. The monochromator is masked such

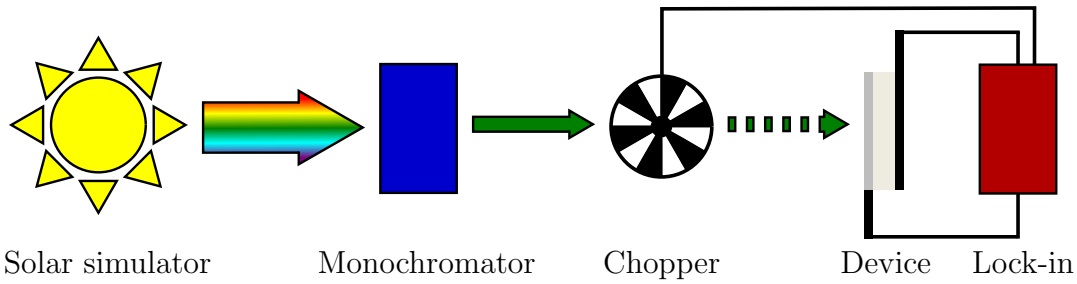


Figure 3.7: Experimental set-up of in-house high dynamic range EQE system. The solar simulator is fitted with a Xenon 300 W lamp, which is reduced to one wavelength by the monochromator. An optical chopper chops the light and serves as the input for the lock-in amplifier, thus the current due to the monochromator light only is measured.

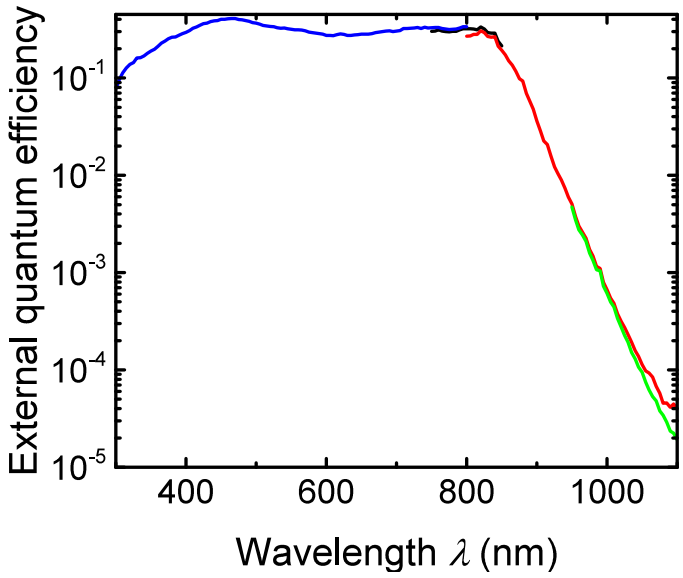


Figure 3.8: Example of the step and glue process for EQE spectra. Each colour is measured with different filters, as listed in Table 3.1.

Table 3.1: The filters used during a high-range EQE measurement, which is performed in steps. All filters are from Thorlabs.

Wavelength range (nm)	Long-pass filter(s)
300 – 800	none
750 – 850	780
800 – 1000	780,850
950 – 1100	850,1000

that the light spot is the same size as the standard pixel. I keep the sample at a fixed distance from the monochromator, and align it by setting the monochromator to a visible wavelength and maximising the current measured by the lock-in amplifier. I set the frequency of the chopper to about 270 Hz. At each wavelength the current is sampled 25 times by the lock-in, outputting an average value.

As already alluded to, measurement of the internal quantum efficiency is a bit more involved. IQE is defined as

$$\text{IQE} = \frac{\text{EQE}}{\text{active layer absorption}} \tag{3.3}$$

It may be tempting to try to directly measure the active layer absorption by, for example, depositing a nominally identical film on glass and directly measuring the transmittance. However the photocurrent is strongly dependent on interference effects [158] and so is very sensitive to small differences in film thickness, as well as the nature of the interface. Therefore it is important to use the behaviour of the actual device as much as possible. Since OPV devices have a reflective back contact, the absorption of the device can be measured via the reflectance R, with whole device absorption $= 1-R$. However the active layer is only one of potentially many layers in the device, and so this approach still does not accurately reflect the active layer absorption [159].

The parasitic absorption is defined as the absorption of all the layers apart from the active layer. Therefore, the active layer absorption is equivalent to $1-R-$parasitic absorption. R can be measured directly, using an ultra-violet visible (UV-Vis) spectrometer fitted with an integrating sphere (see Section 3.4.1). The parasitic absorption cannot be measured experimentally, but can be modelled using the transfer matrix formalism from Section 2.7 so long as the optical constants of every layer is known.

While the transfer matrix model (TMM) can directly calculate the active layer absorption, this approach assumes that the interfaces are perfectly planar, which is not often valid. Limiting the use of TMM to only the parasitic absorption reduces the error of the calculation [160], since the experimentally measured reflectance takes the rough interfaces into account, and parasitic absorption is generally very low.

Ideally the exact same devices would be used for the EQE measurement and reflectance so that sample variation is not an issue. However in practice, this requires a very large device area due to the configuration of the integrating sphere in the UV-Vis spectrometer, which was impractical for the devices measured in

this thesis because the current collected was too low to get a good EQE spectrum. So I compromised and in one evaporation made devices with small areas for the EQE measurements, and devices with large areas for reflectance measurements; I made all the devices using the same coating parameters, and measured repeats to ensure that the sample-to-sample variation was low enough to justify this method.

3.3 Charge Extraction and Transient Photovoltage

Charge extraction (CE) is a technique which is used to measure the density of excess charge carriers in a working solar cell [161]. The set-up uses a ring of twelve white light emitting diodes (Lumileds Luxeon), whose brightness is controlled by a power meter. I calibrate the set-up to one sun conditions by performing a light intensity calibration, which involves switching between open-circuit and short-circuit conditions, in order to determine the light intensity required to simultaneously match the J_{sc} and V_{oc} previously measured using a solar simulator. Due to the different absorption characteristics of different photovoltaic blends, the light intensity required to generate the charge density to match one sun conditions is variable, but it can be assumed that if the J_{sc} and V_{oc} are matched then the charge density and corresponding charge dynamics are well represented. In addition, I take care during measurements to avoid heating up the device.

In order to measure the charge density, the device is held at a certain bias (most usually at short-circuit or open-circuit, although any point along the J-V curve can be accessed) under a light bias for a few hundred milliseconds, in order to reach an equilibrium but without heating up the device, before the light is turned off and simultaneously the device is switched to short circuit and the charge is collected using an oscilloscope (Tektronix TDS 3032B) (Figure 3.9). I take care to tailor the duration of charge collection to ensure that all the possible charge is collected; I monitor the integrated transient to ensure that it reaches a plateau. I repeat this process for a range of light intensities, so that I can monitor the rate of increase of charge density with quasi-Fermi level splitting, i.e. the V_{oc}, which gives information about the density of states. I should note that the charge density measured is not the total charge density in the device, but the excess relative to the density in equilibrium in the dark. Furthermore, this measurement cannot access any spatial variations within the device, and thus gives the average excess charge density.

It should be noted here that we must apply two corrections to the raw data

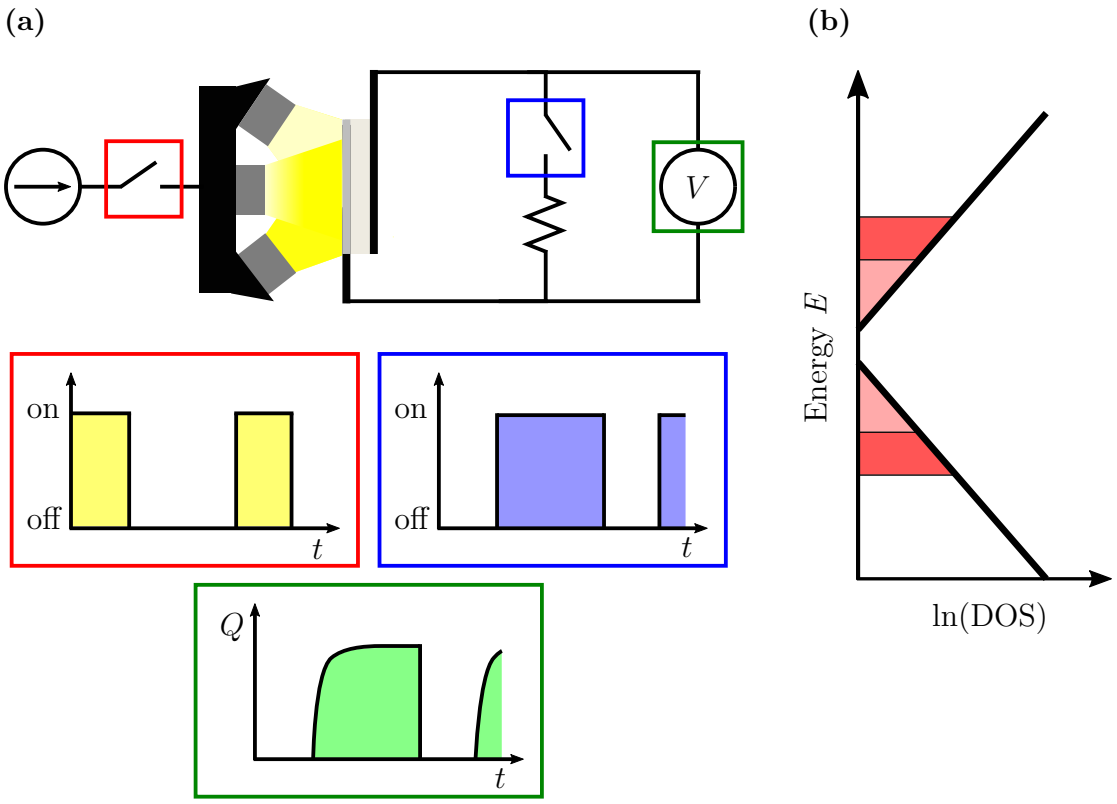


Figure 3.9: Diagrams showing the principles of the charge extraction experiment. (a) The experiment schematic, including (left to right) the power supply, the LED MOSFET (red box), LED light source, solar cell, current collection MOSFET (blue box) and 50 Ω resistance, and oscilloscope (green box). The graphs show the switching behaviour of the two MOSFETS (red and blue), and the measured charge transient (green). The LEDs are on for a few hundreds of milliseconds while the cell is held at open circuit; then the light is turned off while the current collection MOSFET is simultaneously turned on, switching the cell to short-circuit, and the current is collected over enough time to ensure that all excess charge from the device has been collected. (b) Schematic showing how charge extraction can probe the density of states; the greater the light intensity, the greater the Fermi level splitting, so the greater the amount of collected charge. Two light intensities are indicated, the darker colour representing the higher light intensity. Figures adapted from Thomas Kirchartz and Andrew Telford.

in order to get a good measure of the charge density present in the device during illumination [161]. Firstly, the electrodes will act as capacitors and as such store a finite amount of charge. We can estimate the charge stored due to electrode capacitance (eq. (3.4)) using the device thickness d, as measured with a profilometer after measurement, the electrode area A and the device dielectric constant $\varepsilon_0\varepsilon_\mathrm{r}$; the relative dielectric constant ε_r of polymer:fullerene blends is assumed to be 3.8. The stored charge density is typically approximately an order of magnitude smaller than the extracted charge and therefore this correction is relatively minor.

$$Q_\mathrm{cap} = CV = \frac{\varepsilon_0\varepsilon_\mathrm{r} AV}{d} \tag{3.4}$$

The second correction we must apply is to account for any charges which have recombined prior to being extracted; in order to apply this correction we must know the charge carrier lifetime (e.g. by measuring using transient photovoltage, described below). We use an iterative procedure which uses the raw measured charge density and the carrier lifetime to calculate the charge density expected to have recombined; we then calculate a new total charge density which serves as the input for a new iteration. The method is described in more detail in [161]. The resulting charge density follows an empirical exponential relationship to V_oc, such that:

$$n_\mathrm{oc} = n_0 \exp\left(\frac{qV_\mathrm{oc}}{mkT}\right) \tag{3.5}$$

where n_0 and m are fitted parameters; m gives an indication of the shape of the density of states, since it describes the relationship between the rate of growth of charge density with increasing Fermi-level splitting.

At short-circuit, drift current dominates over diffusion current due to the strong electric field, so $J_\mathrm{sc} \approx J_\mathrm{drift}$. The drift current can also be related to the charge mobility through [134]:

$$J_\mathrm{drift} = q\,\mu\,n_\mathrm{sc}\,f(\delta)\frac{V_\mathrm{bi}}{d} \tag{3.6}$$

where μ is the drift mobility, n_sc is the charge density at short-circuit, V_bi is the built-in voltage, d is the device thickness, δ is the reaction order, and $f(\delta) = (2+\delta)(1+2\delta)/(1+\delta)^2$. Charge extraction can be performed at short-circuit, so can be used to measure n_sc and therefore the charge mobility. V_bi is typically taken as the voltage at which the photocurrent is zero, where the photocurrent is defined as the difference between the light and dark currents. The reaction order is given below in eq. (3.12), and is determined from the parameters which describe the relations between the charge density and charge lifetime with respect to the

open-circuit voltage. $f(\delta)$ is a correction factor which takes into account the effect of tail states [134].

Transient photovoltage (TPV) is a complementary technique which we conduct using the same experimental set-up as charge extraction, with the addition of a pulsed laser [162] (here I used a GL-330 PTI nitrogen laser pumping a GL301 PTI dye laser, frequency 4 Hz, pulse duration $\approx$ 1 ns). During measurement, I hold the device at open-circuit, using an oscilloscope with 1 MΩ impedance, under a certain light bias from the LED ring, and pulse the laser which generates a small perturbative photovoltage (typically approximately 20 mV) due to the excess carriers generated (see Figure 3.10). The laser is directed at the device using an optical fibre with a large aperture, which ensures homogeneous illumination of the device. Since the device is held at open-circuit, there is no option for the laser-generated carriers but to recombine, and the photovoltage decay follows a single exponential. I fit this to obtain V_0, the peak perturbation voltage, and $\tau_{\Delta n}$, the decay lifetime. Δn denotes that this is the small perturbation lifetime, as opposed to the full lifetime τ_n which will be derived later. $\tau_{\Delta n}$ is plotted as a function of V_{oc}, and I fit the resulting line to find the empirical parameters ϑ and $\tau_{\Delta n0}$ as follows:

$$\tau_{\Delta n} = \tau_{\Delta n0} \exp\left(-\frac{qV_{\mathrm{oc}}}{\vartheta kT}\right) \tag{3.7}$$

An alternative method to measure the charge density in the device is differential charging [162], which uses the same set-up as TPV, but where we perform an initial transient photocurrent (TPC) measurement to measure the charge injected by the laser pulse; this measurement is analogous to a CE measurement, but where the excess carrier density ΔQ injected by the laser pulse only is extracted relative to the background light intensity, which we typically vary between 0% and 50% of one sun. There is typically very little variation between the injected charge at different background light intensities, and so we take the average of the measurements. We use this charge, ΔQ, and the corresponding initial photovoltage, ΔV_0, to calculate the capacitance, C, induced in the device as a function of V_{oc}:

$$C = \frac{\Delta Q}{\Delta V_0} \tag{3.8}$$

Note that there are two possible ways of obtaining ΔV_0: the simplest is to simply read off the maximum of the $V(t)$ graph, but the data in this region is often noisy and subject to the response of the oscilloscope. And so an alternative method is to use the projected $V(0)$ from the fit of the rest of the exponential. During data analysis, we can compare both methods in terms of how well the

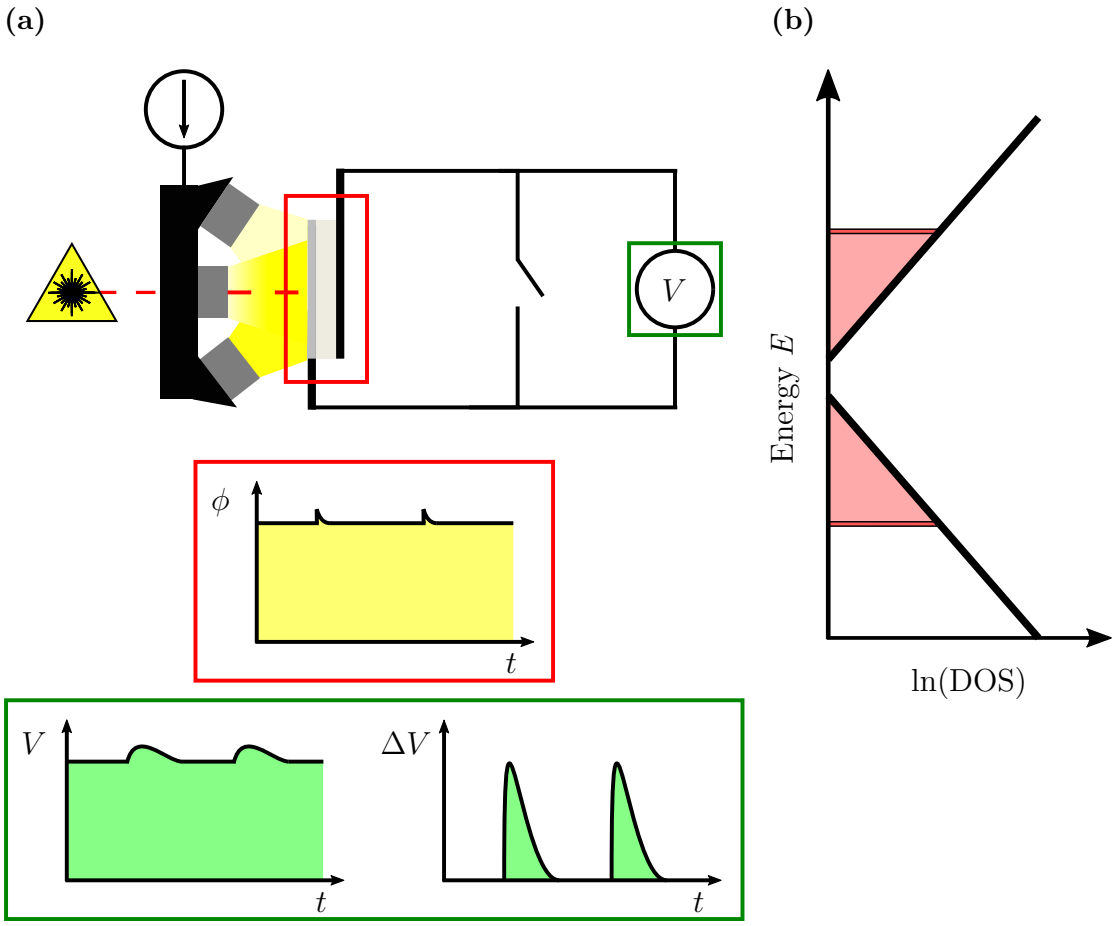


Figure 3.10: Diagrams showing the principles of the transient photovoltage experiment. (a) The experiment schematic, including (left to right) the laser, LED power supply, LED light source, solar cell (red box), and oscilloscope (green box). The solar cell is held at open circuit throughout the experiment. The laser provides a small perturbation to the light intensity impinging on the solar cell (graph in red box), which results in a small perturbation in the solar cell open-circuit voltage, measured by the oscilloscope. The graphs in the green box show the measured voltage and resulting voltage perturbation ΔV. (b) Schematic showing the perturbation effect on the density of states: the background light intensity results in a steady-state population of charge carriers while the laser excites a small number of excess carriers (darker colour). Figures adapted from Thomas Kirchartz and Andrew Telford.

fitted parameters reproduce the $V_{\mathrm{oc}}(\phi)$ data using eq. (3.21). Note also that the geometric capacitance of the electrodes, $C = \varepsilon_0 \varepsilon_{\mathrm{r}} A/d$ as before, also contributes to the capacitance and must be subtracted to obtain the capacitance of the active layer only.

Again, I perform the measurement at many light intensities, resulting in the relation between the capacitance and V_{oc}:

$$C = C_0 \exp\left(\eta V_{\mathrm{oc}}\right) \tag{3.9}$$

We fit the empirical parameters η and C_0 to the data. The charge density n_{oc} is proportional to the integral of the capacitance with respect to voltage as in eq. (3.10), where A is the cell area and d is the device thickness.

$$\begin{aligned} n_{\mathrm{oc}} &= \frac{1}{Aqd} \int_0^{V_{\mathrm{oc}}} C \, \mathrm{d}V \\ &= \frac{1}{\eta}(C - C_0) \end{aligned} \tag{3.10}$$

Once we evaluate $n_{\mathrm{oc}}(V_{\mathrm{oc}})$, we can use the same empirical relationship introduced before (eq. (3.5)) to can fit the parameters m and n_0.

Now we can derive an expression for the full lifetime τ_n. The reaction order δ defines the power law of the recombination current J [163]:

$$J = \frac{\mathrm{d}n}{\mathrm{d}t} = k n^{\delta} = k_{\mathrm{ss}}(n) n \tag{3.11}$$

where k_{ss} is the charge density dependent steady state rate constant. Since recombination current can also be written as $J = n/\tau$, we can determine the reaction order from the parameters we've already introduced, namely:

$$\delta = \frac{m}{\vartheta} + 1 \tag{3.12}$$

Note that the empirical reaction order determined from the CE/TPV experiments cannot necessarily be interpreted as the reaction order of recombination, since it can be affected by spatial inhomogeneities in charge density through the device, which is particularly an issue for thin devices [164].

We can define k_{tr} to be the transient rate constant:

$$\frac{\mathrm{d}\Delta n}{\mathrm{d}\Delta t} = k_{\mathrm{tr}}(n) \Delta n \tag{3.13}$$

This small perturbation represents the difference between the transient measurement and steady state conditions, therefore:

$$\begin{aligned}\frac{\mathrm{d}\Delta n}{\mathrm{d}\Delta t} &= J' - J = k(n+\Delta n)^{\delta} - kn^{\delta} \\ &\approx kn^{\delta}\left(1 + (\delta)\,\frac{\Delta n}{n}\right) - kn^{\delta} \\ &= k\delta n^{\delta-1}\Delta n \end{aligned} \tag{3.14}$$

Now that we have developed expressions for the recombination rate, we can derive the recombination lifetime, which is defined using $\mathrm{d}n/\mathrm{d}t = n/\tau_n$ and $\mathrm{d}\Delta n/\mathrm{d}\Delta t = \Delta n/\tau_{\Delta n}$. Thus:

$$\tau_n = \frac{1}{kn^{\delta-1}} \tag{3.15}$$

$$\tau_{\Delta n} = \frac{1}{k\delta n^{\delta-1}} \tag{3.16}$$

$$\therefore \tau_n = \delta\tau_{\Delta n} \tag{3.17}$$

Now it is useful to combine these relations (eqs. (3.5), (3.7), (3.12) and (3.19)) to obtain an expression for τ_n as a function of n.

$$\begin{aligned} n^{\delta-1} &= n_0^{\delta-1}\exp\left(\frac{qV_{\mathrm{oc}}}{mkT}\frac{m}{\vartheta}\right) \\ &= \frac{n_0^{\delta-1}}{\exp\left(-\frac{qV_{\mathrm{oc}}}{\vartheta kT}\right)} \\ &= \frac{n_0^{\delta-1}\tau_{\Delta n0}}{\tau_{\Delta n}} \\ &= \frac{\delta n_0^{\delta-1}\tau_{\Delta n0}}{\tau_n} \end{aligned} \tag{3.18}$$

$$\therefore \tau_n = \frac{\delta\tau_{\Delta n0}n_0^{\delta-1}}{n^{\delta-1}} \tag{3.19}$$

So once we perform both the excess charge carrier density and the charge carrier lifetime measurements as a function of V_{oc}, we can plot $\tau(n)$, which is the carrier lifetime independent of effects due to the density of states. We can also now

express the open-circuit voltage as a function of the parameters derived from these experiments by considering that at open-circuit, the net current is zero, so the recombination current J_{rec} equals the generation current J_{gen}. Furthermore, we can assume that the generation current is approximately given by the short-circuit current density, which assumes that at short-circuit, negligible current density recombines before being collected. Under these conditions, we have:

$$J_{\mathrm{rec}}(V_{\mathrm{oc}}) = ed\,\frac{n_{\mathrm{oc}}}{\tau_n} \approx J_{\mathrm{sc}} \tag{3.20}$$

Using eqs. (3.5), (3.12) and (3.19), we can re-arrange the above to find an expression for V_{oc}, as a function of the experimentally-determined parameters [165, 166]:

$$V_{\mathrm{oc}} = \frac{kT\vartheta m}{q(m+\vartheta)} \ln \frac{J_{\mathrm{sc}}\tau_{\Delta n_0}\delta}{qdn_0} \tag{3.21}$$

Equation (3.21) therefore describes the expected behaviour of V_{oc} as a function of J_{sc}, if the assumptions made during the analysis, particularly that non-geminate recombination is the primary loss mechanism, are valid. The J_{sc} and V_{oc} can both be measured as a function of light intensity; the comparison between the experimentally measured V_{oc} and the V_{oc} calculated using eq. (3.21) provide a validation of the derived parameters, while confirming that non-geminate recombination is dominant.

3.4 Steady-state spectroscopy

3.4.1 Ultraviolet-visible spectroscopy

Ultraviolet-visible absorption (UV-Vis) is a popular preliminary assay for new materials. The absorption of either a film or a solution can be measured, and by comparing absolute values the absorbing strength of the material can be probed. It can also be used to assess the shape and peak of the optical absorption of the material, by looking at the absorption peak wavelength and the dependence of the spectral shape to environmental conditions such as temperature or solvent. The UV-Vis spectra of a material in solution and in a thin film can also be compared; differences in, for example, the structure of the peaks can provide hints to the material microstructure.

I used two different UV-Vis spectrometers for different purposes: a simple reference system (Shimadzu UV-2550) for solution measurements, and a system with an integrating sphere (Shimadzu UV-2600) for film measurements; the two

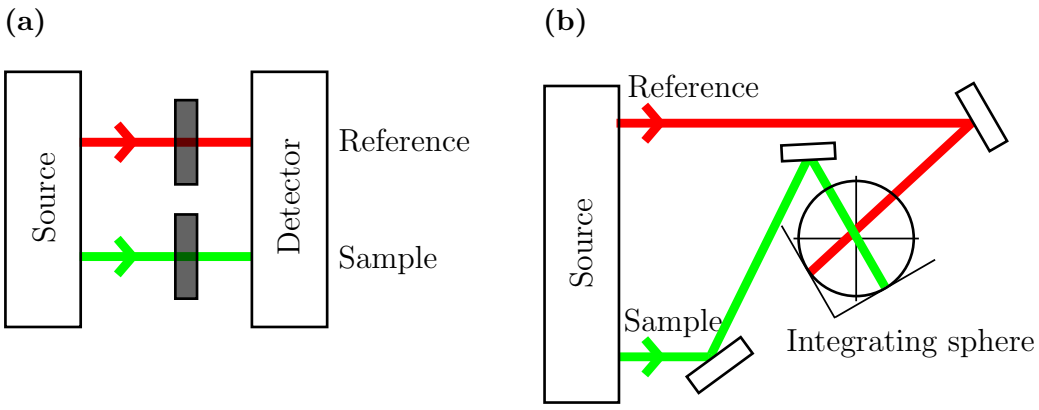


Figure 3.11: Configurations of the two ultraviolet-visible spectrometers used in this thesis. (a) The configuration used to measure solutions, where the absorbance of the sample is calculated as the difference between the absorbances of the sample and reference beams. (b) The configuration used to measure film absorption and reflection, including an integrating sphere. The configuration of the integrating sphere can be altered to measure different quantities (i.e. transmittance vs. reflectance.)

configurations are shown in Figure 3.11. The UV-2550 system can measure the transmittance of films, but due to scattering and interference effects, relying on transmittance to provide absolute information about absorption is not recommended. However for solution measurements, since I use an identical cuvette containing the same solvent as the sample as the reference, there is no additional scattering from the sample cuvette relative to the reference and so the data can be used to provide an absolute absorption measurement.

Thus far I have discussed transmittance and absorption without defining them nor outlining the relations between them. Transmittance T is defined by:

$$\text{Transmittance} = T = \frac{I}{I_0} \tag{3.22}$$

where I is the final light intensity and I_0 is the initial light intensity. Meanwhile the absorbance, or optical density OD, is defined by

$$\text{OD} = -\log_{10}\frac{I}{I_0} = -\log_{10} T \tag{3.23}$$

Another helpful quantity is the decadic extinction coefficient ε, which is the material-dependent absorption, usually in units $\mathrm{l\,mol^{-1}\,cm^{-1}}$:

$$I = I_0 10^{-\varepsilon c d} \tag{3.24}$$

In eq. (3.24), c is the concentration of species (usually in solution) and d is the measurement path length; ε is helpful for comparing the magnitude of absorption in solution, but is less useful in films. Since polymer molar mass is not well defined, an alternative metric is required when measuring polymers. The visible transitions of polymers involve the π-electron system, so the more π-electrons per volume the greater the expected absorption (c.f. the oscillator strength sum rule eq. (2.30)). Therefore it is appropriate to normalise the absorption by the concentration of π-electrons, instead of for example by the molar mass of the monomer unit, since this would favour polymers with larger repeating units.

The number of π-electrons actively participating in the optically active π-system can be debatable however, since aromaticity is not well-defined for multi-ring structures. Table 3.2 lists the number of π-electrons per unit that I used for normalising absorption data.

Often in the literature, the solid-phase absorption coefficient α, typically in units cm^{-1}, is quoted; this is measured from a UV-Vis measurement by assuming Beer-Lambert, i.e. ignoring interference effects, such that:

$$I = I_0 e^{-\alpha d} \tag{3.25}$$

α can be related to κ, the imaginary part of the refractive index by:

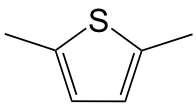
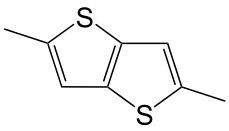
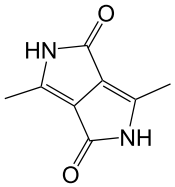
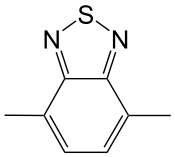
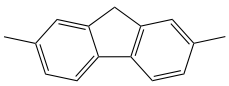
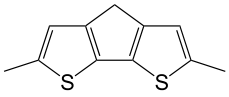
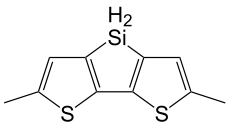
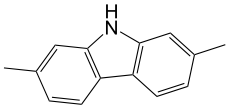
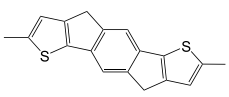
$$\alpha = \frac{4\pi\kappa}{\lambda} \tag{3.26}$$

In order to ensure good signal into the UV range, down to the minimum wavelength of the spectrometer (190 nm), I used spectrosil cuvettes purchased from Hellma for solution measurements, and spectrosil substrates puchased from UQG Optics for film measurements. The transmittance data for spectrosil was shown previously in Figure 3.4.

3.4.2 Ellipsometry

Ellipsometry is an experimental technique which involves measuring changes in polarised light which is reflected off the material being measured [151]. The experimental set-up is shown in Figure 3.12. Ellipsometry is typically used to determine the complex refractive index of a material, and thickness of a thin film. Furthermore, the technique can be used to investigate vertical changes in composition [70] and anisotropy [167]. The experiment measures the change in phase, Δ, and the ratio of initial and final amplitudes, ψ, between s- and p-polarised light

Table 3.2: The number of π-electrons counted per polymer subunit.

Name	Abbreviation	Chemical structure	Number of π-electrons, N_π
Thiophene	T		6
Thienothiophene	TT		10
Diketopyrrolopyrrole	DPP		10
Benzothiodiazole	BT		10
Fluorene	F		12
Cyclopentadithiophene	CPDT		12
Si-cyclopentadithiophene	Si-CPDT		12
Carbazole	CZ		14
Indacenodithiophene	IDT		18

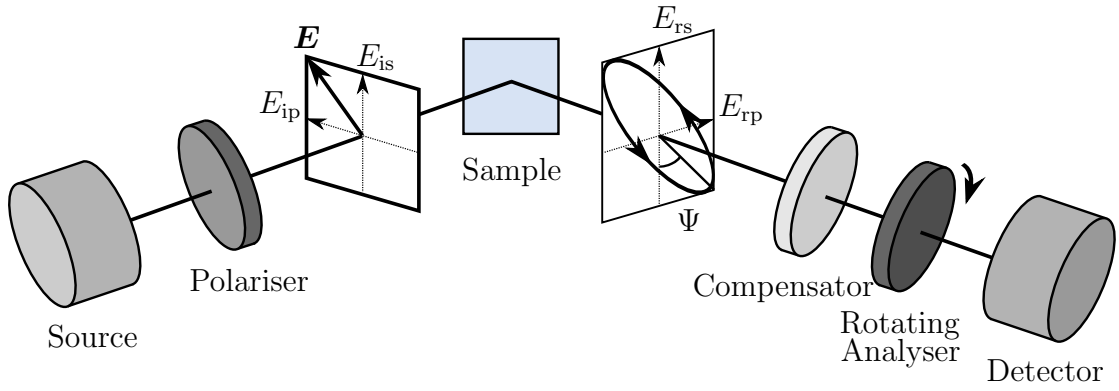


Figure 3.12: Schematic of a typical ellipsometer. The initial polarisation is linear, and upon reflection the relative amplitudes of the s and p components has changed (Ψ); in addition the relative phases have shifted resulting in elliptical polarisation. The ellipsometer configuration is a rotating analyser ellipsometer with compensator, which is the set-up used in this thesis. Figure adapted from Introduction to Spectroscopic Ellipsometry [151].

upon reflection off the sample. The wavelength of the light as well as the angle of incidence can be varied to obtain enough data to adequately describe the system; this mode of ellipsometry is called variable angle spectroscopic ellipsometry, or VASE.

After acquiring data, the experimentalist must then construct an optical model and then attempt to fit the data; assuming a good fit can be reached and the model is appropriate, the complex dielectric function can be derived. However, this indirectness is the principle disadvantage of the technique, since prior knowledge is needed of the system in order to acquire meaningful data. Fortunately, there is a long history of doing ellipsometry on organic systems [168, 169], which provides a context to validate any results.

The principles of s- and p- polarisation were introduced in Section 2.7, and this framework shall be expanded here. First, I will explain the individual optical elements involved in measurement. As shown in Figure 3.12, the components involved in measurement are a polariser, compensator and analyser. A polariser and analyser are essentially the same element, but a polariser is placed before the sample and polarises the light impinging on the sample, while the analyser is placed after the sample and allows measurement of the light intensity at a particular polarisation. A polariser which transmits only the electric field oriented

in the x direction, for example, can be described by a Jones matrix:

$$\boldsymbol{P} = \boldsymbol{A} = \begin{bmatrix} 1 & 0 \\ 0 & 0 \end{bmatrix} \tag{3.27}$$

A compensator induces a phase shift δ between E_x and E_y, such that the corresponding Jones matrix is:

$$\boldsymbol{C} = \begin{bmatrix} 1 & 0 \\ 0 & \exp(-i\delta) \end{bmatrix} \tag{3.28}$$

Both polarisers and compensators exploit materials which exhibit optical anisotropy, which means that their refractive index is different along different axes; this is also called birefringence. Typically these materials are crystals; some common examples are $CaCO_3$ and MgF_2.

The Fresnel reflection coefficients are generally complex numbers, and can be rewritten in polar coordinates, such that s-polarised light can be written $r_s = |r_s| \exp(i\delta_{rs})$; similarly $r_p = |r_p| \exp(i\delta_{rp})$. Therefore the definitions of the ellipsometry coordinate space (ψ, Δ) are:

$$\tan\psi \equiv \frac{|r_p|}{|r_s|} \tag{3.29}$$

$$\Delta \equiv \delta_{rp} - \delta_{rs} \tag{3.30}$$

so $r_p/r_s = \tan\psi \exp(i\Delta)$, and ψ is associated with the refractive index n, while Δ is associated with κ. Most samples measured using ellipsometry are thin film samples on a substrate, and so if the refractive index of the thin film is not known, the refractive index of the substrate must be. In this way multi-layer structures can be built up, where each successive layer is analysed on top of known layers. In addition, it is good practice to measure films on substrates with different refractive indices, such as spectrosil and silicon, and also to measure the film thickness using another method to cross-check.

The general protocol in this thesis was, for each material being studied, to make five films: three on spectrosil and two on silicon, where each film was a different thickness. After we took the data, we measured the film thicknesses using a profilometer, and this measurement served as the starting point for the

modelling.

As standard, the model we choose for the spectrosil substrate is a modified Cauchy relation with no absorption:

$$n = A + \frac{B}{\lambda} + \frac{C}{\lambda^2} \tag{3.31}$$

where A, B and C are fitted parameters, whose values are shown in Table 3.3. The silicon substrates have a native oxide, so must be modelled as two layers. The bottom silicon layer is modelled by a Forouhi interband model [170], with the values in Table 3.4:

$$\begin{aligned} n(E) &= N_\infty + \sum \frac{B_q E + C_q}{(E - B_q)E + C_q} \\ \kappa(E) &= \sum \frac{A(E - E_g)^2}{(E - B_q)E + C_q} \end{aligned}$$

where:

$$\begin{aligned} B_q &= \frac{A}{Q}\left(-\frac{B^2}{2} + E_g B - E_g^2 + C\right) \\ Q &= 0.5\sqrt{4C - B^2} \\ C_q &= \frac{A}{Q}\left(\left(E_g^2 + C\right)\frac{B}{2} - 2E_g C\right) \end{aligned} \tag{3.32}$$

The native oxide is modelled by the Tauc Lorentz model [171], whereby the imaginary part of the dielectric function ε_2 is:

$$\varepsilon_2(E) = \begin{cases} \dfrac{AE_0C(E - E_g)^2}{(E^2 - E_0^2)^2 + C^2E^2}\dfrac{1}{E}, & \text{if } E > E_g \\ 0, & \text{otherwise} \end{cases} \tag{3.33}$$

and the real part ε_1 is:

$$\varepsilon_1(E) = \varepsilon_1(\infty) + \frac{2}{\pi}P\int_{E_g}^{\infty}\frac{\xi\varepsilon_i(\xi)}{\xi^2 - E^2}\mathrm{d}\xi \tag{3.34}$$

where E_g, A, C, E_0 and $\varepsilon_1(\infty)$ are the fit parameters, and P is the Cauchy principal part of the integral [172]. The bare silicon substrate is first fit to determine the thickness of the oxide layer, which is typically approximately 1 nm.

Table 3.3: Parameters used in eq. (3.31) to model spectrosil.

Parameter	Value
A	1.444
B	3.682×10^{-3}
C	3.098×10^{-5}

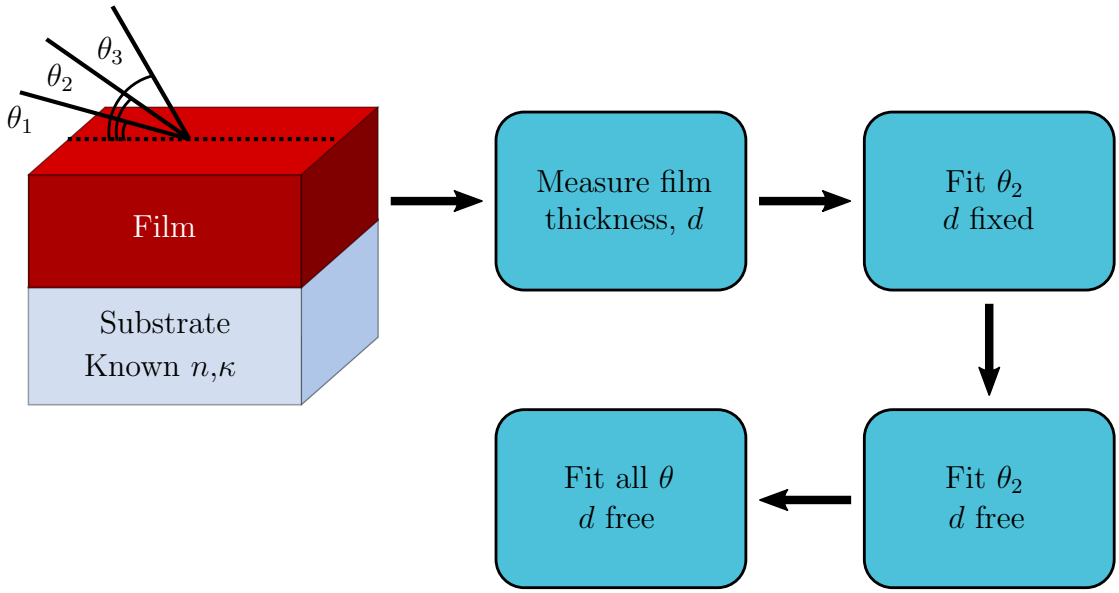


Figure 3.13: Flowchart showing the fitting protocol used generally for thin organic films on a substrate of known refractive index.

The model we choose for pristine organic materials is a standard critical points model [173], which is defined:

$$\varepsilon(E) = UV - \sum_{j=1}^{n} A_j \exp(i\phi_j)(E_{\mathrm{cp},j} - E + i\Gamma_j)^{-1} \tag{3.35}$$

where j is the number of peaks, each described by the set of parameters, A_j, ϕ_j, $E_{\mathrm{cp},j}$ and Γ_j, with UV being a final fit parameter. The fitting algorithm we use is Levenberg-Marquardt, and the general fitting procedure is to first fit the scan at the angle of incidence which gives the greatest range in data values, keeping the film thickness set to the value measured by profilometry, and then allow the film thickness to be a free parameter, and then simultaneously fit all scans with all film parameters free; a flow chart is shown in Figure 3.13.

To model blend systems, we use the Bruggeman effective medium approxima-

Table 3.4: Parameters used in eq. (3.32) to model silicon; the numeric subscripts refer to distinct peaks.

Parameter	Value
N_∞	1.95
E_g	1.06
A_1	4.05×10^{-3}
B_1	6.885
C_1	11.86
A_2	1.427×10^{-2}
B_2	7.4010
C_2	13.75
A_3	6.83×10^{-2}
B_3	8.634
C_3	18.81
A_4	0.1749
B_4	10.65
C_4	29.84

Table 3.5: Parameters used in eq. (3.33) to model the native SiO_2 on the silicon substrate.

Parameter	Value
$\varepsilon_r(\infty)$	1.95
E_g	1.06
A	4.05×10^{-3}
E_0	6.885
C	11.86

tion, defined by:

$$0 = f\frac{\varepsilon_1 - \langle\varepsilon\rangle}{\epsilon_1 + 2\langle\varepsilon\rangle} + (1-f)\frac{\varepsilon_2 - \langle\varepsilon\rangle}{\epsilon_2 + 2\langle\varepsilon\rangle} \tag{3.36}$$

where f is the volume fraction of material 1, $\varepsilon_{1,2}$ are the dielectric functions of materials 1 and 2, and $\langle\varepsilon\rangle$ is the effective dielectric function of the blend. The fitting parameters for the blends are then merely the film thickness and the volume fraction. So the fitting protocol I used was to simultaneously fit all incidence angle scans, letting both parameters be free, using the profilometer-measured thickness as a starting point. As a reality check for both pristine and blend films, we compared the derived complex refractive index spectra to UV-Vis measurements, to ensure that the spectra were consistent in terms of peak position. In addition, by measuring multiple samples at different thicknesses, we could verify the consistency of the derived dielectric function.

3.4.3 Photoluminescence

Photoluminescence is similar to electroluminescence, but instead of populating excited states through electron injection, they are photoexcited. The set-up I used for the work in this thesis uses a 483 nm laser and the same InGaAs detector used in electroluminescence. We use a ThorLabs longpass filter to block any reflected laser beam; the second harmonic is typically in the region of interest for organic films and so can often be seen in spectra. We use the minimum laser power required to get ample signal.

3.4.4 Electroluminescence and voltage losses

Electroluminescence is the phenomenon whereby a device emits light when carriers are electrically injected into it by applying a forward voltage bias. Any light emitted due to the radiative recombination of these charges can be analysed with respect to relative intensity and spectral position to gain information on the available energy states in the device. By reducing the applied bias, and therefore decreasing the energy of the injected electrons, the lowest energy states in the device can be selectively probed. On polymer:fullerene films, therefore, it is possible to directly probe emission from the charge-transfer state, which is lower in energy than either of the blend component band gaps [107]. Therefore, this technique is extremely useful when trying to elucidate the energy losses of OPV systems. It is worth noting that the bias in EL towards low energy states is in contrast to the situation in photoluminescence measurements, where the bias is towards the states which absorb most strongly.

I generally measured working solar devices to collect electroluminescence data; the devices were usually held in a sample chamber under nitrogen although occasionally I used encapsulated devices. We use a Shamrock 303 spectrograph combined with an iDUS InGaAs array detector cooled to −90 °C. The spectra are taken at the lowest possible injection current densities for high enough signal to noise, typically around 40 to 700 $\mathrm{mA\,cm^{-2}}$. The detector is calibrated using a silicon photodetector with a known response. Typically we take measurements using a 10 s integration window, which strikes a balance between getting enough signal but not subjecting the device to relatively high current densities for too long a time, which heats up the device and can cause degradation. The detector has two possible slit widths, 500 µm and 2500 µm; in both cases the data are taken with a series of overlapping windows which are then glued together to obtain the full spectrum, which is typically from 600 - 1800 nm. The narrower slit width allows for better resolution of the data, but worsens the signal to noise ratio so is not always appropriate if, for example, the system is a poor emitter. The background is measured for every integration time window used to collect data, and is subtracted from the raw data, which is then multiplied by the correction data.

Our EL set-up does not measure absolute photon fluxes, but rather relative fluxes are determined which assumes that given the geometry of the system, the detector collects a fixed fraction of the emitted light. In order to use the EL spectra for voltage loss analysis, an EQE spectra must also be measured which overlaps with the EL spectral range. An EL spectrum can be converted to a quantum efficiency through eq. (2.69), and this spectrum is then multiplied by a scaling factor such that the EL and EQE spectra overlap. In this way the effective EQE spectrum can be extended beyond the range of our EQE set-up, over approximately 12 orders of magnitude. Then eqs. (2.67) and (2.68) can be applied to calculate $J_{0,\mathrm{rad}}$ and therefore $V_{\mathrm{oc,rad}}$.

Chapter 4

Understanding voltage losses in indacenodithiophene-based solar cells

4.1 Abstract

In this chapter I present an analysis of the parameters affected by fractionation of an IDTBT polymer. When comparing the non-fractionated polymer with the high molecular weight fraction, I find that the degree of non-radiative recombination is decreased by fractionation. Concurrently, the charge carrier recombination lifetime increases. The charge carrier mobility is not strongly affected by fractionation, so the mobility-lifetime product, a measure of the charge collection efficiency, is higher in the high molecular weight device. I found no effect on the absorption strength of the polymer, nor on the apparent doping in blends. Therefore I conclude that the enhancement in solar cell performance of the high molecular weight devices is due to the reduced recombination and therefore higher charge collection efficiency. A possible explanation is a decreased concentration of impurities and/or chain ends which may act as recombination centres.

Acknowledgements

This work was done in collaboration with Dr Derya Baran while a student in Prof Christoph Brabec's group in the Institute of Materials for Electronics and Energy Technology (i-MEET), Friedrich-Alexander University of Erlangen-Nuremberg (FAU Erlangen). While the data presented in this chapter is my own, I am grateful for the opportunity to cross-check the conclusions. We both received the polymer

from Dr Hugo Bronstein, who synthesised it while a member of Prof Iain McCulloch's group at Imperial College. I am grateful to Prof Thomas Kirchartz for starting this collaboration while a post-doc in my group. I am also grateful for the hours Dr Florent Deledalle, while a member of Prof James Durrant's group at Imperial College, put into this work by training me on the transient photovoltage rig. Similarly, Dr Jizhong Yao built the external quantum efficiency rig and trained me to use it for this project; he was also on hand to help me troubleshoot electroluminescence measurements which were also new.

4.2 Introduction

I previously discussed the limits to solar cell efficiency, specifically examining the limits to the open-circuit voltage (Section 2.6). The maximum possible V_{oc} of a real device with a finite absorption spectrum is when the only recombination is radiative; this value is termed the radiative open-circuit voltage $V_{\mathrm{oc,rad}}$. The difference therefore between this value and the measured device V_{oc} is due to non-radiative recombination and represents a loss; I call this difference $\Delta V_{\mathrm{oc,nr}}$.

Non-radiative recombination losses in organic photovoltaic devices are typically very high, with radiative quantum efficiencies typically around 10^{-9} to 10^{-6} [109, 149]. The voltage loss due to non-radiative recombination is typically approximately 0.35–0.45 V in high-performing organic solar cells, whereas for some inorganic solar cells this value can approach zero [27]. Therefore it is of interest to investigate the sources of non-radiative recombination, in order to try and avoid this loss. Proposed factors which may enhance non-radiative recombination include the concentration of impurities or possibly polymer chain end-groups which act as recombination centres, and/or low charge mobility, which inhibits the charges from being collected efficiently before they recombine. Both of these factors may be influenced by the molecular weight and/or polydispersity [174] of the polymer used in OPV, and so here I focus on assessing the impact of molecular weight on $V_{\mathrm{oc,nr}}$.

To this end, I studied a batch of an indacenodithiophene (IDT) copolymer which was fractionated; the molecular structure of the polymer is shown in Figure 4.1. IDT copolymers are interesting because they have shown promising field-effect transistor mobilities and solar cell performance [124, 175–178]. Enhanced coplanarity of the polymer backbone has been hypothesized to lead to reduced energetic disorder [179, 180]. IDT-co-benzothiadiazole (IDTBT) polymers have achieved up to 6.5% PCE with device optimization and material purification [181],

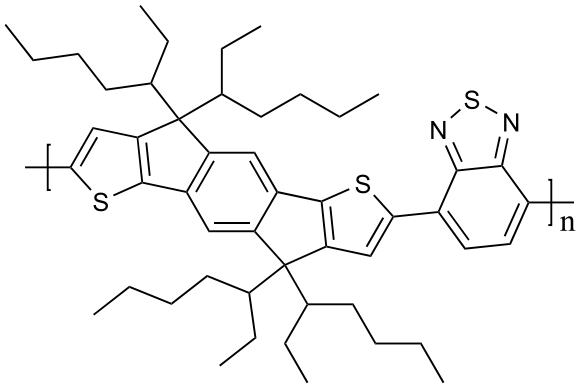


Figure 4.1: Chemical structure of 2-ethylhexyl-indacenodithiophene-co-benzothiadiazole (IDTBT) studied in this chapter.

Table 4.1: The molecular weights of the non-fractionated material (IDT-NF) and the high molecular weight fraction (IDT-HMW). M_n, M_w and PDI are the number-average molecular weight, the weight-average molecular weight and the polydispersity index respectively.

Polymer	M_n ($\mathrm{kg\,mol^{-1}}$)	M_w ($\mathrm{kg\,mol^{-1}}$)	PDI
IDT-NF	27	70	2.6
IDT-HMW	88	130	1.5

and will be the particular system to be studied in this chapter.

The work presented in this chapter was done as part of a collaboration with Dr Derya Baran at FAU Erlangen, and our combined results were subsequently published in the Journal of Physical Chemistry C [149]; any content is reproduced here with permission, copyright 2015 American Chemical Society. However this chapter contains only my data, and so varies slightly from the published version. Furthermore there were some issues with device performance variability so to keep the discussion simpler, I will focus on comparing the non-fractionated batch (NF) with the high molecular weight fraction (HMW). The paper included an additional low molecular weight fraction.

The molecular weights and polydispersity indices of the two materials used are displayed in Table 4.1, and the gel permeation chromatography traces are shown in Figure 4.2.

Throughout the course of the study, multiple batches of devices were made with different coating parameters and J-V curves recorded as the processing conditions were being optimised. Regardless of the precise coating conditions, in each batch the best-performing individual device was a HMW blend, and in all but one batch,

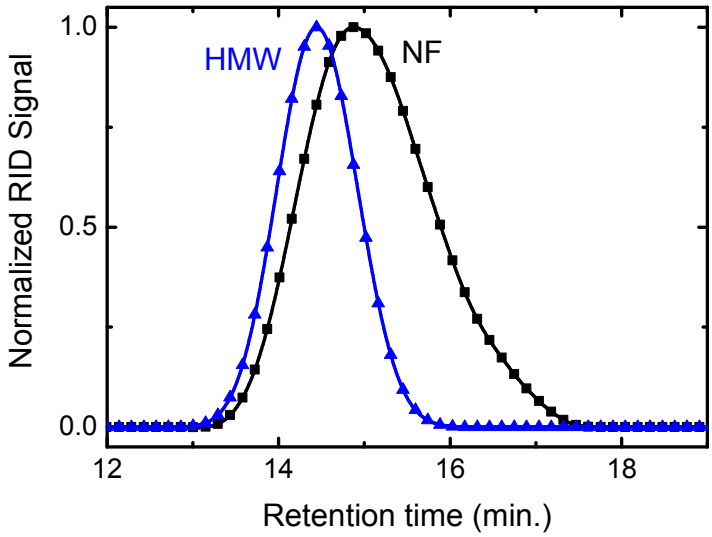


Figure 4.2: Gel permeation chromatography results for the two polymer materials studied in this chapter and tabulated in Table 4.1. IDT-HMW is shown by blue triangles and IDT-NF by black squares. Retention time is normally expected to be inversely proportional to the logarithm of the molecular weight.

the highest substrate average was a HMW blend as well. Table 4.2 displays the best performing devices and substrates for each blend; the experimental conditions of each batch are described in Section 4.6. The variations between batches were as a result of processing conditions: different solution concentrations and coating speeds, resulting in different thicknesses and perhaps film morphology. Figure 4.3 shows current density-voltage data of the best-performing devices of each blend, both from batch 4, and Table 4.3 shows the corresponding performance parameters.

The purpose of this chapter is to clarify which factors are affected by fractionation, in order to explain the performance improvement observed in the HMW blend. Specifically we find that recombination and charge carrier dynamics are particularly affected. I probe these characteristics using an analysis of voltage losses (Section 4.3.3) and the combined transient photovoltage and charge extraction techniques (Section 4.3.4). Unfortunately it was not possible to perform all the characterisation experiments on the same batch of devices, so the voltage loss data I present is on devices from batch 3, while the transient photovoltage data is on devices from batch 4.

Table 4.2: IDTBT solar cell performance across multiple device batches, quantified by power conversion efficiency (PCE). Each substrate has six individual devices, and generally different substrates within a fabrication batch had different coating parameters. Therefore for each batch, it is only appropriate to average across one substrate. Tabulated are the substrate with the greatest average PCE, and the individual device on that substrate with the greatest PCE.

Batch	HMW best device PCE (%)	HMW best substrate average PCE (%)	NF best device PCE (%)	NF best substrate average PCE (%)
1	1.55	1.45	0.73	0.70
2	4.55	3.96	3.55	3.40
3	3.59	3.35	1.97	1.86
4	4.97	4.43	4.79	4.58

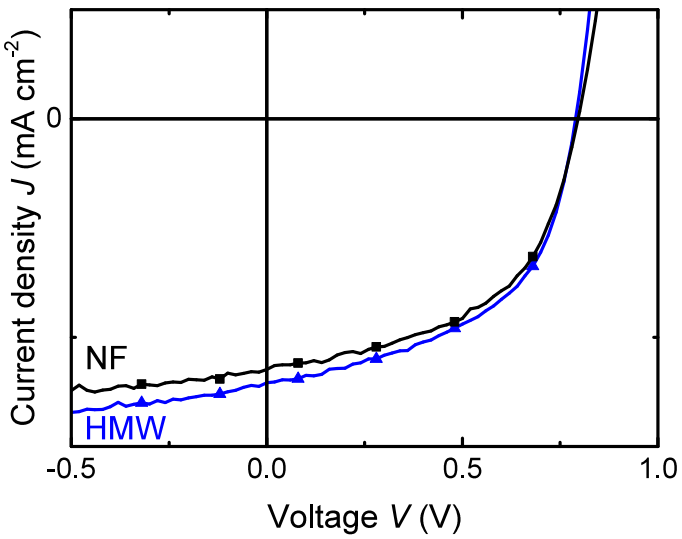


Figure 4.3: Current-voltage curves of devices based on non-fractionated IDTBT (IDT-NF, black squares) and high molecular weight IDTBT (IDT-HMW, blue triangles), whose molecular weight characteristics are displayed in Table 4.1. All devices have an ITO/PEDOT:PSS/IDTBT:$PC_{70}BM$ (1:3.5 w/w)/Ca/Ag architecture. These graphs correspond to the parameters in Table 4.3, and were made in batch 4 (see Table 4.2).

Table 4.3: Solar cell performance parameters of best-performing IDTBT-NF and -HMW devices, both from batch 4, measured under simulated one sun conditions; these parameters correspond to the graphs shown in Figure 4.3. J_{sc} is the short-circuit current, V_{oc} is the open-circuit voltage, FF is the fill factor, and PCE is the power conversion efficiency.

Blend	Thickness (nm)	J_{sc} (mA cm^{-2})	V_{oc} (V)	FF	PCE (%)
IDT-NF	112	11.5	0.796	0.52	4.74
IDT-HMW	113	12.1	0.789	0.52	4.97

4.3 Results

4.3.1 Capacitance-voltage

Given that the non-fractionated batch performed the worst, I measured the doping of the two blends using the capacitance-voltage technique. The apparent doping is plotted as a function of active layer thickness in Figure 4.4 for devices made from IDT-HMW and IDT-NF blends, and shows no difference as a result of fractionation. The devices were dropcast and were approximately 500 nm thick. Therefore we can rule out differences in the electric field profile within the device, due to different levels of unintentional doping, as a possible source for the differences in solar cell performance observed.

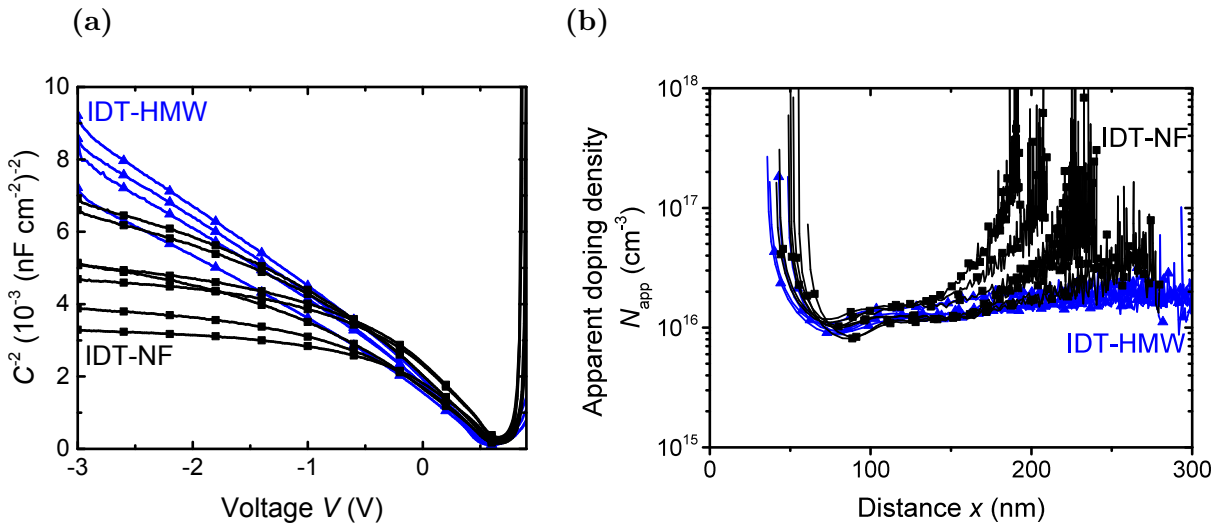


Figure 4.4: Apparent doping concentration of IDTBT-NF (black line, squares) and IDTBT-HMW (blue line, triangles) devices. (a) Mott-Schottky plots of different devices made from the two blends; C is the device capacitance. (b) Apparent doping as a function of film depth x, calculated from the data displayed in (a). In all cases, the devices had the architecture ITO/IDTBT:$PC_{70}BM$ (1:3.5 w/w)/Ca/Al.

4.3.2 UV-Vis

We made films and solutions of the two polymers and found no difference in the magnitude of the absorption in solution (Figure 4.5, top panel), nor in the spectral shape of the absorption in thin films (Figure 4.5, middle panel). Furthermore we made films of the two blends and did not find significant differences in absorption (Figure 4.5, bottom panel).

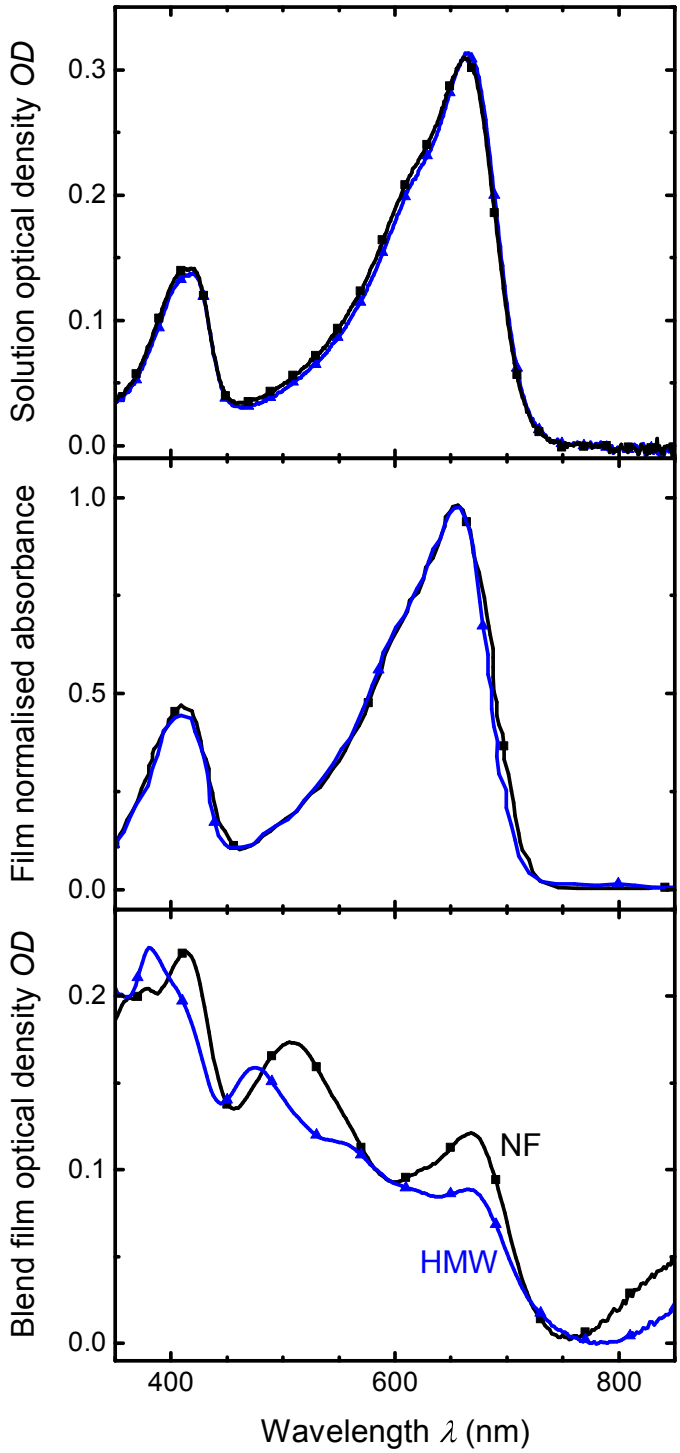


Figure 4.5: Ultraviolet-visible absorption spectra of IDTBT polymers: IDT-HMW (blue lines with triangles) and IDT-NF (black lines with squares). Top panel: optical density of 5 µg ml^{-1} solutions of IDTBT in 1,2-dichlorobenzene, in a spectrosil cuvette with a 1 cm path length. Middle panel: normalised absorbance of IDTBT polymer films on spectrosil. Bottom panel: optical density of IDTBT:$PC_{70}BM$ (1:3.5 w/w) blend films on spectrosil; these films were prepared and measured by Dr Derya Baran.

4.3.3 Voltage losses

In this section I present the determination of voltage losses of IDT-NF and -HMW devices. The devices presented in this section are from batch 3 in Table 4.2; the current density-voltage graphs are shown in Figure 4.6 and the corresponding solar cell performance parameters are tabulated in Table 4.4. Unfortunately I was unable to acquire data on the best-performing IDT-NF device from batch 3, but the V_{oc} of the device I did measure is very similar and so I do not expect any conclusions to be compromised.

Figure 4.7 shows the electroluminescence (EL) spectra of the IDT-NF and -HMW blend devices. As is evident from the right panel of Figure 4.7, the spectral shape of the electroluminescence of these devices is not affected by the fractionation or polymer molecular weight. It is possible that the luminescence is primarily from the HMW fraction of the NF polymer, since it might be that the longer chains form the most efficient electrical network in the film. Evidence for this hypothesis is the behaviour of the device voltage required for a given injected charge density (Figure 4.8): the HMW device appears to have greater conductivity than the NF device, although this may also be due to the reduced film thickness of 107 nm vs 148 nm.

The left panel of Figure 4.7 indicates that there is a difference in the luminescence efficiency of the devices, with the HMW device emitting more light, when scaled to an absolute value using the EQE data presented below. Furthermore, the EL spectrum position does not appear to vary significantly with injection current, in the range of currents tested here (Figure 4.9).

Figure 4.10 shows the high dynamic-range external quantum efficiency (EQE) spectra of the same devices measured in the EL experiment. Overlaid the directly-measured EQE are $\mathrm{EQE}_{\mathrm{EL}}$ data, the EQE calculated from the electroluminescence spectra using the detailed balance formalism. Since the measured EL flux is not an absolute measurement, but is instead relative, the portion overlapping with the directly-measured EQE is used to scale the values, thus extending the effective EQE spectrum well into the infrared.

Converting the EL spectra to $\mathrm{EQE}_{\mathrm{EL}}$ allows calculation of the radiative dark saturation current $J_{0,\mathrm{rad}}$ and hence the radiative open-circuit voltage $V_{\mathrm{oc,rad}}$. The difference between this value and the J-V open-circuit voltage is the non-radiative open-circuit voltage loss $\Delta V_{\mathrm{oc,nr}}$; the values of these parameters for an EL injection current density of 178 $\mathrm{mA\,cm^{-2}}$ are tabulated in Table 4.5. For the range of injection current densities used to collect EL spectra, neither $V_{\mathrm{oc,rad}}$ nor $\Delta V_{\mathrm{oc,nr}}$ have a strong dependence on injection current (Figure 4.11) which validates the

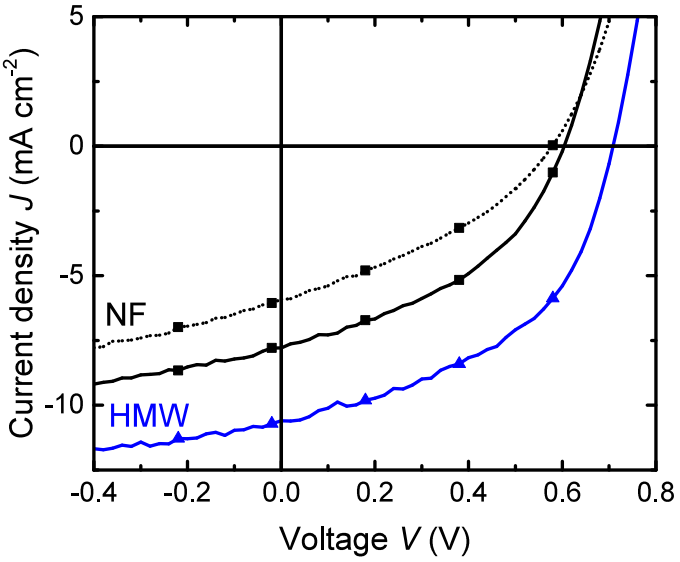


Figure 4.6: Current-voltage curves of devices based on non-fractionated IDTBT (IDT-NF, black squares) and high molecular weight IDTBT (IDT-HMW, blue triangles), made in fabrication batch 3. For the case of IDT-NF, the best device in the batch is shown by a solid line, while the particular device used for the voltage analysis here is shown by a dotted line. All devices have an ITO/PEDOT:PSS/IDTBT:$PC_{70}BM$ (1:3.5 w/w)/Ca/Ag architecture. These graphs correspond to the parameters in Table 4.4.

Table 4.4: Solar cell performance parameters of IDTBT-NF and -HMW devices measured under simulated one sun conditions; these parameters correspond to the graphs shown in Figure 4.6. J_{sc} is the short-circuit current, V_{oc} is the open-circuit voltage, FF is the fill factor, and PCE is the power conversion efficiency. All devices have an ITO/PEDOT:PSS/IDTBT:$PC_{70}BM$ (1:3.5 w/w)/Ca/Ag architecture, and the devices were made in batch 3. The IDT-NF-2 and IDT-HMW devices were used in the voltage loss analysis; IDT-NF-1 was the best-performing IDT-NF device in this fabrication batch, included for reference.

Blend	Thickness (nm)	J_{sc} (mA cm^{-2})	V_{oc} (V)	FF	PCE (%)
IDT-NF-1	105	7.8	0.604	0.42	1.97
IDT-NF-2	148	5.9	0.579	0.35	1.21
IDT-HMW	107	10.6	0.708	0.48	3.59

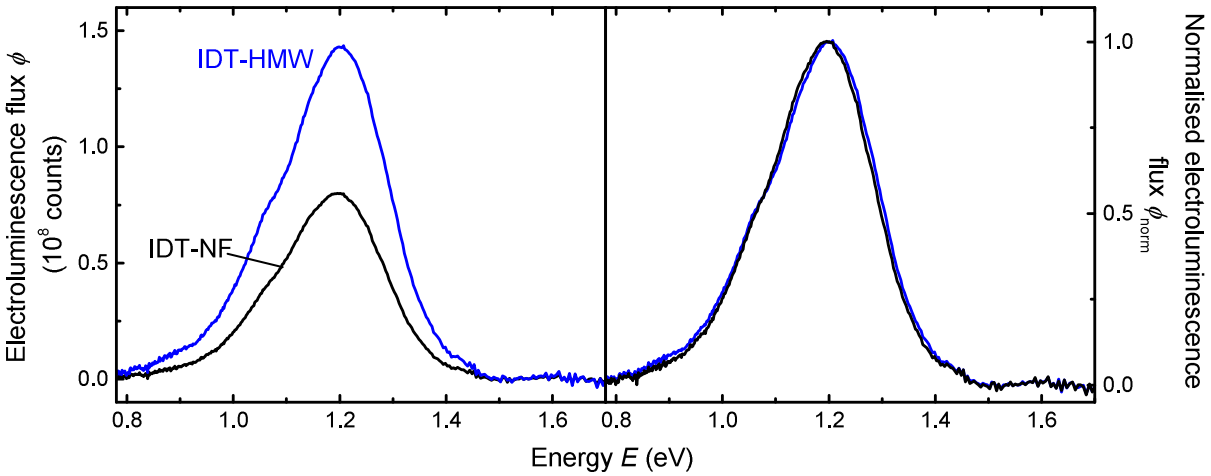


Figure 4.7: Electroluminescence spectra of IDTBT:$PC_{70}BM$ blend devices at the same current injection of 178 mA cm^{-2}. IDT-HMW is the blue line and IDT-NF is the black line. The left panel is the measured flux multiplied by the scaling factor acquired by comparing with the EQE spectra, and the right panel is the normalised flux. Both devices have an ITO/PEDOT:PSS/IDTBT:$PC_{70}BM$ (1:3.5 w/w)/Ca/Ag architecture, and are taken from fabrication batch 3.

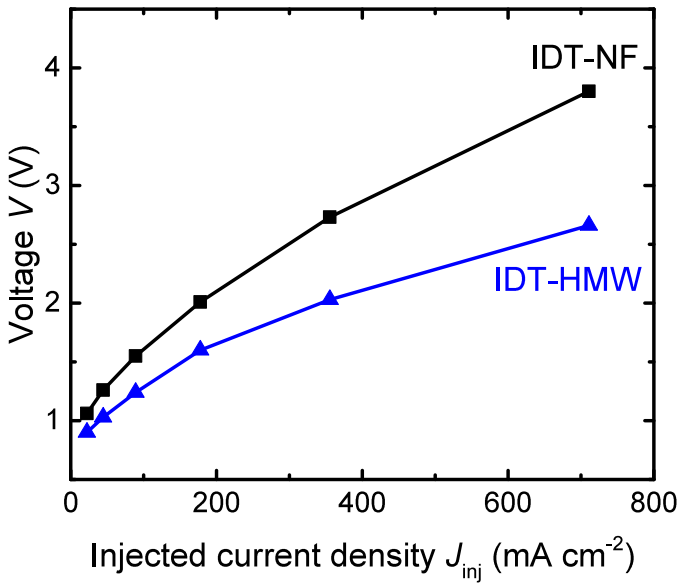


Figure 4.8: Device voltage as a function of injection current density during the EL measurement for IDTBT-NF:$PC_{70}BM$ (black squares) and IDTBT-HMW:$PC_{70}BM$ (blue triangles) blend devices. Both devices have an ITO/PEDOT:PSS/IDTBT:$PC_{70}BM$ (1:3.5 w/w)/Ca/Ag architecture, and are taken from fabrication batch 3.

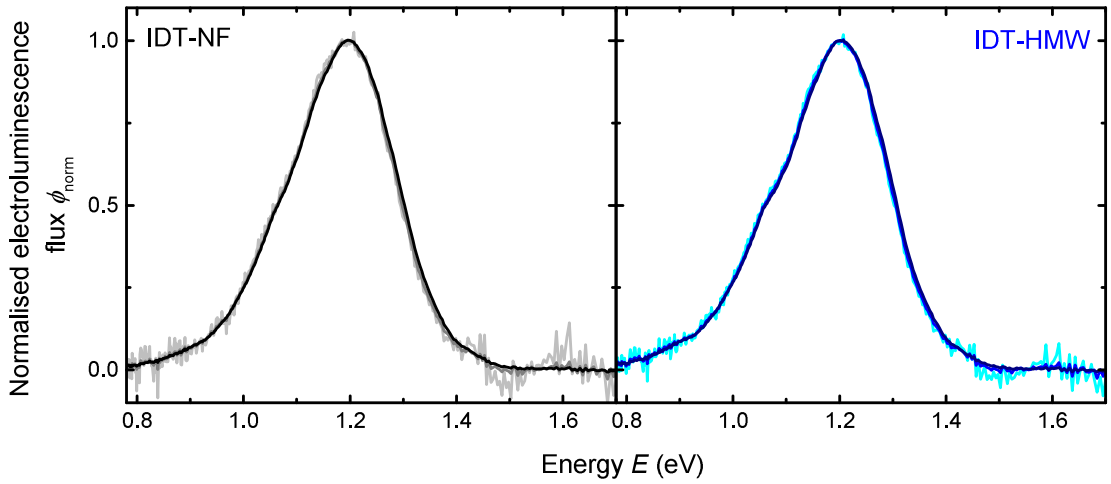


Figure 4.9: Electroluminescence spectra of IDTBT:$PC_{70}BM$ blend devices at different injection currents. Left panel: IDT-NF:$PC_{70}BM$ devices (grey-black), right panel: IDT-HMW:$PC_{70}BM$ devices (blue). In both cases, spectra measured at 4, 8 and 16 mA (89, 178 and 356 mA cm^{-2} respectively); the light coloured lines represent lower currents. Both devices have an ITO/PEDOT:PSS/IDTBT:$PC_{70}BM$ (1:3.5 w/w)/Ca/Ag architecture, and are taken from fabrication batch 3.

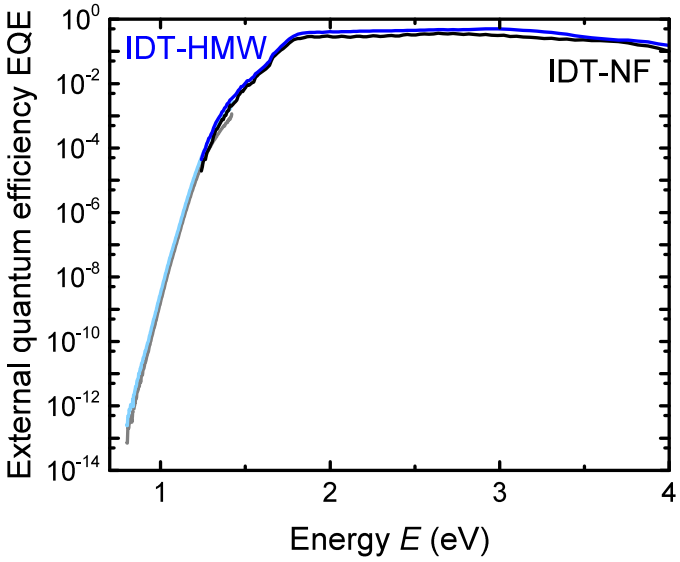


Figure 4.10: Semilogarithmic plots of experimental photocurrent external quantum efficiency (EQE_{PV}, darker lines) as a function of energy for IDT-NF:PC70BM (black) and IDT-HMW:$PC_{70}BM$ (blue). Overlaid the EQE_{PV} data are the EL-derived EQE data (EQE_{EL}, lighter lines), extending the effective EQE spectra across many more orders of magnitude. Both devices have an ITO/PEDOT:PSS/IDTBT:$PC_{70}BM$ (1:3.5 w/w)/Ca/Ag architecture, and are taken from fabrication batch 3. The EL spectra were taken at an injection current density of 178 mA cm^{-2} and were shown in Figure 4.7.

Table 4.5: Non radiative voltage losses $\Delta V_{\mathrm{oc,nr}}$ and contributing parameters for devices made from IDTBT:$PC_{70}BM$ (1:3.5) blend devices. The polymer band gap energy E_g was estimated by extrapolating the optical absorption and is included to emphasise that differences in voltage are not due to the polymer energetics. The open-circuit voltage V_{oc} was taken from the J-V curves shown in Figure 4.6. $J_{0,\mathrm{rad}}$ and $V_{\mathrm{oc,rad}}$ were calculated from the combined EL and EQE measurements. The values shown here are for an injection current of 8 mA (178 mA cm^{-2}), corresponding to the EL spectra shown in Figures 4.7 and 4.10.

Blend	E_g (eV)	$J_{0,\mathrm{rad}}$ (mA cm^{-2})	V_{oc} (V)	$V_{\mathrm{oc,rad}}$ (V)	$\Delta V_{\mathrm{oc,nr}}$ (V)
IDT-NF	1.7	3.05×10^{-19}	0.579	1.149	0.57
IDT-HMW	1.7	5.64×10^{-19}	0.708	1.148	0.44

choice of single values.

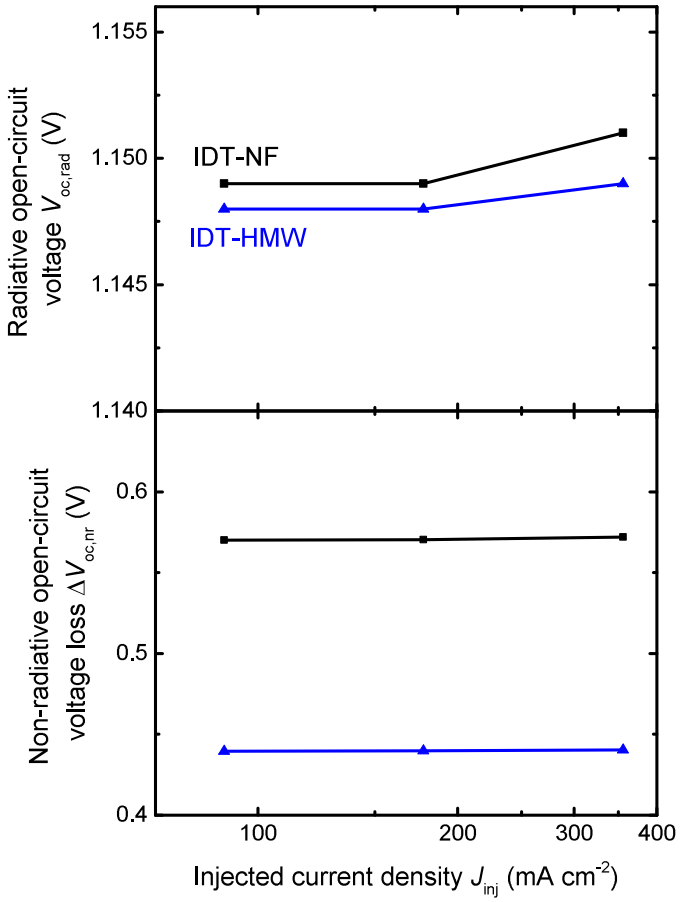


Figure 4.11: Electroluminescence injection current density dependence of voltage loss parameters for IDT-NF:$PC_{70}BM$ (black squares) and IDT-HMW:$PC_{70}BM$ (blue triangles) devices. Top panel: radiative open-circuit voltage $V_{\mathrm{oc,rad}}$, bottom panel: non-radiative open-circuit voltage loss $\Delta V_{\mathrm{oc,nr}}$. Both devices have an ITO/PEDOT:PSS/IDTBT:$PC_{70}BM$ (1:3.5 w/w)/Ca/Ag architecture, and are taken from fabrication batch 3.

4.3.4 Charge carrier dynamics

In order to probe the recombination and carrier collection dynamics of the IDTBT devices, I carried out transient photovoltage and charge extraction experiments, which were introduced in Section 3.3. The particular devices I used in this experiment were from batch 4, but were selected for fill factor rather than power conversion efficiency. The charge extraction technique relies on the assumption that at short-circuit, the excess charges can be extracted before they recombine. A high fill factor implies that extraction competes well against recombination, so high fill factor devices are necessary in order to be able to rely on the charge extraction data. The fill factors of the devices from batch 4, shown in Table 4.6, are greater than those from batch 3, displayed in Table 4.4. The current density-voltage curves of the particular devices I measured are displayed in Figure 4.12 while the solar cell performance parameters are tabulated in Table 4.6.

Figure 4.13 shows the measured data from the transient photovoltage and charge extraction experiments. Transient photovoltage is a small perturbation technique, and the lifetimes plotted in Figure 4.13 (top left) describe the exponential decay of the photovoltage induced by a laser pulse over a constant white light bias of varying intensity. The data in Figure 4.13 are the small perturbation lifetimes $\tau_{\Delta n}$, which have an empirical relationship to V_{oc} which follows $\tau_{\Delta n} = \tau_{\Delta n0} \exp(-qV_{\mathrm{oc}}/\vartheta kT)$.

In order to determine material properties, the corresponding charge density must be measured; in this work differential charging was the employed technique. This involves calculating the induced differential capacitance by measuring the total charge induced by the same perturbative laser pulse used in TPV, as well as the induced photovoltage. The capacitance C has an empirical exponential relationship to V_{oc} (Figure 4.13, top right), such that $C = C_0 \exp(\eta V_{\mathrm{oc}})$; C_0 and η are the fit parameters. The charge Q is then proportional to the integral of the capacitance over V_{oc}, which can also be expressed:

$$Q = \frac{1}{\eta}(C - C_0) \tag{4.1}$$

The charge is then converted to a charge density n, which is plotted in Figure 4.13 (bottom left), which also has an empirical exponential relationship to V_{oc} such that $n = n_0 \exp(-qV_{\mathrm{oc}}/mkT)$. m gives an indication of the shape of the density of states, since it describes the relationship between the rate of growth of charge density with increasing Fermi-level splitting. The reaction order for recombination, δ is defined by $\mathrm{d}n/\mathrm{d}t = kn^{\delta} = n/\tau$, and is therefore given by $\delta = 1 + (m/\vartheta)$.

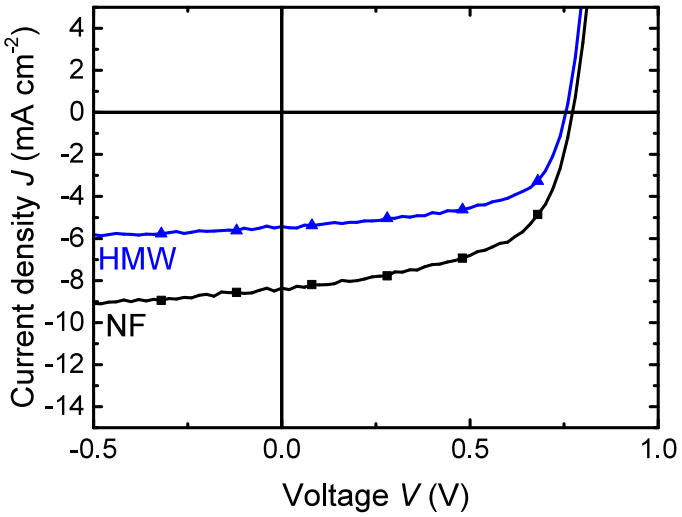


Figure 4.12: Current-voltage curves of devices based on non-fractionated IDTBT (IDT-NF, black squares) and high molecular weight IDTBT (IDT-HMW, blue triangles), made in fabrication batch 4. These devices were chosen for optimal fill factor; the best performing devices of the batch are shown in Table 4.3. All devices have an ITO/PEDOT:PSS/IDTBT:$PC_{70}BM$ (1:3.5 w/w)/Ca/Ag architecture. These graphs correspond to the parameters in Table 4.6.

Table 4.6: Solar cell performance parameters of IDTBT-NF and -HMW devices measured under simulated one sun conditions; these parameters correspond to the graphs shown in Figure 4.12. J_{sc} is the short-circuit current, V_{oc} is the open-circuit voltage, FF is the fill factor, and PCE is the power conversion efficiency. All devices have an ITO/PEDOT:PSS/IDTBT:$PC_{70}BM$ (1:3.5 w/w)/Ca/Ag architecture, and the devices were made in batch 4. These devices were used in the transient photovoltage and charge extraction experiments, and were chosen for optimal fill factor.

Blend	Thickness (nm)	J_{sc} (mA cm^{-2})	V_{oc} (V)	FF	PCE (%)
IDT-NF	81	8.4	0.772	0.57	3.71
IDT-HMW	64	5.4	0.755	0.60	2.45

Table 4.7: Fit parameters and calculated reaction order from differential charging and transient photovoltage analysis. These fit parameters correspond to the fit lines displayed in Figure 4.13. $\tau_{\Delta n_0}$ and ϑ describe the small perturbation lifetime data, C_0 and η describe the differential capacitance data, n_0 and m describe the excess charge density data, and $\delta = (m/\vartheta) + 1$ is the reaction order.

Blend	$\tau_{\Delta n_0}$ (s)	ϑ	C_0 (F)	η (V^{-1})	n_0 (cm^{-3})	m	δ
IDT-NF	40.5	1.70	6.7×10^{-11}	6.5	1.7×10^{14}	5.99	4.5
IDT-HMW	220	1.56	7.2×10^{-10}	3.5	4.1×10^{15}	11.13	8.1

Also plotted in Figure 4.13 (bottom right) is the charge carrier mobility, which is derived from the charge extraction at short-circuit experiment, assuming drift-dominated transport. All the fit parameters are tabulated in Table 4.7, and their validity can be checked by calculating the open-circuit voltage using eq. (3.21), reproduced here for convenience:

$$V_{\mathrm{oc}} = \frac{kT\vartheta m}{q(m+\vartheta)} \ln \frac{J_{\mathrm{sc}} \tau_{\Delta n_0} \delta}{q d n_0} \tag{4.2}$$

The calculated and measured V_{oc} as a function of light intensity are plotted in Figure 4.14, and show very good agreement across a wide range of light intensities. This implies that the assumptions made in the analysis, particularly that non-geminate recombination is the primary loss mechanism, are valid.

As already mentioned, it is important to plot the lifetime and mobility as a function of charge carrier density in order to be able to compare between devices and properly assess the material properties. Therefore Figure 4.15 displays the IDT-NF and IDT-HMW data plotted as a function of n. Note that I have converted the small perturbation lifetime to the large perturbation lifetime τ using the relation $\tau = \delta \tau_{\Delta n}$ derived in Section 3.3.

The mobility-lifetime product $\mu\tau$ can be used as a measure of the charge carrier collection efficiency, as already described in Section 2.5.3, and again this parameter should be calculated as a function of charge density. However since the mobility is measured at short-circuit, but the lifetime is measured at open-circuit, the charge density regimes covered by the two measurements do not overlap sufficiently. Since mobility is a much weaker function of charge density than recombination lifetime, I fit the mobility data to a straight line (shown in Figure 4.15) in order to extrapolate mobility values into the recombination lifetime charge density regime. This then allowed me to calculated $\mu\tau$ as a function of charge density, as shown

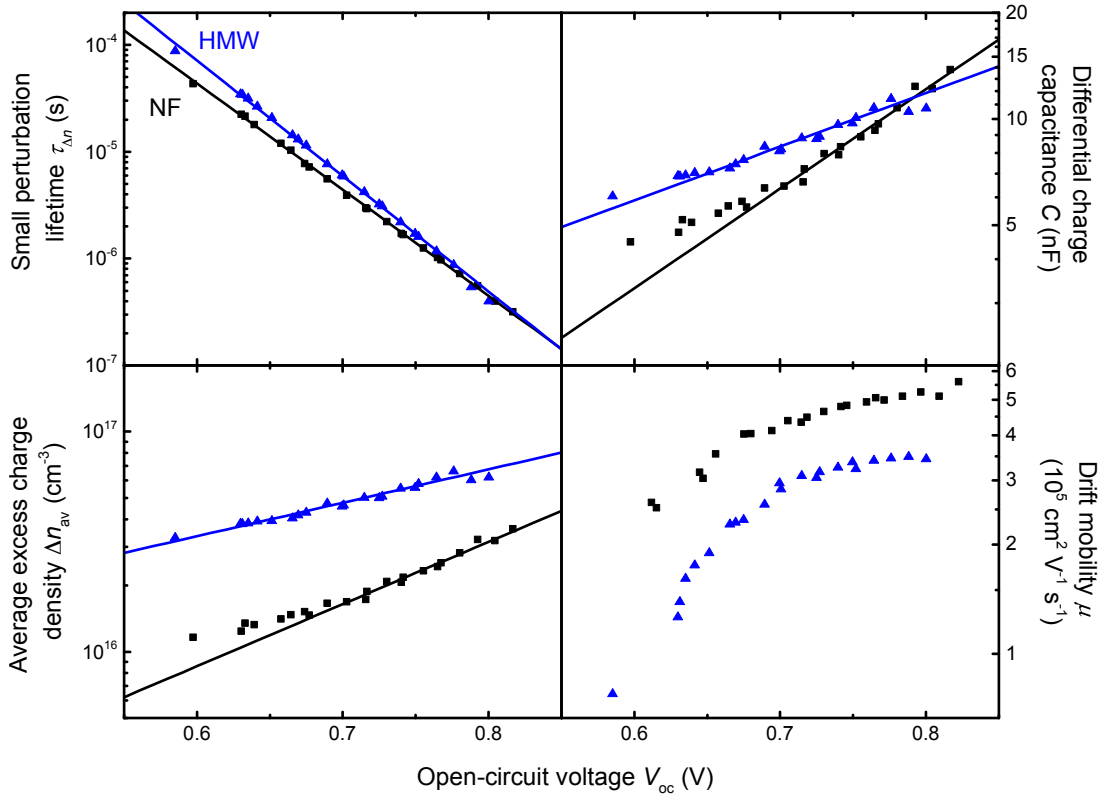


Figure 4.13: Transient photovoltage and charge extraction data of devices based on non-fractionated IDTBT (IDT-NF, black squares) and high molecular weight IDTBT (IDT-HMW, blue triangles). Top left panel: small perturbation charge carrier lifetime, as measured by transient photovoltage. The lifetimes are taken from the exponential decay of the small perturbation photovoltage induced by a weak laser pulse. The straight lines are fits of the data to the equation $\tau_{\Delta n} = \tau_{\Delta n0} \exp(-qV_{oc}/\vartheta kT)$. Top right panel: differential charge capacitance data, measured with the differential charging technique using the same laser pulse used in transient photovoltage. The straight lines are fits of the data to the equation $C = C_0 \exp(\eta V_{oc})$. Bottom left panel: excess charge carrier density, calculated from the differential capacitance. The straight lines are fits of the data to the equation $n = n_0 \exp(-qV_{oc}/mkT)$. Bottom right panel: charge carrier mobility, measured using charge extraction at short-circuit. The data are plotted as a function of open-circuit voltage, which is varied by changing the light intensity impinging on the device. All the fit parameters are displayed in Table 4.7, and all devices have an ITO/PEDOT:PSS/IDTBT:$PC_{70}BM$ (1:3.5 w/w)/Ca/Ag architecture.

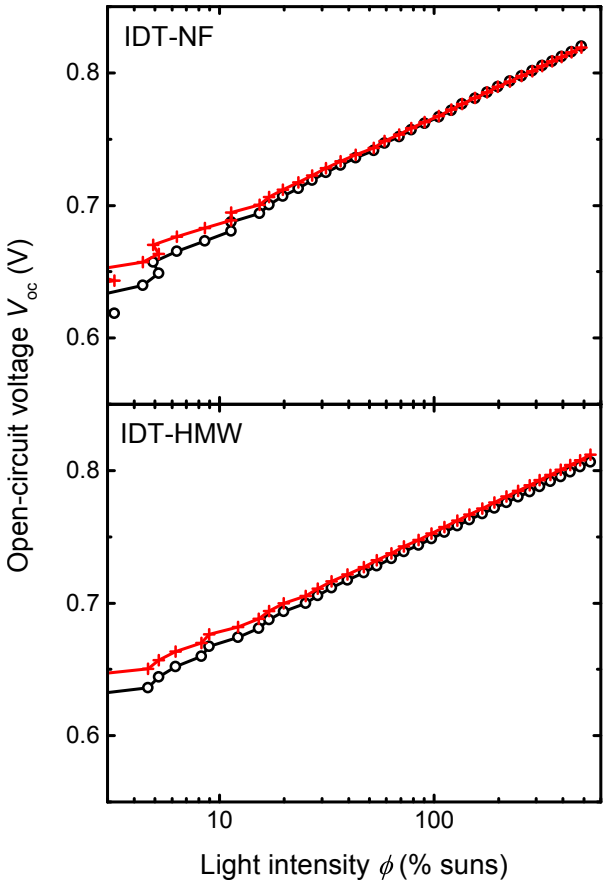


Figure 4.14: Measured (black circles) and calculated (red crosses) open-circuit voltage as a function of light intensity for IDT-NF:$PC_{70}BM$ (top panel) and IDT-HMW:$PC_{70}BM$ (bottom panel) devices. The calculated V_{oc} is determined using eq. (4.2), with the parameters tabulated in Table 4.7. All devices have an ITO/PEDOT:PSS/IDTBT:$PC_{70}BM$ (1:3.5 w/w)/Ca/Ag architecture.

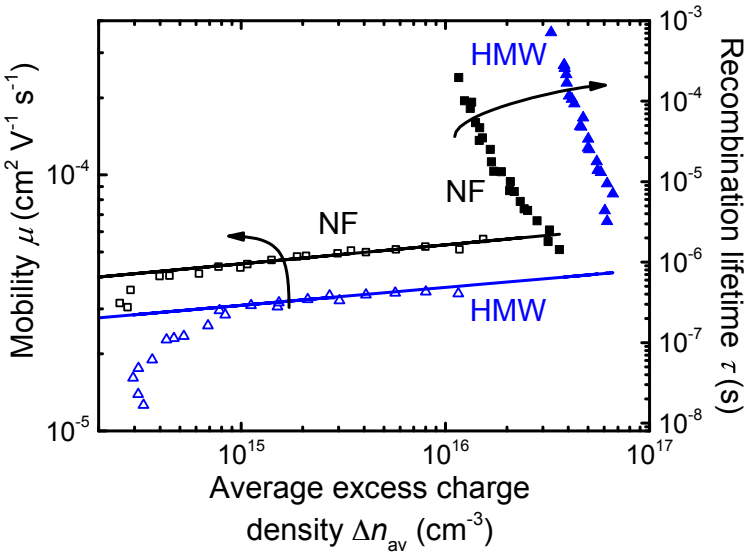


Figure 4.15: Large perturbation charge carrier lifetime (right axis, filled symbols) and mobility (left axis, open symbols) of IDT-NF (black squares) and IDT-HMW (blue triangles) blend devices, plotted as a function of excess charge density. Straight lines have been fit to the mobility data in order to extrapolate the mobility values into the charge density regime of the lifetime data. All devices have an ITO/PEDOT:PSS/IDTBT:$PC_{70}BM$ (1:3.5 w/w)/Ca/Ag architecture.

in Figure 4.16.

4.4 Discussion

The experiments presented in the previous section intended to identify which aspects of device performance are affected by fractionating a sample and using the high molecular weight fraction. In general, the IDT-HMW devices exhibited higher J_{sc} and FF than IDT-NF devices. The short-circuit current enhancement does not appear to be due to enhanced optical absorption by the IDT-HMW polymer, as the ultraviolet-visible spectroscopy data of the polymers in solution are identical, and there were no significant differences in film absorbance. Furthermore, there were no differences in the apparent doping concentration of the blends, as measured by the capacitance-voltage experiment, using Mott-Schottky analysis.

However the IDT-HMW blend appears to have a higher emission efficiency, exhibited by the higher electroluminescence flux for a given injection current. Subsequent analysis of the radiative open-circuit voltage and non-radiative voltage loss demonstrates that the IDT-HMW blend has a smaller non-radiative voltage loss than the IDT-NF blend. This difference arises primarily from the lower V_{oc} of the IDT-NF device relative to the IDT-HMW device, as the $V_{oc,rad}$ values of the two

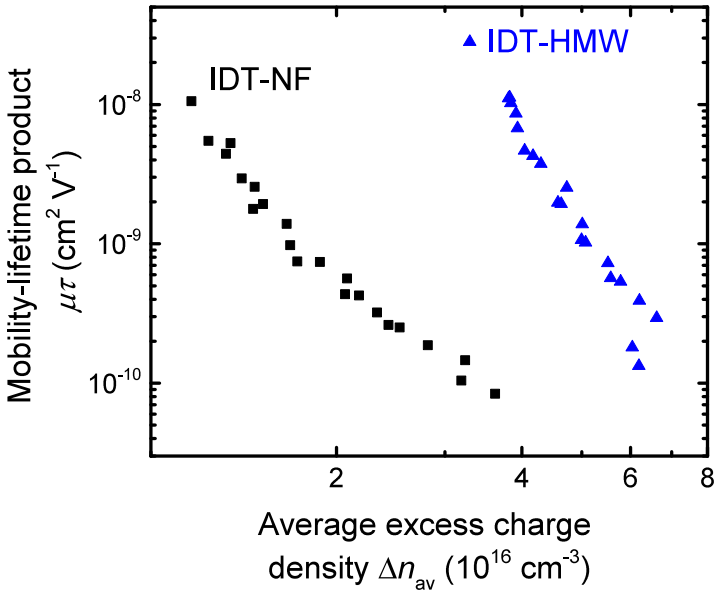


Figure 4.16: Mobility-lifetime product $\mu\tau$ of IDT-NF (black squares) and IDT-HMW (blue triangles) blend devices, plotted as a function of excess charge density. The data are calculated from the recombination lifetime and extrapolated mobility data plotted in Figure 4.15. All devices have an ITO/PEDOT:PSS/IDTBT:$PC_{70}BM$ (1:3.5 w/w)/Ca/Ag architecture.

blends are very similar. Furthermore, these quantities are relatively independent of injection current within the range used in the experiment. This non-radiative voltage loss is indicative of increased non-radiative recombination in the IDT-NF device.

Recombination can also be probed by the transient photovoltage (TPV) technique. The $\tau(n)$ data indicate that the lifetime within the IDT-HMW device is greater than that in the IDT-NF device, indicative of a lower recombination rate. TPV measures all recombination, but since the radiative efficiency of OPV devices is very low, this is dominated by non-radiative recombination. It should be noted here that the IDT-HMW device was significantly thinner than the IDT-NF device, which places a caveat on the conclusions of the data. The thinner a device, the less likely it is that there is a uniform charge density profile throughout the film thickness, which is an assumption of the analysis. The effect of device thickness on the TPV and CE analysis was investigated by Deledalle et al. [182]; they found that the gradient of the $\tau(n)$ graph gets artificially steeper as the device thickness is decreased. The authors also found that the high light-intensity data is more robust since the charge density is more uniform through the film thickness. Therefore it is plausible that the steepness of the IDT-HMW $\tau(n)$ data is an artefact, but that the conclusion that the IDT-HMW charge recombination

is slower is robust. Two possible explanations for this observation of increased lifetime in IDT-HMW devices are that the IDT-NF blend has a higher concentration of impurities and chain ends which may act as recombination centres, and/or differences in morphology.

The difference in mobility between the devices is small, and so even though the IDT-HMW mobility is less than the IDT-NF mobility, the recombination lifetime dominates $\mu\tau$. These data therefore suggest that carrier collection within the IDT-HMW devices is better than that in the IDT-NF devices. A previous study had identified morphological differences between the blends [181], which is a possible reason for the difference.

As mentioned previously, some of the data in this chapter has been published, but the work was a collaboration with Dr Derya Baran, and so the paper [149] comprised a combination of our experimental data. Dr Baran was able to achieve higher-performing devices, and did her own voltage loss analysis on these devices; instead of using a high dynamic range EQE set-up, she used Fourier-transform photocurrent spectroscopy (FTPS) to measure the high energy part of the EQE spectrum, and then used EL just as I did to acquire the low energy EQE data. The voltage losses Dr Baran calculated follow a similar trend to my data, but overall the values are lower. Our independent $V_{\mathrm{oc,rad}}$ values are very similar, and so the primary difference is due to higher non-radiative recombination in my devices. This result therefore corroborates the data presented in this chapter, as we were able to measure the same trends with polymer fractionation in two completely separate laboratories.

4.5 Conclusion

I have been able to identify non-radiative recombination as the parameter most affected by fractionating the IDTBT polymer to a high molecular weight. This is evident in the analysis of voltage losses using EQE combined with EL, and is also evident in the charge carrier lifetime data obtained by the TPV experiment. A possible explanation for this observation is that non-fractionated polymer contains a greater concentration of sites, such as impurities or chain ends, which act as recombination centres. The greater charge carrier lifetime of the IDT-HMW blend dominates the mobility-lifetime product, indicating that the IDT-HMW blend has increased carrier collection efficiency relative to the IDT-NF blend. These data have been supported by independent measurements done by Dr Derya Baran while a student of Prof. Christoph Brabec at FAU Erlangen.

4.6 Experimental Details

The IDTBT polymer studied in this chapter was made by Dr Hugo Bronstein according to the synthesis described in Refs [177, 183]. The polymer, IDT-NF, was subsequently fractionated according to [181] and the high molecular weight fraction IDT-HMW was isolated.

The devices all had an ITO/PEDOT:PSS/IDTBT:$PC_{70}BM$ (1:3.5 w/w)/Ca/Ag architecture; the PEDOT:PSS film fabrication method was described previously. The active layer was bladecoated from the blend solution in 1,2-dichlorobenzene. The bed temperature was 60 °C, and the blade height was 200 µm. The devices made for the capacitance-voltage experiment were an exception: they were spincoated at 100 rpm from a 7 $mg\,ml^{-1}$ solution. This low spincoating speed meant that no solution was spun off the substrate, so the film was essentially dropcast but without the coffee-staining problem.

The experiments were done according to the methods described in Chapter 3.

Table 4.8: Fabrication batch parameters of IDTBT devices; the batch numbers and the fabrication parameters are for the substrates tabulated in Table 4.2. For the case of batches 3 and 4, where the device measured in EL/EQE and TPV (respectively) were not necessarily from the best-performing substrate, the suffix -JV denotes the substrate with the highest PCE, while the suffixes -EL and -TPV denote the substrates used in those experiments. All of the blend solutions were polymer:fullerene 1:3.5 (w/w), and the solvent was 1,2-dichlorobenzene. The films were all bladecoated, at the blade speed indicated above. The calcium and silver evaporated thicknesses d are indicated.

Batch	Device	Total concentration ($\mathrm{mg\,ml^{-1}}$)	Coating speed ($\mathrm{mm\,s^{-1}}$)	Ca d (nm)	Ag d (nm)
1	NF	7	10	14	105
	HMW				
2	NF	31.5	20	8	130
	HMW		15		
3	NF-JV	31.5	3	8	100
	NF-EL		7		
	HMW		5		
4	NF-JV	18	20	15	115
	NF-TPV		10		
	HMW-JV		15		
	HMW-TPV		5		

Chapter 5

Understanding enhanced photocurrent in polymer:fullerene solar cells

5.1 Abstract

I present work on a series of diketopyrrolopyrrole (DPP) polymers with varying alkyl side chains and molecular weights. I found a significant dependence of absorption coefficient on molecular weight, with the high molecular weight polymers absorbing more strongly than low molecular weight polymers in both thin film and solution; this absorption increase was concurrent with increased solar cell performance. In addition I found higher mobilities in blends based on high molecular weight polymer, but also shorter recombination lifetimes. An analysis of the estimated internal quantum efficiencies suggests that the electronic quality of high molecular weight polymer blends is greater than low molecular weight blends, but this difference cannot fully account for the differences in solar cell performance. A simple analysis of current generation indicates that in the relatively poor charge collection regime of organic photovoltaics increased light absorption can increase the maximum current available.

Acknowledgements

The work presented in this chapter would not exist save for the contributions of some key people. Firstly, I am indebted to Dr Iain Meager for synthesising all the materials presented herein, save for C1-24 which was synthesised by Dr Weimin Zhang. Secondly, I am very grateful to Dr Shahid Ashraf for making the devices

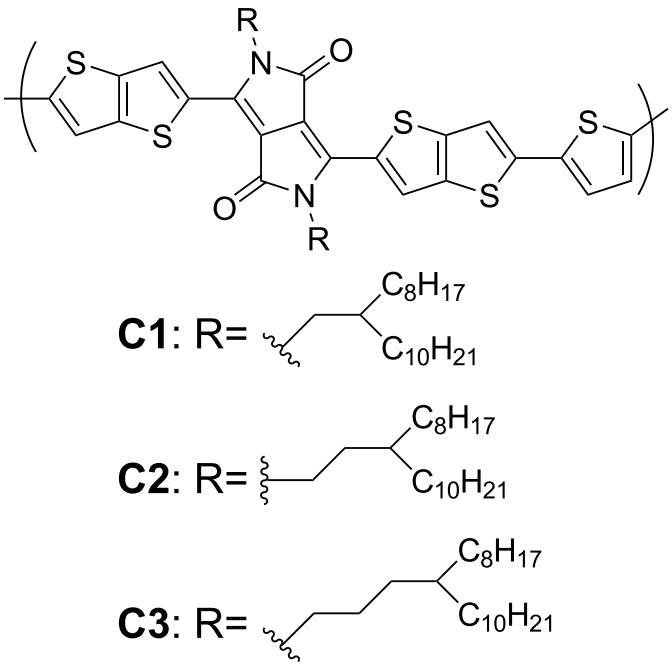


Figure 5.1: Chemical structure of DPP-TT-T. Three analogs with side-chains of various lengths were studied: C1, C2 and C3.

which formed the basis of many of the results shown here. Iain Meager, Weimin Zhang and Shahid Ashraf are all members of Professor Iain McCulloch's group in the Chemistry department of Imperial College. And finally but certainly not least I owe a debt to Dr Mariano Campoy-Quiles, of the Institute of Materials Science of Barcelona (ICMAB-CSIC) for doing the ellipsometry measurements.

5.2 Introduction

One of the more promising conjugated polymer sub-units for use in solar cells or transistors is diketopyrrolopyrrole (DPP) [125, 184, 185]. In this chapter, I discuss work done on a particular DPP co-polymer, thieno[3,2-b]thiophene-diketopyrrolopyrrole (DPP-TT-T, Figure 5.1), which has shown high field-effect transistor mobilities, promising performance as the donor in solar cells [186] and high photostability [187].

As mentioned previously, the behaviour of a polymer is affected not only by the chemical structure of the backbone, but also by the design of the solubilising alkyl side-chains and the polymer molecular weight. It is these latter factors which are the focus of this chapter. The polymer was synthesised by Dr Iain Meager with three different side-chains of varying lengths, shown in Figure 5.1; all side-chains are branched, and the number of carbons between the branching point and the backbone was varied from one (C1) to three (C3). The long alkyl branches can

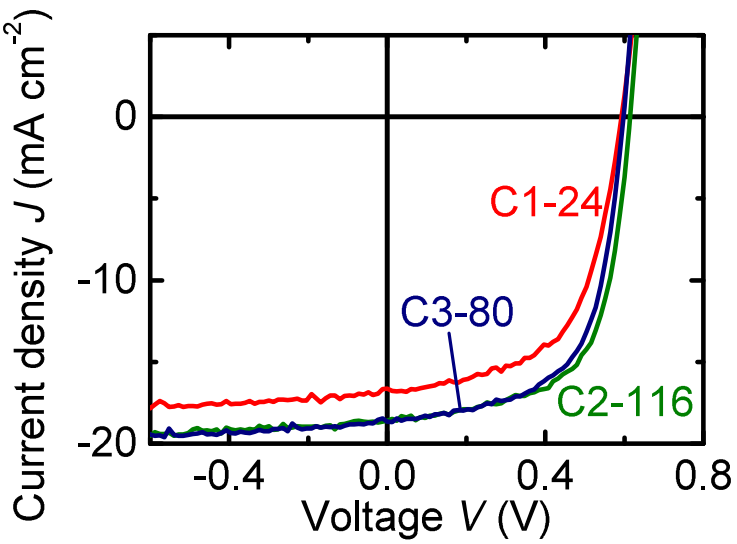


Figure 5.2: Current density-voltage characteristics of solar cells based on C1-24 (red), C2-116 (green) and C3-80 (blue) measured under simulated AM1.5G irradiation. The molecular weights of the polymers are listed in Table 5.3. All devices are a conventional architecture with ITO/PEDOT:PSS/DPP-TT-T:$PC_{70}BM$ (1:2 w/w)/LiF/Al, and were made and measured by Dr Shahid Ashraf.

provide some steric hindrance so the hope of the initial study was that by moving the branching point away from the backbone, neighbouring conjugated backbone sections would be able to associate more closely, reducing the π-π stacking distance of the aromatic rings and generally increasing the degree of order, hence improving the transport.

Solar cells made by Dr Shahid Ashraf from the three polymers indeed showed that the C2 and C3 side-chains resulted in better solar cell performance than the C1 polymer (Tables 5.1 and 5.2 and Figure 5.2) [188]. This increase in device performance was attributed to an increased degree of crystallinity as determined using grazing incidence wide-angle X-ray scattering (GIWAXS), although the π-π stacking distance was not significantly affected.

The design of alkyl side-chains can also affect the solubility of the polymer in solvents, with longer side-chains tending to result in higher solubility [48–50, 52]. Higher solubility can in turn affect the polymer molecular weight, since the polymer is more likely to stay dissolved during polymerisation; therefore the molecular weight achieved in the C2 and C3 synthesis was higher than that of the C1 synthesis. This highlights the difficulty in studying polymers, since often parameters are inter-related. Furthermore, a study on a similar polymer (DPP-TT-T backbone with 2-decyltetradecyl side-chains) found solar cell performance increased upon polymer fractionation, with the higher molecular weight fractions performing better than the low molecular weight fractions [189]. Therefore in order to elucidate

Table 5.1: The solar cell performance parameters corresponding to the devices shown in Figure 5.2: short-circuit current J_{sc}, open-circuit voltage V_{oc}, fill factor FF and power conversion efficiency PCE. The devices are ITO/PEDOT:PSS/DPP-TT-T:$PC_{70}BM$ (1:2 w/w)/LiF/Al, and were made and measured by Dr Shahid Ashraf.

Polymer	J_{sc} (mA cm^{-2})	V_{oc} (V)	FF	PCE (%)
C1-24	16.6	0.59	0.60	5.9
C2-116	18.6	0.61	0.64	7.3
C3-80	18.7	0.60	0.62	6.9

Table 5.2: Statistics of devices based on C1, C2 and C3, compiled for the best substrates of each blend. The standard deviation is of the PCE distribution. The data shown in Figure 5.2 and Table 5.1 are part of these data sets. All devices were measured by Dr Shahid Ashraf.

Polymer	Number	Standard Deviation	Mean PCE (%)
C1-24	10	0.4	5.4
C2-116	9	0.9	5.9
C3-80	7	0.5	6.1

Table 5.3: The molecular weights of each batch of C1-, C2- and C3-DPP-TT-T used in this thesis. M_n is the number-average molecular weight, M_w is the weight-average molecular weight, and PDI is the polydispersity index.

Material Batch	M_n ($\mathrm{kg\,mol^{-1}}$)	M_w ($\mathrm{kg\,mol^{-1}}$)	PDI
C1-20	20	85	4.4
C1-24	24	89	3.7
C1-55	55	100	1.8
C1-85	85	160	1.9
C1-120	120	265	2.2
C2-116	116	357	3.1
C3-9	9	28	3.1
C3-16	16	51	3.1
C3-80	80	154	1.9
C3-84	84	264	3.1
C3-99	99	228	2.3

which factor, side-chain design or molecular weight, had the strongest effect on solar cell performance, we needed to study fractionated batches of each polymer with different side-chain lengths. Thus batches of C1 and C3 were synthesised and fractionated for further study: the molecular weights of each batch/fraction are shown in Table 5.3. Figure 5.3 shows the corresponding gel permeation chromatography traces of the different C1 and C3 batches listed in Table 5.3, collected by Dr Iain Meager.

This chapter therefore attempts to identify the mechanism underlying the observations of improved solar cell performance. Solar cell performance can be affected by doping concentration, charge carrier mobility and lifetime, non-radiative voltage losses, and light harvesting. I investigate each of these factors in turn to establish the pertinent factor(s) affecting solar cell performance.

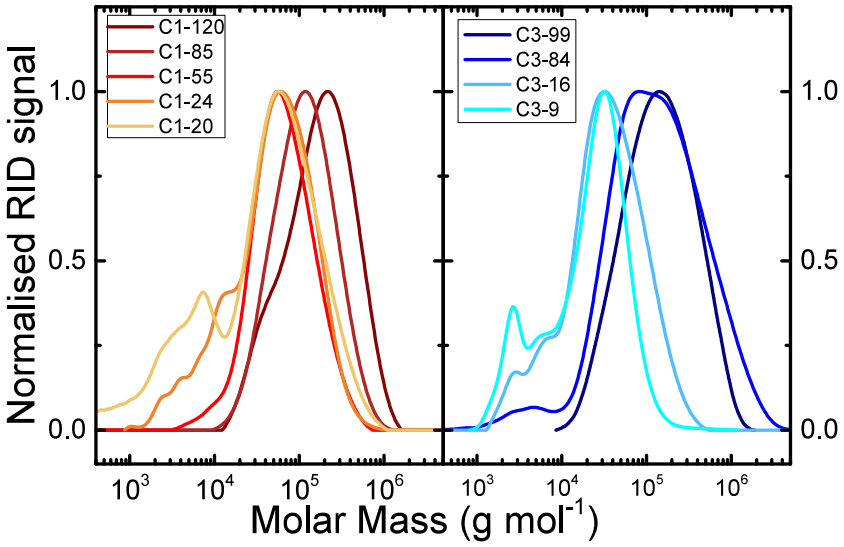


Figure 5.3: Gel permeation chromatography (GPC) traces of C1- and C3-DPP-TT-T (left and right, respectively) polymer batches used in this study; data was collected by Iain Meager. The M_n and M_w values tabulated in Table 5.3 were calculated from these distributions.

5.3 Results

5.3.1 Solar cell performance

Shahid Ashraf made and measured solar cells from low and high molecular weight C1 and C3 blended in a 1:2 weight ratio with $PC_{70}BM$. The devices had an inverted architecture with ITO/ZnO (approximately 30 nm)/blend/MoO_3 (10 nm)/Ag (100 nm). I measured the blend layer thicknesses for each device using a Dektak profilometer; the resulting values are listed in Table 5.4. It should be noted though that it is very difficult to achieve a clean scratch when ZnO is underneath the blend layer and so there is a significant level of uncertainty in these values. Figure 5.4 shows the current density-voltage curves of the devices, and Tables 5.4 and 5.5 shows the solar cell performance parameters and available statistics. It is apparent from these results that molecular weight, rather than side-chain design, is the principal factor affecting solar cell performance. The solar cell parameter most affected by molecular weight was the short-circuit current density, and so the rest of this chapter is devoted to determining the source of this increased current collection.

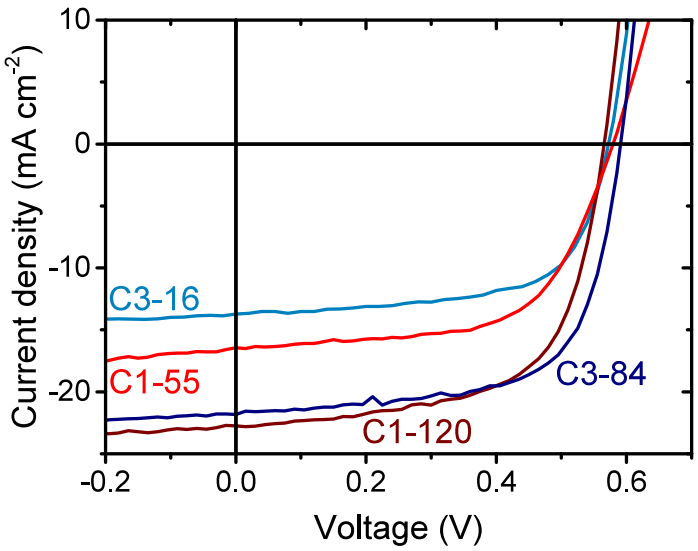


Figure 5.4: Solar cell current density-voltage characteristics under simulated one sun illumination conditions for blend devices of low and high molecular weight C1 and C3; C1-55 and C1-120 are shown by red and dark red lines respectively, and C3-16 and C3-84 are shown by light and dark blue lines respectively. All devices have an inverted architecture with structure ITO/ZnO/polymer:$PC_{70}BM$ (1:2 w/w)/MoO_3/Ag, and were made by Shahid Ashraf.

Table 5.4: The solar cell performance parameters corresponding to the devices shown in Figure 5.4: short-circuit current density J_{sc}, open-circuit voltage V_{oc}, fill factor FF, and power conversion efficiency PCE. The thickness was measured using a Dektak profilometer. All devices had an ITO/ZnO/DPP-TT-T:$PC_{70}BM$ (1:2 w/w)/MoO_3/Ag architecture.

Polymer	Dektak thickness (nm)	J_{sc} (mA cm^{-2})	V_{oc} (V)	FF	PCE (%)
C1-55	69	16.4	0.58	0.61	5.9
C1-120	101	22.8	0.57	0.63	8.1
C3-16	60	14.3	0.52	0.62	4.6
C3-84	69	21.8	0.59	0.66	8.5

Table 5.5: Statistics of devices based on C1-55, C1-120, C3-16 and C3-84 blends, compiled for the best substrates of each blend, from the same device batch as the hero devices shown in Figure 5.4. The standard deviation is of the PCE distribution.

Polymer	Number	Standard Deviation	Mean PCE
C1-55	3	0.2	5.7
C1-120	10	0.4	7.5
C3-16	5	0.3	4.8
C3-84	11	0.9	7.9

5.3.2 Capacitance-Voltage

As described in Section 2.5.1, the concentration of unintentional dopants can affect the performance of solar cells by reducing the effective collection thickness of the films. Organic solar cells rely on the electric field generated in the active layer by the difference in workfunctions of the contacts; in an undoped solar cell the field is uniform throughout the device, and this drives the drift collection current necessary for adequate current collection. Dopants however can induce a depletion region which is thinner than the total device thickness; this results in two regions in the device: the depletion region with an electric field, and a flat-band region where there is no net electric field. The only current possible from the flat-band region is by diffusion, which is negligible when compared to drift current. Therefore the only significant current collection is from the depletion region, which is thinner when the dopant level is higher. Highly doped devices therefore tend to exhibit smaller J_{sc} values if the depletion thickness is less than the overall film thickness [26].

In order to quantify the level of any such doping, I measured the capacitance of C1, C2 and C3 blend devices as a function of voltage, which then allows calculation of the apparent doping concentration, as outlined in Section 3.2.2. The blend layers were all approximately 500 nm thick, so that the depletion region was smaller than the full device thickness. I fabricated the devices with a glass/ITO/PEDOT:PSS/DPP-TT-T:$PC_{70}BM$ (1:2 w/w)/Ca/Al architecture. Figure 5.5b shows the resulting doping concentration obtained from the C-V data in Figure 5.5a as a function of side-chain branching point. Recalling eq. (2.44) for the depletion width $w = \sqrt{2(V_{bi} - V)\varepsilon/qN_A}$, we can calculate the doping concentration which results in the same electric field as a 100 nm film, for example. Assuming a built-in voltage of 0.8 V, and a relative permittivity of 3.8, the doping

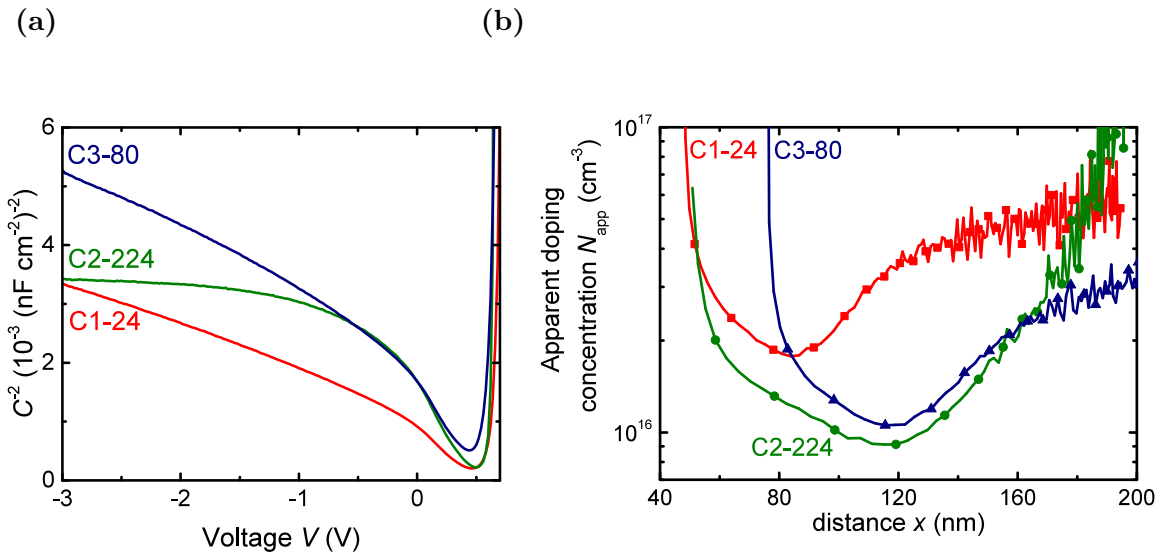


Figure 5.5: Mott-Schottky analysis of C1, C2 and C3 devices. (a) Mott-Schottky plot of devices based on C1-24 (red), C2-224 (green) and C3-80 (blue). The differential of C^{-2} with respect to voltage is inversely proportional to the apparent doping concentration. (b) Apparent doping concentration profiles based on analysis of the data in (a). All devices were glass/ITO/PEDOT:PSS (30 nm)/DPP-TT-T:$PC_{70}BM$ (1:2) ($\approx$ 500 nm)/Ca/Al.

concentration leading to a depletion thickness of 100 nm is 3.4×10^{16} cm^{-3}. The doping concentrations, taken as the minima of the curves in Figure 5.5b, of the different polymers are all below or close to this value, indicating that different levels of doping are unlikely to be the source of different current densities.

5.3.3 Charge carrier dynamics

In order to probe whether charge carrier dynamics are the source of the photocurrent improvement in high molecular weight devices, I performed transient photovoltage, differential charging and charge extraction measurements as described in Section 3.3 on the same set of devices which were used to measure the solar cell J-V characteristics in Figure 5.4. The device architecture was ITO/ZnO/polymer:$PC_{70}BM$ (1:2 w/w)/MoO_3/Ag.

The devices were chosen from the same substrates but selected for optimal fill factor rather than PCE so are not necessarily the exact same devices as those in Figure 5.4. In addition, the TPV measurements were conducted some time after the initial J-V measurements. Table 5.6 shows the J-V characteristics measured at the time of the TPV experiment under simulated one sun conditions. The

Table 5.6: The solar cell performance parameters of C1 and C3 blend devices at time of transient experiments; these particular devices were chosen for optimal fill factors. All devices have an inverted architecture with structure ITO/ZnO/polymer:$PC_{70}BM$ (1:2 w/w)/MoO_3/Ag, and were made by Shahid Ashraf.

Polymer	J_{sc} (mA cm^{-2})	V_{oc} (V)	FF	PCE (%)
C1-55	14.8	0.58	0.68	5.8
C1-120	20.4	0.57	0.64	7.3
C3-16	12.0	0.56	0.62	4.2
C3-84	18.2	0.58	0.62	6.5

TPV experiment uses white LEDs instead of a solar spectrum, and as a result I found it was necessary to use a background ultraviolet lamp (254 nm) to promote conductivity of the zinc oxide interlayer [190, 191]; negligible photocurrent at this wavelength was generated (Figure 5.6a) and the J-V characteristics of the devices did not degrade appreciably during measurement (Figure 5.6b).

I used differential charging to calculate the open-circuit charge density n through measurement of the capacitance C, and TPV to measure the small perturbation recombination lifetime $\tau_{\Delta n}$, all as a function of background light intensity or open-circuit voltage (Figure 5.7). I fit single exponentials to the $\tau_{\Delta n}(V_{oc})$, $C(V_{oc})$ and $n(V_{oc})$ data, which are shown in the figure; the fitted parameters are shown in Table 5.7. I checked the validity of these fitted parameters by calculating the predicted open-circuit voltage as a function of light intensity using eq. (3.21), reproduced here:

$$V_{oc} = \frac{kT\vartheta m}{q(m+\vartheta)} \ln \frac{J_{sc}\tau_{\Delta n_0}\delta}{qdn_0}$$

The resulting measured and calculated values for each device are plotted in Figure 5.8. In addition I measured the mobility using charge extraction at short-circuit applying eq. (3.6): $J_{drift} = q\mu n_{sc} V_{bi} f(\delta)/d$. I approximated the built-in voltage V_{bi} as the voltage when the corrected photocurrent (the difference between the light and dark currents) was zero. The mobility as a function of open-circuit voltage is also plotted in Figure 5.7.

In order to compare material systems independent of factors such as device thickness, it is important to compare quantities as a function of charge density rather than light intensity; the recombination lifetime and charge mobility as a function of charge density are plotted in Figure 5.9a. As mentioned in Section 2.5.3, the mobility-lifetime product $\mu\tau$ can be a useful measure of charge

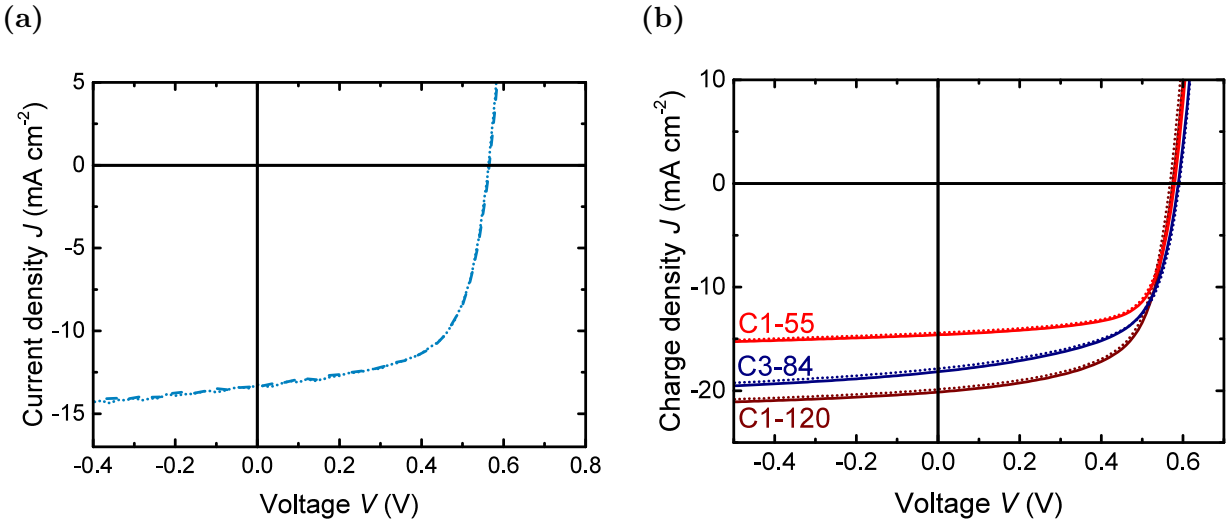


Figure 5.6: J-V curves of the devices used in the transient photovoltage, differential charging and charge extraction experiments. (a) Comparison between a J-V curve taken under simulated one sun illumination (dashed line) and under the same conditions plus a UV lamp (254 nm) (dotted line). The particular device shown is a C3-16 blend device. (b) The effect of extended UV illumination on devices used in TPV measurements. The measurements before the TPV experiment, when the device was exposed to illumination by a UV lamp (254 nm) as well as white LEDs, are the solid lines, and after the experiment are dotted lines; C1-55 is in red, C1-120 in dark red, and C3-84 in dark blue. I did not take a post measurement of the C3-16 device so it is not included above. The device architecture was ITO/ZnO/polymer:$PC_{70}BM$ (1:2 w/w)/MoO_3/Ag.

Table 5.7: Fit parameters from transient photovoltage and differential charging data analysis of the data shown in Figure 5.7, corresponding to the fit lines. $\tau_{\Delta n_0}$ and ϑ describe the small perturbation lifetime data, C_0 and η describe the differential capacitance data, and n_0 and m describe the excess charge density data derived from the differential charging data.

Polymer	$\tau_{\Delta n_0}$ (s)	ϑ	C_0 (F)	η (V^{-1})	n_0 (cm^{-3})	m
C1-55	0.95	0.66	1.43×10^{-11}	11.7	2.43×10^{13}	0.30
C1-120	0.19	0.60	9.70×10^{-12}	12.9	1.95×10^{13}	0.30
C3-16	24.5	0.63	5.60×10^{-10}	5.5	1.69×10^{15}	0.16
C3-84	25.9	0.67	5.65×10^{-10}	5.3	1.41×10^{15}	0.16

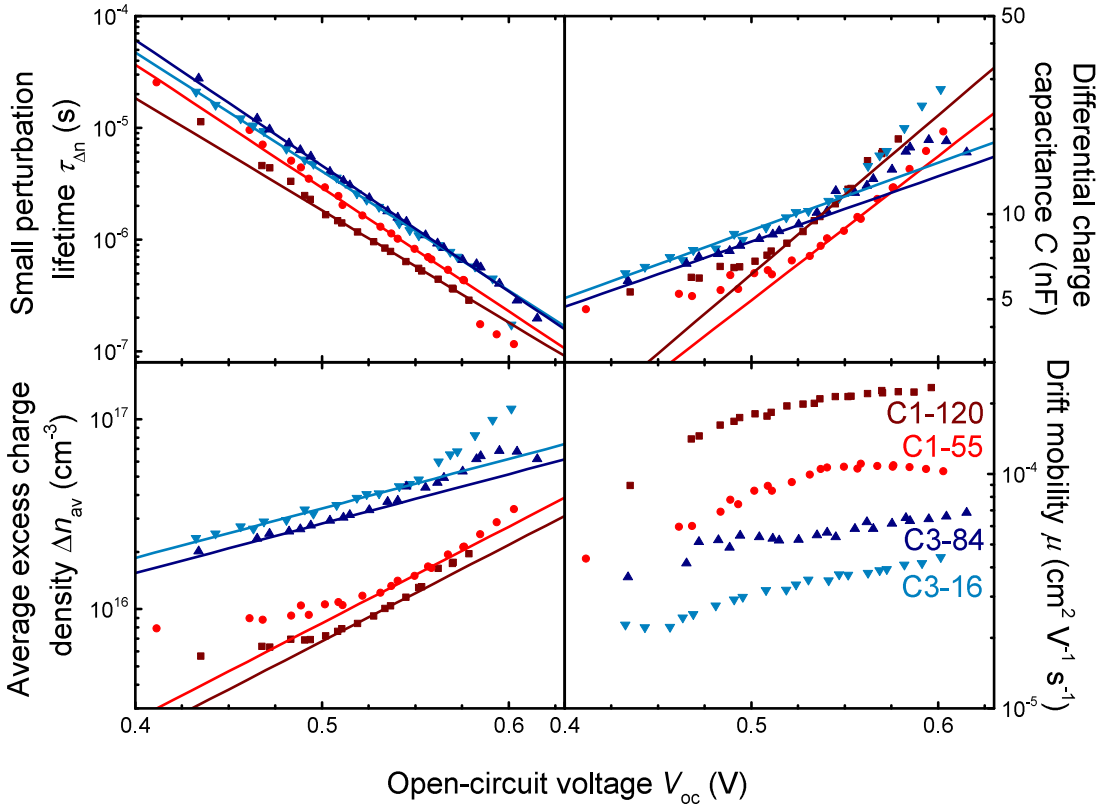


Figure 5.7: Measured transient photovoltage and charge extraction data of C1 and C3 DPP-TT-T blend devices. Top left: small perturbation charge recombination lifetime (symbols) as measured using transient photovoltage. The lifetimes are taken from the exponential decay of the small perturbation photovoltage induced by a weak laser pulse. The straight lines are fits of the data to the equation $\tau_{\Delta n} = \tau_{\Delta n0} \exp(-qV_{oc}/\vartheta kT)$. Top right panel: differential charge capacitance data, measured with the differential charging technique using the same laser pulse used in transient photovoltage. The straight lines are fits of the data to the equation $C = C_0 \exp(\eta V_{oc})$. Bottom left panel: excess charge carrier density, calculated from the differential capacitance. The straight lines are fits of the data to the equation $n = n_0 \exp(-qV_{oc}/mkT)$. Bottom right panel: charge carrier mobility, measured using charge extraction at short-circuit. The data are plotted as a function of open-circuit voltage, which is varied by changing the light intensity impinging on the device. All the fit parameters are displayed in Table 5.7.

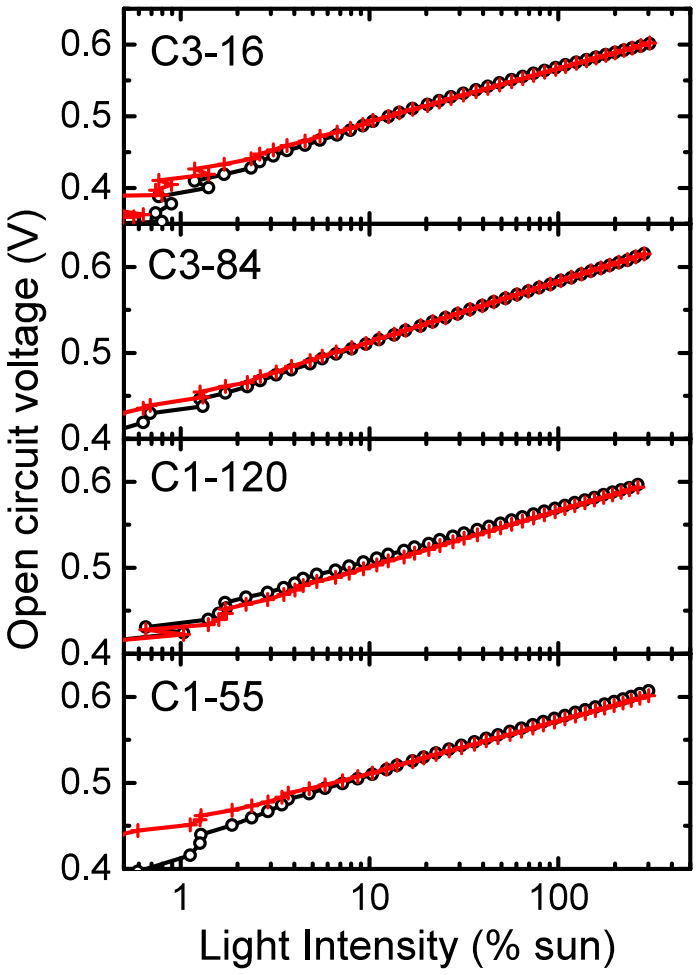


Figure 5.8: Measured (black circles) and calculated (red crosses) open-circuit voltage as a function of light intensity. The calculated V_{oc} is calculated using eq. (3.21) using the parameters in Table 5.7.

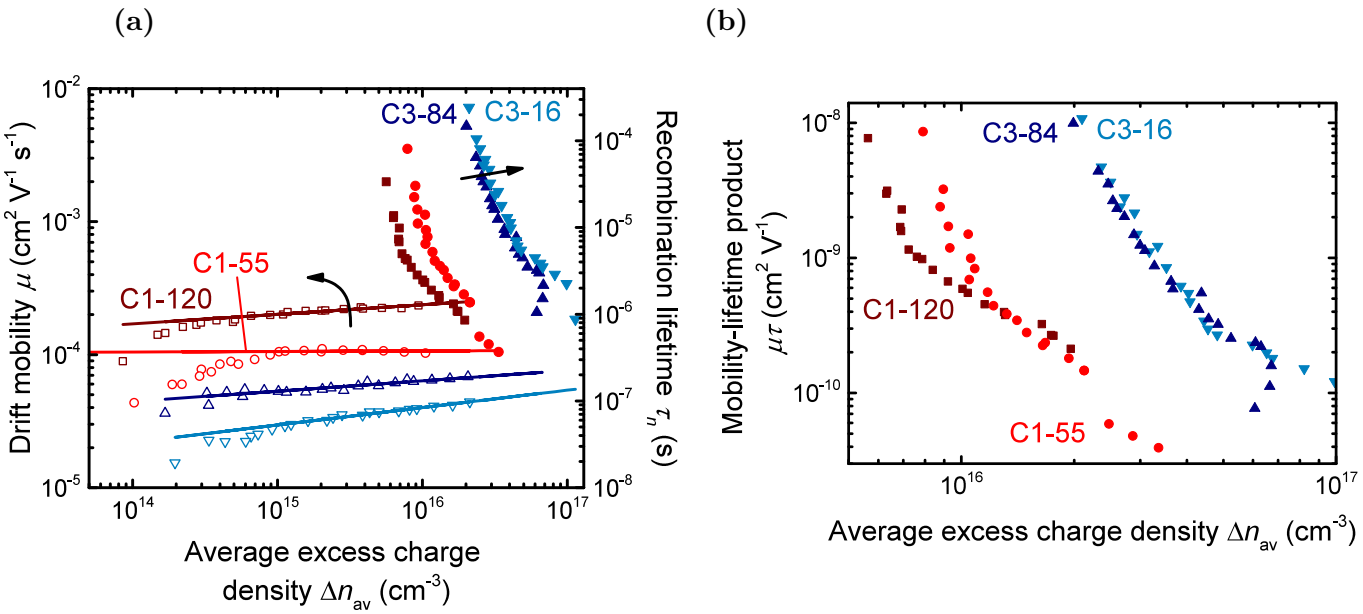


Figure 5.9: Charge dynamics parameters as a function of charge density of DPP-TT-T blend devices. (a) Charge carrier mobility (left axis, open symbols) and large perturbation recombination lifetime (right axis, solid symbols), both plotted as a function of average excess charge density. The lines are fits to the mobility data, in order to extrapolate into the charge density regime accessed by the transient photovoltage experiment. (b) Mobility-lifetime product, calculated using the data shown in (a), and using the extrapolated $\mu(n)$ data. In all cases, C1-120 is shown by dark red squares, C1-55 by red circles, C3-84 by dark blue up-triangles, C3-16 by light blue down-triangles. The devices are all ITO/ZnO/polymer:$PC_{70}BM$ (1:2, w/w)/MoO_3/Ag.

collection. As is evident from Figure 5.9a, the TPV and charge extraction at short-circuit data do not have a large overlap in charge density. Therefore, since the mobility is a weaker function of charge density than the recombination lifetime, I fit the $\mu(n)$ data to a linear log-log relationship, and extrapolated the mobility into the charge density regime probed using TPV, and hence plotted $\mu\tau(n)$ as shown in Figure 5.9b.

As has been mentioned previously in Chapter 4, the slope of the $\tau(n)$ graph can be superficially steep if the active layer is too thin, due to inhomogeneities in the charge density [182]. Therefore since all of the devices studied with the exception of the C1-120 device are quite thin (< 70 nm), it is certainly possible that the steepness of the graphs is an artefact. This factor may account for the difference between the C1-120 and C1-55 data at low light intensities, where the device is most likely to have the strongest inhomogeneities. Especially given that the C3 devices and the C1-55 device have comparable thicknesses, it appears safe

to conclude that the C3 devices overall have higher $\mu\tau$ values at the same charge density.

5.3.4 Electroluminescence

In order to probe the charge-transfer state of the devices, I measured the electroluminescence of the devices selected for solar cell J-V measurements, shown in Figure 5.4. Figure 5.10 shows the electroluminescence spectra of C1 and C3 low and high molecular weight devices, both normalised and not normalised. The data shown are for an injection current of 16 mA, or 356 mA cm^{-2}; it is important to compare data at the same injection current density if possible. It is also important to measure electroluminescence at the lowest injection current possible, to ensure that the lowest energy states are being probed. To this end, I monitored the spectra as a function of injection current to make sure that the peak does not shift hugely with current density (Figure 5.11).

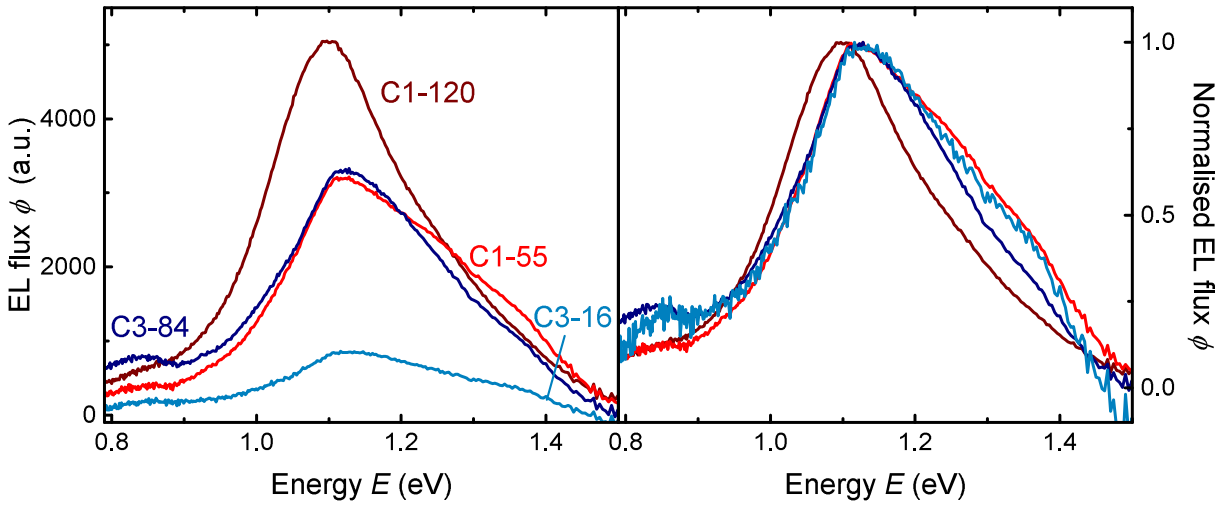


Figure 5.10: Electroluminescence spectra of C1 and C3 DPP-TT-T blend devices, with an injection current of 356 mA cm^{-2}. C1-120 is in dark red, C1-55 in red, C3-84 in dark blue, and C3-16 in light blue. The left panel is the measured EL photon flux, while the right panel is normalised by the maximum flux value. All devices have an inverted architecture with structure ITO/ZnO/polymer:$PC_{70}BM$ (1:2 w/w)/MoO_3/Ag, and were made by Shahid Ashraf.

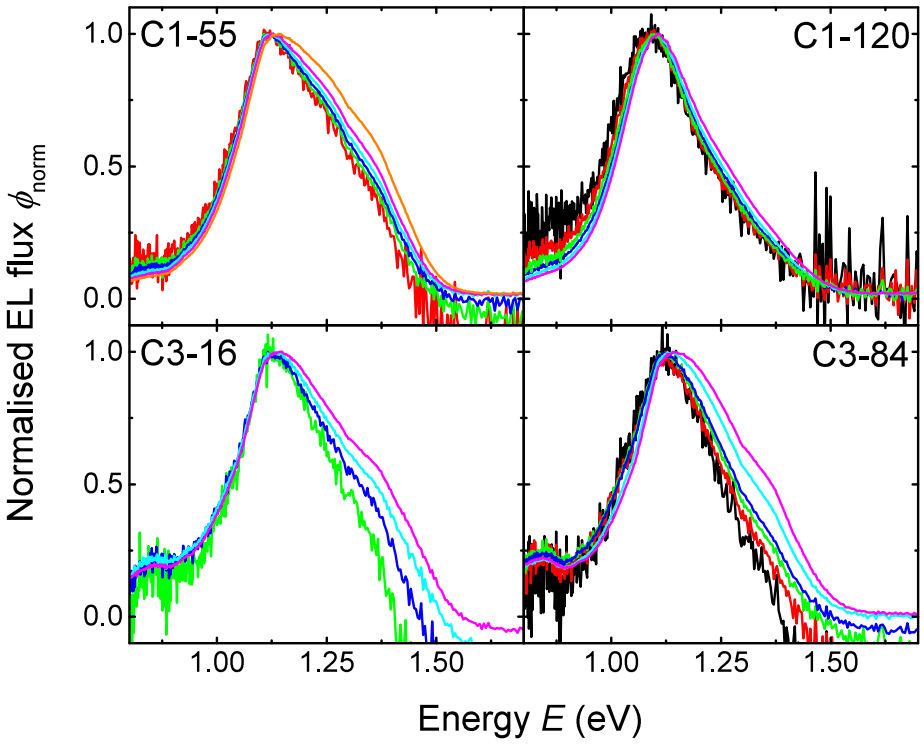


Figure 5.11: Normalised electroluminescence spectra for different injection currents. In each panel the same colour scheme was used: black lines are 2 mA (44.4 mA cm^{-2}), red lines are 4 mA (88.9 mA cm^{-2}), green lines are 8 mA (177.8 mA cm^{-2}), blue lines are 16 mA (355.6 mA cm^{-2}), cyan are 32 mA (711.1 mA cm^{-2}), magenta are 64 mA (1422.2 mA cm^{-2}), orange are 128 mA (2844.4 mA cm^{-2}).

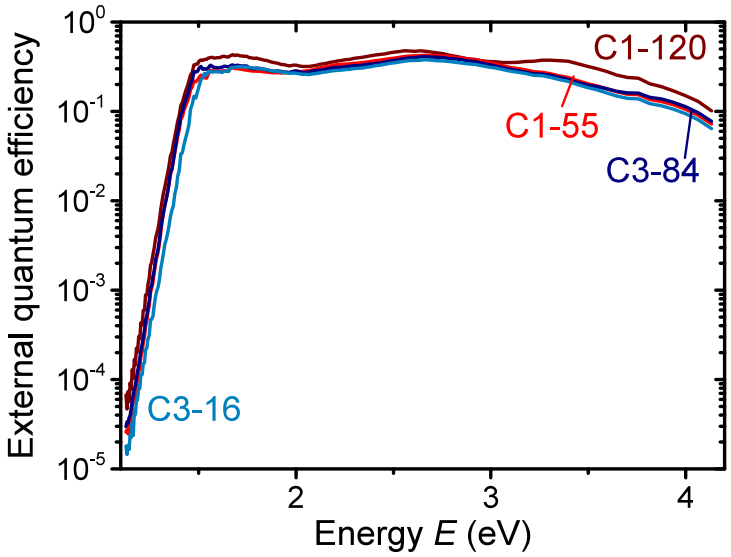


Figure 5.12: High dynamic range external quantum efficiency spectra of C1-120 (dark red), C1-55 (red), C3-84 (dark blue) and C3-16 (light blue) devices, all blended 1:2 with $PC_{70}BM$. All devices have an inverted architecture with structure ITO/ZnO/polymer:$PC_{70}BM$ (1:2 w/w)/MoO_3/Ag, and were made by Shahid Ashraf but measured by myself.

5.3.5 External quantum efficiency and voltage losses

In order to probe both the current generation as a function of light wavelength, and measure the voltage loss due to non-radiative recombination, I measured high-dynamic range external quantum efficiency spectra on the same devices used for EL measurements. Figure 5.12 shows the data plotted on a logarithmic scale. Using the method described in Section 2.6, I used the EL spectra shown above to extend the effective EQE spectra to lower currents; the resulting composite EQE data are shown in Figure 5.13. I was then able to calculate the radiative open-circuit voltage at one sun, which I calculated for a range of injection currents to ensure that the radiative voltage is not a strong function of injection current (Figure 5.14, top panel). Using these data I then calculated $\Delta V_{\mathrm{oc,nr}}$, a measure of the voltage loss due to non-radiative recombination (Figure 5.14, bottom panel).

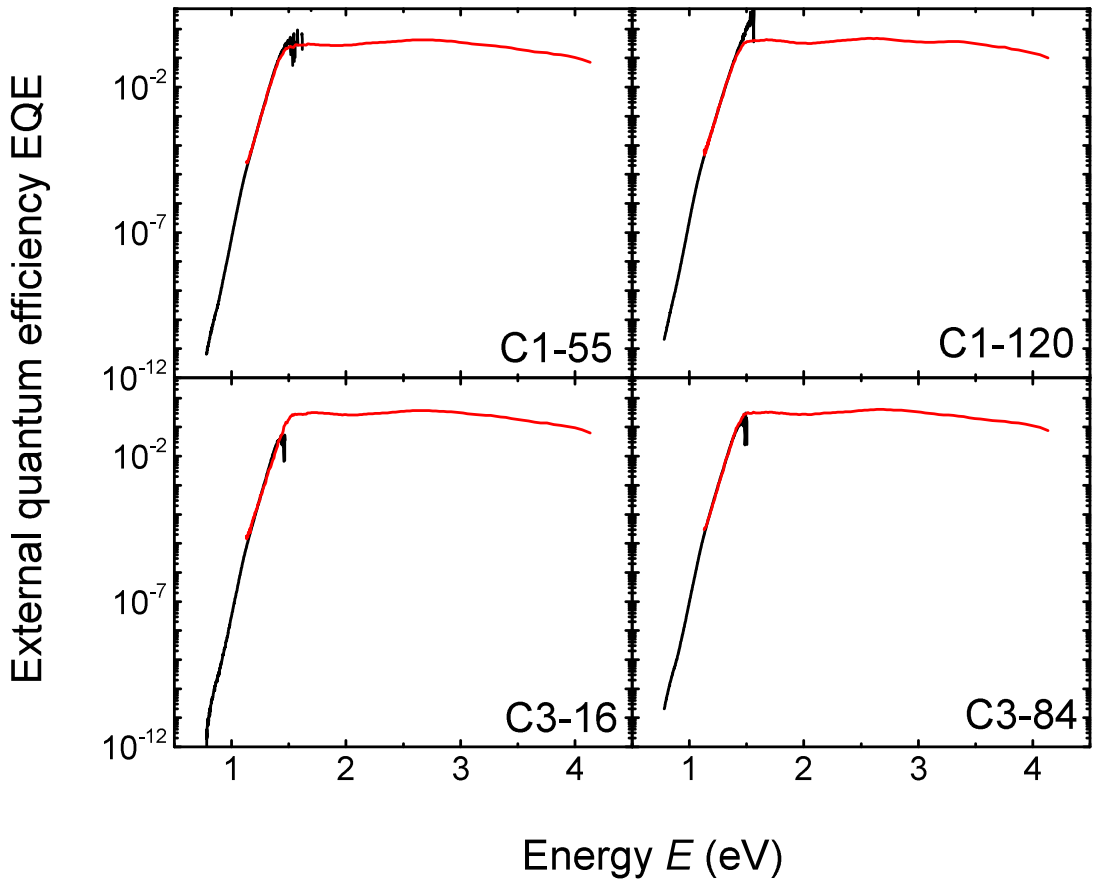


Figure 5.13: Full EQE spectra using both directly measured EQE (red lines) and converted EL spectra (EQE_{EL}, black lines). In each panel, the injection current of the EL spectrum is 16 mA (356 mA cm^{-2}). The EQE_{EL} data is scaled manually to match the magnitude of the EQE data in the overlapping region.

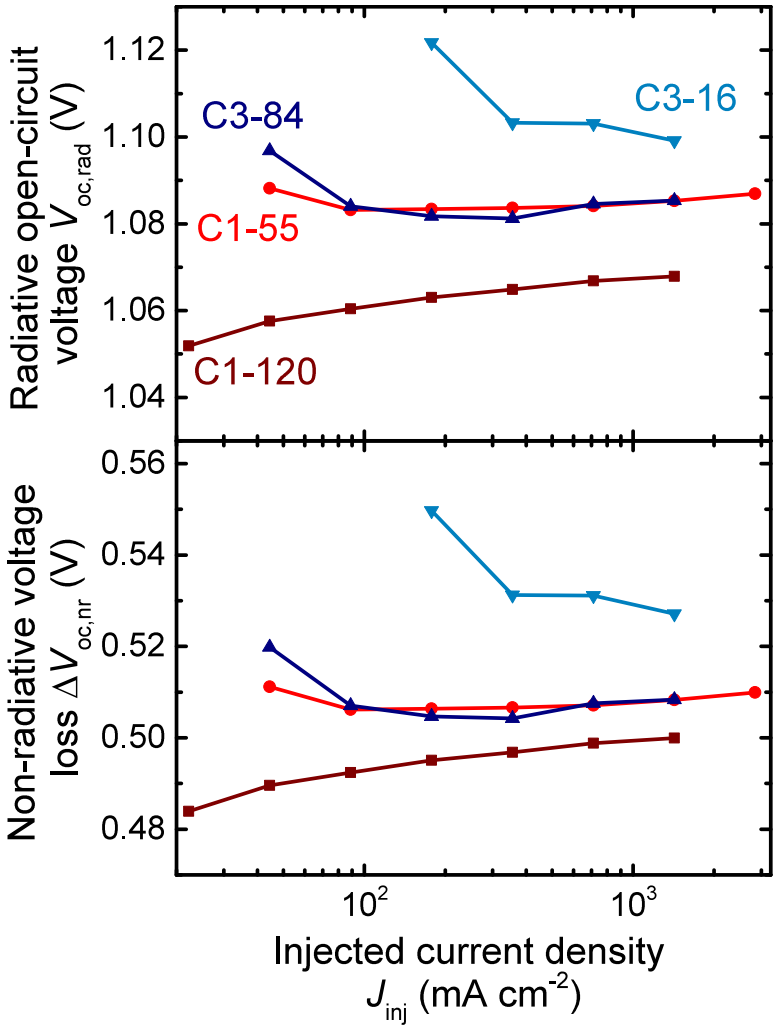


Figure 5.14: Radiative open-circuit voltage $V_{\mathrm{oc,rad}}$ (top panel) and open-circuit voltage loss due to non-radiative recombination $\Delta V_{\mathrm{oc,nr}}$ (bottom panel). Both data sets are plotted as a function of the EL injection current density J_{inj}. In both panels, C1-120 is dark red squares, C1-55 is red circles, C3-84 is dark blue up-triangles and C3-16 is light blue down-triangles.

5.3.6 Ellipsometry

We investigated the optical absorption of the polymer films using variable angle spectroscopic ellipsometry (VASE), and found that the extinction coefficient κ of pristine polymer films increased with molecular weight (Figure 5.15); the samples I made were measured by Mariano Campoy-Quiles. Furthermore, this absorption increase in the polymer region persisted in blend films of the polymer with $PC_{70}BM$. As described in Section 3.4.2, I made five films of each polymer and blend system: three on spectrosil and two on silicon. The purpose of this is to check whether there is a thickness or substrate dependence of the refractive index. Figure 5.16 shows that there was a small effect of thickness on the refractive index values extracted, with thicker films tending to exhibit a greater refractive index. The standard critical point (SCP) model was used to fit the data for both pristine polymer films and the corresponding blends; a couple examples of the resulting fits are shown in Figure 5.17. The resulting refractive index difference between low and high molecular weight polymers was insensitive to the model chosen: similar results were obtained when the SCP model was replaced by a collection of Gaussian or Lorentzian peaks.

In order to test for the anisotropic optical response that might result from preferential orientation of the polymer chains parallel to the substrate [192], Dr Campoy-Quiles attempted to model the VASE data using uniaxial anisotropic models, using either the SCP or Tauc-Lorentz models for the entire spectral range. No significant improvement in the fit quality was observed when using these models. The possibility of anisotropy was further tested by depositing samples on Si/SiO_2 (1030 nm) substrates in order to perform interference enhanced VASE [167]. Fitting these data could again be achieved without anisotropic models. These results therefore suggest that the large enhancement of absorption we observed when increasing molecular weight is not mainly due to chain orientation relative to the substrate.

For the case of blends it is possible for components to segregate vertically. We tested this using a modelling approach used previously [70], and found no clear evidence for vertical segregation of components or anisotropy. These considerations taken with the consistency of the fitted parameters across different substrates mean that we can be confident in the derived refractive index values.

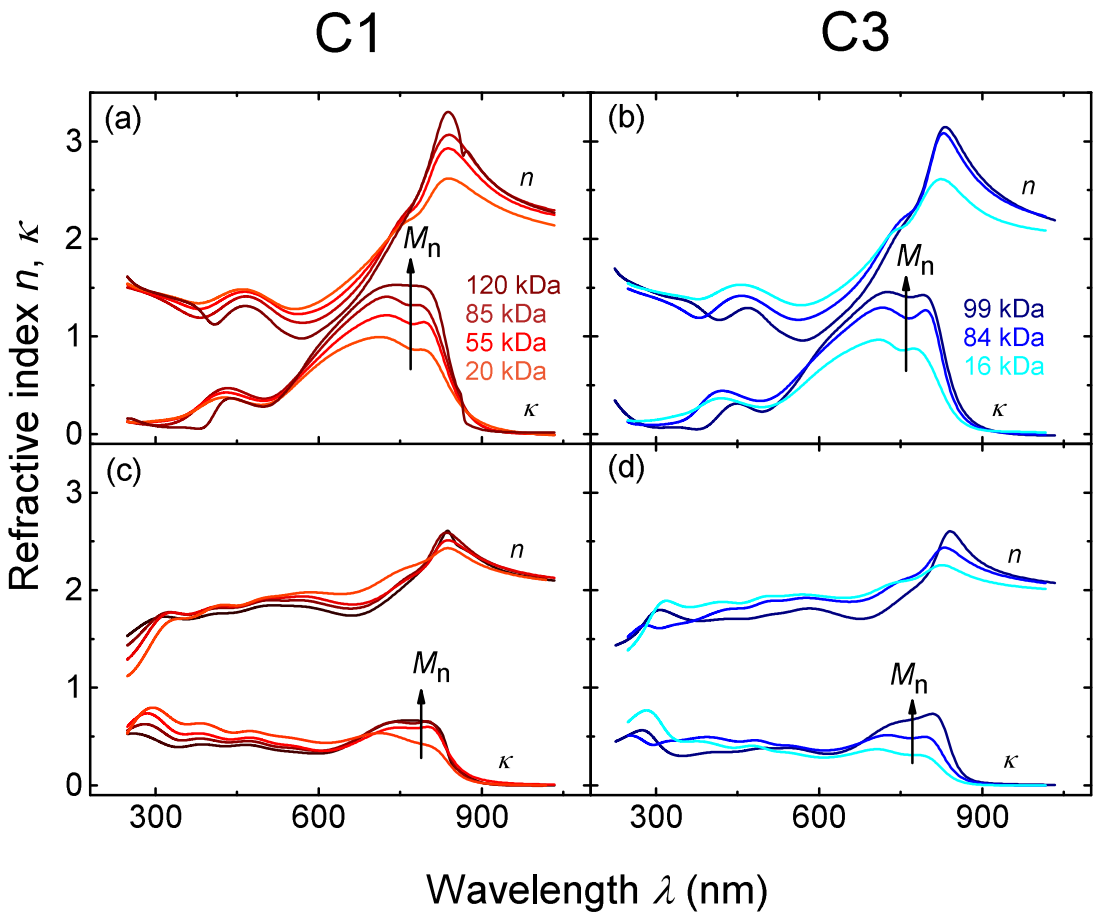


Figure 5.15: Molecular weight dependence of C1 (a,c) and C3 (b,d) refractive index (n,κ) as measured by VASE. (a,b) pristine polymer refractive index, (c,d) refractive index of 1:2 blends of the same polymers with $PC_{70}BM$. The M_n of each polymer sample is noted in the pristine polymer panels: the C1 samples were C1-20, C1-55, C1-85, C1-120 and the C3 samples were C3-16, C3-84 and C3-99, with darker lines representing higher molecular weights. Data were collected and analysed by Mariano Campoy-Quiles.

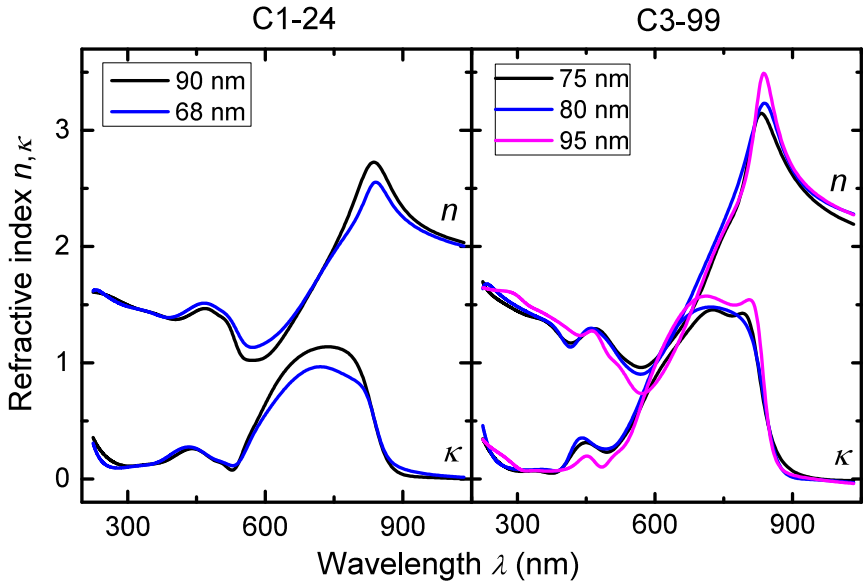


Figure 5.16: Thickness effect on refractive index as measured using ellipsometry. The left panel is pristine C1-24 while the right panel is C3-99. In both cases, the refractive index obtained is weakly dependent on film thickness; greater thicknesses result in a slightly stronger extinction coefficient. In light of this dependence, when comparing materials we took care to compare samples of similar thickness. Data were collected and analysed by Mariano Campoy-Quiles.

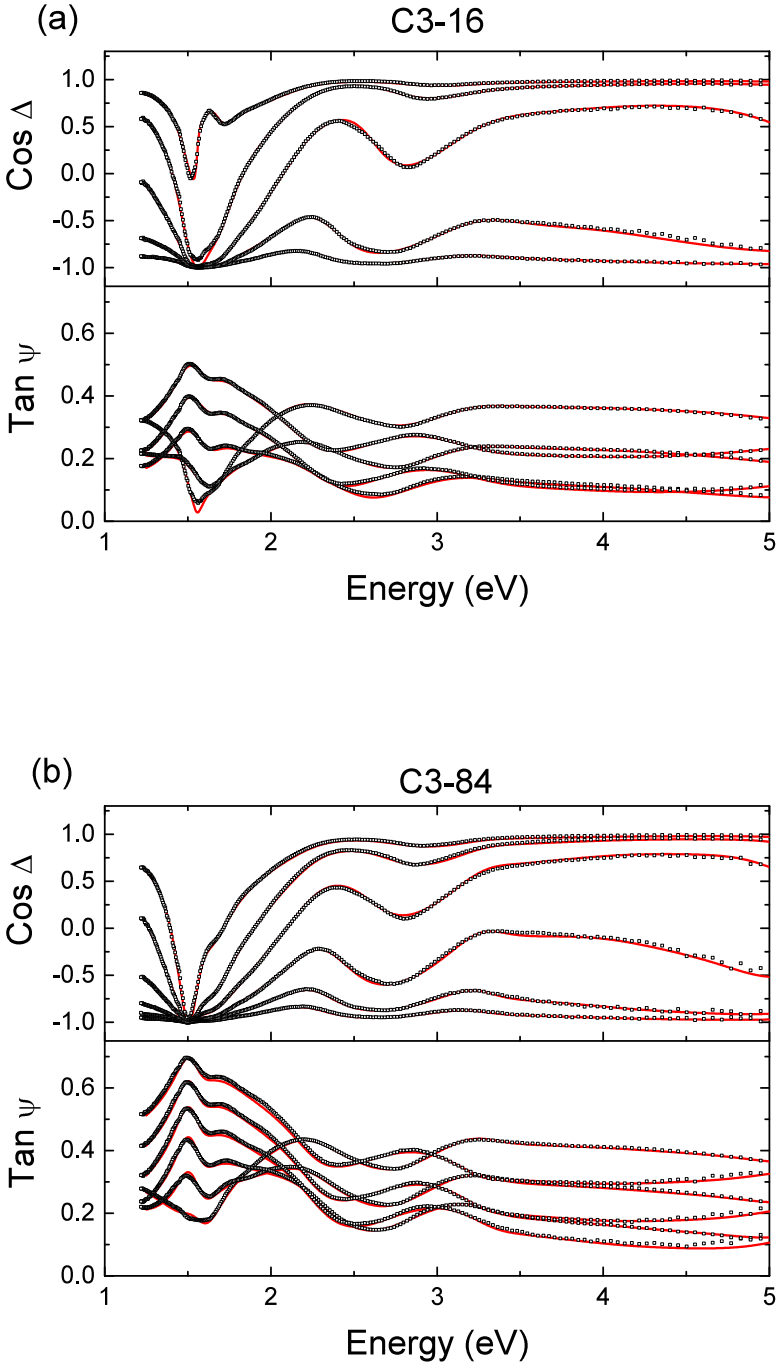


Figure 5.17: Fitting (red lines) of the experimental (open squares) ellipsometric angles $\tan\Psi$ (lower panels) and $\cos\Delta$ (upper panels) for DPP-TT-T-C3 with two different M_n: C3-16 (a) and C3-84 (b). The different series in each graph corresponds to different incidence angles.

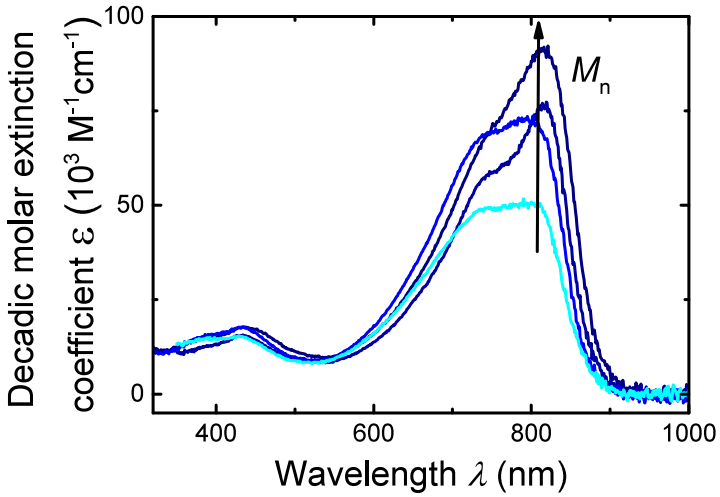


Figure 5.18: Decadic molar extinction coefficient, calculated per mole of monomer, of different molecular samples of C3: C3-9, C3-16, C3-84 and C3-99. The darker lines correspond to higher M_n. All solutions are 5 µg ml^{-1} in chloroform.

5.3.7 Ultraviolet-visible spectroscopy

In order to ascertain whether the differences in extinction coefficient observed in thin films using ellipsometry were material properties or related to film effects, I measured the ultraviolet-visible (UV-Vis) absorption spectra of dilute solutions of the materials; Figure 5.18 shows the absorption of C3 dissolved in chloroform (CF) as a function of molecular weight. I also measured solutions in 1,2-dichlorobenzene (ODCB); the maximum extinction coefficient of each material was relatively insensitive to solvent (Figure 5.19), although there was some variation in lineshape. I also found that the spectral shape and intensity were reasonably insensitive to solution concentration within the sensitivity limits of our set-up (Figure 5.20).

Furthermore I measured the temperature-dependence of the solution absorption by heating an ODCB solution up to 150 °C and subsequently allowing it to cool. I took UV-Vis spectra during this cooling process to acquire a temperature-dependent assay of the absorption (Figure 5.21). As shown in the figure, the absorption peak decreases in intensity and undergoes a hypsochromic shift upon heating, and the relative intensity of the blue shoulder of the main peak increases, consistent with a population of higher energy conformations according to Boltzmann statistics [193]. However these changes are fully reversible: also shown in the figure are the pre- and post-heating room temperature spectra, which are identical.

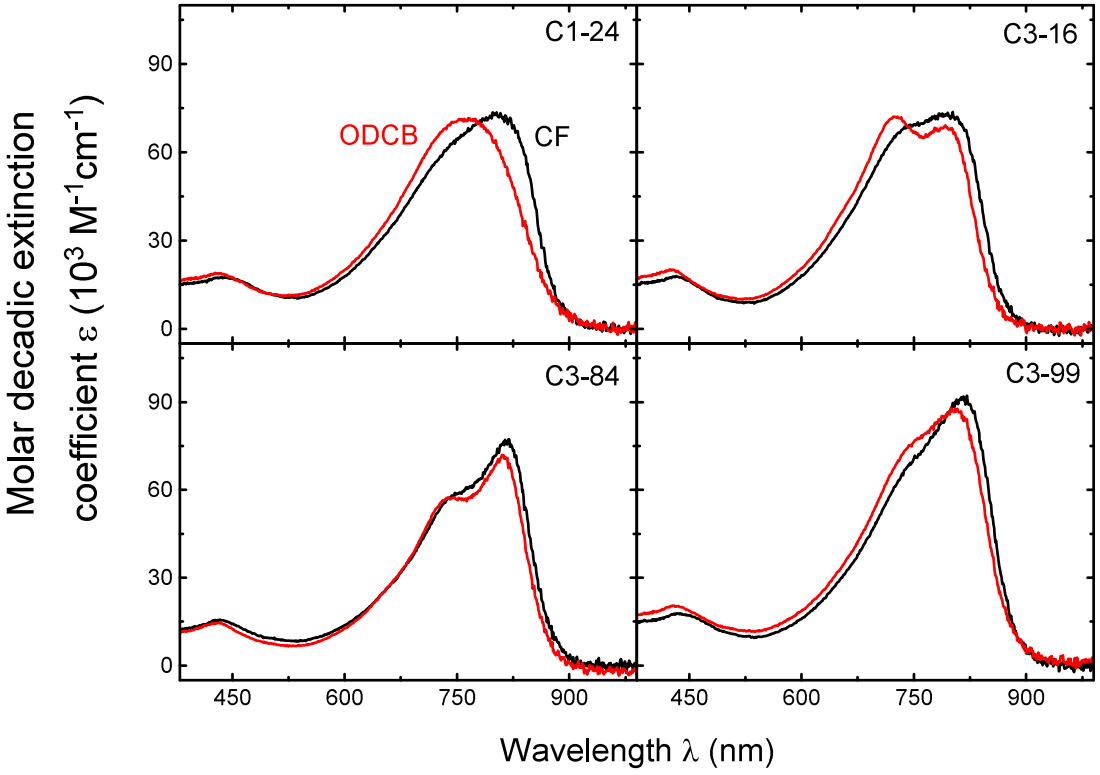


Figure 5.19: Solvent dependence of C1 and C3 solution absorption. Solution ultraviolet-visible absorption spectra of four different polymer materials in chloroform (black lines) and 1,2-dichlorobenzene (ODCB, red lines). All solutions are 5 µg ml^{-1}, and the molar decadic extinction coefficient was calculated per mole of monomer.

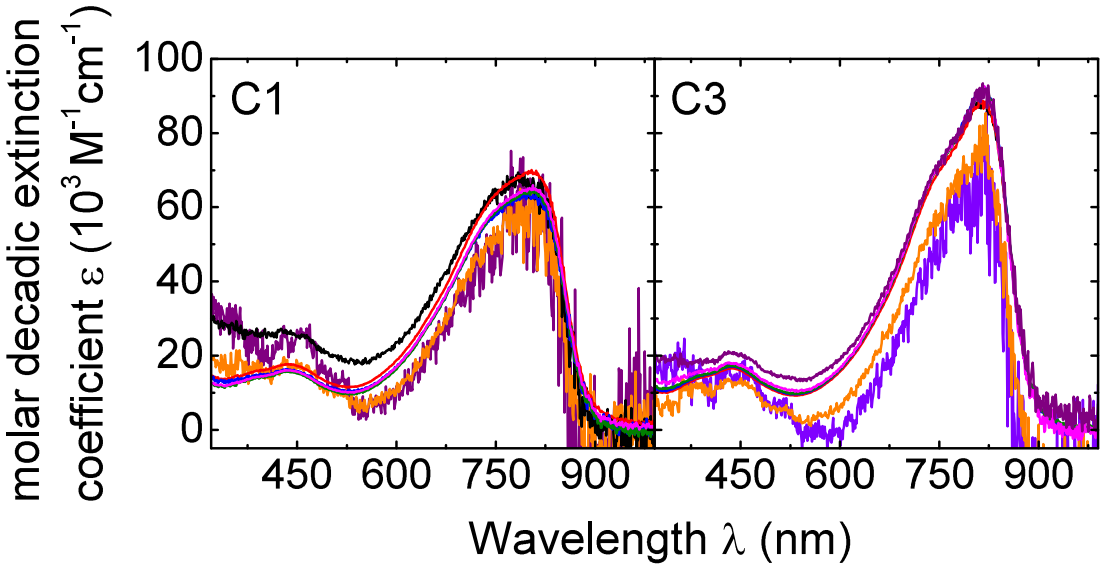


Figure 5.20: Concentration dependence of C1 and C3 solution absorption. Dilution series for C1-24 and C3-99 polymers in a 4:1 chloroform:1,2-dichlorobenzene solvent mixture. The left panel shows DPP-TT-T C1 spectra for a range of concentrations between 0.25 and 10 µg ml^{-1}, and the right panel shows DPP-TT-T C3 spectra for 0.25-25 µg ml^{-1} solutions. In all cases a spectrasil cuvette with a 1 cm path length was used, and the molar extinction coefficient was calculated per mole of monomer to enable comparison between concentrations.

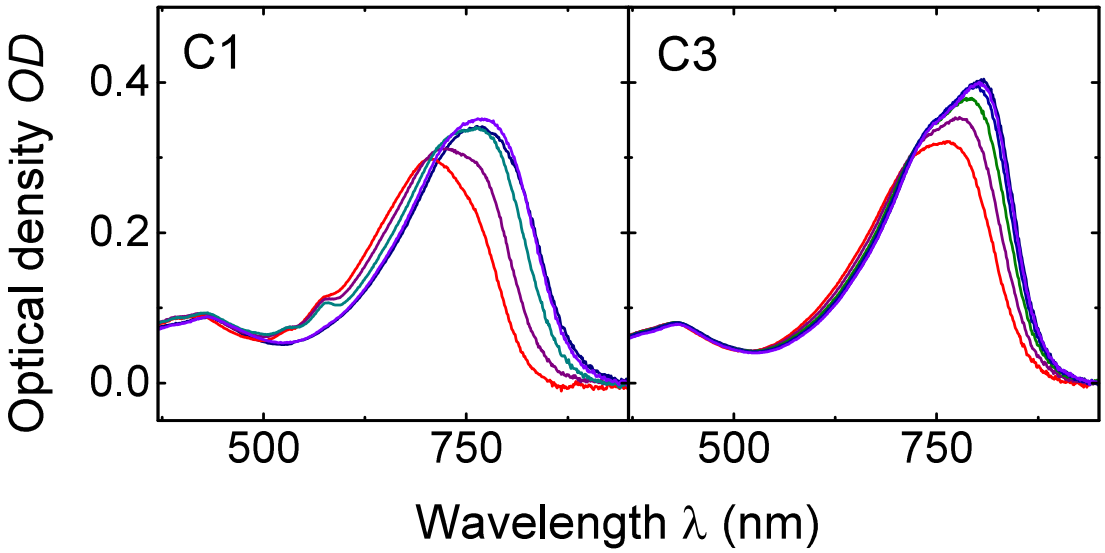


Figure 5.21: Temperature dependence of C1 and C3 solution absorption. Absorption spectra of 5 µg ml^{-1} solutions of C1 and C3 in 1,2-dichlorobenzene, which was heated to 150 °C and allowed to cool back to room temperature; the path length was 1 cm. The dark blue line shows the room temperature spectrum before heating, the red line is the spectrum at 140 °C, and the purple line is the spectrum once the solution has reached room temperature again. The other spectra were collected at regular intervals during the cooling process. In both polymer solutions, any changes in the spectrum are reversible and the spectrum before heating is recovered.

5.3.8 Transfer matrix modelling and current collection

In order to ascertain the proportion of short-circuit current density increase due to optical factors versus possible electrical factors, I estimated the internal quantum efficiency (IQE) using the measured EQE and a transfer matrix model to calculate the approximate absorption in the active layer of a device stack using the measured optical constants. If the IQE is 1, by definition the active layer absorption is exactly equal to the EQE. Therefore the IQE can be approximated by the active layer absorption multiplied by a scalar value; I do not anticipate the IQE being wavelength-dependent [159]. This determination is only approximate, since the transfer matrix method does not include any scattering effects, and is very sensitive to the thickness of each layer.

The thicknesses were inherently difficult to determine, since each device had two solution-processed layers. The organic layer can be scratched off relatively easily, but with ZnO as the layer underneath the scratch profile was very rough and so the measured thicknesses had a large uncertainty. Nevertheless the measured thicknesses, using a Dektak profilometer, are tabulated in Table 5.9 along with the standard deviation of the measurements. For the thicknesses of the other layers I had to rely on the nominal values: ITO - 200 nm, ZnO - 30 nm, MoO_3 - 10 nm, Ag - 100 nm. The initial calculation of the absorption profile did not match the measured IQE very well. Therefore I developed a fitting procedure which allowed the layer thicknesses to vary. Since the devices were all made using the same batch of ITO substrates, I constrained the ITO thickness to be constant across all the substrates. However the ZnO layer was solution-processed, so I would expect some sample-to-sample variation. I found that the MoO_3 and Ag thicknesses had very little effect or no effect on the absorption profile and so for ease of calculation I kept these constant at 10 nm and 100 nm respectively.

My fitting procedure was a brute force method, whereby I allowed each layer thickness to vary within certain bounds, and the absorption profile of each possible device stack combination was calculated. I then integrated each profile over the solar spectrum to acquire a fit short-circuit current density, and then I defined the IQE as the ratio of the experimental J_{sc} over the fit value. I acquired the experimental J_{sc} by integrating the experimental EQE in the same way over the same wavelength range. I limited the wavelength to 350 - 800 nm in order to limit the effect of errors in the ellipsometry values at the two ends of the range. I then multiplied the calculated absorption profile by the scalar IQE value, and then the error was calculated as the root sum of squares of the difference between the calculated IQE $\times$ absorption and the experimental EQE. I varied the ITO

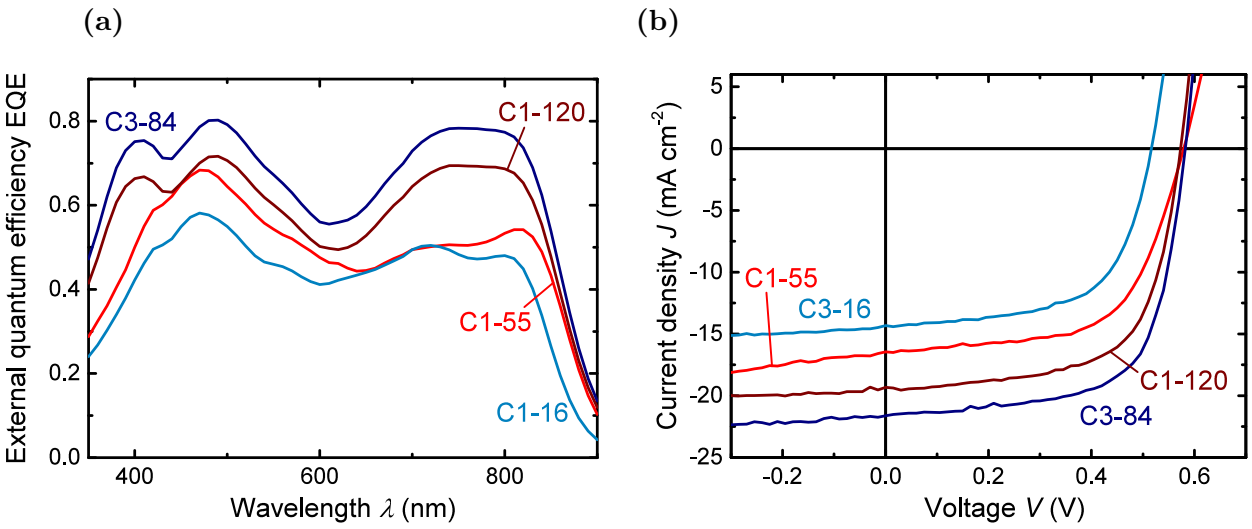


Figure 5.22: (a) EQE data used for the IQE estimation of DPP-TT-T devices and (b) corresponding current density-voltage curves measured under simulated one sun conditions. The devices are all ITO/ZnO/DPP-TT-T:$PC_{70}BM$ (1:2, w/w)/MoO_3/Ag; C1-120 is shown by dark red lines, C1-55 by red lines, C3-84 by dark blue lines and C3-16 by light blue lines. The devices were made and measured by Dr Shahid Ashraf.

thickness separately from the active layer and ZnO thicknesses, such that the single ITO thickness which minimised the error across all the devices was chosen. Then the ZnO and active layer thicknesses were minimised separately for each individual device.

The experimental EQE values I used for this analysis were different from the ones shown in Figure 5.12 because we had problems with our set-up which meant that there was too much error in the absolute values, such that the integrated EQE gave a J_{sc} which was significantly less than the measured J_{sc} from the solar simulator (by a factor of 1.5-1.9). Therefore I used data from the same batch of devices which were previously measured by Dr Shahid Ashraf on a different EQE experimental rig, which much more closely matched the measured J_{sc} (Table 5.8). For the case of C1-55 and C3-16, these were actually the same substrates as shown previously in Figures 5.4 and 5.12, but for C1-120 and C3-84 the substrates were different. The J-V and EQE graphs are shown in Figure 5.22.

Table 5.9 shows the blend and ZnO thicknesses acquired from the fitting procedure, as well as the measured profilometer values. Figure 5.23 shows the fit EQE spectra for each blend, compared to the experimentally measured EQE data. The resulting ITO thickness from the fitting procedure was 205 nm. The resulting IQE values from this procedure are shown in Tables 5.10 and 5.11; these values represent the loss in J_{sc} due to electrical factors such as charge collection efficiency. As

Table 5.8: DPP-TT-T J_{sc} values measured directly from J-V curves measured under simulated one sun conditions, and J_{sc} calculated by integrating the measured EQE spectrum over the solar spectrum. The J-V and EQE data are shown in Figure 5.22, and were measured by Dr Shahid Ashraf. The devices are all ITO/ZnO/DPP-TT-T:$PC_{70}BM$ (1:2, w/w)/MoO_3/Ag, and were made by Dr Shahid Ashraf.

Blend	$J_{sc,J-V}$ (mA cm^{-2})	$J_{sc,EQE}$ (mA cm^{-2})
C1-120	19.3	19.6
C1-55	16.4	16.7
C3-84	21.6	21.1
C3-16	14.3	14.5

Table 5.9: Measured and fit film thicknesses for IQE estimation. The Dektak and fit thickness values refer to the blend layer. The Dektak values were measured using a Dektak profilometer, and the indicated error is the standard deviation of the ten individual measurements with the exception of C3-16 which was fourteen measurements. The fit thickness arose from fitting the experimental EQE to a transfer matrix model active layer absorption. The ZnO thickness was also fit as part of the modelled device stack.

Blend	Dektak thickness (nm)	Fit thickness (nm)	ZnO thickness (nm)
C1-120	123 ± 14	117	15
C1-55	69 ± 3	63	45
C3-84	83 ± 9	77	18
C3-16	62 ± 5	66	18

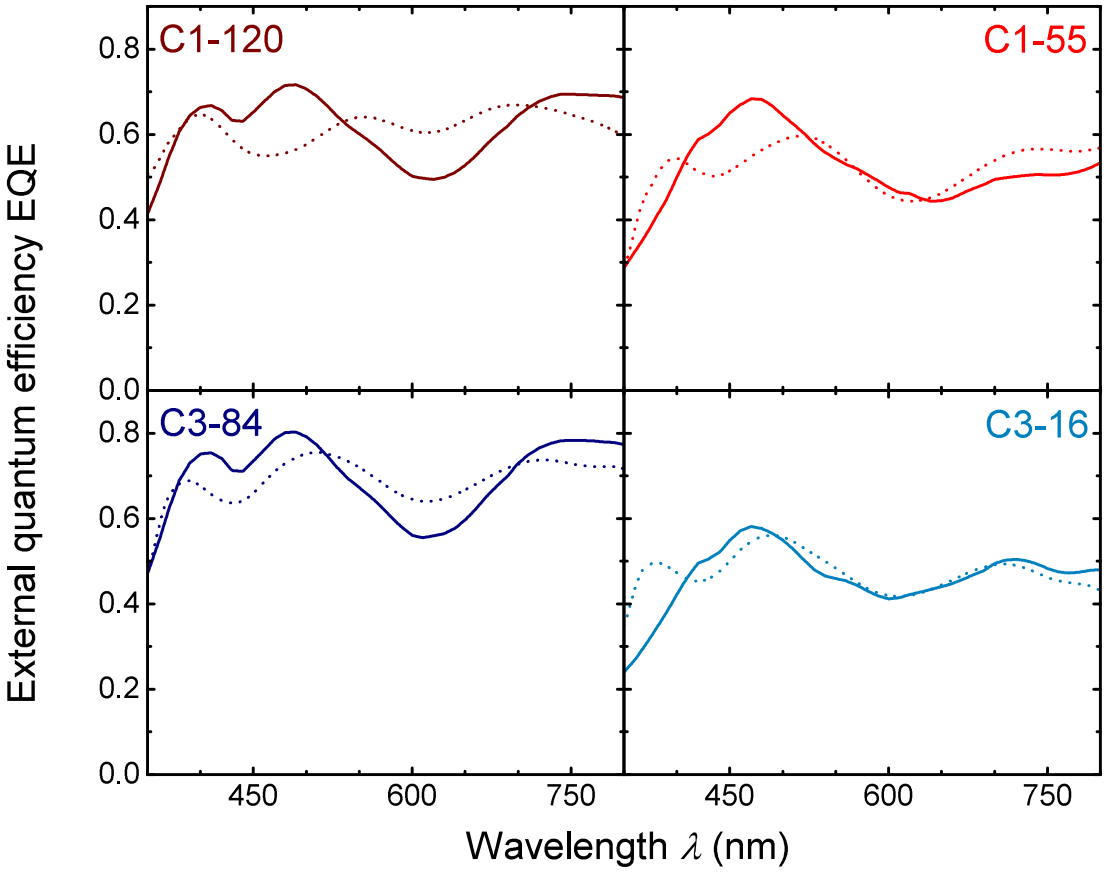


Figure 5.23: EQE fits from the estimation of IQE of C1-120 (dark red, top left), C1-55 (red, top right), C3-84 (dark blue, bottom left) and C3-16 (light blue, bottom right) blend devices. In each case the experimentally measured EQE is shown by solid lines, and is the same as the data displayed in Figure 5.22a. The fit EQE are shown by dashed lines, and were determined by calculating the absorption spectrum of the active layer in a device stack and scaling by an estimated IQE which was defined as the experimental J_{sc} divided by the integrated J_{sc} from the calculated absorption. In each case the device stack is ITO (205 nm)/ZnO/DPP-TT-T:$PC_{70}BM$/MoO_3 (10 nm)/Ag (100 nm), where the ZnO and blend layer thicknesses for each blend are shown in Table 5.9.

Table 5.10: Assessment of the breakdown of short-circuit current density increase of DPP-TT-T C1 devices. The measured J_{sc} is derived from the integral of the external quantum efficiency EQE, and the IQE is estimated by comparing the magnitude of the measured EQE and the absorption as calculated using transfer matrix modelling (TMM). The J_{sc} from TMM is the integral of the calculated active layer absorbance over the solar spectrum, if the IQE is assumed to be 100%. The ratio of HMW/LMW for each of the values is calculated to determine the relevant proportional increase. For comparison, the extinction coefficient value of the blends at 600 nm, chosen as a representative typical value, are shown.

	J_{sc} (mA cm^{-2})	Estimated IQE	J_{sc} from TMM, 100% IQE (mA cm^{-2})	κ at 600 nm
C1-120	19.6	0.77	25.4	0.33
C1-55	16.7	0.71	23.6	0.29
Ratio	1.17	1.09	1.08	1.11

Table 5.11: Assessment of the breakdown of short-circuit current density increase of DPP-TT-T C3 devices, as in Table 5.10.

	J_{sc} (mA cm^{-2})	Estimated IQE	J_{sc} from TMM, 100% IQE (mA cm^{-2})	κ at 600 nm
C3-16	22.1	0.86	25.6	0.36
C3-84	14.5	0.65	22.1	0.29
Ratio	1.52	1.32	1.16	1.26

the discussion above indicates, these values are merely an estimate, and were used to approximate the relative contribution of electrical and optical factors to the differences in J_{sc} as a function of polymer molecular weight. As such, for each of C1 and C3, I compared the ratio of the J_{sc} values with the ratio of the estimated IQE values and the extinction coefficient κ of the blend films taken at 600 nm. This wavelength was chosen as a representative value for the blend as a whole, as opposed to just capturing the absorption due to the polymer. As can be seen from Tables 5.10 and 5.11, in both cases, the optical factors account for a little less than half of the increase in J_{sc} upon increasing molecular weight.

5.4 Discussion

As Figure 5.4 makes evident, the polymer molecular weight has a larger effect on solar cell performance than alkyl side-chain branching point. Furthermore, this increase in solar cell performance is dominated by an increase in short-circuit current density, which cannot readily be explained by variation in active layer thicknesses. This chapter therefore attempts to elucidate the source of this J_{sc} enhancement. The first possible factor I eliminated was the level of doping in the blends: the doping concentration in every blend was low enough that the active layer thicknesses used in the solar cells was thinner than the depletion width from the doping concentration, so the differences in current cannot be attributed to band-bending due to doping. Since all the electrodes were processed at the same time and in the same evaporation batch for the case of the top anode, I can also plausibly rule out interfacial effects as the source of the difference in performance.

In principle the higher J_{sc} for the high MW fractions could result from improved electrical properties leading to higher collection efficiency. Therefore I measured the charge carrier lifetimes and mobilities in each blend to try and assess the electronic quality of the blends. As shown in Figure 5.9, when plotted as a function of charge density, the side-chain branching point had a much larger impact on the mobility-lifetime product $\mu\tau$ than the polymer molecular weight, with different molecular weights exhibiting almost identical $\mu\tau(n)$ behaviour. However there are some differences in carrier lifetime and mobility, with both HMW polymers showing slightly lower recombination lifetime and higher mobility, consistent with previous reports [194, 195].

Plotting these parameters as a function of charge density n allows comparison of materials, independent of the particular devices being studied. However in this case, in order to explain the behaviour of a particular set of devices, it is helpful to examine the behaviour as a function of light intensity (Figure 5.24). These data show the same trends, but the difference in mobility for different molecular weights is greater than that of recombination lifetimes, suggesting that low molecular devices could possibly suffer from poorer charge carrier collection due to poor mobility. The analysis of voltage losses due to non-radiative recombination however suggests that both low MW polymer blends suffered from greater non-radiative recombination. Therefore it appears that the low molecular weight devices have lower electronic quality, and that this likely impacts the performance. However, these differences in electronic quality do not appear sufficient to fully explain the differences in J_{sc}, as seen from the estimation of IQE.

The VASE data in Section 5.3.6 show a strong effect of molecular weight on

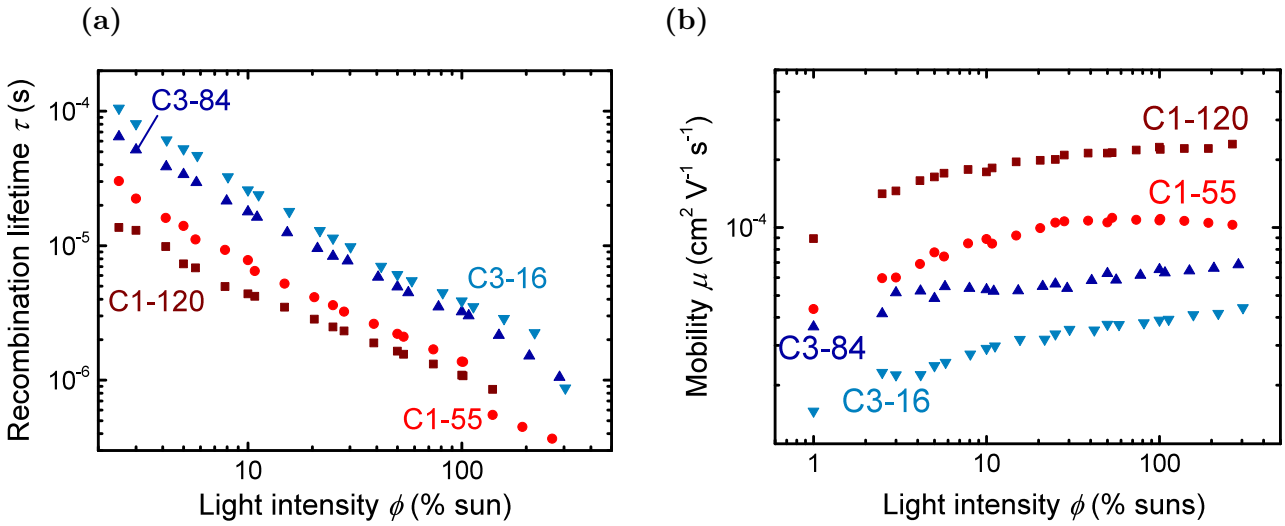


Figure 5.24: Charge dynamics parameters of C1 and C3 devices plotted as a function of light intensity. (a) Large perturbation recombination lifetime, and (b) drift mobility. These data are the same as those plotted in Figure 5.7, but by plotting as a function of light intensity, the behaviour of devices under the same illumination, for example one sun conditions, can be compared. The devices are all ITO/ZnO/DPP-TT-T:$PC_{70}BM$ (1:2, w/w)/MoO_3/Ag; C1-120 is shown by dark red squares, C1-55 by red circles, C3-84 by dark blue up-triangles and C3-16 by light blue down-triangles. The devices were made by Dr Shahid Ashraf.

complex refractive index. Notably, higher MW polymers exhibited a higher extinction coefficient κ. We confirmed these results using samples of different film thicknesses, different substrates, and using different ellipsometers. The trend in extinction coefficient of pristine polymer films was reproduced in measurements of blend films (Figure 5.15 (c,d)). The inability of anisotropic models to fit the data suggest that the extinction coefficient enhancement arises from intrinsic properties of the molecules, as opposed to being due to changes in chain packing with molecular weight. However, since ellipsometry is a solid-state technique, it is difficult to rule out other soild-state properties such as aggregation. Therefore we measured UV-Vis absorption spectra of dilute solutions of the pure polymers in chloroform and 1,2-dichlorobenzene. The trend in solution is identical to that of films, with the HMW materials absorbing light more strongly at the peak absorption wavelength than the LMW materials (Figure 5.18). Within the sensitivity of the UV-Vis spectrometer, the pseudo molar extinction coefficient per monomer was unchanged for the range of concentrations studied (0.25-25 µg ml^{-1} in the case of C3) and the spectral shape was insensitive to dilution (Figure 5.20). These observations suggest that the absorption phenomena are not the result of chain aggregation in solution; however, we cannot rule out any degree of association between chains.

The estimated IQEs, using the measured EQEs and calculated active layer absorption via TMM, indicate that enhanced optical absorption is responsible for an increase in J_{sc} of 8-16% and improved IQE is responsible for a further, similar increase of 9-32% (Tables 5.10 and 5.11). It is worth here considering more generally under which conditions enhanced optical absorption can be expected to result in increased current collection. For a given absorption strength, thicker films allow absorption of more light, however in a collection-limited regime, the efficiency of carrier collection in thick films decreases due to recombination during transit. Therefore, the optimum thickness for a solar cell is a compromise involving the optical absorption coefficient as well as the charge carrier lifetime and mobility. To assess the effect of absorption coefficient on photocurrent generation we can use the simple Hecht relation, which was derived in Section 2.5.3 and is reproduced here:

$$\mathrm{EQE}(E) = \frac{L_{\mathrm{dr}}}{d}\left[1 - \exp(-\alpha(E)\, d)\right]\left[1 - \exp\left(-\frac{d}{L_{\mathrm{dr}}}\right)\right]$$

where $L_{\mathrm{dr}} = \mu\tau(V_{\mathrm{bi}} - V)/d$ is the drift length. In the case of ideal collection ($L_{\mathrm{dr}} \gg 1/\alpha$), when layers are optically thick the effect of an enhancement in α of a factor of X results in an enhancement of less than X in EQE, and this enhancement decreases toward unity as thickness is increased (Figure 5.25, top panel).

However in the case of organic solar cells, where typical values for lifetimes are 10^{-6} seconds, mobilities 10^{-8} $m^2\,V^{-1}\,s^{-1}$, $V_{bi} \approx 1$ V and $d \approx 100$ nm, and maximum absorption coefficient is less than 10^5 cm^{-1}, the collection depth is 10^{-7} m which is similar to the absorption depth $1/\alpha$ only at peak absorption, and smaller than $1/\alpha$ everywhere else (Figure 5.25, bottom panel). In these conditions an increase in α is expected to cause a substantial increase in the maximum available photocurrent, which tends towards a proportionate effect on the photocurrent when $L_{dr} \ll 1/\alpha$. For the typical values given above, an enhancement of 1.5 in α leads to an enhancement of a factor of 1.2 in the maximum EQE. Note that the model employed here is for monochromatic light and no reflection; the wavelength chosen to approximate the blend absorption is 600 nm.

The increase in EQE may be larger than expected from the simple model when the change in absorption coefficient is accompanied by a change in electrical quality. Figure 5.25 also illustrates the case when, in collection limited devices, higher absorption is accompanied by better collection (improved $\mu\tau$). The enhancement in maximum photocurrent is greater than expected from the enhancement in α. Therefore, enhancement in absorption coefficient impacts solar cell performance especially when charge collection efficiency is limited and its effect will be enhanced by any synergy between absorption coefficient and collection efficiency.

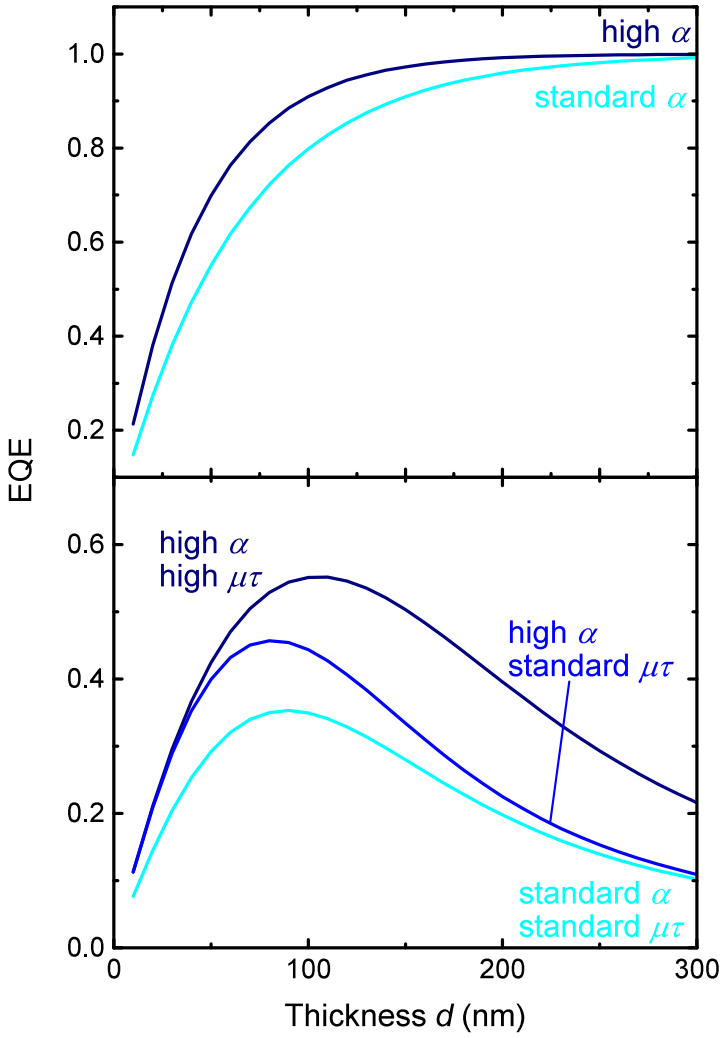


Figure 5.25: Simple model of photocurrent external quantum efficiency as a function of thickness, calculated assuming drift-dominated current and first order carrier recombination. (a) The case of standard ($\alpha = 1.6 \times 10^5$ cm^{-1}, light blue line) and enhanced $\alpha = 2.4 \times 10^5$ cm^{-1}, dark blue line) absorption when collection length is infinite. (b) The effect of absorption and mobility-lifetime product when carrier collection is limited: for the cases of standard absorption and standard carrier collection ($\alpha = 1.6 \times 10^5$ cm^{-1}, $\mu\tau = 10^{-14}$ m^2 V^{-1}) (light blue line), enhanced absorption and standard carrier collection ($\alpha = 2.4 \times 10^5$ cm^{-1}, $\mu\tau = 10^{-14}$ m^2 V^{-1}) (medium blue), and enhanced absorption and enhanced carrier collection ($\alpha = 2.4 \times 10^5$ cm^{-1}, $\mu\tau = 2 \times 10^{-14}$ m^2 V^{-1}) (dark blue).

5.5 Conclusion

We have determined that molecular weight, as opposed to side-chain design, is the pertinent factor in this set of DPP-TT-T polymers. Furthermore, we have identified enhanced optical absorption, in concert with improved electronic quality, as the source of the enhanced photocurrent generated in high molecular weight DPP-TT-T devices. Furthermore, we have highlighted the regime in which optical absorption can be expected to have the greatest impact on current available from solar cell devices. However, the underlying mechanism behind the higher absorption in high molecular weight polymer has not yet been established; this will be the subject of the following chapter.

5.6 Experimental Details

The polymers were all made by Iain Meager according to the synthesis described in [188]. The molecular weights were determined by gel permeation chromatography using low-PDI (< 1.10) polystyrene standards, and chlorobenzene as the eluent.

The fabrication method used to make bulk heterojunction solar cells varied through the project, although the active layer was always a polymer: $PC_{70}BM$ blend with a ratio of 1:2 (w/w). The blend was solution-processed from a 15 $mg\,ml^{-1}$ (total concentration) solution in a 4:1 volume mixture of chloroform:1,2-dichlorobenzene. The solar cells shown in Figure 5.2 were fabricated by Shahid Ashraf with a conventional device configuration (ITO/ PEDOT:PSS/ polymer:$PC_{70}BM$/ LiF/ Al), where the PEDOT:PSS and blend layers were spin-coated. The solar cells I used to measure the data in Figure 5.5 also had a conventional architecture, namely ITO/PEDOT:PSS/polymer:$PC_{70}BM$/Ca/Al. In this case, I blade-coated both the PEDOT:PSS and blend layers; the PEDOT:PSS layer was standard, but the blend layer was coated at a speed of 99 $mm\,s^{-1}$ to ensure the thickest possible film. The solar cells shown in Figure 5.4 on the other hand were an inverted architecture: ITO/ZnO/polymer:$PC_{70}BM$/MoO_3/Ag, with a spincoated active layer, made by Shahid Ashraf. With the exception of the devices measured in Figures 5.2 and 5.5, the devices shown in this chapter were all this latter architecture, made in the same batch, with the MoO_3 and Ag electrodes evaporated at the same time.

I bladecoated the DPP-TT-T films and corresponding polymer:$PC_{70}BM$ (1:2) blends for ellipsometry at speeds ranging from 10 $mm\,s^{-1}$ to 70 $mm\,s^{-1}$ in order to vary film thickness in a range between 40 nm and 140 nm. Mariano Campoy-

Quiles performed a multi-sample investigation, which typically included three film thicknesses and two different substrates (spectrosil and silicon) for each material (5 to 6 samples). He performed additional measurements on selected systems using two other substrates: glass/PEDOT:PSS (30 nm) and silicon/SiO_2 (1030 nm). Mariano measured a total of 92 samples across multiple batches of the three polymers, and acquired variable-angle spectroscopic ellipsometry (VASE) and, in some cases, photometry data for the samples described above at three to five angles of incidence between 55 and 75 degrees using a Sopralab GES-5E rotating polarizer spectroscopic ellipsometer (SEMILAB) coupled to a CCD detector. The standard critical point model (SCP) [173] was used to fit the data for both pristine DPP-TT-T films and corresponding blends.

I prepared the solutions for the solution UV-Vis measurements taking care to weigh out enough material such that the error of the mass balance was $< 10\%$. I set the solutions stirring overnight on a hotplate; I varied the temperature according to the particular solvent being studied, and the solubility of the polymer. I took care to ensure that each sample had the same thermal history so that results could be compared. I used both chloroform and 1,2-dichlorobenzene as solvents, as well as a 4:1 mixture of the two, to simulate the coating solution for devices. However 1,2-dichlorobenzene was more appropriate especially for the temperature-dependent measurements. The typical concentration I used was 5 $\mu g\,ml^{-1}$, as this provided a balance between good signal to noise ratio given our set-up with a cuvette pathlength of 1 cm, and ensuring that the solutions were dilute enough to reduce any multi-chain effects. To this end, I also performed a concentration-dependent measurement, varying the concentration between 0.25 $\mu g\,ml^{-1}$ and either 10 $\mu g\,ml^{-1}$ or 25 $\mu g\,ml^{-1}$ for C1 and C3 solutions respectively. The concentration range was achieved by consecutively diluting a stock solution, heating the solution on a hotplate in between dilutions to ensure full dissolution and dispersion.

The temperature dependence absorption spectra were taken using a 1,2-dichlorobenzene polymer solution, at a concentration of 5 $\mu g\,ml^{-1}$, which was heated in a cuvette to 150 °C. I then transferred the cuvette to the UV-Vis spectrometer and measured absorption spectra as the solution cooled; I minimised the range and increased the acquisition speed to ensure as little variability during measurement as feasibly possible. I then verified the temperature during measurement by subsequently repeating the experiment with a thermocouple in the solution to measure the rate of cooling. Unfortunately I was unable to use the thermocouple during spectrum acquisition because the thermocouple was in the beam path.

Chapter 6

Understanding absorption in conjugated polymers

6.1 Abstract

The work presented in this chapter is a direct extension of the work in Chapter 5, specifically the observation that polymer molecular weight can affect the magnitude of light absorption. Furthermore a review of the literature reveals that the peak extinction coefficient of high MW DPP-TT-T is about 50% greater than any polymer previously measured. With the help of quantum chemical calculations, we establish that polymer persistence length is the pertinent factor, and can predict high absorption in other polymer structures. We also find that the difference in absorption due to MW is related to the chain conformations, and postulate that for the case of high MW polymer, the polymer-polymer interactions out-compete the polymer-solvent interactions resulting in a greater proportion of linear chains. In order to probe the chain length dependence more fundamentally, I studied the solution absorption of a systematic series of oligomers.

Acknowledgements

The work presented in this chapter is the result of multiple collaborations with individuals from various institutions. Firstly, I am further indebted to Mariano Campoy-Quiles and his group for doing the many ellipsometry measurements involved in this work. Sheridan Few, while a co-member of the Jenny Nelson group, did many calculations which are reported here in Section 6.3.1. These calculations have been truly invaluable in informing the direction of my experimental work and I am truly grateful. As ever, I owe a debt to the synthetic chemists who make

the materials I am lucky enough to use. C8-IDTBT was made by Hugo Bronstein while a member of Iain McCulloch's group in the Chemistry department of Imperial College, while the DPP oligomers were made by Anastasia Leventis under the supervision of Hugo Bronstein at his current post in the Chemistry department of University College London. And finally Sophia Hayes and her post-doctoral researcher Galatia Pieridou from the Chemistry department of the University of Cyprus did an extensive resonance Raman spectroscopy investigation of the DPP-TT-T polymers which provided insight into the molecular weight dependence of the polymer absorption reported in Chapter 5.

6.2 Introduction

The previous chapter identified optical absorption as a possible design target for enhancing organic solar cell performance. However most of the polymer design efforts to date have focussed on broadening and red-shifting the optical absorption as the means of increasing photon harvesting [15], without considering the strength of the optical transitions, although there have been some exceptions [196]. So in light of our observation of molecular weight-dependent absorption of a particular polymer, we wanted to first determine how this absorption compares to other conjugated polymers.

Figure 6.1 shows that there is a large variation in the maximum extinction coefficient of organic materials, as measured using spectroscopic ellipsometry. However, regardless of the wavelength of maximum absorption the extinction coefficient of the best-performing materials never exceeds unity. The data shown are for polymers and small molecules with a wide range of different chemical structures as well as self-organising tendency. Expressed in terms of the imaginary part of the dielectric function instead, this maximum lies around 3.9 ± 0.2 (corresponding to a linear absorption coefficient α of 1.6×10^5 cm^{-1} at 700 nm). Figure 6.1, right panel, also shows the spectral lineshapes of some of the highest absorbing materials displayed in the left panel; the energetic breadth of the primary optical transition is relatively consistent, varying by $< 20\%$. In this context, the maximum extinction coefficients of 1.5 observed for high molecular weight DPP-TT-T (Figure 5.15) are remarkable.

Therefore there are two important questions to address: firstly, why DPP-TT-T polymers exhibit an optical absorption strength so much higher than the values normally observed for conjugated polymers, and second, how MW affects the magnitude of absorption in DPP-TT-T. In addition, systematically study-

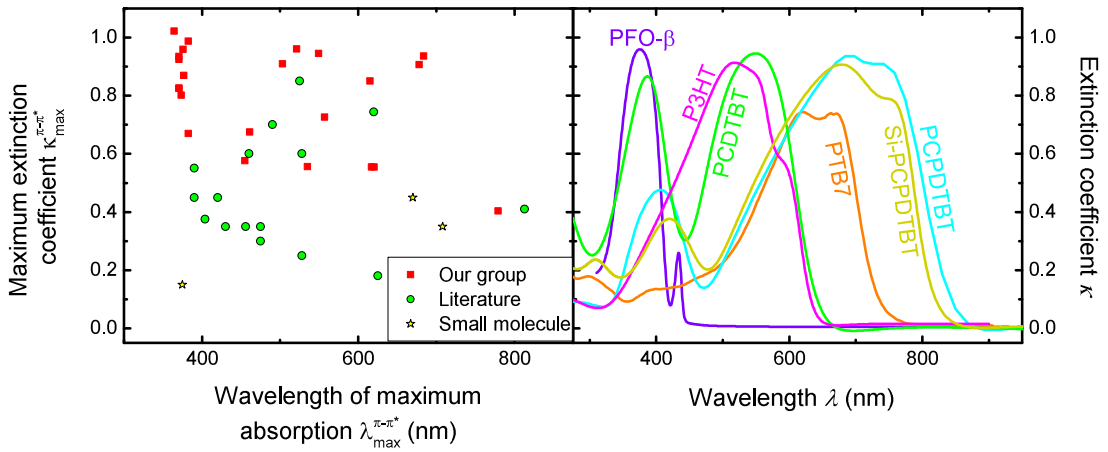


Figure 6.1: Extinction coefficient κ spectra and maximum value of κ for a range of conjugated polymers. Left panel: extinction coefficient maximum, $\kappa^{\pi-\pi*}_{\max}$, as a function of peak absorption wavelength for a large set of polymers based on one or more of the following moieties: fluorene, para-phenylene, thiophene, cyclopentadithiophene, carbazole, isoindigo, benzodithiophene and quinoxaline. The specific materials and relevant references used to prepare this figure are tabulated in Section 6.6. Right panel: extinction coefficient spectra for a smaller selection of conjugated polymers that have been widely studied for organic solar cells. The maximum κ lies at around 1, whereas the energetic breadth of the primary optical transition varies by $< 20\%$. Data collated and figures prepared by Mariano Campoy-Quiles.

ing oligomers of increasing length has been a successful strategy to understand molecular weight-dependent effects in conjugated polymers [197, 198]. Therefore I applied this by studying oligomers based on the DPP subunit.

This chapter will therefore tackle each of these open questions through both theoretical and experimental techniques. Firstly, quantum chemical calculations of the oscillator strength for different materials were done by my colleague Dr Sheridan Few to elucidate the important factors in polymer chemical structure. Secondly, we apply these insights to identify and test other polymer systems which might exhibit high optical absorption. Furthermore, with the help of resonance Raman spectroscopy performed by Prof Sophia Hayes we investigate the origin of the MW-dependent absorption in DPP-TT-T. Finally we conduct an investigation of the solution absorption of DPP-based oligomers to further investigate chain-length absorption dependence.

6.3 Results

6.3.1 Calculations

Section 2.3 outlined the relationships between the transition dipole moment, oscillator strength and complex dielectric function (eqs. (2.28) and (2.29)), which form the basis of the calculations in this section. Sheridan Few used time-dependent density functional theory (TDDFT) to calculate the oscillator strength and transition energies of the first set of excited state transitions for oligomers of $n = 1$ - 8 or more repeat units. The structures of the oligomers studied are displayed in Table 6.1, along with the corresponding polymer name.

Dr Few used GaussView [199] and Gaussian 09 [200] to prepare the optimised geometries of the structures. For most of the oligomers studied, the torsional potential between successive monomers has two minima: when successive monomers are rotated by approximately 180° relative to each other (here referred to as '*trans*') and when monomers are oriented in the same sense (referred to as '*cis*'). The notable exception to this trend is polyfluorene, which is generally not planar, but can adopt a β-phase which is planar and *trans* by definition. The *trans* conformation tends to lead to more linear oligomer structures, whereas *cis* structures tend to exhibit curvature of the backbone within the conjugated plane. The degree of non-linearity in the ground state structure is captured by the angles θ_{mon} and θ_{ring}, which are defined as in Figure 6.2. Two limiting cases can be considered when calculating properties of the oligomers: when all the monomers are in the *trans* configuration, and when all the monomers are in the *cis* configuration. These resulting all-*trans* and all-*cis* structures are displayed in Table 6.2.

The oscillator strength of oligomers can be calculated by constructing first the natural transition orbitals ψ_i and ψ_f, where ψ_f is defined by the electron and hole molecular orbitals:

$$\psi_f = \sum \phi_i^e \phi_f^h \tag{6.1}$$

where $\phi_{i,f}^{e,h}$ are the molecular orbitals corresponding to the electron and hole respectively. Thus the transition dipole moment is calculated by $\mu = e \int \psi_f^* \mathbf{r} \psi_i \mathrm{d}^3 r$. Figure 6.3 shows typical oscillator strength line spectra: specifically those of oligothiophene and oligo-DPP-TT-T. As is evident from the figure, the lowest energy transition is by far the strongest in both cases; we found that this appears to be a property of all the *trans* conjugated oligomers we studied. The spectra for both *trans* and *cis* conformations of oligo-DPP-TT-T are displayed; this shows clearly how the two conformations have transitions at very similar energies, but with dif-

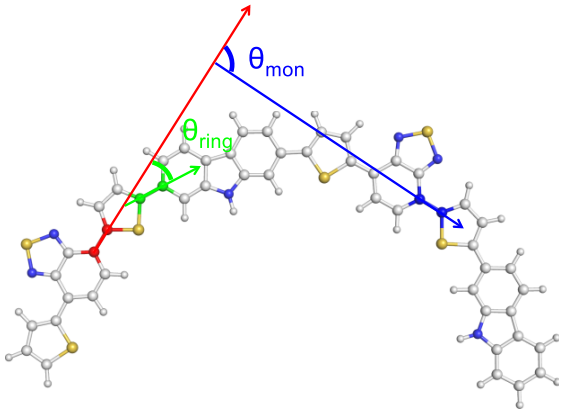
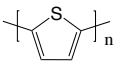
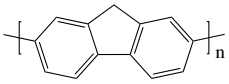
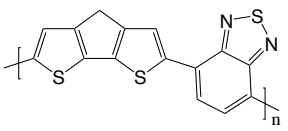


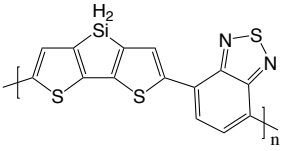
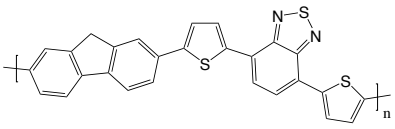
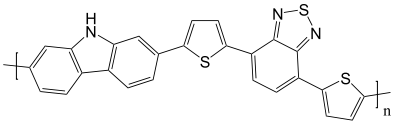
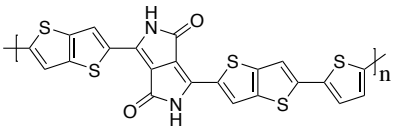
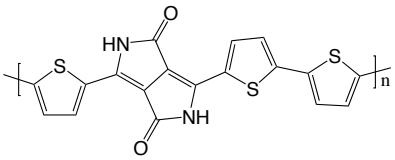
Figure 6.2: The definitions of θ_{mon} and θ_{ring}. θ_{ring} (green) is the angle between the bonds preceding and succeeding a conjugated ring, for example between the red and green bonds above. θ_{mon} (blue) is the angle between the bonds preceding and succeeding a monomer unit, for example between the red and blue bonds above. Figure prepared by Sheridan Few.

Table 6.1: Names and chemical structures of oligomers studied. For cases where the oligomer name differs from the polymer name, the oligomer name is in parentheses. The oligomers have hydrogen atoms instead of side-chains in order to ease the computational demand.

Polymer (oligomer) abbreviation	Polymer full name	Oligomer structure
P3HT (T)	Poly-3-hexylthiophene-2,5-diyl	
PFO (F)	Poly-9,9-di-n-octylfluorenyl-2,7-diyl	
PCPDTBT	Poly-2,6-(4,4-bis-(2-ethylhexyl)-4H-cyclopenta [2,1-b;3,4-b]dithiophene)-alt-4,7(2,1,3-benzothiadiazole)	

Continued overleaf

Table 6.1: (cont.) Names and chemical structures of oligomers studied.

Polymer (oligomer) abbreviation	Polymer full name	Oligomer structure
Si-PCPDTBT	Poly((4,4'-bis(2- ethylhexyl)-dithieno(3,2- b:2',3'-d)silole)-2,6-diyl-alt- (4,7-bis(2-thienyl)-2,1,3- benzothiadiazole)-5,5'-diyl)	
FODTBT (FTBT)	Poly 2,7-(9,9- dioctylfluorene)-alt-4,7- bis(thiophen-2-yl)benzo-2,1,3-thiadiazole	
PCDTBT	Poly(9-(1-octylnonyl)-9H- carbazole-2,7-diyl)-2,5- thiophenediyl-2,1,3-benzothiadiazole-4,7-diyl- 2,5-thiophenediyl	
DPP-TT-T	Poly[[2,5-bis(2-octyldodecyl)-2,3,5,6-tetrahydro-3,6-dioxopyrrolo[3,4-c]pyrrole-1,4-diyl]-alt-[[2,2'-(2,5-thiophene)bis-thieno[3,2-b]thiophen]-5,5'-diyl]]	
DPP3T	Poly(3-(2,2'-bithiophen- 5,5'-yl)-2,5-bis(2- octyldodecyl)-6-(thiophen- 2,5-yl)pyrrolo[3,4-c]pyrrole-1,4(2H,5H)-dione)	

Continued overleaf

Table 6.1: (cont.) Names and chemical structures of oligomers studied.

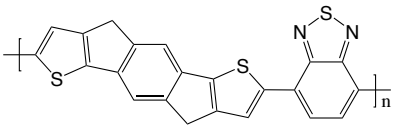
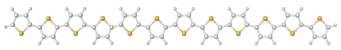
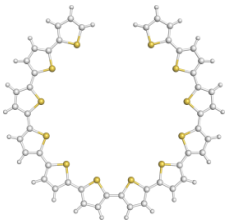
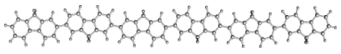
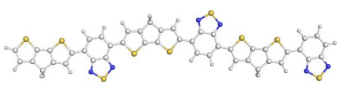
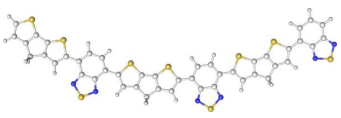
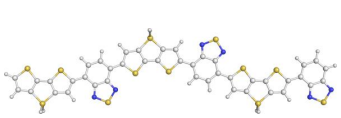
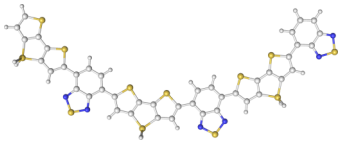
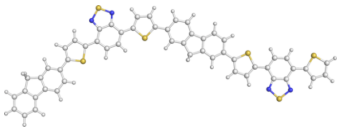
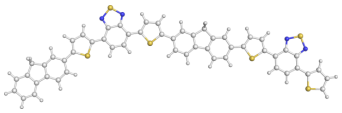
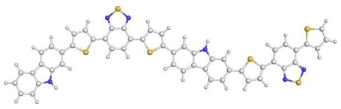
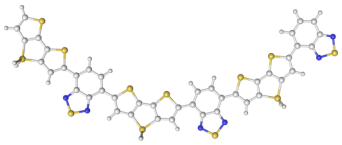
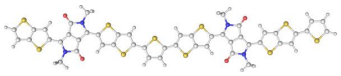
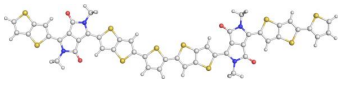
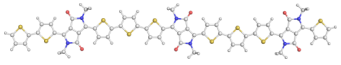
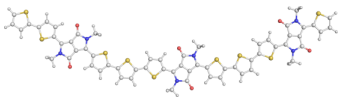
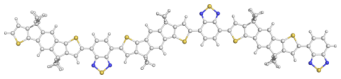
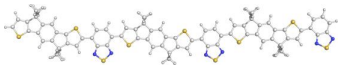
Polymer (oligomer) abbreviation	Polymer full name	Oligomer structure
IDTBT	Poly-4,4,9,9-tetraoctyl-4,9-dihydro-s-indaceno[1,2-b:5,6-b']dithiophene-alt-benzo[c][1,2,5]thiadiazole	

Table 6.2: Optimised geometry for planar oligomers of $60 < N_\pi < 85$, and associated monomer length and θ_{mon}. The all-*trans* and all-*cis* conformations are shown for all oligomers except for β-F, for which a *cis* conformation is not defined.

Name	All-*trans* conformation	All-*cis* conformation	Monomer length (Å)	θ_{mon} (°)
T			4.0	27
β-F			8.6	23
CPDTBT			12.3	28

Continued overleaf

Table 6.2: (cont.) Optimised geometry for planar oligomers of $60 < N_\pi < 85$, and associated monomer length and θ_{mon}.

Name	All-*trans* conformation	All-*cis* conformation	Monomer length (Å)	θ_{mon} (°)
Si-CPDTBT			12.3	44
FTBT			19.3	40
CDTBT			19.1	35
DPP-TT-T			20.7	27
DPP3T			18.8	27
IDTBT			16.4	0

ferent intensities. Most significantly, the second transition for the *trans* case is dark while for the *cis* conformation it is bright. In addition, similar calculations of the excitation spectra of various polymer sub-units showed that the DPP unit has a low excitation energy with a high oscillator strength. Therefore it is possible that the low excitation energy and high oscillator strength of DPP-based polymers is due to coupling of the polymer excitation to the DPP unit alone.

In order to compare between different oligomer lengths and material systems,

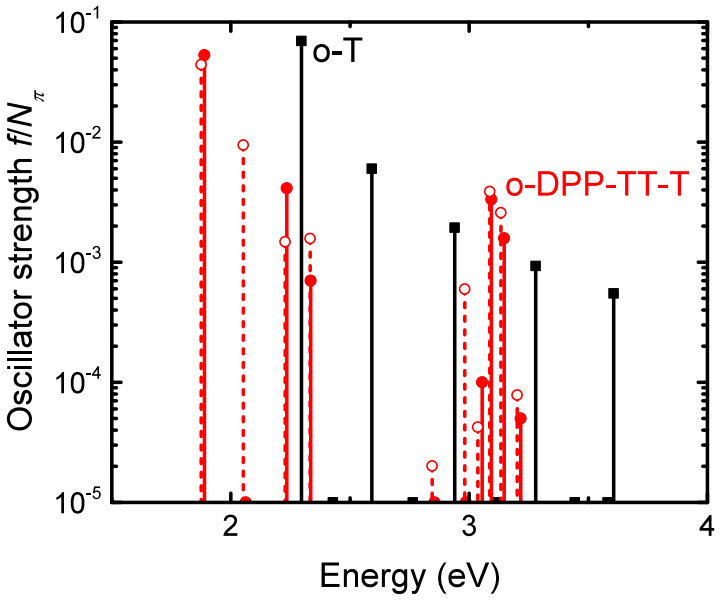


Figure 6.3: Calculated oscillator strength spectra, normalised by the number of π-electrons N_π. The spectra for oligothiophene (o-T, black squares) and oligo-DPP-TT-T (red circles) were calculated using TDDFT with CAM-B3LYP/6-31g*; the oligomer lengths were chosen such that in both cases, $140 < N_\pi \leq 150$. Thus, o-T is 25 monomer units long while DPP-TT-T is four monomer units long, resulting in N_π values of 150 and 144 respectively. The spectrum for o-T is shown for the *trans* conformation, while for o-DPP-TT-T both the *trans* (filled circles, solid lines) and *cis* (open circles, dashed lines) are shown. In all cases, any dark transitions are also indicated. These values were calculated by Dr Sheridan Few.

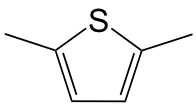
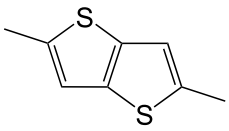
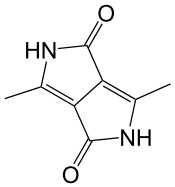
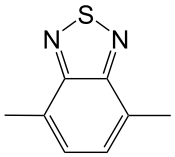
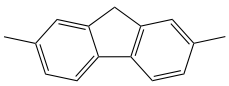
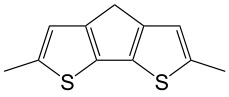
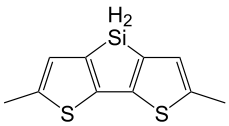
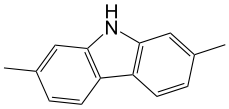
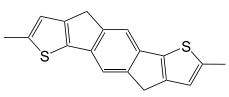
a normalised oscillator strength for the dominant transition, f_1, was obtained by dividing f_{01} (the oscillator strength of the first excited state) by the estimated number of π-electrons in the system, N_π (see Table 6.3); this is justified since most of the oscillator strength in the visible region resides in this first electronic transition for the systems we studied.

The principal strategy employed to design low band-gap polymers is to alternate electron-rich ('donor') and electron-deficient ('acceptor') components along the polymer chain, resulting in some charge transfer character in the first transition [201, 202]. This push-pull character of the transition could plausibly result in the transition strength decreasing, due to the diminished electron-hole spatial overlap. To check this, Dr Few calculated the degree of charge transfer between the donor and acceptor units, and found little correlation between this and the normalised transition dipole moment μ_{01}/N_π of the first transition. That said, for the case of DPP-TT-T, there was very little charge transferred in the first transition between the DPP and thiophene block; the little charge that was transferred actually appeared to be from the DPP (commonly thought of as the acceptor) to the thiophene (commonly the donor). This observation is consistent with a previous study [187].

Figure 6.4 shows f_1 as a function of N_π for several conjugated oligomers in both the all-*trans* and all-*cis* conformations. In all systems, f_1 rises with N_π for small N_π. For the case of the all-*trans* conformation, f_1 rises monotonically before levelling off. However, for the case of the all-*cis* conformation, f_1 decreases with N_π after reaching a maximum. It is evident from these data that while the homo-oligomers studied appear to do well in the all-*trans* limit, they especially suffer when the all-*cis* limit is considered instead. DPP-TT-T however is notable in that its normalised oscillator strength is less strongly dependent on conformation than the other structures.

Although there is little experimental data on oligomer specific absorption, these results are consistent with experimental measurements of highly monodisperse oligomers of 3-hexylthiophene, which show a rising mass attenuation coefficient in solution with oligomer length up to $N \approx 25$ repeat units [197]; the calculations are also consistent with published data on absorption by fluorene [203] and the trend is consistent with data of thiophene-co-quinoxaline oligomers [204]. This rise in f_1 with N can be attributed to a superlinear increase in polarisability with oligomer length, as reported for thiophene, acenes, and other elongated conjugated molecules at short lengths [205]. In the first excited state, the transition dipole moment μ_{01} is strongly aligned with the long axis of the oligomer, and capable of

Table 6.3: The number of π-electrons counted per polymer subunit.

Name	Abbreviation	Chemical structure	Number of π-electrons, N_π
Thiophene	T		6
Thienothiophene	TT		10
Diketopyrrolopyrrole	DPP		10
Benzothiodiazole	BT		10
Fluorene	F		12
Cyclopentadithiophene	CPDT		12
Si-cyclopentadithiophene	Si-CPDT		12
Carbazole	CZ		14
Indacenodithiophene	IDT		18

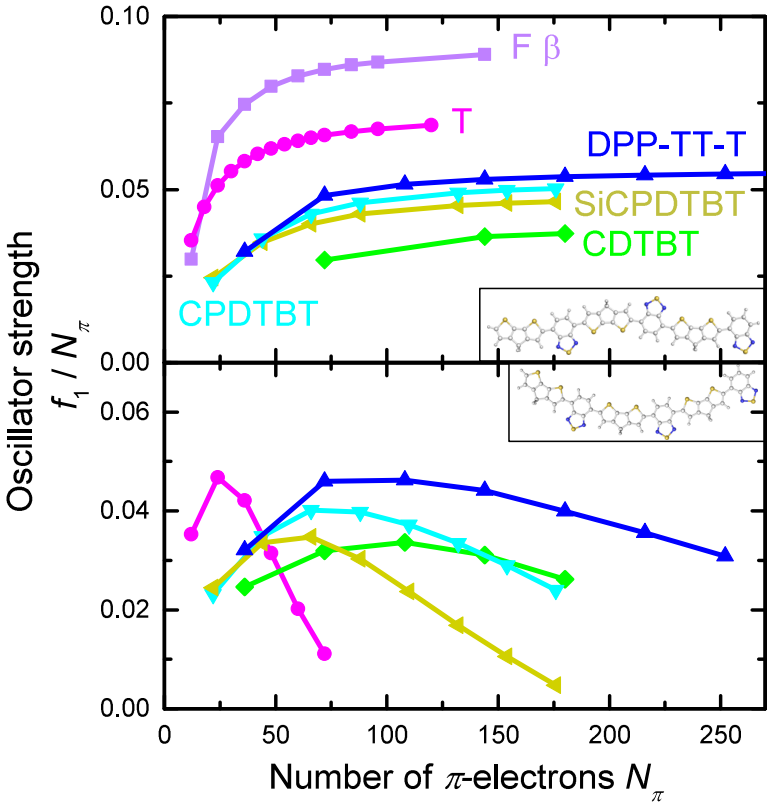


Figure 6.4: Calculated oscillator strength for the first transition, normalised by the number of π-electrons N_π. F β refers to β-phase oligo-fluorene (lilac squares) and T refers to oligo-thiophene (magenta circles). Oligo-DPP-TT-T is represented by blue up-triangles, oligo-Si-CPDTBT by yellow left-triangles, oligo-CPDTBT by cyan down-triangles, and oligo-CDTBT by green diamonds. Top panel: normalised oscillator strength f_1 of the lowest energy transition as a function of N_π, for oligomers calculated in the alternating (*trans*) configuration, calculated using TDDFT with CAM-B3LYP/6-31g* with the inter-monomer angles constrained to the *cis* or *trans* values during geometry optimisation. The inset shows the calculated all-*trans* conformation of a CPDTBT oligomer. Bottom panel: as top panel for the *cis* conformation. The inset shows the calculated all-*cis* conformation of a CPDTBT oligomer. Note that oligofluorene does not normally planarise, and so the *trans*/*cis* representation does not apply. It can form a meta-stable phase, the β-phase, which is planar in the *trans* configuration so is included in the top panel, but it does not form the *cis* conformation so is omitted from the bottom panel. These data were calculated by Dr Sheridan Few.

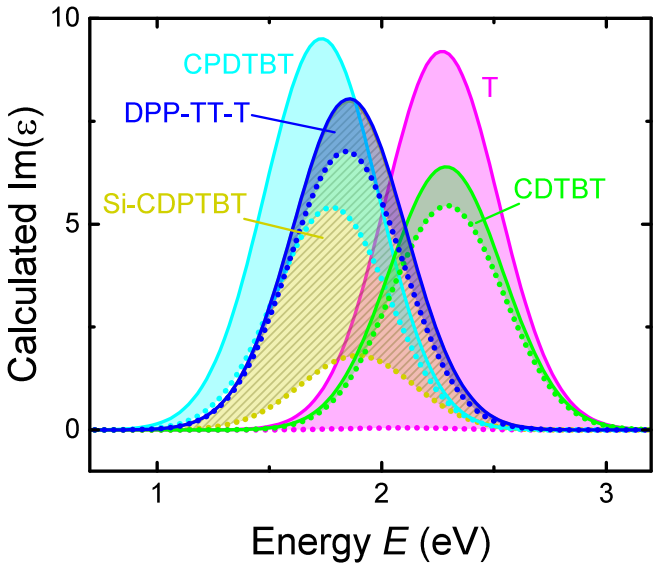


Figure 6.5: Modelled ε_2 spectra calculated from eq. (2.28) using calculated f_1 values for oligomers containing a similar number (around 140-160) of π-electrons. The transitions are broadened with a Gaussian function of width 0.25 eV. The all-*trans* case for each oligomer is represented by solid lines, whereas the all-*cis* case is represented by dotted lines. The shaded area represents the range of intermediate conformations which the oligomer is expected to adopt.

coupling strongly with a plane-polarized electromagnetic field.

Both homo-oligomers studied (fluorene and thiophene) in the all-*trans* configuration show a larger value of f_1 than any donor-acceptor structures, across the calculated range of N_π. However this can be attributed in part to their high transition energy relative to the donor-acceptor copolymers (eq. (2.29)), and does not necessarily imply high extinction at any wavelength of interest. In solar cells, for example, we seek high oscillator strength at energies where solar irradiance is high. When the effect of transition energy is removed therefore in Figure 6.5 by calculating ε_2 spectra for the first transition of oligomers of similar size (N_π = 140-150) in the all-*trans* conformation, then the extinction of different materials becomes comparable. Even in this representation though, DPP-TT-T shows an unremarkable extinction strength.

The loss in extinction with increasing length of the all-*cis* oligomers is due to the oligomer curvature, which causes μ_{01} to increase sublinearly with N_π, but the size of the effect is dependent on the chemical structure. For example, Si-CPDTBT suffers a strong loss in specific extinction due to its high curvature, resulting from the large angle θ_{mon} of 44° between vectors joining successive monomer pairs, whereas DPP-TT-T with $\theta_{\text{mon}} = 27°$ and a longer monomer suffers the least (see Figure 6.6). Much of the lost oscillator strength is recovered in higher-lying states,

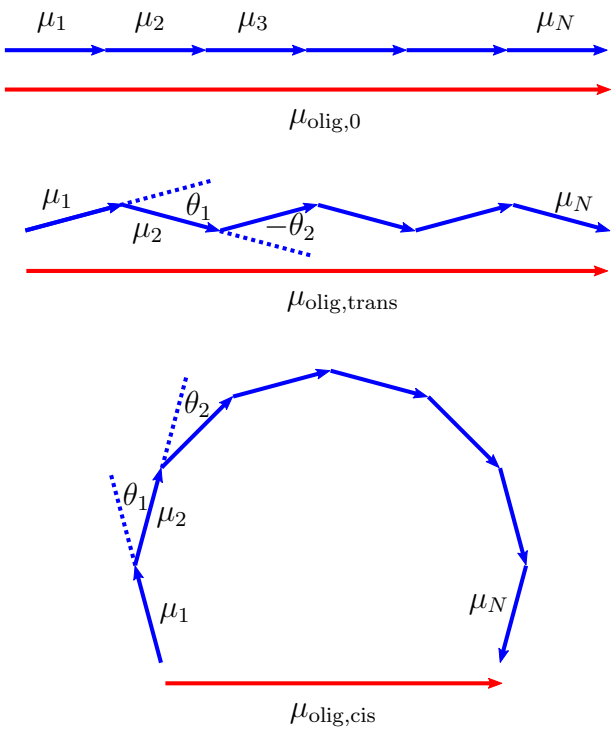


Figure 6.6: Illustration of the influence of oligomer conformation on the overall transition dipole moment. Each monomer contributes a vector of equal magnitude, μ_{mon} (blue arrows), oriented in the direction of the preceding intermonomer bond, to the transition dipole moment of the oligomer, μ_{olig} (red arrows). μ_{olig} will be largest if all monomers are colinear (top case), will be only slightly shortened in the *trans* conformation (middle), and will be much shorter in the *cis* conformation (bottom). Figure adapted slightly from Sheridan Few.

but these are less useful for solar light harvesting. Allowing that, at room temperature, any conjugated polymer will sample a range of conformations, the all-*trans* and all-*cis* cases represent the limits between which the average extinction must lie. In the case of DPP-TT-T, the lower (*cis*) limit lies very close to the upper (*trans*) limit.

It is important to note that curved and linear oligomers differ in their oscillator strength, but not, to a first approximation, in the transition energy, because the different conformers studied here are not strained. The effect is captured in the concept of persistence length, which can be related directly to μ, as opposed to conjugation length, which is usually related to transition energy [206, 207]. The persistence length represents the average projection of all bonds in the polymer onto any selected bond. We can assume that the polymer remains completely planar, with bends allowed only as a result of *cis*/*trans* isomerism of neighbouring conjugated rings. Therefore the possible bond directions are limited and each possible configuration can be weighted by the expected population at room tem-

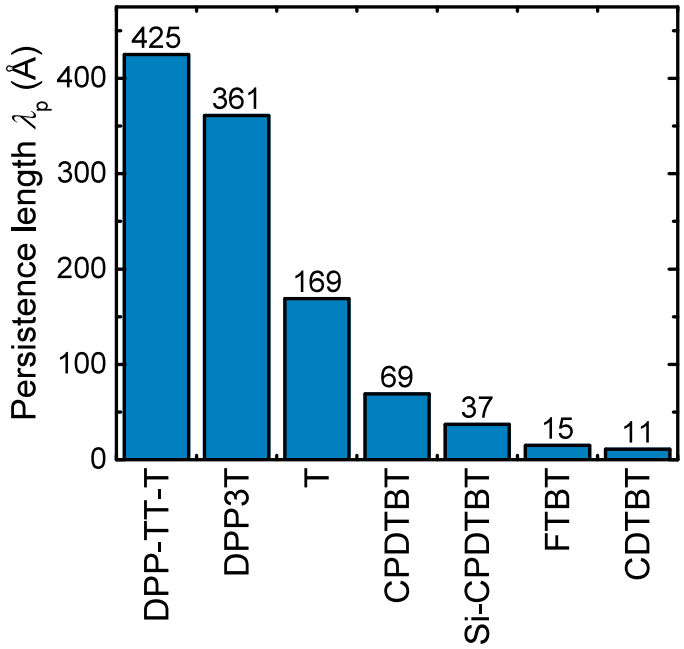


Figure 6.7: Calculated persistence length for a range of polymer structures. Data calculated by Sheridan Few using the method outlined above and in [206, 207].

perature by considering the energy required to flip a single ring in the chain. Further details of the method are described in [208].

Figure 6.7 shows the calculated persistence lengths λ_p for a range of conjugated polymers using the above method. These results show that DPP-TT-T exhibits a substantially higher persistence length than any other polymer we studied. Specifically, DPP-TT-T benefits from the relatively long monomer, small θ_{mon} and relative preference for *trans* alignment. The high linearity of DPP-TT-T was also noted in a computational study of polymer conformations in solution [209]. The positive correlation between persistence length and extinction coefficient has been used previously to infer conformation from extinction [210], but not in the context of designing strongly absorbing conjugated polymers. The calculated values of λ_p are generally greater than values determined experimentally [210, 211], suggesting that factors other than the theoretical potential energy surface, such as intermolecular interactions and torsional disorder, may influence chain extension in practice. In addition, although the relative depths of torsional minima influence λ_p, the steepness of the torsional potential alone is not a critical parameter.

Within this picture it is possible to rationalise a chain length dependence of oscillator strength in DPP-TT-T. In a solution-processed polymer sample, many conformers will be present in a variety of permutations of relative monomer alignment, with chain extension lying between the all-*trans* and all-*cis* limits. The estimated persistence length reflects this distribution. The range of conformations

- together with the monomer length, monomer alignment and torsional potential - results in a range of absorption strengths. In the case of DPP-TT-T, the chain curvature, and hence oscillator strength, is relatively insensitive to chain conformation (that is, all likely conformations are relatively straight), leading to an average extinction that exceeds that of all other materials studied here.

6.3.2 Test of persistence length-absorption relationship in polymers

To test the proposal that persistence length dominates optical extinction in solution we identified additional polymers with long monomers and high expected co-linearity (small θ_{mon}). Namely, we studied an indacenodithiophene-co-benzothiadiazole polymer (C8-IDTBT) [177] and an alternative DPP-based polymer diketopyrrolopyrrole-terthiophene (DPP3T); see Figure 6.8 for chemical structures. C8-IDTBT is the same polymer backbone as shown in Chapter 4 but the alkyl side-chains are different. The benefits of the high co-linearity of IDTBT (but with C_{16} side-chains) is mentioned in [124]. C8-IDTBT has a theoretically co-linear monomer structure (i.e. $\theta_{\text{mon}} = 0$), resulting in an infinite persistence length. Meanwhile the persistence length of DPP3T was calculated and presented in Figure 6.7, and is comparable to DPP-TT-T. DPP3T has also exhibited good ambipolar transport and solar-cell performance [212], and is interesting on account of its low radiative losses [27]. I therefore investigated the absorption of these two polymers to test our proposal.

I measured the absorption of the polymers in solution, taking UV-Vis measurements of the polymers at room temperature in 1,2-dichlorobenzene (Figure 6.9). I chose a dilute concentration of 5 µg ml^{-1} in order to minimise the interchain interactions. However, some reports in the literature suggest that there are still likely to be multichain species in solution [213, 214]. As Figure 6.9 shows, the maximum extinction coefficient, when normalised per mole of π-electrons, of DPP3T and C8-IDTBT are very similar to that of high molecular weight DPP-TT-T. For the case of C8-IDTBT, a range of molecular weights were available (see Table 6.4 for molecular weight information), and I found no trend with molecular weight for this polymer. I should also note that the UV-Vis absorption of C_2C_6-IDTBT measured in Chapter 4 (displayed in Figure 4.5) has a maximum of 1894 cm^{-1} mol e-$^{-1}$, which is less than the maximum of C8-IDTBT. It is possible therefore that for this polymer, the side-chains affect the polymer linearity.

In addition to the solution measurements, Dr Mariano Campoy-Quiles per-

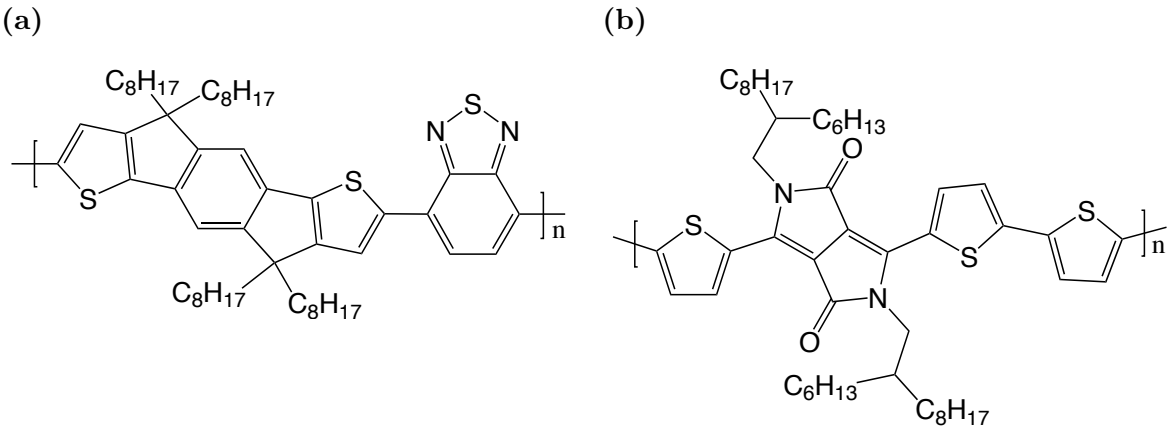


Figure 6.8: Chemical structures of (a) octyl-indacenodithiophene-co-benzothiadiazole (C8-IDTBT) and (b) diketopyrrolopyrrole-terthiophene (DPP3T).

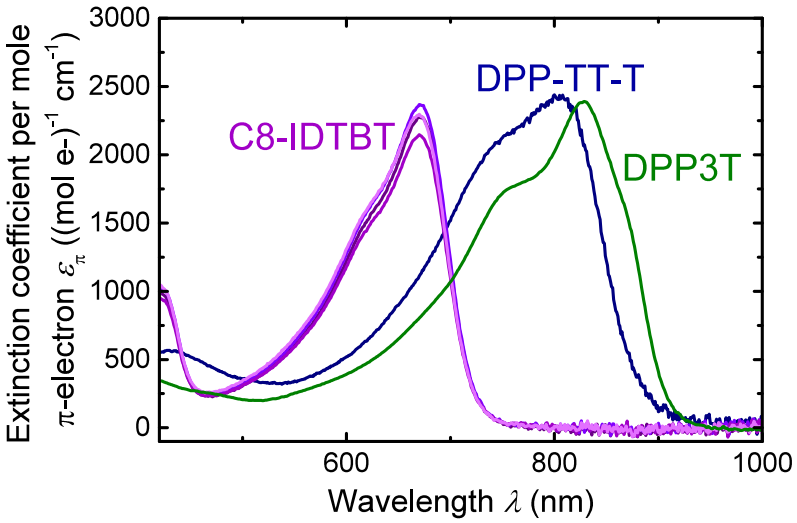


Figure 6.9: Solution ultraviolet-visible absorption spectra of DPP3T (green) and C8-IDTBT (purple); solutions were 5 µg ml^{-1} in 1,2-dichlorobenzene. All data were normalised per mole of π-electron. Four molecular weight fractions, C8-IDTBT-2, -3, -5 and -8, were available for C8-IDTBT: the lower molecular weights represented by lighter colours. The M_n values range from 43 to 459 kg mol^{-1}, and the full molecular weight information is listed in Table 6.4. For reference, the analogous data of high molecular weight DPP-TT-T C3 (C3-99) (dark blue) is shown.

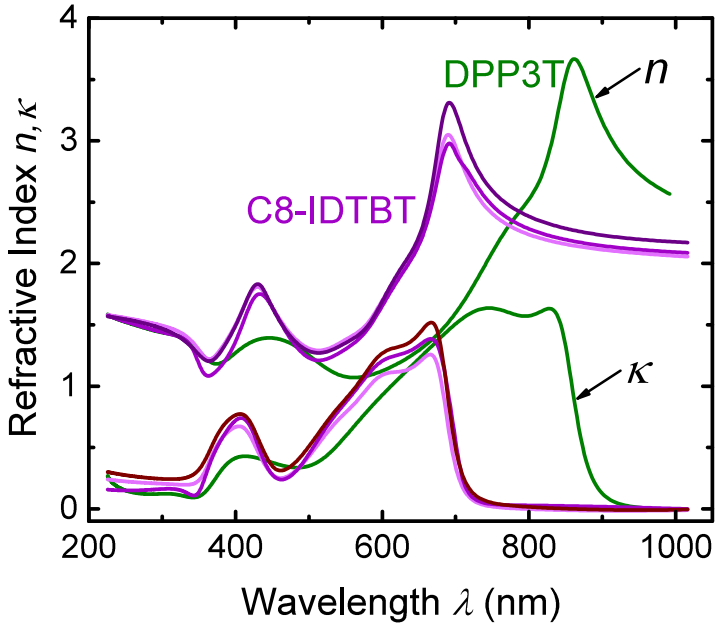


Figure 6.10: VASE-derived complex refractive index data for C8-IDTBT films (purple) and DPP3T (green). In the case of C8-IDTBT, multiple molecular weight fractions were available: C8-IDTBT-7 (light purple, lowest MW), -4 (purple) and -2 (dark purple, highest MW). The M_n values of the C8-IDTBT polymers range from 52 to 459 kg mol^{-1}. The data shown here correspond to thin films (30-50nm).

formed VASE on films of the polymers, and found that the optical extinction maxima are indeed comparable to DPP-TT-T (Figure 6.10). Dr Campoy-Quiles measured samples of three molecular weights of C8-IDTBT: -2, -4 and -7 (see Table 6.4), and this time we found a small dependence of extinction coefficient on molecular weight for this polymer. These results therefore confirm persistence length as a useful metric to possibly screen for high-absorbing materials.

6.3.3 Probing the origin of molecular weight dependence of absorption in DPP-TT-T

Thus far, the molecular weight dependence of DPP-TT-T absorption has not yet been adequately addressed. Examining the gel permeation chromatography data, it is evident that for both low- and high-MW fractions, the majority of the MW distributions lie at MWs beyond the point where the calculated specific extinction begins to saturate (Figure 5.3). Therefore, the lower extinction coefficient of low-MW polymer is not explained by limited polymer chain length. An alternative hypothesis is that the chains in the LMW and HMW samples are present in different distributions of conformation. This idea is supported by the higher relative strength of the second shoulder (apparent 0-1 vibronic peak) in the ab-

sorption spectrum for the LMW than the HMW sample (Figures 5.15 and 5.18). It has been shown by theoretical studies that oscillator strength is transferred from the 0-0 to higher vibronic transitions as a polymer is curved [45, 215]. Interestingly, another study also showed that, as a polymer becomes more coiled, oscillator strength is lost from the lowest electronic transition and gained by higher electronic transitions [45].

Raman spectroscopy is the inelastic scattering of laser photons; some of the photons leaving the sample are shifted in energy relative to the incoming photons. This occurs because the incoming photons can excite a molecule to a virtual state, which can then relax down to the initial state, which would result in elastic Rayleigh scattering, or can relax to a different vibrational mode of the ground electronic state (see Figure 6.11). Therefore any shift in photon energy is due to the vibrational modes of the molecule. Resonance Raman (RR) spectroscopy is a particular case, and involves exciting a sample at a wavelength within an absorption band of the sample being measured. The vibrational modes particularly associated with the electronic transition are selectively enhanced, so the RR spectrum can probe structural changes on electronic excitation. Specifically, the intensities of RR bands are directly related to the displacement between the ground and excited state potential energy surface minima along specific normal coordinates. Therefore it is possible to quantify the Raman spectrum and model the RR cross-sections as a function of excitation wavelength for the most intense bands simultaneously with the absorption spectrum; this is called RR intensity analysis (RRIA). From this analysis it is possible to model the shape of absorption spectra, thus providing the most appropriate combination of displacements between the ground and excited state potential energy surfaces, and transition dipole moments to describe the optical response [216].

Professor Sophia Hayes and her group are experts in RRIA analysis, and so we collaborated with them to investigate solutions of DPP-TT-T. The purpose of this work was to investigate the origin of the difference between high and low molecular weight DPP-TT-T, from the perspective of the vibrational modes in the material.

Figure 6.12 shows the RR spectra of dilute solutions of low and high molecular weight C3 DPP-TT-T (C3-16 and C3-99) in 1,2-dichlorobenzene and chloroform, excited at two different wavelengths (683 nm and 737 nm), both of which are in resonance with the main absorption band of the polymer. Interestingly, the relative intensities of the bands change significantly with excitation wavelength, suggesting contributions from different electronic transitions to the absorption spectrum.

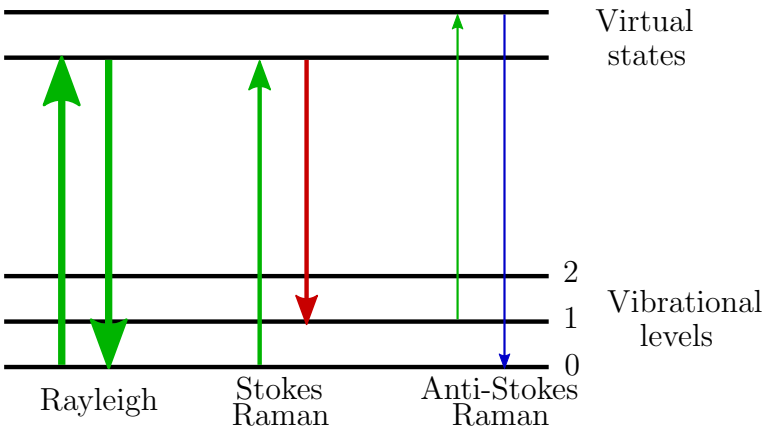


Figure 6.11: Schematic showing Rayleigh elastic scattering, and the two types of Raman scattering. Stokes Raman scattering results in the photon energy being down-shifted in energy, because the molecule relaxes to a vibrational level above the ground vibrational state. Conversely, anti-Stokes Raman scattering results in the photon energy being up-shifted in energy, because the molecule is excited from a higher vibrational state than the level it relaxes down to. The magnitude of Stokes scattering is greater than anti-Stokes, because the population of the ground vibrational state is larger than in higher vibrational states. Elastic scattering meanwhile is by far the dominant process. Indicated on the diagram are the ground state vibrational levels $\nu = 0 - 2$, and the virtual energy states.

Moreover, the analysis showed that the RR cross-sections and absorption spectra could not be fitted simultaneously with a single dipole-allowed electronic transition; such fits greatly overestimated the RR cross-sections (Figures 6.13 and 6.14). This behaviour is atypical and was not expected; other conjugated polymers can be well-modelled by a single electronic transition.

However, when a second electronic transition lying 160 meV above the first was introduced, the RR cross-sections were reproduced well (Figures 6.15 and 6.16), and the analysis was very sensitive to the position of this second transition. In fact, the second calculated electronic transition lies at around this energy, at around 170 meV above the first calculated transition for tetramers of DPP-TT-T (from Sheridan Few's calculations, see Figure 6.3). This second calculated transition is dark for linear oligomers because of the high symmetry of the oligomer, but moderately bright in curved (all-*cis*) oligomers with a transition dipole moment μ_{02} oriented perpendicular to the backbone.

From this analysis therefore, it appears that the high-energy shoulder observed experimentally in the absorption spectrum can be assigned to the sum of two contributions: the second vibronic peak of the first electronic transition, and the first vibronic peak of the second electronic transition for curved chain segments.

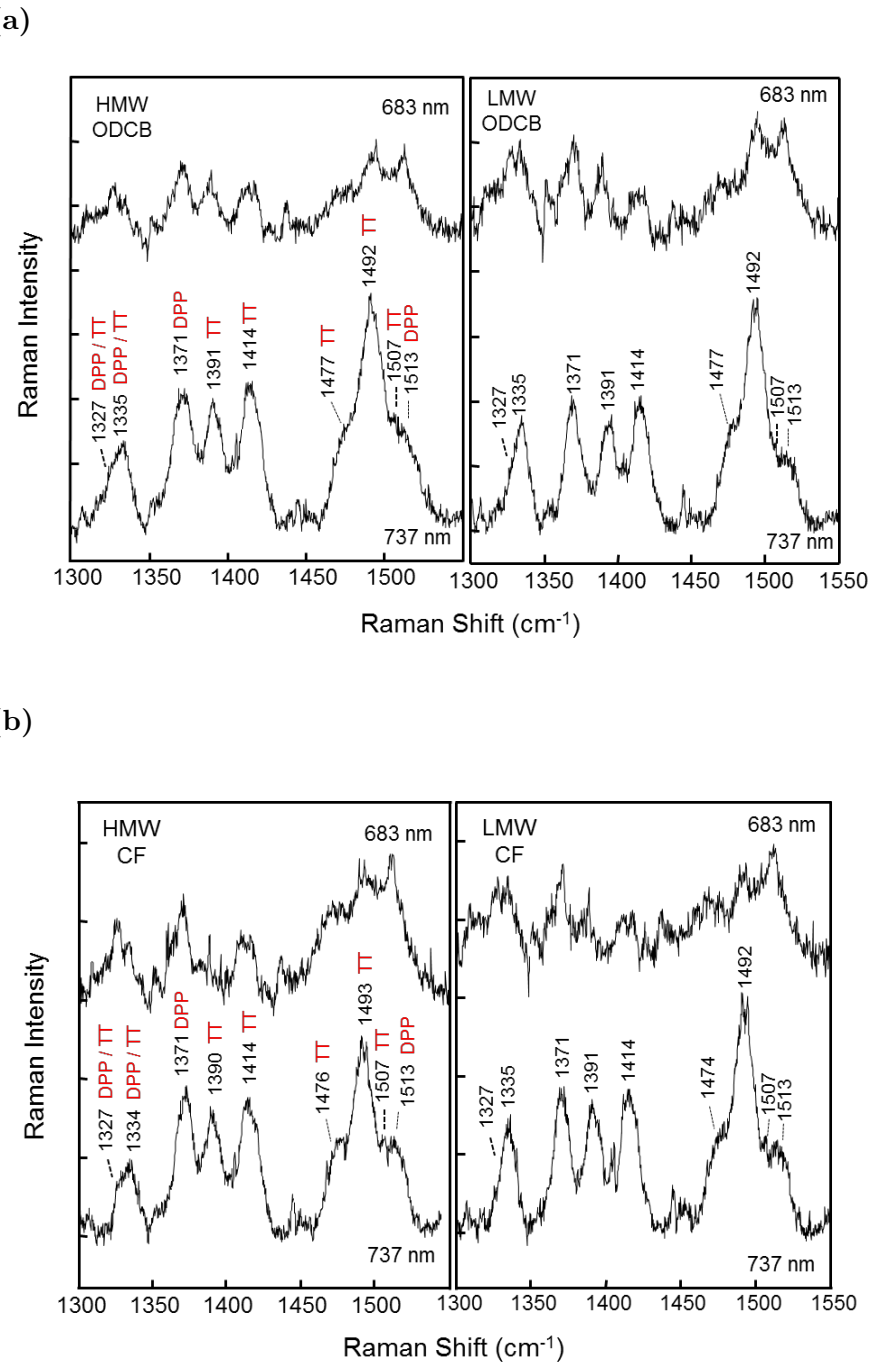


Figure 6.12: Resonance Raman spectra of dilute solutions of C3-99 and C3-16 polymers in (a) 1,2-dichlorobezene and (b) chloroform. Excitation was at 683 and 737 nm; both of these wavelengths are in resonance with the main absorption band of the polymer. Assignment of the bands was done with the aid of calculations of IR spectra of oligomers of the polymers and is indicated according to the part of the monomer they correspond to. This figure was prepared by Sophia Hayes and Galatia Pieridou and reproduced from [208].

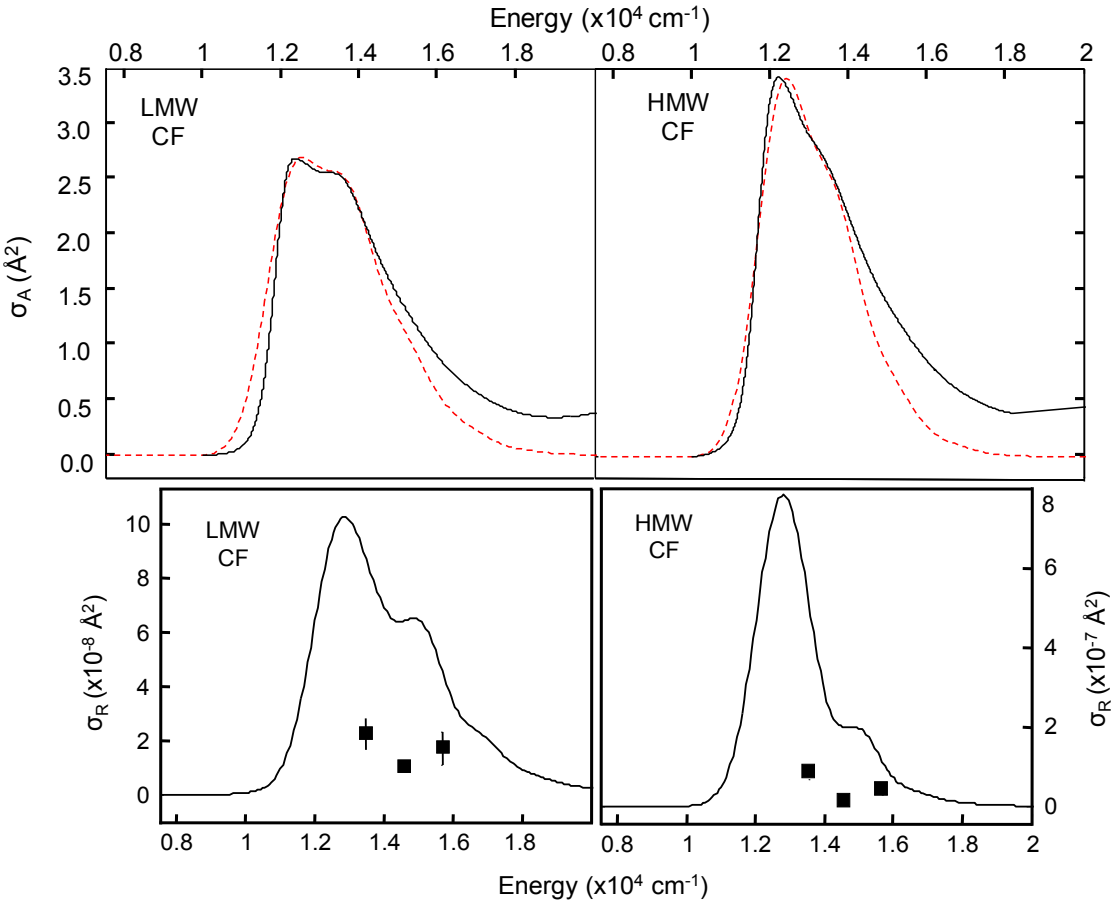


Figure 6.13: Resonance Raman intensity analysis (RRIA) of dilute solutions of high- and low-MW C3 polymer (C3-16 and C3-99) in chloroform, assuming only one electronic transition. Top row: experimental (solid black line) and calculated (dashed red line) absorption cross-sections σ_A. Bottom row: corresponding experimental (points) and calculated (solid line) Raman cross-sections (σ_R) as a function of excitation wavelength for the 1,492 cm^{-1} mode of LMW and HMW C3 polymer. The error bars are the standard deviation from three measurements of the absolute cross-section of each mode at each excitation wavelength. It is clear that when the magnitude of the absorption is fitted, the magnitude of the Raman cross-section is overestimated. Figure prepared by Sophia Hayes and Galatia Pieridou, and reproduced from [208]

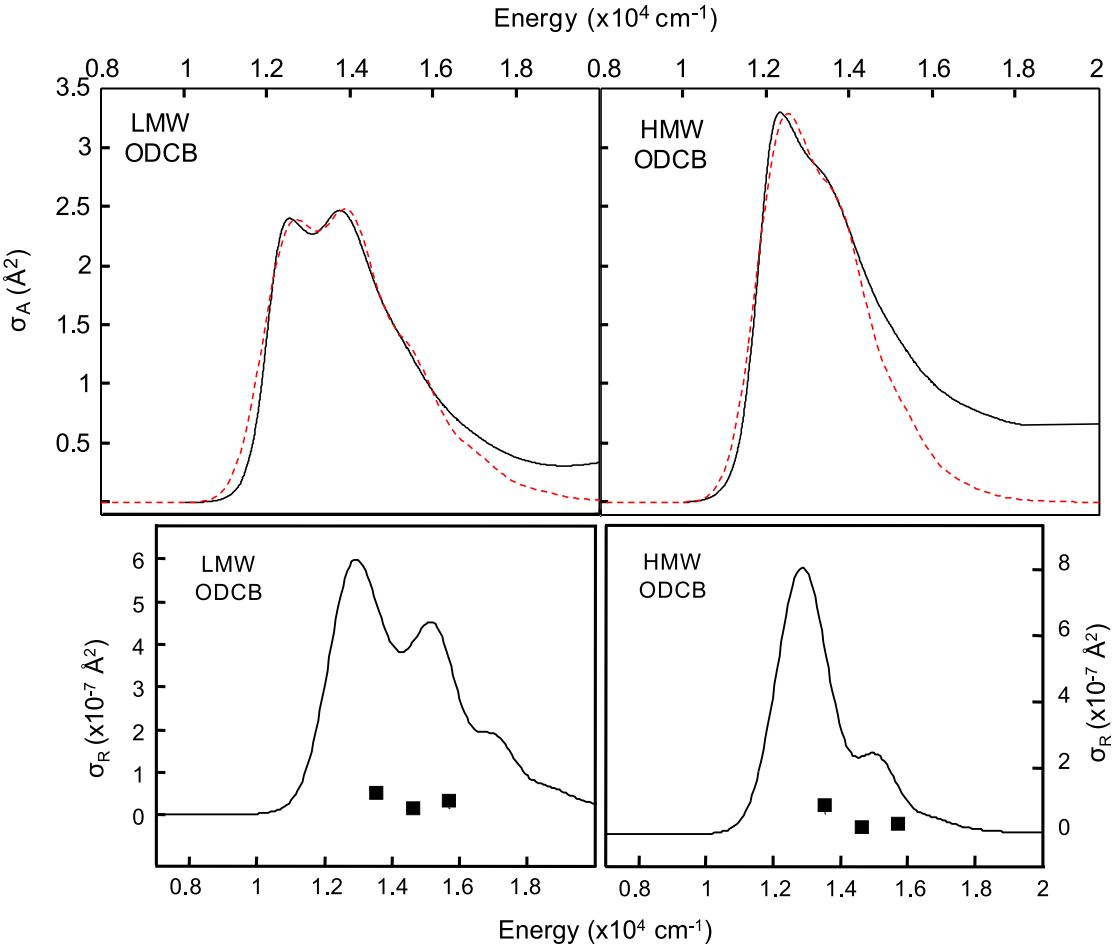


Figure 6.14: Resonance Raman intensity analysis (RRIA) of dilute solutions of high- and low-MW C3 polymer (C3-16 and C3-99) in 1,2-dichlorobenzene (ODCB), assuming one electronic transition. Top row: experimental (solid black line) and calculated (dashed red line) absorption cross-sections σ_{A}. Bottom row: corresponding experimental (points) and calculated (solid line) Raman cross-sections (σ_{R}) as a function of excitation wavelength for the 1,492 cm^{-1} mode. The error bars are the standard deviation from three measurements of the absolute cross-section of each mode at each excitation wavelength. It is clear that when the magnitude of the absorption is fitted, the magnitude of the Raman cross-section is overestimated. Figure prepared by Sophia Hayes and Galatia Pieridou, and reproduced from [208]

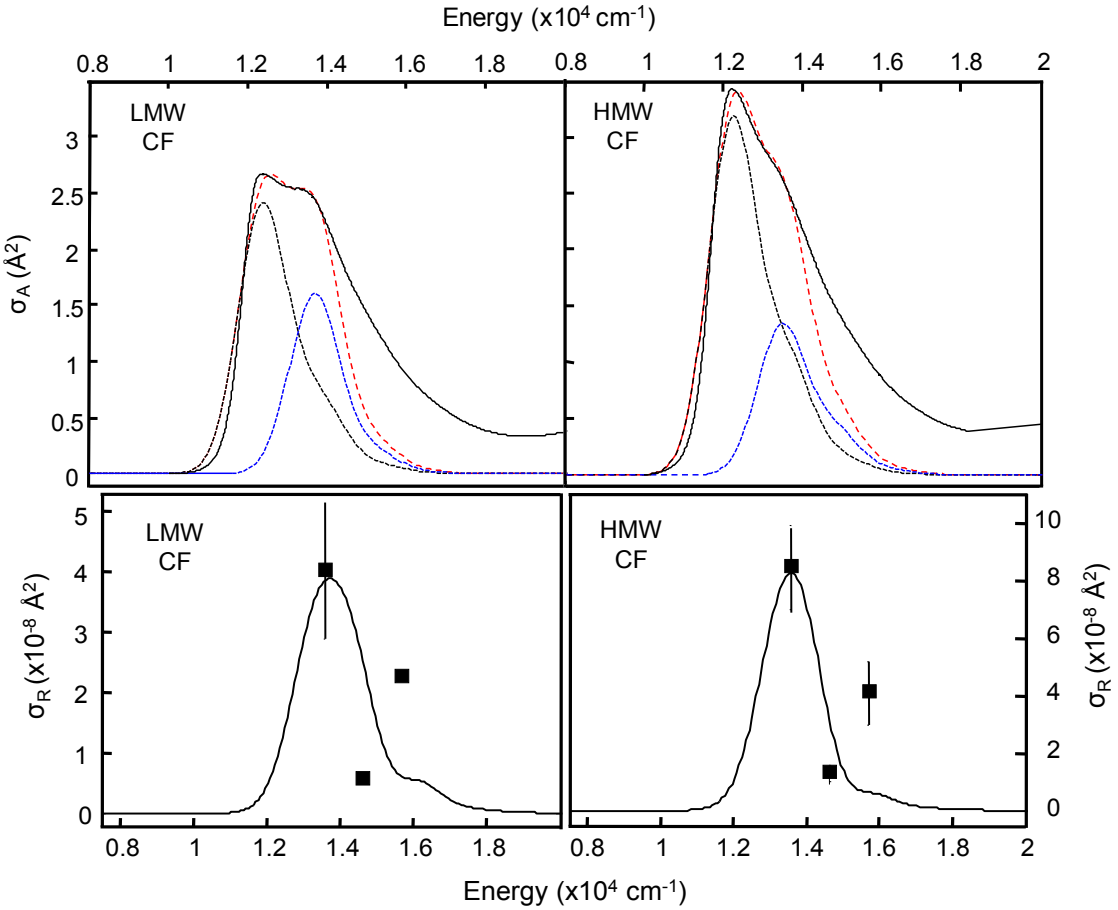


Figure 6.15: Resonance Raman intensity analysis (RRIA) of dilute solutions of high- and low-MW C3 polymer (C3-16 and C3-99) in chloroform, now assuming two electronic transitions at different energies. Top row: experimental (solid black line) and calculated (dashed red line) absorption cross-sections σ_A. The dashed black and blue lines represent the absorption spectra for the two transitions that contribute to the overall absorption band. Bottom row: corresponding experimental (points) and calculated (solid line) Raman cross-sections (σ_R) as a function of excitation wavelength for the 1,492 cm^{-1} mode. The error bars are the standard deviation from three measurements of the absolute cross-section of each mode at each excitation wavelength. Figure prepared by Sophia Hayes and Galatia Pieridou, and reproduced from [208]

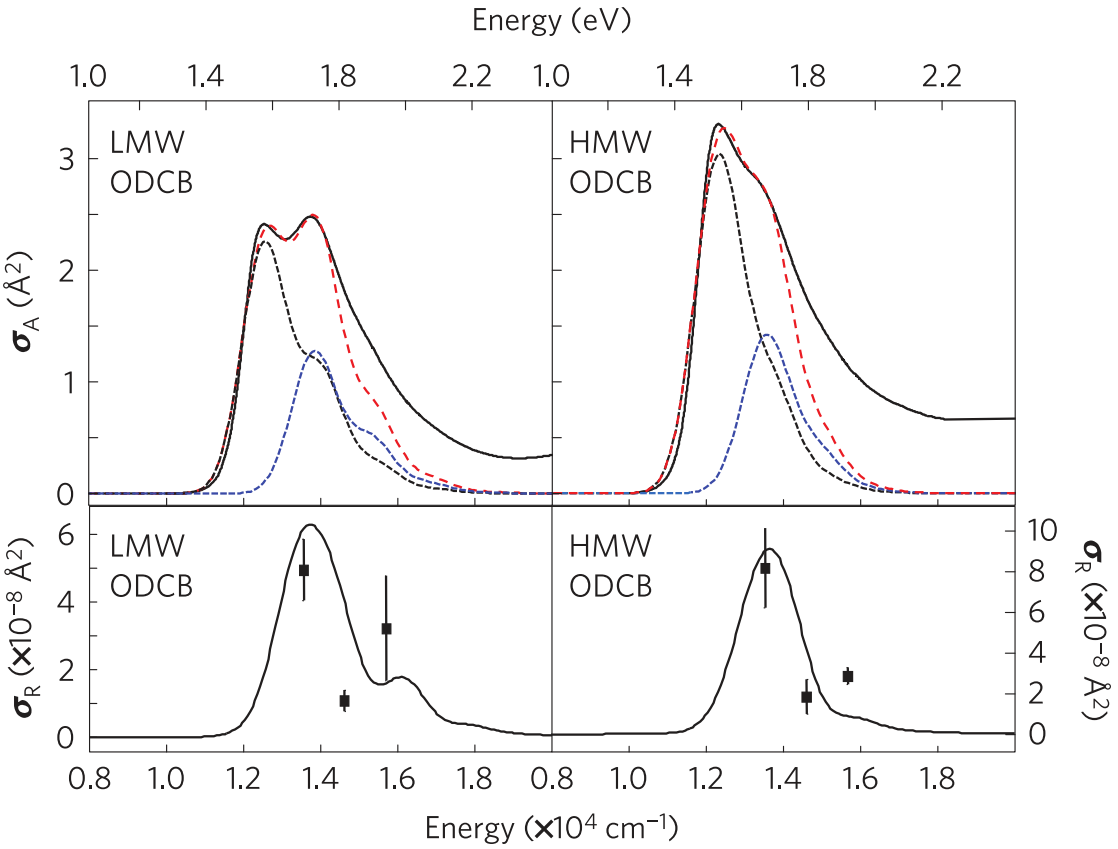


Figure 6.16: Resonance Raman intensity analysis (RRIA) of dilute solutions of high- and low-MW C3 polymer (C3-16 and C3-99) in 1,2-dichlorobenzene, assuming two electronic transitions. Top row: experimental (solid black line) and calculated (dashed red line) absorption cross-sections σ_A. The dashed black and blue lines represent the absorption spectra for the two transitions that contribute to the overall absorption band. Bottom row: corresponding experimental (points) and calculated (solid line) Raman cross-sections (σ_R) as a function of excitation wavelength for the 1,492 cm^{-1} mode. The error bars are the standard deviation from three measurements of the absolute cross-section of each mode at each excitation wavelength. Figure prepared by Sophia Hayes and Galatia Pieridou, and reproduced from [208]

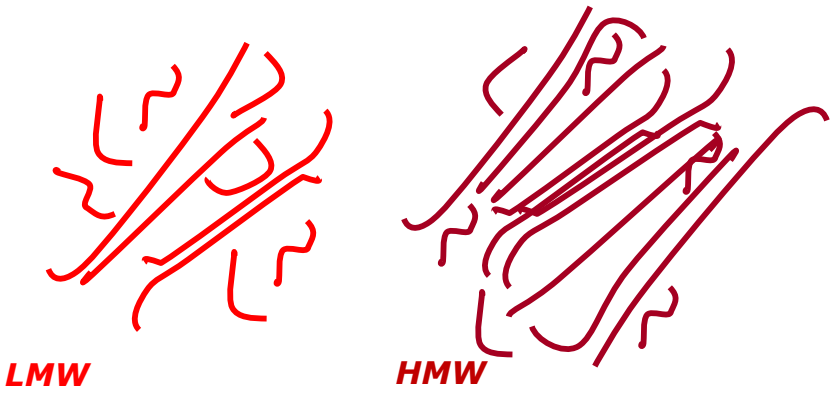


Figure 6.17: Schematic showing the proposed effect of molecular weight on DPP polymer conformation. The RRS data suggest that HMW polymer samples have a higher proportion of linear chains than LMW polymer samples. Schematic drawn by Jenny Nelson.

Both of these higher-energy contributions are expected to be stronger in curved oligomers [45, 215].

The analysis indicates that both electronic transitions, and therefore both linear (more *trans*) and curved (more *cis*) conformers, exist in both LMW and HMW samples in both CF and ODCB, but the fraction of linear conformers is relatively greater in the HMW samples (schematic shown in Figure 6.17), giving rise to the higher overall oscillator strength. The higher tendency of chains to adopt a linear conformation in the HMW case can be tentatively attributed to the increased strength of chain-chain interactions (which will be maximised for linear chains) over the chain-solvent interactions. This idea is consistent with the lower solubility of the longer chains. The hypothesis that chain-chain interactions are more important for higher MW is consistent with the stronger effect of solvent on the absorption spectrum for the LMW than the HMW polymer (Figure 5.19).

6.3.4 Case study: diketopyrrolopyrrole-based oligomers

In order to better understand length-dependent properties of conjugated polymers, it can be useful to study series of oligomers [197, 198]. To this end, I studied a DPP-based oligomer, whose length was systematically increased (Figure 6.18). The polymer, DPP-TPT, has been shown to give good solar cell efficiencies [217]. I measured the solution absorption of the oligomers dissolved in chlorobenzene. Figure 6.19 shows the absorption data normalised per π-electron. As expected, as the oligomer length increases, the absorption onset red-shifts due to the greater conju-

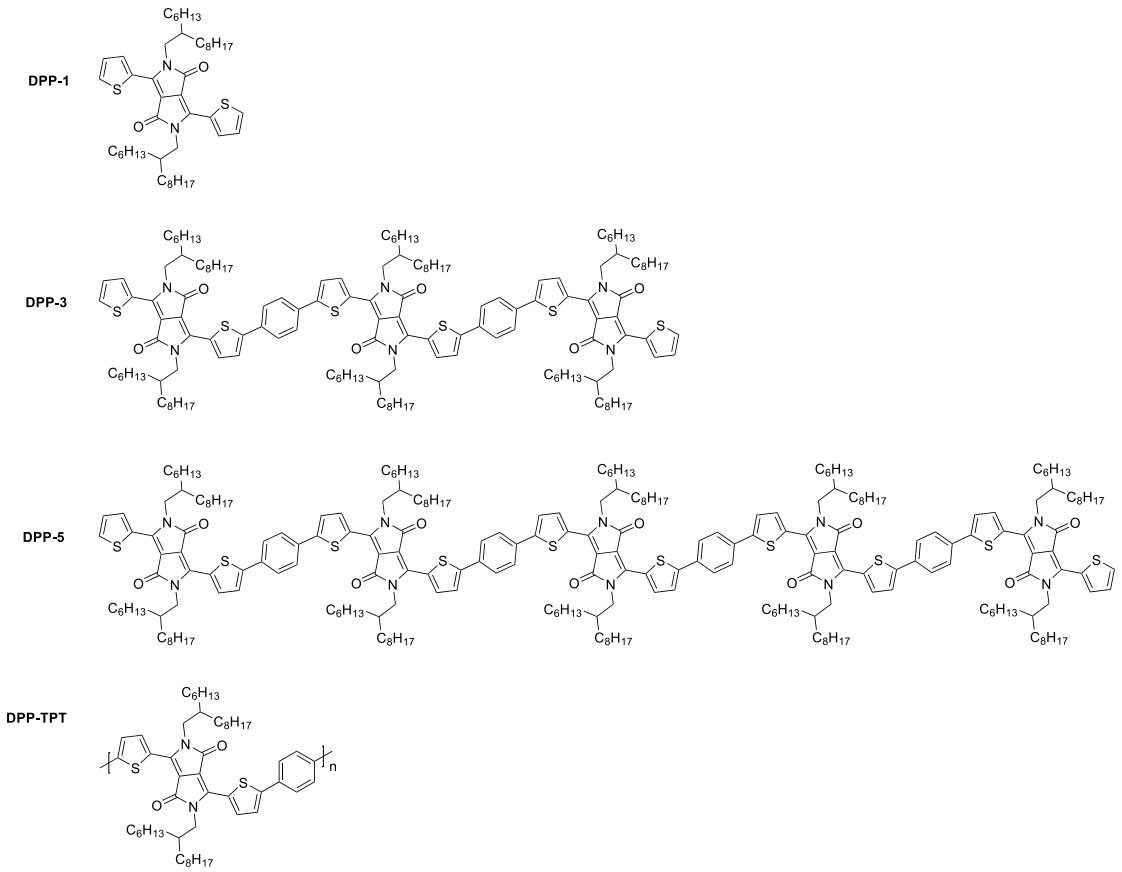


Figure 6.18: Chemical structures of DPP oligomers. DPP-1 is the monomer, DPP-3 is the trimer, DPP-5 is the pentamer and DPP-TPT is the polymer. Note that DPP-1 is different from the monomer of the polymer, missing a benzene ring in order to be symmetric, and similarly the oligomers only have linking benzene rings. Structures drawn by Anastasia Leventis.

gation length possible for longer structures. However the trend of the magnitude of absorption is unexpected and is not monotonic for the oligomers I measured.

Some authors have proposed the possibility of single chain folding in solution [218], and work is ongoing to measure DPP-2, -4 and -6, as well as complementary computational studies.

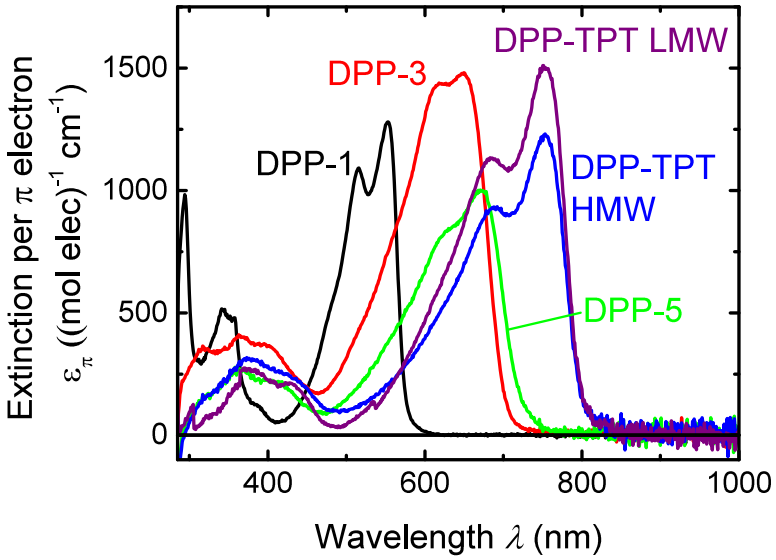


Figure 6.19: Solution UV-Vis absorption spectra for DPP oligomers and two different molecular weight batches of the DPP-TPT polymer. All materials were dissolved in chlorobenzene. The data are normalised per mole π-electron, in order to be able to compare between different size molecules.

6.4 Discussion

The results presented in this chapter illustrate how the spatial configuration of conjugated polymers, as well as the component moieties, affect the optical absorption. Persistence length is a simple metric which can be calculated with relatively little computational cost, and is therefore potentially very useful to the field with regards to improving light harvesting. To this end, it is helpful to consider the question of the limit to absorption for a conjugated polymer. According to the Thomas-Reiche-Kuhn rule (eq. (2.30)), the sum of the oscillator strength of conjugated polymers should converge on the number of electrons available in the system. Thus for the oscillator strength normalised per π-electron, the summed oscillator strength should converge to unity.

Figure 6.20a shows the calculated integral of oscillator strength as a function of photon energy for long oligomers ($120 < N_\pi < 165$) of a range of chemical structures. The first transition contributes the majority of oscillator strength in the visible. In every case, the integrated f reaches a value much less than unity in the visible, showing that most of the available oscillator strength for the π-system must reside in higher-energy transitions outside the visible range. The low excitation energy and relatively high oscillator strength of DPP-TT-T agree well with the trend shown by the experimental results in Figure 6.20b. Also shown in Figure 6.20b are plots of oscillator strength per atom for the conventional

inorganic semiconductors: silicon, germanium and gallium arsenide. Because the component atoms are, on average, tetravalent in these materials, the limiting oscillator strength per atom due to the valence electrons is four. The convergence of the data towards that limit shows that these inorganic materials achieve a much higher fraction of their limiting extinction within the visible region than do the organic semiconductors studied. This is possibly due to the greater crystallinity and hence higher spatial density of electrons, as well as the greater density of states due to the band structure. The low value of convergence for organic materials indicates that there is certainly room for improvement in terms of designing higher-absorbing conjugated polymers.

The DPP oligomers provide an extremely valuable test-case to understand in more detail the effect of chain length on absorption. Different factors are likely to dominate at different length scales, and the possibility of complementary calculations means that it should be possible to probe these factors in detail. Work is in progress to make a molecular dynamics model, which would allow simulation of the oligomer conformation, and subsequent assessment of the persistence length. If this is done alongside quantum chemical calculations, we could directly probe the effect of conformation on the magnitude of the oscillator strength. The principal advantage of studying oligomers as opposed to polymers is that there is no need to curtail the length of the chain to make the calculations manageable.

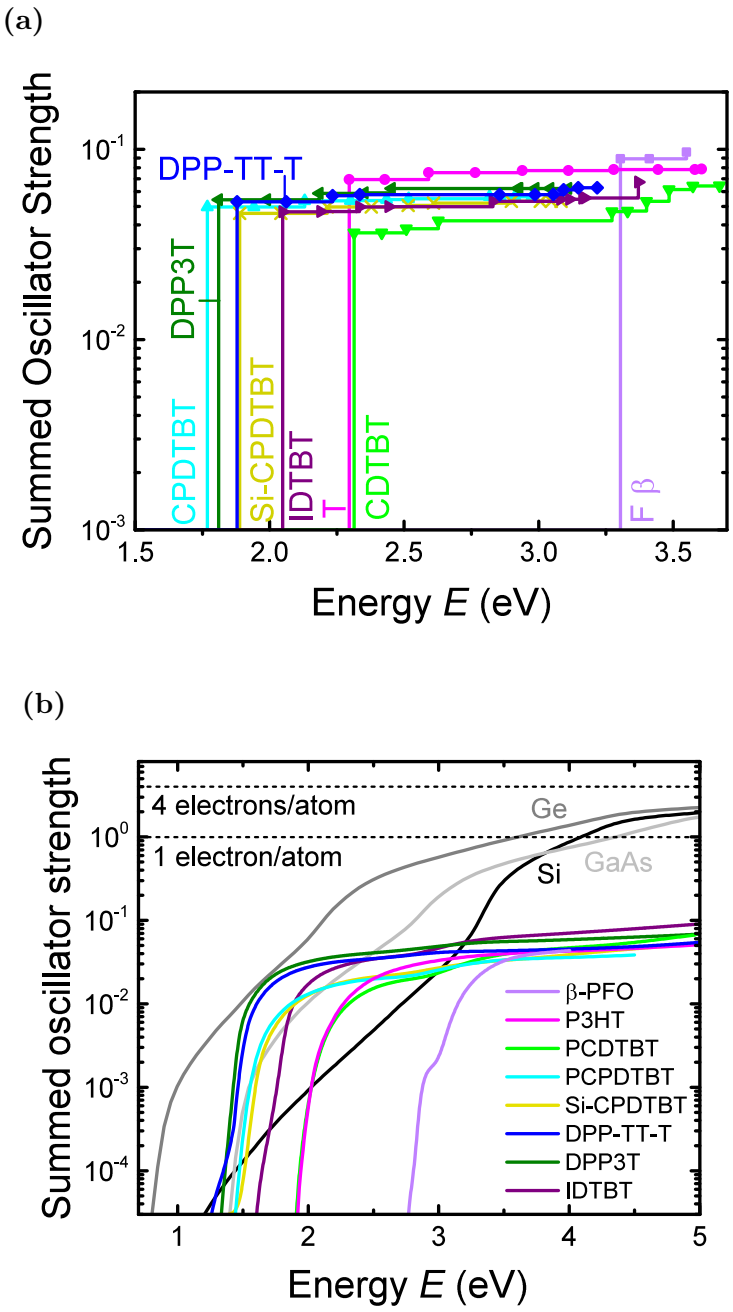


Figure 6.20: Calculated and experimental summed oscillator strength per π-system electron. (a) Calculated summed oscillator strength per electron in the π-system at increasing photon energies for oligomers in the all-trans conformation with $120 < N_\pi < 165$, using TDDFT and CAM-B3LYP/6-31g*. (b) Experimental summed oscillator strength per π-system electron for a range of polymers. The corresponding data for key inorganic photovoltaic materials (Si, Ge and GaAs) are shown for comparison.

6.4.1 Design considerations

The analysis using the Hecht equation in Section 5.4, and especially Figure 5.25 showed that, with a simple model, there is some advantage to be had in harvesting more light for solar cell applications, or for any application where it is beneficial to absorb light strongly in a thin layer. Therefore with the findings of this chapter, it is possible to derive some design considerations to target conjugated polymers which absorb visible light more strongly. Firstly, in order to make use of polymer's one-dimensionality, the transition dipole of the first transition should be directed along the polymer backbone, as in all polymers studied here [219]. Furthermore, use of units such as DPP, with a low π-π^* excitation energy and high oscillator strength can increase the overall oscillator strength of the polymer.

With the transition dipole directed along the polymer backbone, it is then beneficial to target relatively long monomers with high co-linearity of successive monomers. This results in the benefit shown in Figure 6.6, whereby the magnitude of the polymer transition dipole moment can be thought of to a certain extent as the sum of monomer transition dipole moments. Furthermore, it is advantageous to design the torsional potential to be strong and to favour the alternating *trans* monomer orientation, perhaps by the design of side-chains or side-groups to provide steric hindrance. By employing these design considerations, polymers can be designed such that their absorption is less sensitive to conformation, thus allowing their full potential to be realised.

In this vein, we propose that it can also be useful to exploit the competition between polymer-polymer and polymer-solvent interactions to maximise chain extension or association in solution. We have not investigated this question explicitly, merely finding that different solvents can result in different proportions of straight and curved chain segments. Traditionally in polymer science a good solvent will result in greater polymer chain extension than a bad solvent, and a study has found that solvation of conjugated polymers is principally due to dispersive interactions with the extended π system [209], thus implying that a solvent which maximises dispersive interactions will be most likely to result in extended polymer chains. Other studies have also found that the conformation of polymer chains in solution affect the morphology of thin-films [59, 220], thus confirming that the polymer solvation is an important factor to consider.

Another strategy might be to reduce the volume fraction taken up by solubilising side chains, thus increasing the concentration of visible-light chromophores. In practice, however, reducing the volume of side-chains may require non-solution processing techniques. It has been shown that it can be possible to solid-state

process conjugated polymers [221], which resulted in greater extinction coefficient but due to concomitant increase in n, the material had a higher reflectivity. This finding highlights a limiting factor when designing optical cavity devices: since a greater extinction coefficient often results in greater variation of the refractive index n, the design of the optical device, with regards to other layers in the device, becomes very important.

6.5 Conclusion

The examples of DPP-TT-T, DPP3T and C8-IDTBT show that, by enhancing the coupling of a conjugated polymer to light through extended persistence length, it can be possible to pull more of the available oscillator strength into the visible region. Our studies indicate several design considerations to maximise this effect: namely, to target relatively long monomers with high co-linearity of successive monomers; to design the torsional potential to be strong and to favour an alternating (*trans*) monomer orientation; to achieve low transition energies by using components with low π-π^* excitation energy and high oscillator strength, such as the DPP unit; and to exploit the competition between polymer-polymer and polymer-solvent interactions to maximise chain extension in solution. By employing these design considerations, our results indicate that polymers can be designed such that their absorption is less sensitive to conformation, thus allowing their full potential to be realised. Exploiting these aspects, along with usual considerations such as charge transport, could open the way to significant improvements in device performance, as shown here in the case of solar cells. The caveat to this is that care must be taken in the design of the optical cavity to ensure that reflection is minimised, much in the same manner as for inorganic solar cells.

Thus far, the conjecture that high-absorbing polymers have high persistence lengths in solution has not been experimentally verified. The persistence length is a difficult quantity to measure experimentally, but it can be possible either using small angle neutron scattering [213] or via measurements of the intrinsic viscosity [211, 222]. Work is underway to attempt to determine the persistence length of some of the polymers studied in this chapter.

Meanwhile, initial studies of a series of DPP-based oligomers has provided some very interesting results. Particularly of interest is the lack of monotonic rise in absorption strength per π-electron with oligomer length; currently the most likely cause is the conformation of the molecules in solution, and work is underway to acquire more experimental data and calculations to further probe the system.

Table 6.4: Molecular weights of C8-IDTBT and DPP3T polymer fractions studied. M_n and M_w are the number- and weight-average molecular weights respectively, and PDI is the polydispersity index.

Polymer	M_n ($\mathrm{kg\,mol^{-1}}$)	M_w ($\mathrm{kg\,mol^{-1}}$)	PDI
C8-IDTBT-2	459	551	1.2
C8-IDTBT-3	242	460	1.9
C8-IDTBT-4	144	346	2.4
C8-IDTBT-7	52	151	2.9
C8-IDTBT-8	43	168	3.9
DPP3T	151	484	3.2

6.6 Experimental Details

The data shown in Figure 6.1 were collected from the literature and his own measurements by Mariano Campoy-Quiles. The assorted references for each data point are tabulated in Table 6.5.

DPP3T was purchased from Solarmer while C8-IDTBT was synthesised and fractionated by Hugo Bronstein while a member of Iain McCulloch's group at Imperial College; the synthesis was done according to [183] and was previously reported in [177]. The molecular weights for each material showed in this chapter are displayed in Table 6.4. The solution UV-Vis and ellipsometry measurements were performed exactly as described in Chapter 5; again I did the solution measurements and made the films for ellipsometry while Mariano Campoy-Quiles did the ellipsometry measurements. Figure 6.10 shows data for comparably thin films (30-50 nm), and a weak dependence of the maximum κ on molecular weight is observed in the case of IDTBT. For each material Mariano analysed multiple films with different thicknesses; DPP3T showed no dependence of the complex refractive index on film thickness, whereas a significant degree of variation was observed in higher molecular weight IDTBT films (Figure 6.21).

In light of the thickness dependence of the IDTBT complex refractive index and previous work showing anisotropy in a very similar material [178], Mariano attempted to fit the ellipsometry data using an anisotropic model. The resulting fits were not an improvement on the data fit using an isotropic model for the thin films, and a possible moderate improvement was observed for the thick films which does not affect the trend of the data shown in Figure 6.10.

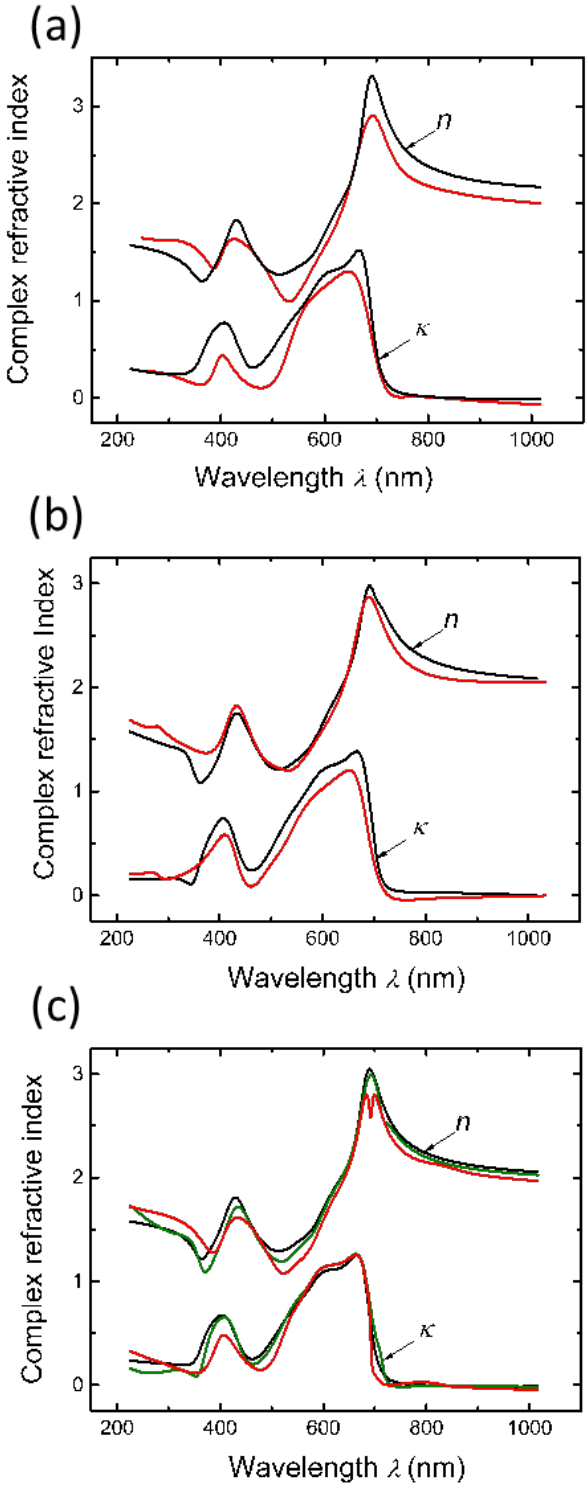


Figure 6.21: Thickness dependence of the VASE-derived complex refractive index for C8-IDTBT thin films. (a) C8-IDTBT-HMW, (b) C8-IDTBT-MMW, and (c) C8-IDTBT-LMW. In every case the thinnest film is represented by black lines, and the thickest by red lines. For the case of C8-IDTBT-LMW, an intermediate thickness is shown by a green line. Data collected and figure prepared by Mariano Campoy-Quiles.

Table 6.5: Materials and maximum extinction coefficients from the literature, as shown in Figure 6.1.

Material abbreviation	Reference	Wavelength of maximum absorption λ_{max} (nm)	Maximum extinction coefficient κ_{max}
PFO	[223]	370.6	0.826
F6	[223]	370.6	0.824
DowRed F	[223]	455	0.577
F8BT	[223]	461.1	0.675
F8DP	[223]	376.6	0.870
P3HT	[173]	521.4	0.960
PFO-β	[173]	375.6	0.960
SC005	[224]	370.6	0.935
SC006	[224]	373.6	0.802
SC007	[224]	382.7	0.988
SC008	[224]	364.6	1.022
SC010	[224]	370.6	0.924
TFMO	[208]	382.7	0.670
P3BT	[208]	503.3	0.909
IsoindigoD16B	[208]	615	0.85
APFO3	[225]	535	0.555
APFOGreen9	[226]	779	0.403
TQ1	[227]	617.2	0.554
Si-PCPDTBT	[87]	678.3	0.907
PCPDTBT	[228]	683.9	0.937

Continued overleaf

Table 6.5: (cont.) Materials and maximum extinction coefficients from the literature

Material abbreviation	Reference	Wavelength of maximum absorption λ_{max} (nm)	Maximum extinction coefficient κ_{max}
PCDTBT	[228]	549.5	0.945
MEHPPV	[229]	490	0.7
P3OT	[230]	528	0.6
P3OT	[231]	528	0.25
NDA	[232]	375	0.15
APFOG1	[233]	813	0.41
APFOG2	[233]	625	0.18
LPPP	[234]	475	0.35
Pentacene	[235]	670	0.45
Perfluoropentacene	[235]	708	0.35
poly(arylenephenylene)s P1	[236]	420	0.45
poly(arylenephenylene)s P2	[236]	404	0.375
poly(arylenephenylene)s P3	[236]	456	0.35
poly(arylenephenylene)s P4	[236]	475	0.3
poly(arylenephenylene)s P5	[236]	460	0.6
F8BT	[237]	460	0.6
OC1C10-PPV	[237]	525	0.85
PFB	[238]	390	0.45
TFB	[238]	390	0.55
PTB7	[239]	620	0.744

The RR data was collected and analysed by Sophia Hayes and Galatia Pieri-

dou on dilute solutions ($\sim 5.5 \times 10^{-5}$ M - 6.5×10^{-5} M) of low- and high-MW batches of DPP-TT-T C3 (C3-16 and C3-99 respectively), prepared in chloroform (HPLC, 99.9%, Aldrich) and 1,2-dichlorobenzene (HPLC, 99.9% Aldrich), which were used as received. The exact concentration of each DPP-TT-T solution was obtained from the ultraviolet-visible spectrum (Shimadzu), using the pseudo molar extinction coefficient of DPP-TT-T at high MW (C3-99) in chloroform at 823 nm (90×10^3 l mol^{-1} cm^{-1}) and in 1,2-dichlorobenzene at 811 nm (85×10^3 l mol^{-1} cm^{-1}). The pseudo molar extinction coefficient of low-MW DPP-TT-T (C3-16) in chloroform was 70×10^3 l mol^{-1} cm^{-1} at 807 nm and in 1,2-dichlorobenzene was 65×10^3 l mol^{-1} cm^{-1} at 796 nm.

The absolute resonance Raman (RR) intensities of DPP-TT-T for the two molecular weights dissolved either in chloroform or 1,2-dichlorobenzene were measured with excitation at 636.8, 682.9 and 737.8 nm. The 682.9 and 636.8 nm excitation wavelengths employed in the RR experiments were produced by Raman shifting the second and third harmonics from a Q-switched Nd:YAG laser (PRO-230, 30 Hz, Spectra Physics) at 532 and 355 nm, respectively, in an in-house-built 1 m stainless-steel tube containing H_2 gas at 1.5 bar. The 737.8 nm excitation wavelength was produced by Raman shifting the fundamental from a Q-switched Nd:YAG laser (Lab-190, 30 Hz, Spectra Physics) at 1,064 nm, in a 1 m stainless-steel tube containing H_2 gas at 40 bar (Light Age). The excitation light was focused into a spinning cell consisting of an EPR Suprasil tube (diameter: 4 mm) attached to a rheostat-controlled motor for choice of rotation speed. Use of the spinning cell prolonged the lifetime of the samples. Modest excitation energies ($\sim$ 15 µJ per pulse) were employed to avoid decomposition of the sample. The Raman-scattered light was collected in a backscattering geometry and delivered to a 0.75 m focal-length Czerny-Turner spectrograph, equipped with a 1,200-grooves mm^{-1} holographic grating. The slit width was set to 100 µm, providing a 2 cm^{-1} spectral resolution at the wavelengths used in this work. The scattered light was detected by a thermoelectrically cooled 1340 × 400 pixel, back-illuminated deep depletion CCD detector (PIXIS-XB:400 BR, Princeton Instruments). Each spectrum presented here is the accumulation of 12-24 10 minute spectra. Frequency calibration of the spectra was accomplished using toluene. In the calculation of the absolute RR cross-sections, the 1,002 cm^{-1} mode of toluene (9.4 M) was used as an external standard.

The DPP oligomers were dissolved in chlorobenzene and heated overnight to ensure full dissolution. The UV-Vis spectra were taken as described previously.

Chapter 7

Understanding the LUMO-LUMO offset required for charge generation

7.1 Abstract

This chapter addresses one of the primary energy loss mechanisms in organic photovoltaics: the need for a type II heterojunction and the concomitant energy offsets between the donor and the acceptor in bulk heterojunction blends. Reducing the offset required is desirable for higher photovoltage, but must not then result in a loss of photocurrent available. The work presented in this chapter examines two sets of similar polymer:fullerene blend systems, in which the polymer LUMO and that of PCBM are approximately aligned, leading to a zero LUMO-LUMO offset. I use another acceptor, a ketolactam fullerene with frontier energy orbitals approximately 200 meV deeper than those of PCBM, to probe the energy offset required for efficient charge generation. With a combination of device data and spectroscopy, I determine that polymer exciton splitting is indeed the limiting step in the polymer:PCBM blends, and by replacing PCBM with the ketolactam, the polymer excitons can contribute current to the external circuit.

Acknowledgements

As ever my research would not be possible without materials; for the work in this chapter I am grateful to Dr Bob Schroeder for making BTT-DPP while a member of Prof Iain McCulloch's group in the Chemistry department of Imperial College, and to Kealan Fallon in Dr Hugo Bronstein's group in the Chemistry department

of University College London for making INDT-S. Furthermore, I am indebted to Solenne BV for providing the ketolactam and giving me the opportunity to work with it. Dr Mariano Campoy-Quiles did the ellipsometry measurements and analysis of the BTT-DPP-based films, as well as the ketolactam and various other interlayer materials. He also helped teach me how to do ellipsometry myself; I am grateful to StableNextSol for funding a Short-Term Scientific Mission which enabled me to travel to Barcelona to learn the technique in person. Dr Stoichko Dimitrov helped with some initial transient absorption spectroscopy measurements and invaluable discussions while a member of Prof James Durrant's group at Imperial College; later on I was lucky enough to collaborate with Dr Artem Bakulin and his student Tom Hopper (Imperial College, Chemistry), and Dr Tracey Clarke (University College London, Chemistry) who did the pump-push photocurrent and transient absorption spectroscopy measurements respectively. In addition, a summer student Anna Jungbluth, supervised by Dr Andrew Telford in my group, was an invaluable help and carried out electrical measurements of INDT-S devices shown here. And last but not least, Prof Thomas Kirchartz is responsible for the initial idea of using ketolactam to probe the BTT-DPP system which was the springboard for this project.

7.2 Introduction

The energy offset between the polymer and the acceptor frontier orbitals in bulk heterojunction solar cells represents a significant loss in electrochemical potential energy, which is however necessary for efficient charge separation (Section 2.5.2). Therefore it is of considerable interest to reduce this loss, thereby increasing the available voltage, while maintaining sufficient free charge generation. However since the precise mechanism of charge separation is not well understood, it is difficult to design systems which achieve this balance.

Focussing on polymer:fullerene solar cells, the majority of the free charges originate from polymer excitons, since conjugated polymers absorb light more strongly in the visible than fullerenes, especially if the fullerene is a C_{60} derivative. Therefore the pertinent energy offset is that between the LUMOs of the two materials in the blend. This LUMO-LUMO offset is the focus of this chapter. I should note here that another pertinent energy level is the triplet level of the polymer, and its position relative to the CT state [240]. Determination of these energy levels is possible with calculations of the electronic structure; this chapter however focuses on the experimental results and so I do not present any such calculations.

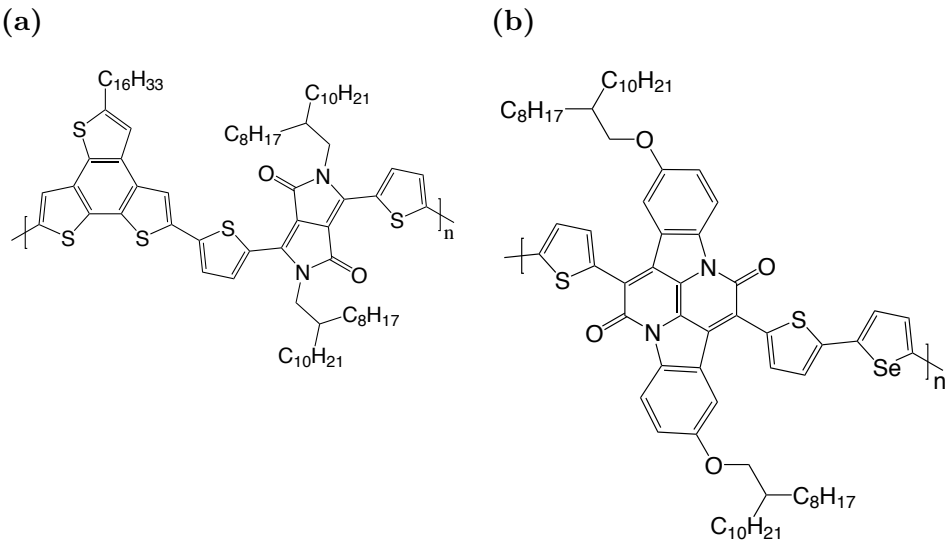


Figure 7.1: Chemical structures of (a) BTT-DPP and (b) INDT-S. BTT-DPP was made by Dr Bob Schroeder when he was a member of Prof Iain McCulloch's group at Imperial College, and INDT-S was made by Kealan Fallon, a member of Dr Hugo Bronstein's group at University College London.

Some time ago Stoichko Dimitrov (Chemistry department, Imperial College) observed wavelength-dependent charge generation in a blend of BTT-DPP (see Figure 7.1a for structure) and $PC_{70}BM$ [241], whereby the blend generated more current from short wavelength light than long wavelength light, as determined by the external quantum efficiency spectrum. Dimitrov et al. also measured the polymer polaron yield as a function of excitation wavelength using transient absorption spectroscopy (TAS). They found that both the polymer polaron yield after 0.2 µs and the external quantum efficiency of the solar cell tracked the absorption spectrum of the fullerene (Figure 7.2). Therefore their hypothesis was that the current generation was predominantly from the separation of fullerene excitons, enabled by a sufficient HOMO-HOMO energy offset, whereas the polymer excitons were unable to separate due to an insufficient LUMO-LUMO energy offset, which was estimated to be 0 eV.

Another study investigated further this current generation energy dependence, specifically in the spectral region dominated by polymer absorption [242]. For this study, BTT-DPP was blended with PCBM, instead of $PC_{70}BM$, in order to reduce the absorption spectral overlap of the two components. A new technique was used, which is called pump-push spectroscopy, and involves exposing a device to a visible light pump pulse, followed by, after a certain delay, an IR push pulse (Figure 7.3b). The wavelength of the second pulse is chosen such that it is selectively absorbed

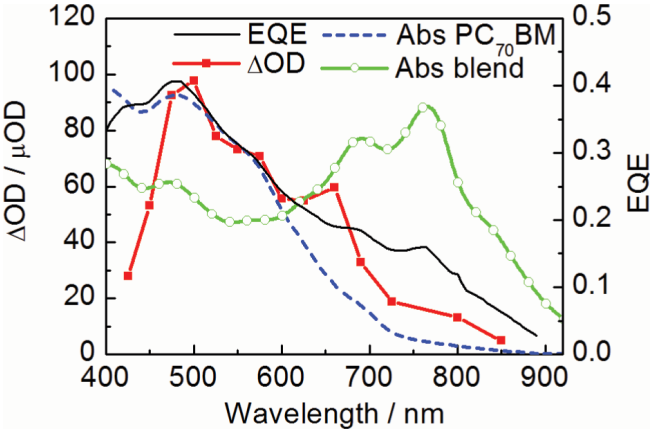


Figure 7.2: Transient absorption excitation spectrum (TES, ΔOD) (red line, filled squares), and external quantum efficiency (EQE) (black line) of BTT-DPP:$PC_{70}BM$ (1:1 w/w) blends. The TES experiment was done on blend films, whereas the EQE measurement was done on blend devices with an ITO/PEDOT:PSS/blend/Ca/Al architecture. Also shown are the blend (green line, open circles) and $PC_{70}BM$ (dashed blue line) film absorbances. The TES data were collected using a 1150 nm probe, and the signal was collected at a 0.2 μs time delay. This figure was reproduced with permission from [241], copyright 2012 American Chemical Society.

by polymer hole polarons, as opposed to the neutral polymer. To the extent that these hole polarons are bound at the interface, the additional push pulse activates higher states within the bound state manifold, resulting in hot polarons which may then be able to fully charge separate and result in current. The experiment measures the relative increase in external current, $\delta J/J$, which is proportional to the ratio of bound charges to free charges.

Figure 7.3b shows that the BTT-DPP blend exhibits a significantly higher ratio of bound charges upon excitation at 900 nm, as opposed to 680 nm. This result therefore suggests that in this blend, the polymer exciton must have excess energy if it is to fully dissociate into separated charges. Figure 7.4 shows the proposed energy level diagram derived from this work. The pump-push result is supported by the TAS data, which indicates that there are more free charges after polymer excitation at shorter wavelengths than longer wavelengths (Figure 7.3a). Photoluminescence was also measured which shows some PL quenching which is independent of excitation wavelength, although the range of wavelengths tested is much smaller than in the other experiments. This result means that excess excitation energy does not affect the fraction of polymer excitons which reach the fullerene interface to become bound CT states. From this experiment, it is difficult to determine the precise nature of the bound states freed by the pump-push experiment. They could be polymer-only intramolecular bound CT states,

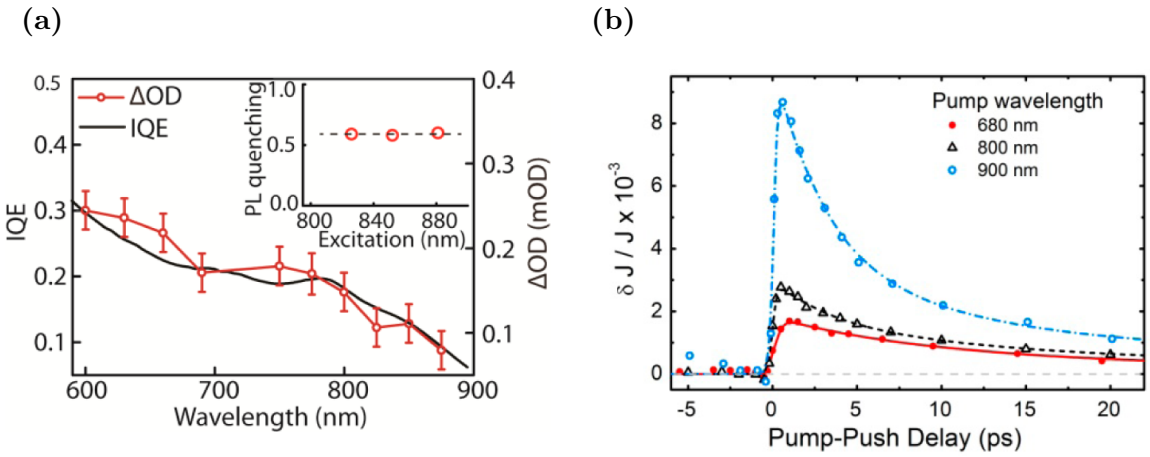


Figure 7.3: BTT-DPP blend spectroscopy data from previous studies. (a) Transient absorption excitation spectrum (TES) (red line, open circles) and internal quantum efficiency (black line) of BTT-DPP:PCBM (1:1 w/w) blend films and devices, respectively. Inset: PL quenching of the same blends. The data were collected using a 1150 nm probe, and the signal was collected at a 0.2 µs time delay. (b) Pump-push photocurrent measurements of BTT-DPP:PCBM devices, for pump pulse wavelengths of 680 nm (red circles), 800 nm (black triangles) and 900 nm (blue open circles). In each case, the push pulse wavelength was 2200 nm. The lines are exponential fits convoluted with a 200 fs response function. The devices in (a,b) had an ITO/PEDOT:PSS/blend/LiF/Al architecture. These figures were reproduced with permission from [242], copyright 2012 American Chemical Society.

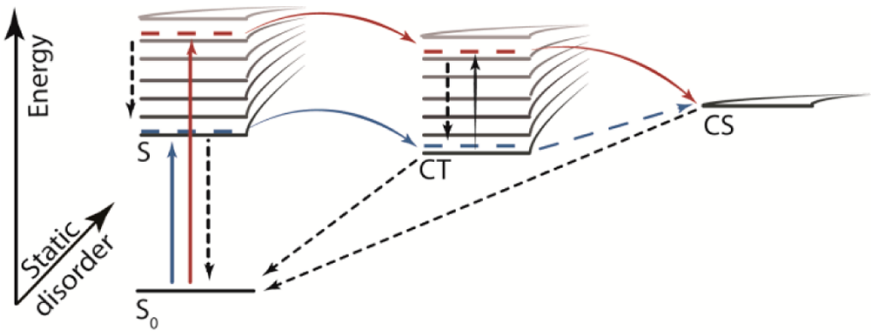


Figure 7.4: Proposed energy level diagram from a previous study. Shown are the polymer singlet manifold (S), the charge transfer state manifold (CT) and the separated charges. The blue line shows the case of low energy excitation of the polymer, while the red line shows the case of high energy excitation. The proposed model is that the energy of the singlet affects which energy levels in the CT state manifold are accessible, and that only high energy CT states are able to efficiently generate separated charges. The upwards arrow in the CT state manifold represents the push in the pump-push experiment. This figure was reproduced with permission from [242], copyright 2012 American Chemical Society.

or exciton-CT hybrid states [110], or interfacial CT states. Put another way, it is not clear from these experiments whether the excess energy requirement is a consequence of the density of states of the polymer itself, irrespective of the fullerene, or of the blend at the interfaces.

7.2.1 Research question

The previous studies proposed that in a BTT-DPP blend with PCBM or $PC_{70}BM$, the polymer singlet must have excess energy if it is to result in separated charges. It was proposed that the lack of LUMO level offset between the blend components was the cause of this energy requirement, but since no other blends were available this could not be tested. Therefore the purpose of my work was to test this hypothesis that the LUMO-LUMO energy offset is to blame for the lack of efficient charge generation from polymer excitons. To do this, I made solar cells and films using a ketolactam (KL) (Figure 7.5) instead of PCBM. The frontier energy orbitals of KL are both about 170 meV deeper than those of PCBM (see Table 7.1), but the electronic structure is otherwise fairly similar, and so this molecule provides a good opportunity to test the effect of deeper energy levels without changing the absorption. Figure 7.6 shows a schematic of the proposed model, whereby deeper energy orbitals for the case of KL result in a deeper CT state manifold, such that the polymer singlet is degenerate with a more delocalised CT state than if the

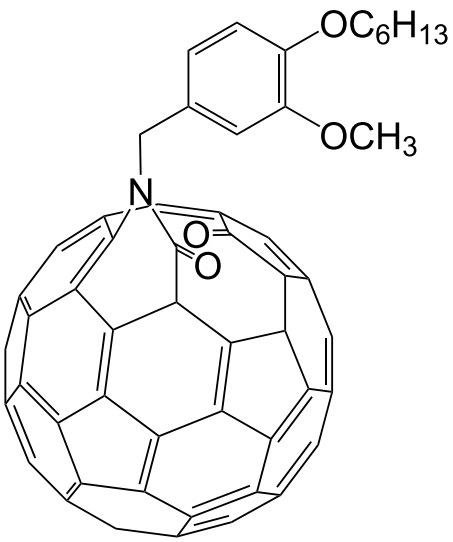


Figure 7.5: Chemical structure of ketolactam (KL), an acceptor with frontier energy orbitals about 170 meV deeper than those of PCBM. KL was kindly provided by Solenne BV.

Table 7.1: PCBM and KL cyclic voltammetry results. Both measurements were done in the same set-up, using ferrocene as the reference at approximately +0.4 V vs NHE, which in turn is approximately +4.44 V. The LUMO level is determined from these data by taking IP $= -(\text{NHE} + E_{1/2}(\text{Fc/Fc}^+) + E_{1/2}(\text{Fc/Fc}^+))$. Data provided by Dr Alex Sieval at Solenne BV; experimental set-up is as described in [244].

Fullerene	$E_{1/2}$ vs. Fc/Fc+ (V)	IP (eV)
PCBM	-1.08	-3.75
KL	-0.91	-3.92

acceptor energy levels are higher in energy, when the polymer singlet might be degenerate with the lowest, and more localised, CT state.

This study is similar in scope to a previous study [243], which also studied the effect of changing the acceptor energy levels on overall charge generation. My work however specifically examines the wavelength-dependence of charge generation, comparing spectral regions where the polymer is excited versus regions where the fullerene is predominantly excited. I also wanted to probe the nature of the states generated at very short times after excitation, in order to identify which states are involved in efficient charge generation.

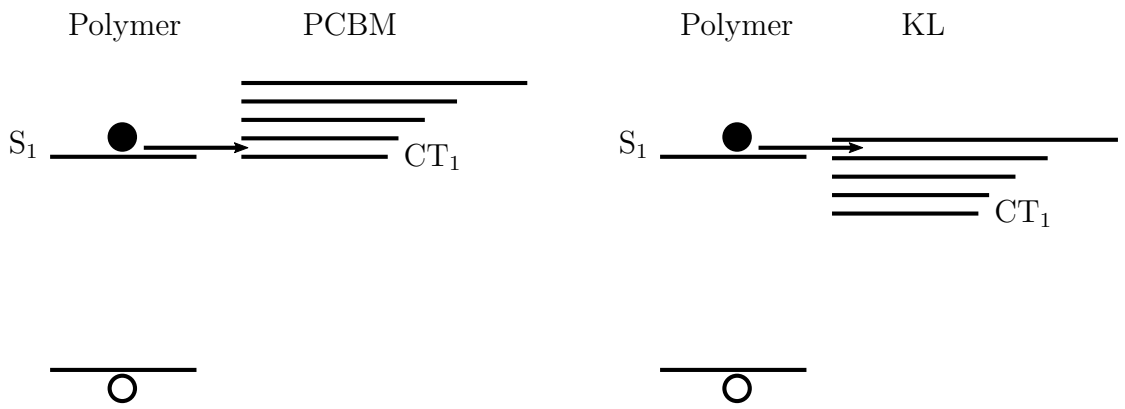


Figure 7.6: Schematic of the proposed effect of replacing PCBM by KL, with respect to the energetics of the charge transfer state manifold. The longer lines at higher energies in the CT state manifold represent states with greater delocalisation, which are more likely to result in charge separation than the localised states at the bottom of the manifold. Deeper acceptor energy levels will tend to result in a deeper CT state manifold, thus the difference between the KL and PCBM cases.

7.2.2 Research approach: investigating another polymer with possible excitation wavelength dependence of charge generation

In order to generalise my findings, I also investigated another polymer which exhibited a similar external quantum efficiency profile to BTT-DPP [245] (Figure 7.7). This polymer is called indolo-naphthyridine-6,13-dione thiophene-co-selenophene (INDT-S), and its structure is shown in Figure 7.1b; the polymer was made by Kealan Fallon in Dr Hugo Bronstein's group at University College London. The HOMO and LUMO levels have been determined to be -4.99 eV and -3.77 eV respectively, meaning that there is a +0.02 eV nominal LUMO-LUMO offset with PCBM. I should note that there are significant sources of error in the determination of these frontier energies. Firstly, the cyclic voltammetry which was used to determine the fullerene redox potentials was done in solution. Since care was taken to perform the measurement using the same experimental set-up, the relative difference between the two materials should be approximately reliable. However since in OPV devices, the fullerene is in the solid state, there may be some differences from the solution case, which may be dependent on chemical structure. Cyclic voltammetry was not used to determine the INDT-S HOMO and LUMO levels; instead, ultraviolet photoelectron spectroscopy (UPS) was used to determine the HOMO levels, and the LUMO was determined by adding the optical energy gap to these values. The advantage of this method is that the material is in the solid state for the UPS measurement, but there can be significant error in the LUMO

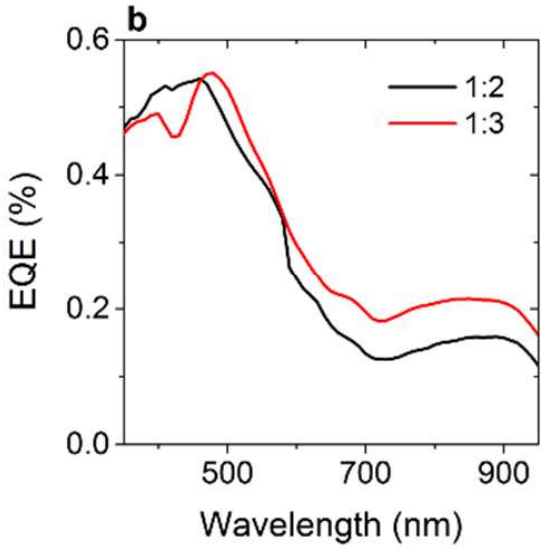


Figure 7.7: External quantum efficiency data of INDT-S:$PC_{70}BM$ blends, with 1:2 w/w (black line) and 1:3 w/w (red line) blend ratios. The device architecture was ITO/blend/LiF/Al. This figure was reproduced with permission from [245], copyright 2016 American Chemical Society.

level since there are often discrepancies in how optical energy gap is determined, and this value can differ from the electronic energy gap. A further consideration when using either of these methods to investigate materials for OPV is that the relevant quantities are the energy levels at the polymer:fullerene interface, as opposed to the values for the materials in isolation. For example, the formation of interfacial dipoles, or the blend microstructure, can alter the electronic structure of the materials at the interface, thus changing the effective HOMO and LUMO levels [71]. Therefore the values mentioned above are useful for determining the approximate energy level offsets, but should not be considered definitive.

The external quantum efficiency is not an adequate measurement of the energetic dependence of charge generation, since it is affected by the absorption of the blend components as well as any interference effects. Therefore the internal quantum efficiency (IQE), defined as the current generated per photon absorbed, is the more pertinent metric; see Section 3.2.3 for further details. For each blend presented in this chapter, I calculate the IQE to estimate the efficiency of charge generation at each wavelength. This method has been used previously to probe the relative efficiency of polymer and fullerene exciton separation [246].

However, IQE cannot distinguish between charge generation and collection efficiency, whereas time-resolved spectroscopy allows us to observe charge states soon after generation, without being reliant on charge collection. Therefore I collaborated with Dr Artem Bakulin in the Chemistry department at Imperial

College, who performed the pump-push experiment described above on INDT-S-based devices. Furthermore I collaborated with Dr Tracey Clarke from University College London, who performed TAS measurements on INDT-S-based films, in order to probe the nature of the states involved at short times. In this chapter therefore I will briefly present the spectroscopic measurements in addition to my own measurements in order to shed light on the full picture.

I should note here that while I made devices of BTT-DPP blended with PCBM, $PC_{70}BM$ and KL, in the device batch which I used for measuring IQE I was unable to acquire EQE data of the PCBM devices. In order to estimate the reflectance of the devices, I evaporated very large contacts on one half of the substrates in a particular run, while the other half had the usual configuration of six 0.045 cm^2 devices per substrate; for this I used a custom evaporation mask. Unfortunately device runs prior to this one were unsuitable for measuring IQE because I did not use this mask and therefore did not have any devices suitable for a reflectance measurement. After this point I did not have sufficient polymer to re-do the experiment, so the BTT-DPP data presented in this chapter is only the comparison between $PC_{70}BM$ and KL, which is not ideal because the absorption of $PC_{70}BM$ overlaps with that of BTT-DPP. However in the INDT-S study, I only compared PCBM with KL, thus simplifying the comparison.

7.3 Results

7.3.1 Ultraviolet-visible spectroscopy

The absorption spectra of all the individual components are very important for this study especially because it is important to know which species are likely to be present after excitation at different wavelengths. Figure 7.8 shows the ultraviolet-visible absorption spectra of BTT-DPP, $PC_{70}BM$ and KL in solution and in films, as well as the film absorption of BTT-DPP:acceptor (1:2 w/w) blends. It is clear from these data that $PC_{70}BM$ exhibits significant absorption in the visible resulting in a flatter blend absorption spectrum. The figure plots the optical density of the films, normalised to enable comparison of the spectral shapes, without having to assume the Beer-Lambert conditions necessary for calculating the solid state absorption coefficient α.

Figure 7.9 shows the solid state absorption spectrum of INDT-S, with the absorption spectra of PCBM and KL included as reference. It is evident from these data that at long wavelengths, only INDT-S is absorbing, and at short

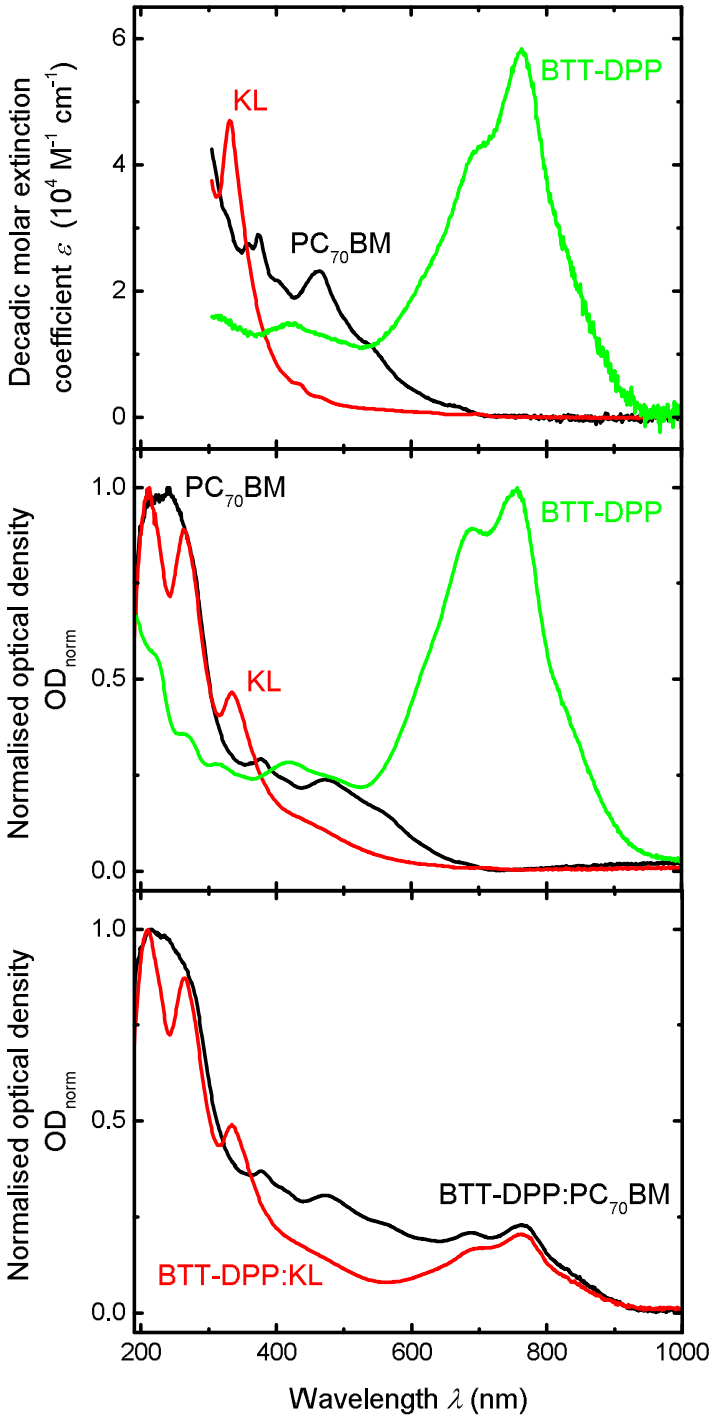


Figure 7.8: Absorption spectra of BTT-DPP, ketolactam and $PC_{70}BM$ and associated blends. Top panel: solution decadic molar extinction coefficients of BTT-DPP (green), $PC_{70}BM$ (black) and KL (red) dissolved in 1,2-dichlorobenzene. The concentrations of the BTT-DPP, $PC_{70}BM$ and KL solutions were 0.005, 0.01 and 0.05 mg ml^{-1} respectively. The molar extinction coefficient of BTT-DPP was calculated per mole of monomer. Middle panel: normalised optical density of thin films of BTT-DPP (green), $PC_{70}BM$ (black) and KL (red) on spectrosil. Bottom panel: normalised optical density of thin films of BTT-DPP:$PC_{70}BM$ (black) and BTT-DPP:KL (red), both 1:2 w/w.

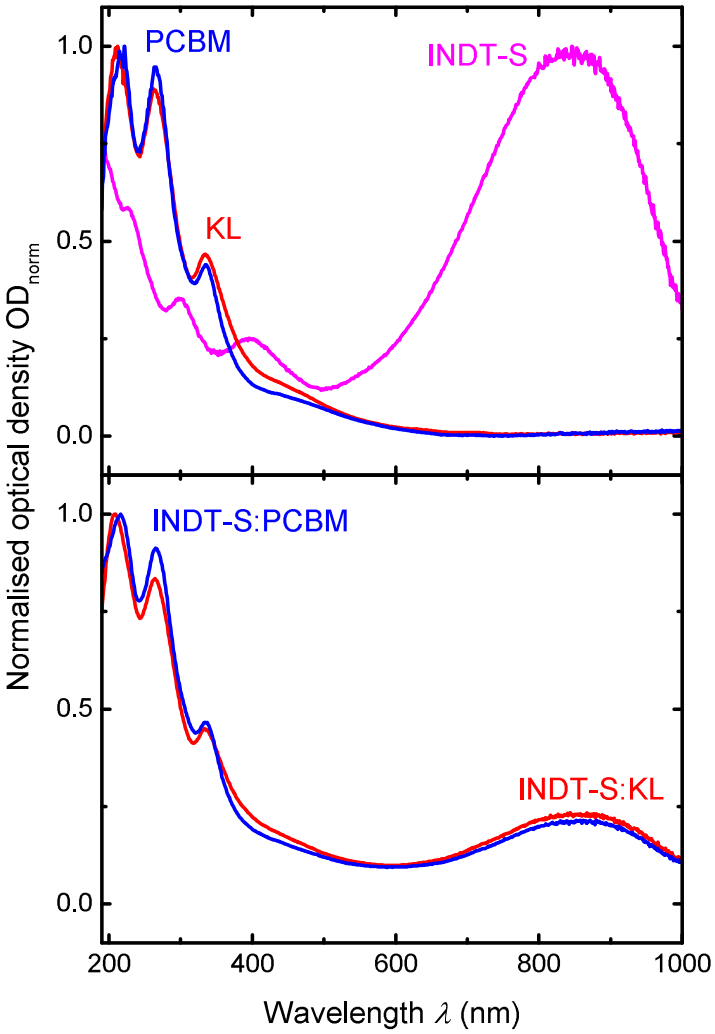


Figure 7.9: Normalised optical density spectra of INDT-S, ketolactam and PCBM thin films on spectrosil. Top panel: normalised optical density of INDT-S (34 nm, magenta line), PCBM (blue) and KL (red) films on spectrosil. Bottom panel: normalised optical density of INDT-S:PCBM (84 nm, blue line) and INDT-S:KL (75 nm, red line), both 1:2 w/w.

wavelengths both blend components contribute. The absorption spectra of the blends, also shown in Figure 7.9, subsequently exhibit two distinct spectral regions corresponding to the polymer and the acceptor.

7.3.2 Ellipsometry

I collaborated with Dr Mariano Campoy-Quiles to obtain the complex refractive index data of BTT-DPP, KL and the derived blends. Figure 7.10 shows the n and κ values of BTT-DPP and KL, as well as previously measured data for $PC_{70}BM$ for reference. Figure 7.10 also shows the complex refractive indices of the blends based on BTT-DPP. It should be noted here that the BTT-DPP pristine polymer

and especially the blend films were difficult to fit satisfactorily. Mariano used a standard critical points model (see eq. (7.1) below) for the polymer but was unable to satisfactorily fit all the films. The data shown in Figure 7.10 corresponds to an adequate fit, although there is more uncertainty in these values than usual.

Nevertheless, Mariano used these data to model the blends using the Bruggeman effective medium approximation (EMA) (see eq. (7.2) below), as well as a unique SCP model (i.e. one which is not based on other sets of (n,κ)). He found that while the SCP models afforded better fits to the data, the resultant (n,κ) values did not match the film transmission satisfactorily. Therefore the data shown in Figure 7.10, which I subsequently used for the transfer matrix modelling, were the EMA data. However I did repeat the TMM analysis using the different sets of (n,κ) data and did not find a significant effect. These uncertainties and difficulties in fitting the VASE data flagged that the film may not be homogeneous. Mariano therefore estimated the vertical fullerene concentration profile for both KL- and $PC_{70}BM$-based blends, and found weak and strong vertical segregation respectively (Figure 7.11). The primary purpose of acquiring the ellipsometry data is to calculate the parasitic absorption, which is a small contributor to the overall calculation of the IQE. Therefore I proceeded with the spectra shown in Figure 7.10, which do not account for vertical segregation, but tested for any effect of changes in the refractive index on the end result by repeating the calculations using different refractive index data. This will be discussed further in Section 7.3.5.

I was able to measure and analyse INDT-S films myself to acquire the complex refractive index data set. I fit pristine INDT-S films using the standard critical points model with four peaks, eq. (3.35) and reproduced here:

$$\varepsilon(E) = UV - \sum_{j=1}^{n} A_j \exp(i\phi_j)(E_{\mathrm{cp},j} - E + i\Gamma_j)^{-1} \tag{7.1}$$

For each material I deposited films on five substrates: three on spectrosil quartz and two on silicon, aiming for a range of film thicknesses. To determine the INDT-S n and κ I focussed on the spectrosil films since the films were more homogeneous, and the derived refractive index data are shown in Figure 7.12; the analysis of each INDT-S film results in a distinct complex refractive index. For each sample, I measured the film thickness using a profilometer, and I used this thickness as the starting point of the fit. The fit for sample 1 was well-behaved and the particular refractive index I used for the blends; the fit thickness was very close to the measured thickness. The fits for samples 2 and 3 were less well-behaved, especially sample 3 which gave a fit thickness approximately 20 nm less than the

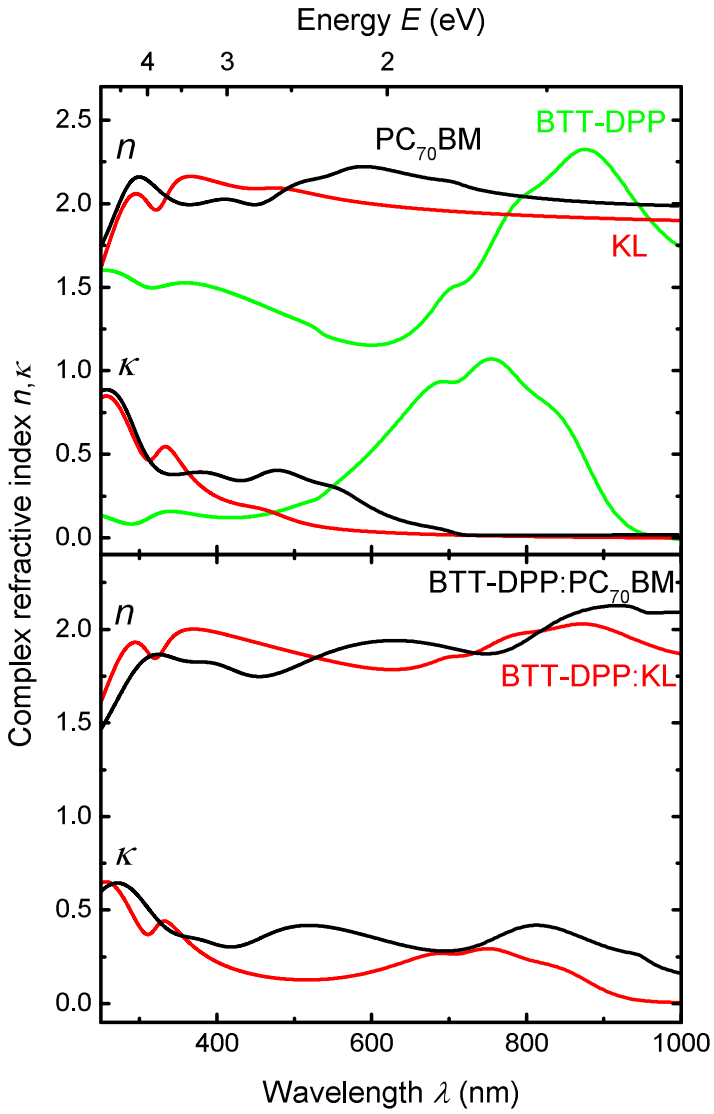


Figure 7.10: Real (n) and imaginary (κ) parts of the complex refractive index spectra of BTT-DPP polymer and blend films, as measured using VASE. Top panel: n and κ of BTT-DPP (green), $PC_{70}BM$ (black) and KL (red). Bottom panel: n and κ of BTT-DPP:$PC_{70}BM$ (black) and BTT-DPP:KL (red) blends, both 1:2 w/w. The ellipsometry data was collected and analysed by Dr Mariano Campoy-Quiles.

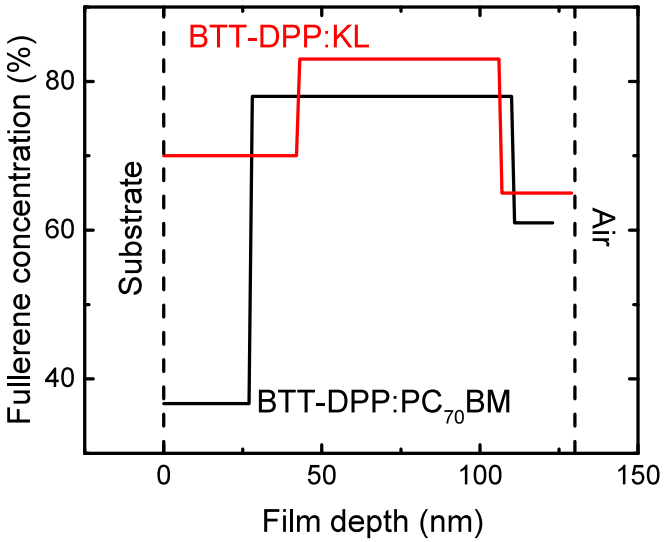


Figure 7.11: Vertical fullerene concentration profile of BTT-DPP:$PC_{70}BM$ (black) and BTT-DPP:KL (red) blends, both 1:2 w/w and the same films used to derive the complex refractive index data shown in Figure 7.10. The substrate/film interface is set at zero depth, while the film/air interface is at the film's thickness d.

measured thickness resulting in a refractive index with greater magnitude than the others; therefore for this sample I constrained the film thickness to the measured value and obtained a decent fit. Table 7.2 tabulates the fit values for each sample, while Figure 7.13 shows the fits to the data.

Furthermore I cross-checked the VASE-derived complex refractive index with the extinction coefficient calculated from ultraviolet-visible absorption spectroscopy (data shown in Figure 7.9), using the relations $\kappa = \alpha\lambda/4\pi$ and $T = \exp(-\alpha d)$, where κ is the extinction coefficient, α is the absorption coefficient, λ is the wavelength, T is the transmittance, and d is the film thickness. The resulting comparison is shown in Figure 7.14, and the close agreement of the peak positions, especially at low energies, validates the ellipsometry fit. Variance in the peak heights is expected since the calculation of α involves a measured value of the film thickness, which may well have some error, and also assumes no scattering or interference and a Beer-Lambert exponential decay of intensity through the film. This latter point especially affects the accuracy of the higher energy part of the spectrum, since interference fringes have a stronger effect on the spectral shape.

I followed a similar fitting approach for the blend films, analysing the data of each sample of each blend, but instead of the SCP model I used the Bruggeman effective medium approximation, which is defined by (see Section 3.4.2):

$$0 = f\frac{\varepsilon_1 - \langle\varepsilon\rangle}{\epsilon_1 + 2\langle\varepsilon\rangle} + (1-f)\frac{\varepsilon_2 - \langle\varepsilon\rangle}{\epsilon_2 + 2\langle\varepsilon\rangle} \tag{7.2}$$

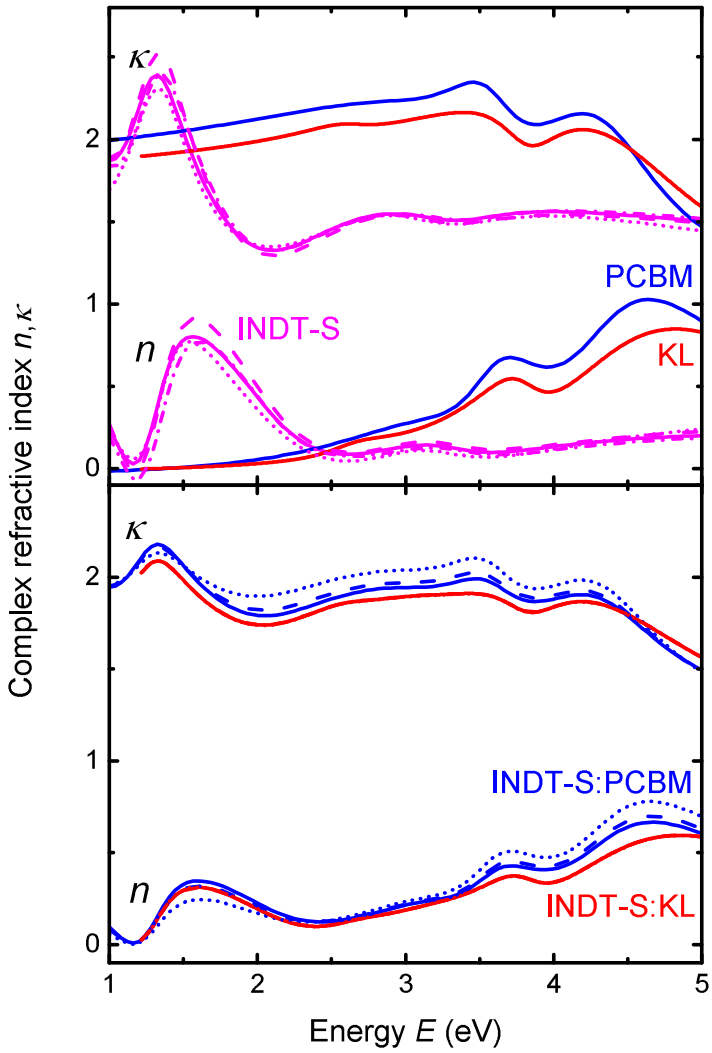


Figure 7.12: Real (n) and imaginary (κ) parts of the complex refractive index spectra of INDT-S polymer and blend films, as measured using VASE. Top panel: n and κ of INDT-S (magenta), PCBM (blue) and KL (red), reproduced for ease of comparison. The solid line corresponds to sample 1, and is the refractive index used for the blends. Sample 2 with fit thickness is the dashed line, sample 2 with the thickness fixed to the profilometer value is the dash-dot line, and sample 3 with the thickness fixed to the profilometer value is the dotted line. Bottom panel: n and κ of INDT-S:PCBM (blue) and INDT-S:KL (red) blends, both 1:2 w/w. For both blends, the solid line corresponds to sample 1 of that blend, while the dashed line corresponds to sample 2 and the dotted line corresponds to sample 3. (Note that the KL blend data are all overlapping.)

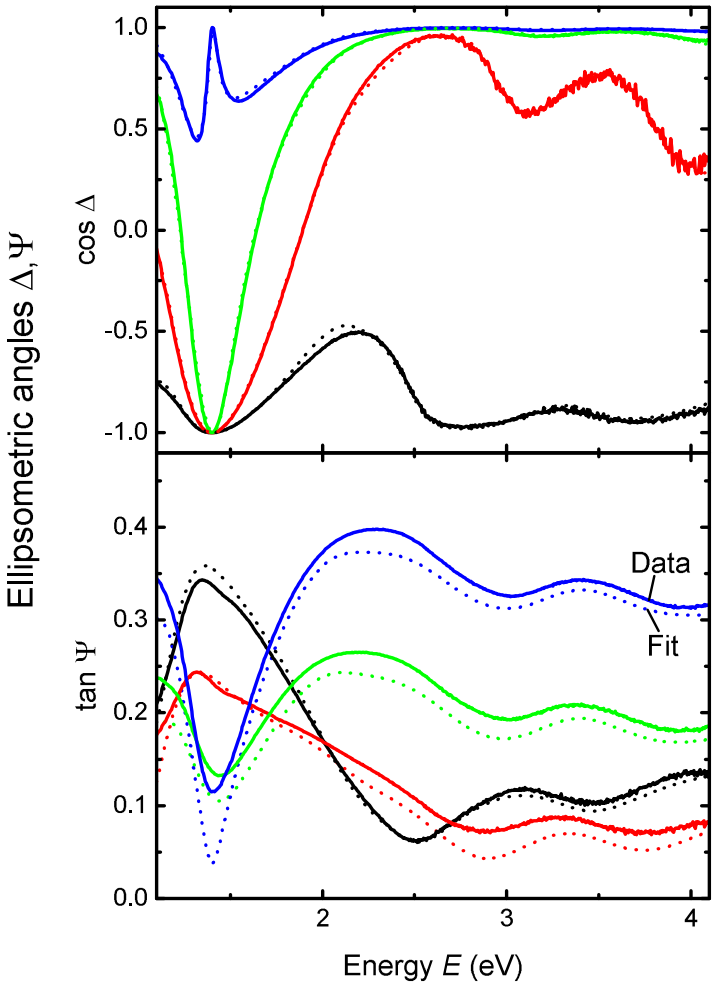


Figure 7.13: Experimental and fit ellipsometric angles $\cos\Delta$ (top panel) and $\tan\Psi$ (bottom panel) of an INDT-S polymer thin film (sample 1) measured for a range of incident angles. In both panels, the black line is for an incidence angle of 55°, red is 60°, green is 65° and blue is 70°. The measured data is shown by solid lines, while the fits are dashed lines.

Table 7.2: Parameters used in eq. (7.1) to model INDT-S, corresponding to the refractive indices shown in Figure 7.12. Sample 1 was the data set used to generate the blend (n, κ) data. Where there is no fit thickness indicated, the thickness was not allowed as a free parameter. Each row corresponds to one of the composite critical points required for the overall model.

	Fit (measured) thickness (nm)	UV	A	E_{cp}	γ	ϕ
Sample 1	43 (44)	1.2654	0.9114	1.2987	0.2094	-1.7421
			0.2296	3.3112	0.4630	1.5425
			2.9606	2.2732	1.1472	-3.1591
			4.2456	0.2828	0.4986	-1.4876
Sample 2	41 (53)	0.8579	0.9114	1.2987	0.2094	-1.7421
			0.2296	3.3112	0.4630	1.5425
			2.9606	2.2732	1.1472	-3.1591
			4.2456	0.2828	0.4986	-1.4876
Sample 2	(53)	1.2272	1.1391	1.3134	0.2279	-1,9156
			0.1976	3.3499	0.4557	1.4393
			5.0904	2.0067	1.3112	-3.3646
			6.1980	0.4705	0.7852	-1.1875
Sample 3	(34)	0.2784	0.7983	1.333	0.2058	-1.4168
			0.4189	3.1387	0.5177	0.6010
			3.8527	2.7702	1.4668	-2.6943
			4.6680	-0.09	-0.2768	-2.2638

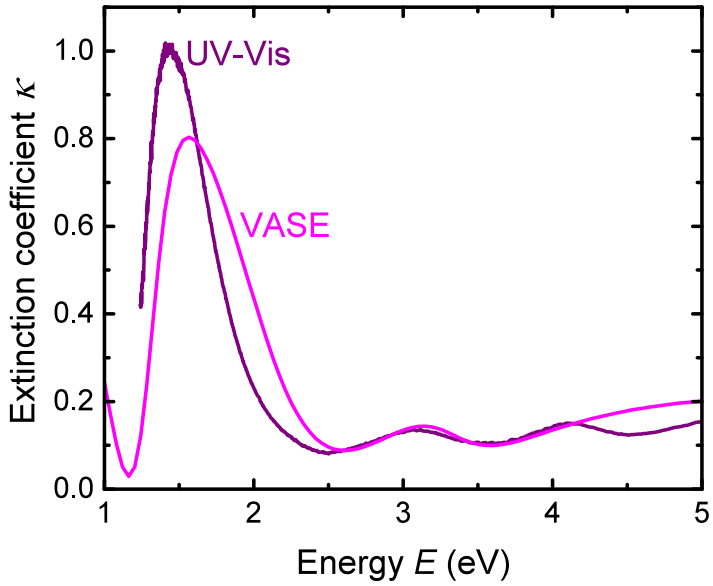


Figure 7.14: Comparison of extinction coefficients derived from ellipsometry and ultraviolet-visible spectroscopy. The magenta line is the data shown in Figure 7.12, derived from variable angle spectroscopic ellipsometry (VASE), while the dark purple line is the data calculated from ultraviolet-visible spectroscopy (UV-Vis) of the same substrate using the relations $\kappa = \alpha\lambda/4\pi$ and $T = \exp(-\alpha d)$, where κ is the extinction coefficient, α is the absorption coefficient, λ is the wavelength, T is the transmittance, and d is the film thickness.

The inputs for this determination of the refractive index are the refractive indices of each of the blend components. I used the KL and PCBM refractive indices previously calculated by Dr Campoy-Quiles, and the INDT-S data shown above. The fitting parameters were both the film thickness and the fullerene concentration; the starting thickness for the fit was measured using a Dektak profilometer. The resulting fit parameters are tabulated in Table 7.3, the corresponding complex refractive indices are shown in the bottom panel of Figure 7.12, and the fits are shown in Figure 7.15.

In addition to the blend refractive index data, in order to model the light propagation through a full device, the refractive indices of each interlayer is also required. The interlayers used in this study were ITO, polyethylenimine (PEIE), ZnO, MoO_3 and Ag. Dr Campoy-Quiles had previously measured the refractive index data of all these materials apart from PEIE, which he measured for this study. The refractive index data of all the interlayers are shown in Figure 7.16.

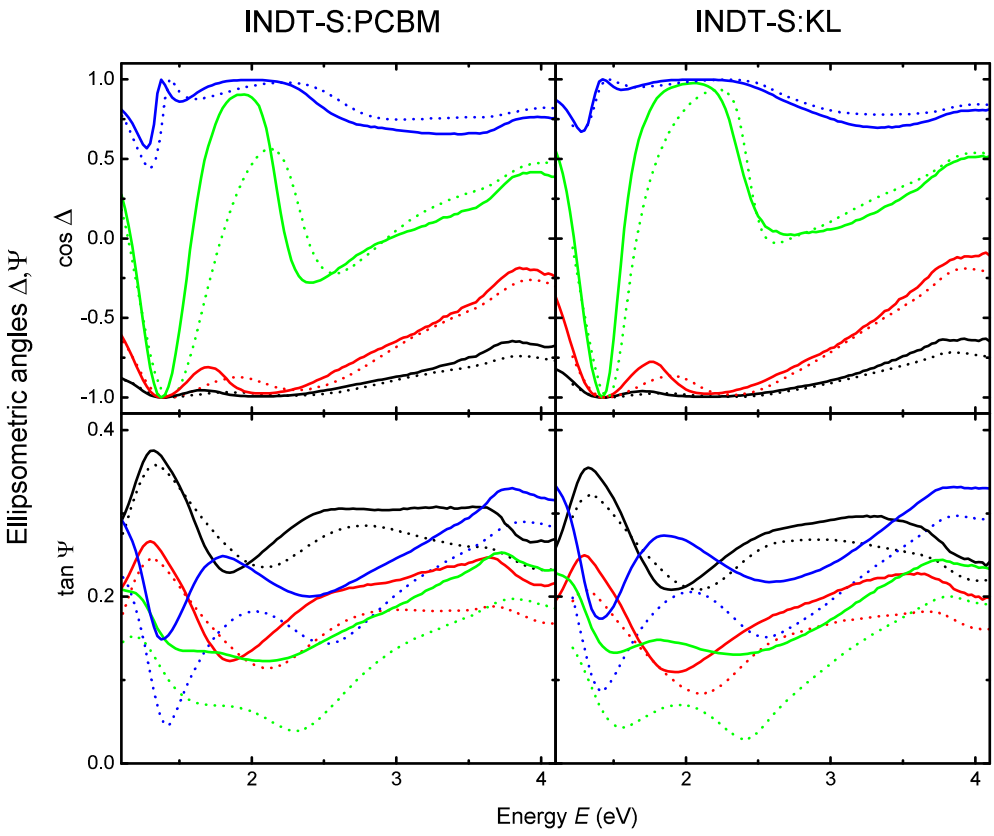


Figure 7.15: Experimental and fit ellipsometric angles $\cos\Delta$ (top panels) and $\tan\Psi$ (bottom panels) of an INDT-S:PCBM (1:2 w/w) blend thin film (left column) and an INDT-S:KL (1:2, w/w) blend thin film (right column). The films were measured over a range of incident angles: black is for an incidence angle of 55°, red is 60°, green is 65° and blue is 70°. The measured data is shown by solid lines, while the fits are dashed lines.

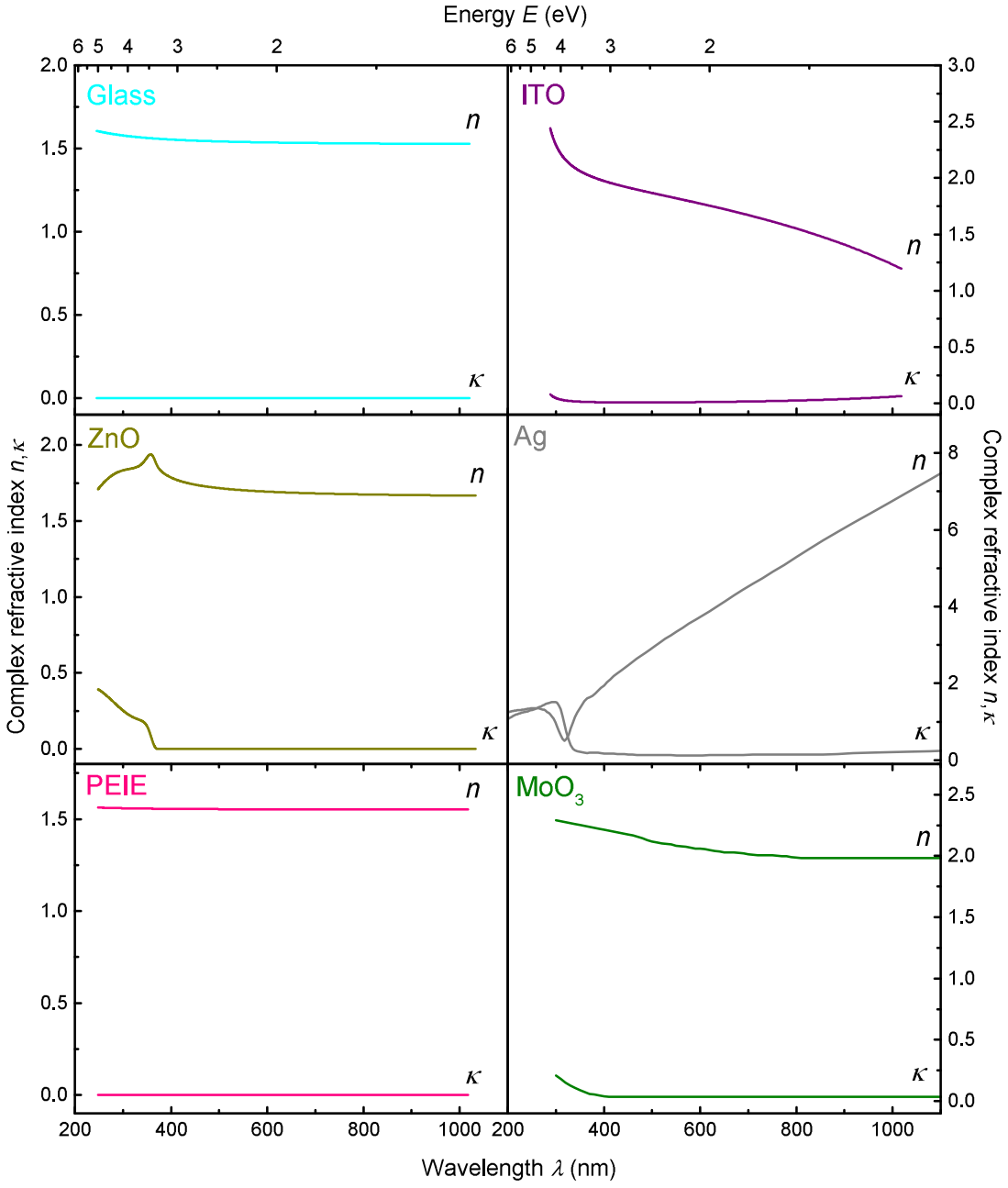


Figure 7.16: Real (n) and imaginary (κ) parts of the complex refractive index spectra of the device interlayers and glass. Clockwise starting from the top left: glass (blue), indium tin oxide (purple), silver (grey), molybdenum oxide (green), polyethylenimine (pink) and zinc oxide (dark yellow). All data were produced by Dr Mariano Campoy-Quiles.

Table 7.3: Parameters used to model INDT-S blend film ellipsometry data. The measured thicknesses were determined using profilometry, and was the starting point of the fit. The blend was modelled using the Bruggeman effective medium approximation, with the only fitting parameters being the film thickness and the blend composition, parameterised by the fullerene concentration. Both films were nominally 1:2 (w/w) polymer:acceptor blends.

	Measured thickness (nm)	Fit thickness (nm)	Fit fullerene concentration
INDT-S:PCBM sample 1	84	75	0.586
INDT-S:PCBM sample 2	124	129	0.624
INDT-S:PCBM sample 3	187	179	0.718
INDT-S:KL sample 1	75	73	0.623
INDT-S:KL sample 2	159	144	0.624
INDT-S:KL sample 3	134	133	0.621

7.3.3 Current-voltage and external quantum efficiency

For both the BTT-DPP and INDT-S studies, I made inverted devices although the cathode interlayer differed: for the BTT-DPP study I used PEIE (10 nm), while for the INDT-S study I used ZnO (30 nm). The difference in interlayer was due to previously optimised device structures. The full architecture was therefore glass/ITO/PEIE or ZnO/polymer:acceptor blend (1:2 w/w)/MoO_3/Ag. Figure 7.17 shows current density-voltage and external quantum efficiency data of the BTT-DPP devices. Unfortunately I was unable to match the device efficiencies previously published, likely due to differences in morphology due to a different polymer batch. The vertical segregation suggested by the ellipsometry data would also inhibit device performance since there appeared to be fullerene-depleted regions at both electrodes. Nevertheless the device performance parameters are displayed in Table 7.4 along with the device thicknesses. The shape of the $PC_{70}BM$ blend EQE closely matches the previously published data.

Meanwhile Figure 7.18 shows the current density-voltage and external quantum efficiency data of the INDT-S devices. I received help from a summer student, Anna Jungbluth, supervised by Dr Andrew Telford from my group, in measuring the devices for the INDT-S study; I made the devices while Anna and Andrew conducted the electrical measurements. The solar cell performances of these devices matches the previously published data well; while higher efficiencies of 3.1 %

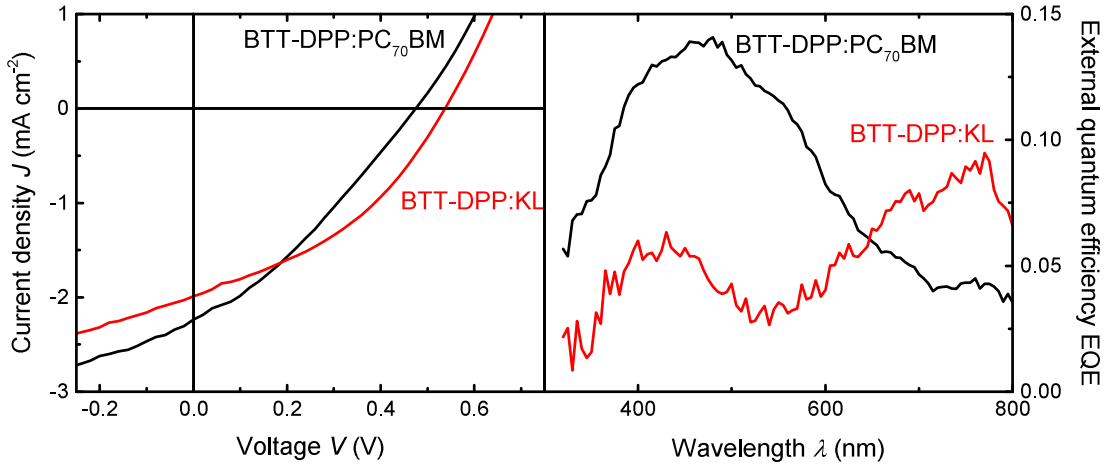


Figure 7.17: Current density-voltage (left panel) and external quantum efficiency (right panel) graphs of devices based on BTT-DPP. In both panels, BTT-DPP:$PC_{70}BM$ is the black line and BTT-DPP:KL is the red line. Both blends are 1:2 w/w, and the device architecture for both devices is ITO/PEIE (10 nm)/BTT-DPP:acceptor/MoO_3 (10 nm)/Ag (100 nm). The current density-voltage data was taken under simulated one sun, AM1.5 conditions.

Table 7.4: *J-V* parameters of BTT-DPP devices. J_{sc} is the short-circuit current, V_{oc} is the open-circuit voltage, FF is the fill factor, PCE is the power conversion efficiency .

Blend	Thickness (nm)	J_{sc} (mA cm^{-2})	V_{oc} (V)	FF	PCE (%)
BTT-DPP:$PC_{70}BM$	94	2.24	0.475	0.31	0.33
BTT-DPP:KL	105	1.99	0.538	0.47	0.50

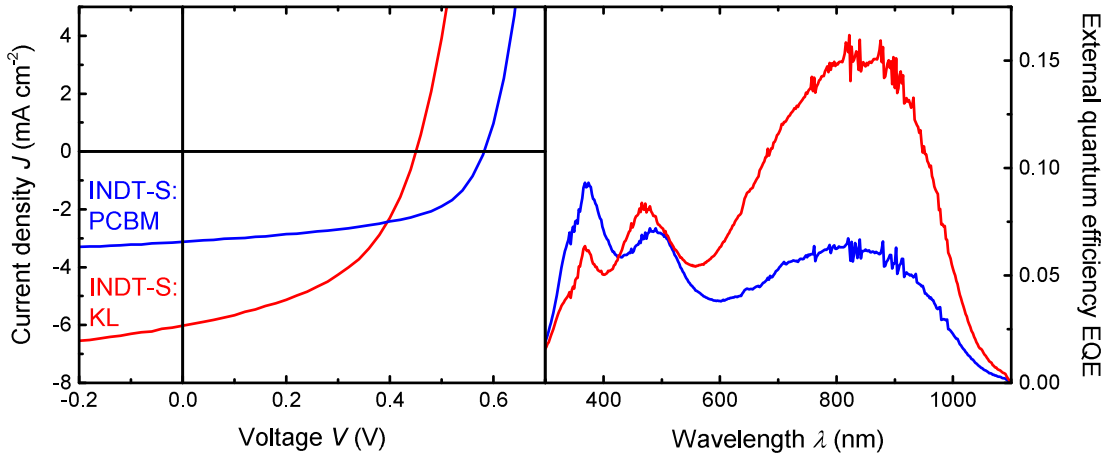


Figure 7.18: Current density-voltage (left panel) and external quantum efficiency (right panel) graphs of devices based on INDT-S. In both panels, INDT-S:PCBM is the blue line and INDT-S:KL is the red line. Both blends are 1:2 w/w, and the device architecture for both devices is ITO/ZnO (30 nm)/INDT-S:acceptor/MoO_3 (10 nm)/Ag (100 nm). The current density-voltage data was taken under simulated one sun, AM1.5 conditions. These data were collected by Anna Jungbluth supervised by Dr Andrew Telford.

Table 7.5: *J-V* parameters of INDT-S devices. J_{sc} is the short-circuit current, V_{oc} is the open-circuit voltage, FF is the fill factor, PCE is the power conversion efficiency .

Blend	Thickness (nm)	J_{sc} (mA cm^{-2})	V_{oc} (V)	FF	PCE (%)
INDT-S:PCBM	77	3.12	0.582	0.55	1.00
INDT-S:KL	57	6.02	0.450	0.47	1.28

have been published [245], those blends used $PC_{70}BM$ and so should be expected to have higher currents and therefore efficiencies.

7.3.4 Reflectivity

As discussed already, it is important to measure the reflectivity of a device stack as part of the IQE calculation. The data shown in this section are the reflection data of large area devices made at the same time and using the same processing conditions as the devices used to measure the EQE and *J-V*. Figure 7.19 shows the reflectance of BTT-DPP-based and INDT-S-based devices; for the case of INDT-S-based devices, I measured multiple substrates to check the consistency of the measurement. For the BTT-DPP-based devices unfortunately this was not possible and so I measured the reflectance at different points on the same device.

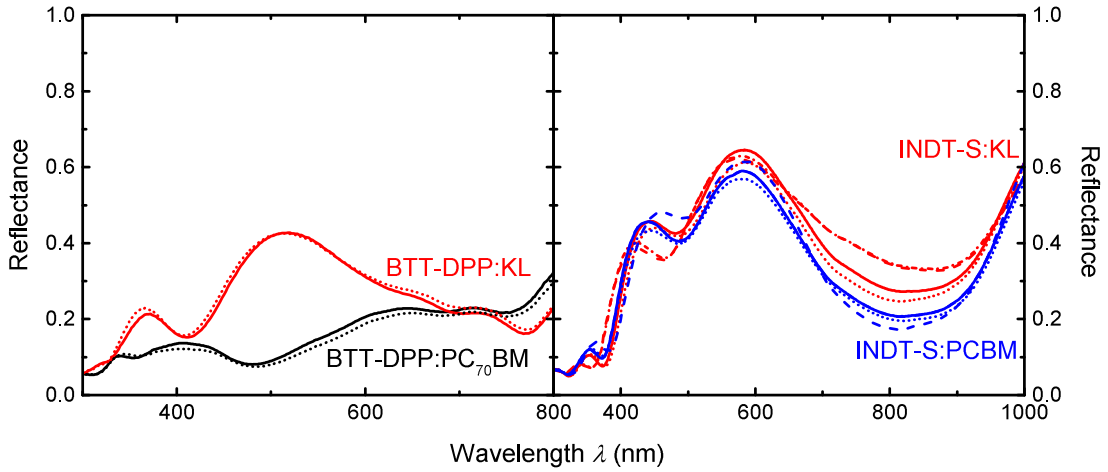


Figure 7.19: Reflectance spectra of full device stacks based on BTT-DPP (left panel) and INDT-S (right panel). Both sets of data complement the device data shown in Figures 7.17 and 7.18, in that these devices were made at the same time and with the same parameters apart from a larger evaporated electrode, enabling the reflectance measurement. The BTT-DPP devices have the architecture ITO/PEIE (10nm)/BTT-DPP:acceptor (1:2, w/w)/MoO_3/Ag, and the INDT-S devices have the architecture ITO/ZnO (30 nm)/INDT-S:acceptor (1:2, w/w)/MoO_3/Ag. In both panels, the blend with KL is shown by red lines, in the left panel the BTT-DPP:$PC_{70}BM$ device are the black lines, and in the right panel the INDT-S:PCBM device are the blue lines. The different lines indicate the reflectance of different substrates and/or in different orientations (achieved by rotating and moving the substrate in the holder) to determine the variation.

7.3.5 Internal quantum efficiency

Using the data shown in Section 7.3.2, I used the transfer matrix method (TMM) to calculate the propagation of light through the BTT-DPP and INDT-S device stacks. I was therefore able to extract the degree of absorption from layers in the device stack other than the current generating active layer; this absorption is termed the parasitic absorption and is plotted in Figure 7.20. TMM assumes perfectly flat interlayers, homogeneous media and an accurate measurement of layer thicknesses. None of these assumptions can be applied to the case of organic solar cells and so it would be ill-advised to use TMM to directly calculate the active layer absorption. Since the parasitic absorption is less significant, however, the error invoked in using this method as part of the calculation of IQE is insignificant if there is a large difference between the two blends being studied. To check the effect of using different (n, κ) values on the parasitic absorption spectra, I did the calculation using different sets of values.

I calculated the IQE of each blend using the data presented in Sections 7.3.2 to 7.3.4, using the relation IQE = EQE/(1 − parasitic absorption − reflection); the resulting spectra are displayed in Figure 7.21. From Figures 7.19 and 7.20, the variation in the reflectance data is more significant than that of the parasitic absorption. Therefore the IQE data presented in Figure 7.21 are calculated using the various reflection data sets presented in Figure 7.19. The increased variation of the INDT-S IQE data is due to the availability of multiple devices for the reflectance measurement, whereas only one device was available for each BTT-DPP blend which was measured in two orientations.

The data show a clear difference in free charge generation efficiency for absorption by the polymer: both polymer:KL blends have a higher IQE in this region than the PCBM blends. For the case of the BTT-DPP blend, this effect is slightly masked since it appears that overall the charge extraction efficiency of the $PC_{70}BM$ blend is greater, as evidenced by the significantly higher IQE in the fullerene absorbing region. For the case of the INDT-S blends though, the improved charge generation from polymer excitons is clear, while at higher energies, in the region dominated by fullerene absorption, the IQE spectra are inconclusive. Interference and small differences in the layer thicknesses mean that the high energy part of the IQE spectrum is less reliable and more likely to be greatly affected by small errors in the component measurements.

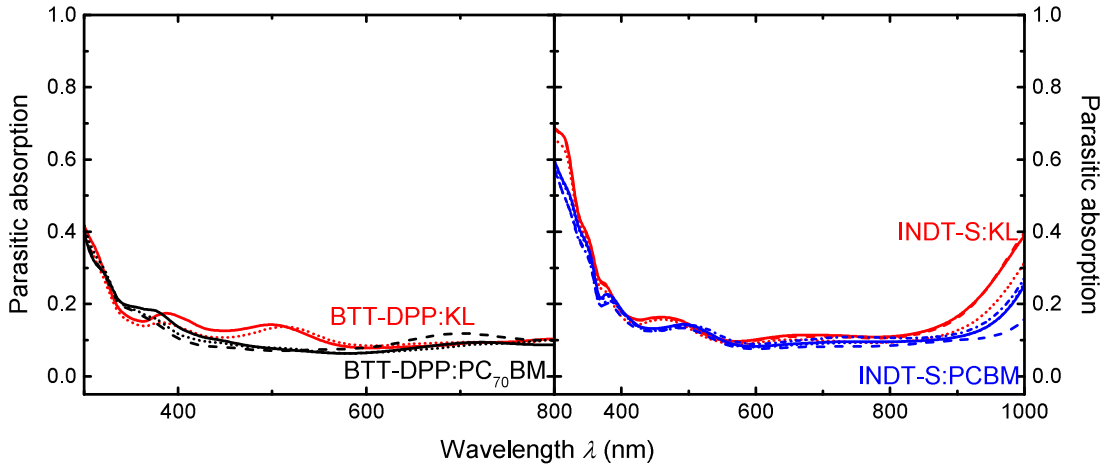


Figure 7.20: Calculated parasitic absorption spectra of BTT-DPP (left panel) and INDT-S (right panel) device stacks. The parasitic absorption is defined as the summed absorption of all the layers in the device apart from the current-generating active layer. The data were calculated using the transfer matrix formalism using the complex refractive index data shown previously. The BTT-DPP devices have the architecture ITO/PEIE (10nm)/BTT-DPP:acceptor (1:2, w/w)/MoO_3/Ag, and the INDT-S devices have the architecture ITO/ZnO (30 nm)/INDT-S:acceptor (1:2, w/w)/MoO_3/Ag. The blend thicknesses are as tabulated in Tables 7.4 and 7.5. In both panels, the blend with KL is shown by red lines, in the left panel the BTT-DPP:PC_{70}BM device is the black lines, and in the right panel the INDT-S:PCBM device is the blue lines. The different lines correspond to the use of different blend (n, κ) data sets, which result from the variation in experimentally determined (n,κ) data sets as reported in Section 7.3.2.

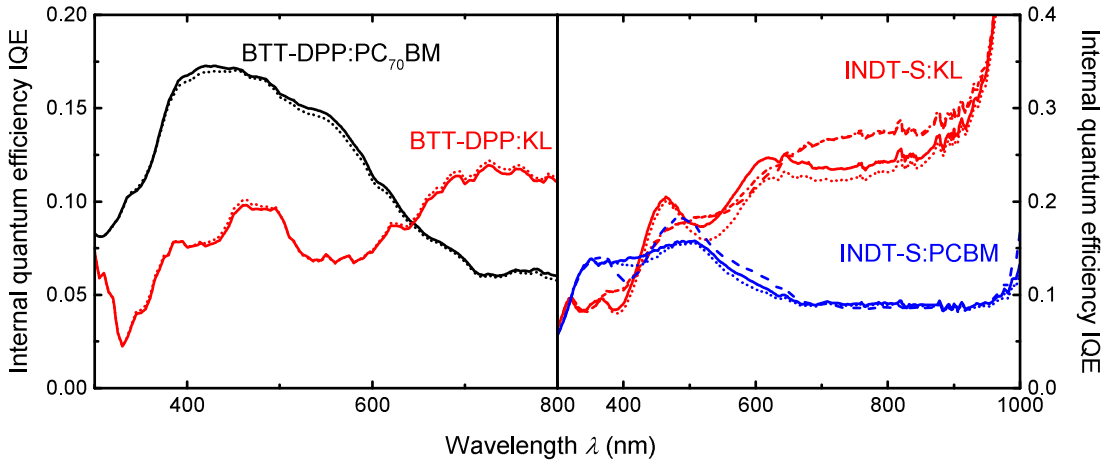


Figure 7.21: Calculated internal quantum efficiency of BTT-DPP (left panel) and INDT-S (right panel) devices, using the data shown in Figures 7.17 to 7.20. The BTT-DPP devices have the architecture ITO/PEIE (10nm)/BTT-DPP:acceptor (1:2, w/w)/MoO_3/Ag, and the INDT-S devices have the architecture ITO/ZnO (30 nm)/INDT-S:acceptor (1:2, w/w)/MoO_3/Ag. The blend thicknesses are as tabulated in Tables 7.4 and 7.5. In both panels, the blend with KL is shown by red lines, in the left panel the BTT-DPP:PC_{70}BM device is the black lines, and in the right panel the INDT-S:PCBM device is the blue lines. The different data sets correspond to the IQE calculated using different reflection spectra; the line style is consistent between this figure and Figure 7.19.

7.3.6 Electroluminescence and voltage losses

In this section I present the determination of voltage losses of BTT-DPP and INDT-S devices. Unfortunately for the case of the BTT-DPP devices, I was unable to measure the high-resolution EQE data on the same batch of devices for which I calculated the IQE, and so the data presented in this section corresponds to a different batch of devices, whose J-V and EQE data are shown in Figure 7.22. This batch had a conventional architecture of ITO/PEDOT:PSS (15 nm)/BTT-DPP:acceptor (1:2 w/w)/Ca (15 nm)/Al (110 nm).

I measured electroluminescence of devices on the same substrate as those shown in Figure 7.22 for a range of injection currents; the data are shown in Figures 7.23 and 7.24. The BTT-DPP:PCBM and BTT-DPP:$PC_{70}BM$ devices are much more emissive than the BTT-DPP:KL device. I was also able to measure the electroluminescence of the pristine BTT-DPP polymer. Examination of the normalised spectra do not show a clear charge transfer state at an energy distinct from the polymer exciton, with the emission of the blends and the polymer all in a similar region. Differences in the total flux make comparing the spectral shapes difficult, but it appears that the KL blend emission especially, and to a smaller extent the PCBM and $PC_{70}BM$ blends, is weighted towards lower energies. The redshift of the KL peak may be expected due to the deeper acceptor LUMO and therefore more stabilised states. However it appears that there is also significant polymer contribution in each of the blend spectra.

Upon conversion of the EL spectra to quantum efficiencies, I was able to calculate the radiative open-circuit voltage $V_{\mathrm{oc,rad}}$ and hence the non-radiative open-circuit voltage loss $\Delta V_{\mathrm{oc,nr}}$; these values plotted as a function of EL injection current are displayed in Figure 7.25. The KL blend $V_{\mathrm{oc,rad}}$ is lower than the PCBM and $PC_{70}BM$ blends, as suggested by the lower energy EL peak. $\Delta V_{\mathrm{oc,nr}}$ of the PCBM and $PC_{70}BM$ blends are nearly identical, while the lower V_{oc} of the KL blend results in significantly higher $\Delta V_{\mathrm{oc,nr}}$ values.

For the case of the INDT-S devices, the data presented in this section were collected from the same devices presented earlier. Again the INDT-S devices were made by myself but measured by Anna Jungbluth, supervised by Dr Andrew Telford.

Figure 7.26 shows the electroluminescence of INDT-S-based devices; as is evident from the figure, the PCBM device has a much higher radiative efficiency, and so to enable comparison of the spectral shapes I have plotted the data corresponding to different injection currents; the flux should be approximately proportional to the injection current, especially at lower currents. The peak position is relatively

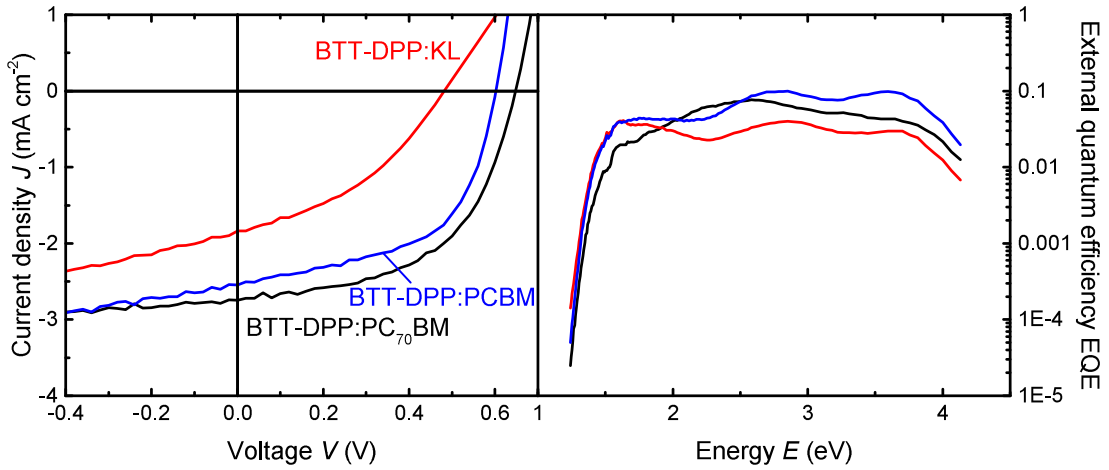


Figure 7.22: Current density-voltage (left panel) and external quantum efficiency (right panel) graphs of devices based on BTT-DPP. In both panels, BTT-DPP:PCBM is the blue line, BTT-DPP:$PC_{70}BM$ is the black line and BTT-DPP:KL is the red line. Both blends are 1:2 w/w, and the device architecture for all devices is ITO/PEDOT:PSS (15 nm)/BTT-DPP:acceptor/Ca (15 nm)/Al (110 nm). The current density-voltage data was taken under simulated one sun, AM1.5 conditions. The *J*-*V* and EQE data correspond from the same substrates but are not necessarily the same devices.

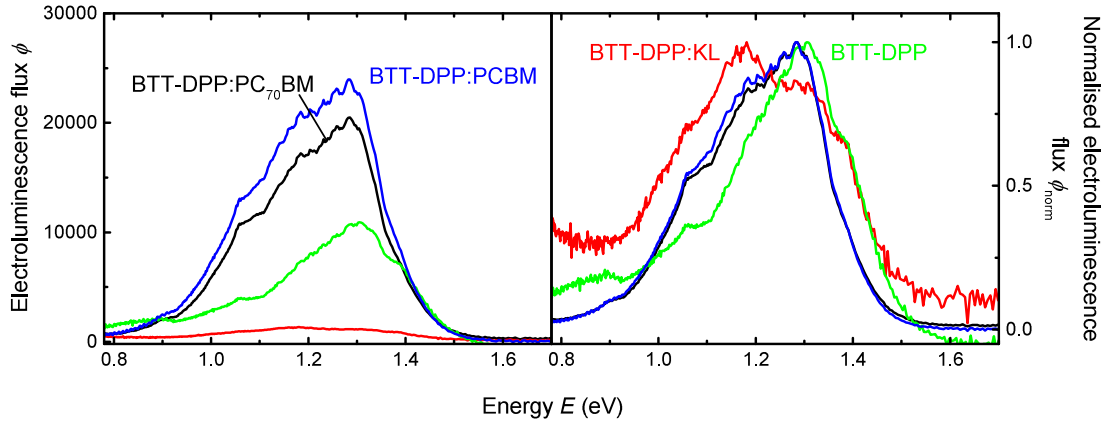


Figure 7.23: Electroluminescence of BTT-DPP (green lines), BTT-DPP:PCBM (blue lines), BTT-DPP:$PC_{70}BM$ (black lines) and BTT-DPP:KL (red lines) devices. The blends are all polymer:acceptor 1:2 w/w, and the device architecture for all the devices is ITO/PEDOT:PSS (15 nm)/BTT-DPP:acceptor/Ca (15 nm)/Al (110 nm). The left panel shows measured flux while the right panel shows the normalised flux. All data were taken at an injection current of 16 mA (356 mA cm^{-2}).

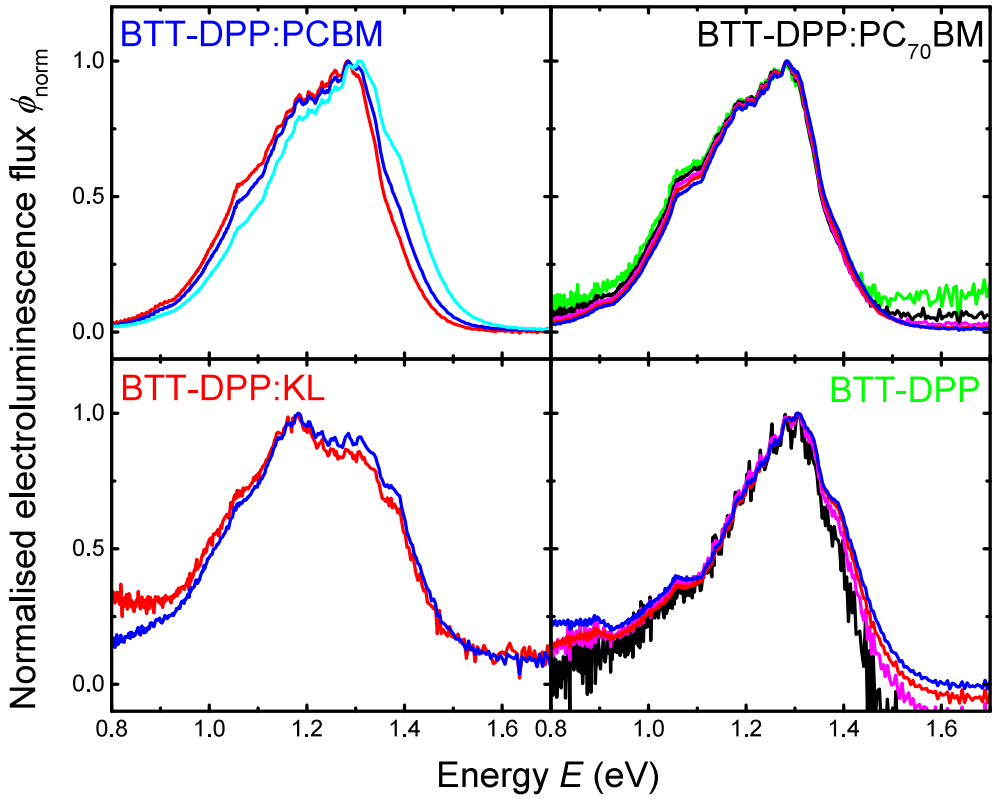


Figure 7.24: Electroluminescence as a function of injection current of BTT-DPP:PCBM (top left), BTT-DPP:$PC_{70}BM$ (top right), BTT-DPP:KL (bottom left) and BTT-DPP (bottom right) devices. The blends are all polymer:acceptor 1:2 w/w, and the device architecture for all the devices is ITO/PEIE (10 nm)/active layer/MoO_3 (10 nm)/Ag (100 nm). The spectra corresponding to a range of injection currents are shown: 44 mA cm^{-2} (green), 89 mA cm^{-2} (black), 178 mA cm^{-2} (magenta), 356 mA cm^{-2} (red), 711 mA cm^{-2} (blue) and 1422 mA cm^{-2} (cyan).

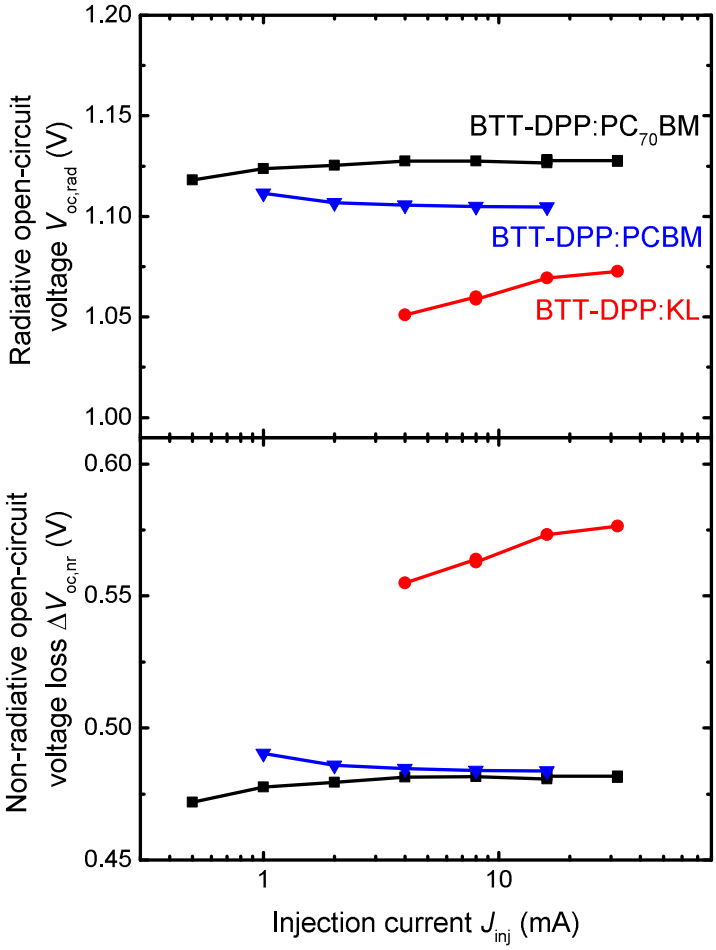


Figure 7.25: Radiative open-circuit voltage $V_{\mathrm{oc,rad}}$ (top panel) and non-radiative voltage loss $\Delta V_{\mathrm{oc,nr}}$ of BTT-DPP:PCBM (blue triangles), BTT-DPP:PC$_{70}$BM (black squares) and BTT-DPP:KL (red circles) devices. The blends are all polymer:acceptor 1:2 w/w, and the device architecture for all the devices is ITO/PEIE (10 nm)/active layer/MoO_3 (10 nm)/Ag (100 nm).

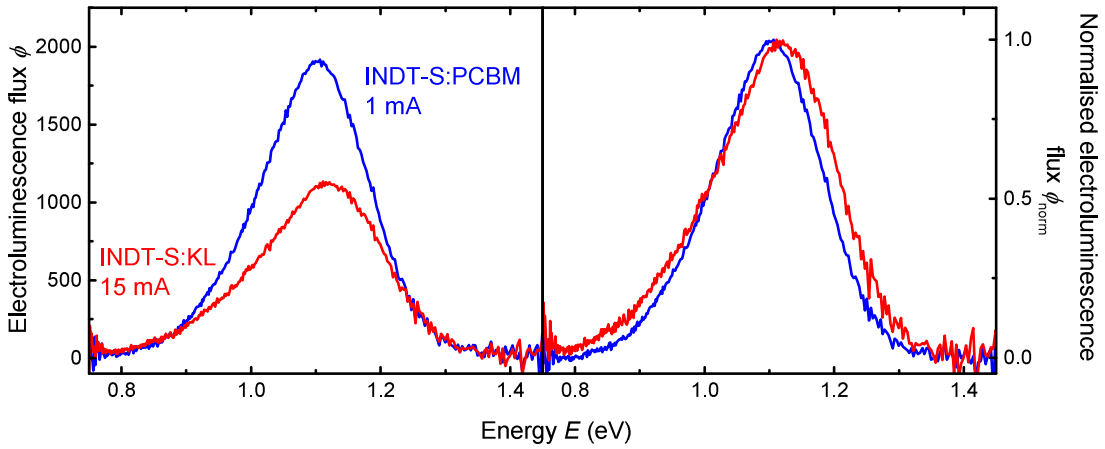


Figure 7.26: Electroluminescence of INDT-S:PCBM (blue) and INDT-S:KL (red) devices. Left panel: measured electroluminescence flux of INDT-S devices with an architecture ITO/ZnO (30 nm)/INDT-S:acceptor (1:2, w/w)/MoO_3/Ag. The INDT-S:PCBM data was taken at an injection current of 1 mA (22 mA cm^{-2}), while the INDT-S:KL data was taken at an injection current of 15 mA (333 mA cm^{-2}).

independent of the magnitude of the injection current, as shown in Figure 7.27. Furthermore the spectra of the two blends are very similar, indicating that the electroluminescence is likely coming from the polymer species. Unfortunately pure polymer electroluminescence was not possible to acquire because the devices were too resistive.

We used these electroluminescence data to obtain high-range external quantum efficiency spectra, shown in Figure 7.28. This then enabled calculation of the radiative open-circuit voltage $V_{oc,rad}$ and hence non-radiative voltage losses $\Delta V_{oc,nr}$. These values are plotted as a function of injection current in Figure 7.29. The similarity in $V_{oc,rad}$ between the two blends arises from the similarity in the EL and low energy EQE, and is likely reflecting the polymer as the radiative species. Therefore the lower V_{oc} of the KL blend results in higher $\Delta V_{oc,nr}$ values.

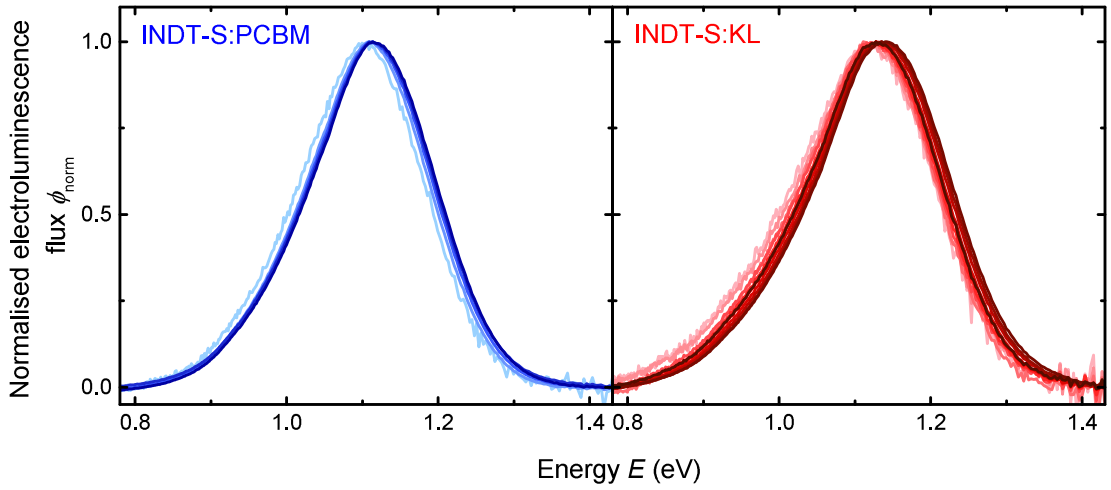


Figure 7.27: Normalised electroluminescence of INDT-S:PCBM (left panel, blue) and INDT-S:KL (right panel, red) devices. Spectra are shown for a range of injection currents J_{inj}; for both blends the darker colours correspond to higher injection currents. For INDT-S:PCBM, 1 mA (22 mA cm^{-2}) $\leq J_{inj} \leq$40 mA (889 mA cm^{-2}), while for INDT-S:KL, 15 mA (333 mA cm^{-2}) $\leq J_{inj} \leq$140 mA (3111 mA cm^{-2}). Both devices have the architecture ITO/ZnO (30 nm)/INDT-S:acceptor (1:2, w/w)/MoO_3/Ag.

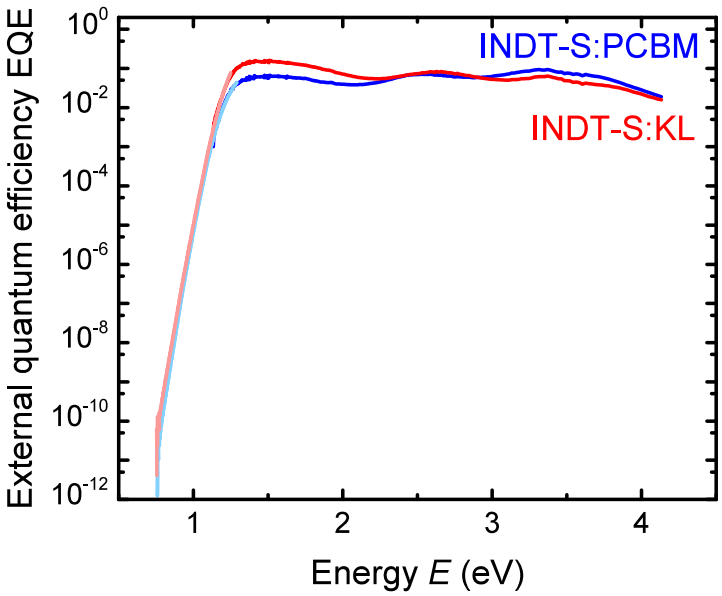


Figure 7.28: High-range external quantum efficiency spectra of INDT-S:PCBM (blue line) and INDT-S:KL (red line) devices. In both cases, the directly measured EQE data is shown by a darker line, while the EQE derived from the EL spectra are shown in lighter lines. Both devices have the architecture ITO/ZnO (30 nm)/INDT-S:acceptor (1:2, w/w)/MoO_3/Ag.

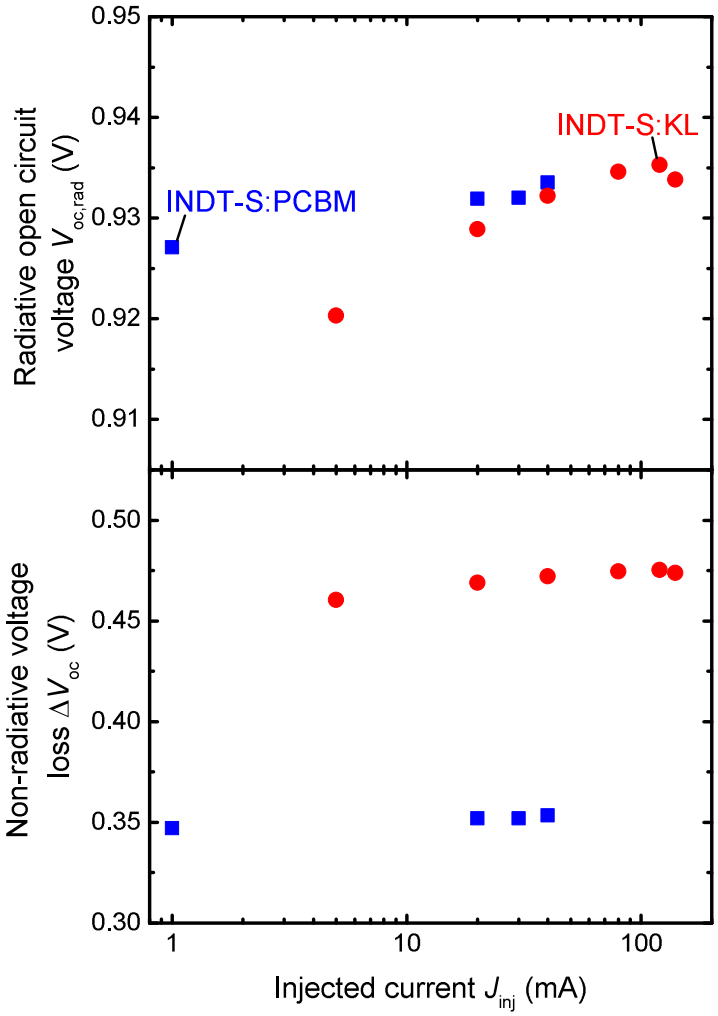


Figure 7.29: Radiative open-circuit voltage $V_{\mathrm{oc,rad}}$ (top panel) and non-radiative voltage loss $\Delta V_{\mathrm{oc,nr}}$ of INDT-S:PCBM (blue squares) and INDT-S:KL (red circles) devices. Both devices have the architecture ITO/ZnO (30 nm)/INDT-S:acceptor (1:2, w/w)/MoO_3/Ag.

7.3.7 Summary of device data and motivation for further measurements

The data presented thus far indicate that for both BTT-DPP and INDT-S devices, blends with KL result in more photocurrent generation from the polymer than blends with PCBM. Furthermore, the electroluminescence spectra do not appear to have a strong contribution from charge transfer states at an energy distinct from the polymer exciton, especially for the BTT-DPP:$PC_{60/70}BM$, INDT-S:PCBM and INDT-S:KL blends; the BTT-DPP:KL appears to have some contribution from a CT state. However without time-resolved measurements which can help to identify the particular species involved, from these data alone it is impossible to determine which species contribute to the charge generation in the KL blends.

One helpful time-resolved measurement is the pump-push experiment introduced previously. This experiment involves exciting the blend at a particular wavelength (the pump), which can be varied, and then after a certain time delay exposing the device to a second push pulse at 2000 nm, and measuring the increase in current as a result. The time scales accessible in this measurement are sub-ps, thus the number of bound states, which can be pushed to separate into free charges, formed very soon after excitation can be measured. In other words, it is possible to probe whether the difference in IQE is a result of differences in the nature of initial photoexcited states, or to do with later charge collection, since the timescale of charge trapping is measured.

A further time-resolved measurement is transient absorption spectroscopy, which again can access sub-ps timescales, and use different excitation wavelengths. Furthermore, the spectrum of the transient absorption at different time-scales can be measured, which along with the dynamics helps to identify the particular species present. Therefore this experiment is a very helpful complement to pump-push photocurrent.

These experiments together could help ascertain the cause for the difference in IQE spectra between the blends. I was particularly interested in probing the difference in charge generation resulting from either polymer excitons or fullerene excitons. In an ideal world, spectral regions would exist where only the polymer or only the fullerene absorbed. Unfortunately that is not quite the case: while the polymer is the only absorbing species at long wavelengths, at short wavelengths, the fullerene absorption dominates but there is an additional significant contribution from the polymer. I should note here that the measurements below were only performed on INDT-S blends, because there was insufficient BTT-DPP material

Table 7.6: Ratio of polymer absorption at pump wavelengths in the pump-push photocurrent experiment. The component extinctions were taken from the VASE-derived extinction coefficients displayed in Figure 7.12. The polymer contribution to absorption is therefore calculated as the INDT-S extinction divided by the total of the two blend components extinction coefficients.

Blend	Wavelength (nm)	INDT-S extinction	Acceptor extinction	Polymer fraction
INDT-S:PCBM	400	0.143	0.300	0.32
	450	0.082	0.154	0.35
	709	0.710	0.007	0.99
	800	0.80	0.01	0.99
INDT-S:KL	400	0.143	0.25	0.36
	450	0.082	0.181	0.31
	709	0.710	0.017	0.98
	800	0.80	0.01	0.99

to do further measurements beyond the ones already described. In order to approximate the proportion of each species absorbing at 800 nm and 400 nm, I used extinction coefficient values from the ellipsometry analysis (Table 7.6).

7.3.8 Pump-push photocurrent

Pump-push photocurrent is able to selectively measure the number of bound states which can result in free charges as a function of time, without being affected by the efficiency of charge extraction. This is demonstrated by considering the plotted quantity $\delta J/J$, the relative increase in current as a result of the second push pulse:

$$\begin{aligned}\frac{\delta J(t)}{J} &\propto \frac{N_{\text{bound}}(t)P_{\text{activation}}\eta_{\text{extract}}}{N_{\text{free}}\eta_{\text{extract}}} \\ &\propto \frac{N_{\text{bound}}P_{\text{activation}}}{N_{\text{free}}}\end{aligned} \tag{7.3}$$

where δJ is the change in current as a result of the pulse, J is the device current, $N_{\text{bound(free)}}$ is the number of bound (free) charges, $P_{\text{activation}}$ is the probability of bound charges being activated into free charges and η_{extract} is the efficiency of charge extraction from the device. I collaborated with Dr Artem Bakulin in

the Chemistry department of Imperial College, who performed pump-push photocurrent on the INDT-S:PCBM and INDT-S:KL devices presented earlier in this section. As mentioned in the motivation section above, the purpose of this experiment was to determine the time scale of charge trapping, and to investigate whether the number of bound charges was affected by whether the polymer or the fullerene was photoexcited.

The two pump wavelengths available were 400 nm and 800 nm. 800 nm is selectively absorbed by the polymer, thus pumping at this wavelength probes the number of bound charges after polymer excitation, or the efficacy of charge generation as a result of electron transfer. 400 nm is mostly absorbed by the fullerene, although I estimate that the polymer absorbs about a third of the photons (see Table 7.6). Therefore pumping at this wavelength probes a mixture of electron and hole transfer, with the dominant contribution being hole transfer from the acceptor.

Figure 7.30 shows the pump-push photocurrent data of the two blends pumped at the two wavelengths. The data show that, regardless of the pump wavelength, the INDT-S:PCBM blend has more bound charges which are activated by the infrared pulse. For the case of the 800 nm pump, the peak ratio of bound charges for the PCBM blend is ten times greater than that of the KL blend, while for the case of the 400 nm pump, the PCBM blend has five times more bound charges. Furthermore, the magnitude of the signal at the 400 nm pump is less for both blends than the signal at the 800 nm pump. These data are therefore consistent with the hypothesis that polymer excitons in the PCBM blend do not have sufficient driving force to charge separate, but this process is enabled in the KL blend. The signal at the 400 nm pump is likely a mix of electron and hole transfer, meaning that there is still a difference between the blends. Furthermore, the fast timescale of the formation of bound charges, exhibited by the large $\delta J/J$ signal at 1 ps, indicates that the bound charges are geminate, as opposed to non-geminate. Overall both blends have a high number of bound charges relative to high-performing blends, which accounts for the low photovoltaic power conversion efficiencies achieved. In addition, the rate of decay of the number of bound charges, reflected in the decay of the $\delta J/J$ signal, is very fast at approximately 30 ps.

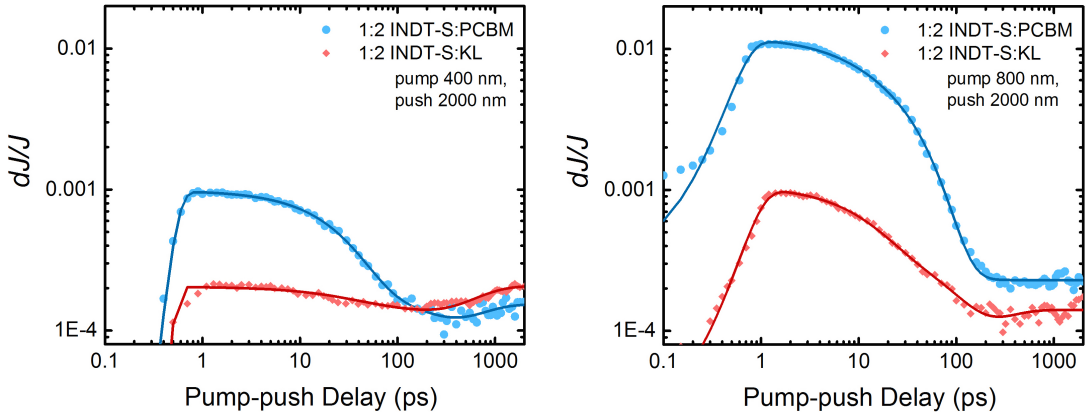


Figure 7.30: Pump-push photocurrent of INDT-S:PCBM (blue) and INDT-S:KL (red) devices. The left panel corresponds to a pump wavelength of 400 nm while the right panel corresponds to a pump wavelength of 800 nm. Regardless of the pump wavelength, the push pulse was 2000 nm. Both devices have the architecture ITO/ZnO (30 nm)/INDT-S:acceptor (1:2, w/w)/MoO_3/Ag, and were the same devices studied earlier in this section. Dr Artem Bakulin and Tom Hopper did the experiment and prepared the figure.

7.3.9 Transient absorption spectroscopy

The pump-push experiment determined that bound states were generated at very fast timescales in all blends, and that the fraction of bound states was greater when the polymer was excited in PCBM blends relative to the fraction upon polymer excitation in KL blends. These bound states could be interfacial polymer-fullerene charge transfer states, exciton-CT hybrid states, or polymer-only states. Transient absorption spectroscopy (TAS) can be performed at the same timescales as the pump-push photocurrent experiment, and can help clarify which particular states are generated at short timescales after photoexcitation. Therefore I collaborated with Dr Tracey Clarke at University College London to acquire these data.

Dr Clarke used pump wavelengths of 450 nm and 800 nm in the TAS experiment; the spectra of the pure polymer and both blend films pumped at the two wavelengths are shown in Figure 7.31. Figure 7.32 shows the corresponding picosecond TAS dynamics, probed at 1200 nm, of the two blends as well as the polymer pumped at both wavelengths. The probe wavelength is absorbed by polymer polarons (Figure 7.31a), which are either bound or free. When pumped at 450 nm (Figure 7.32a), the blends behave similarly, exhibiting the presence of long-lived charged states, whereas the polymer signal quickly decays. The signal from the polymer film decays very quickly because there is not an available pathway for efficient charge separation without an acceptor component. For excitation

at 450 nm, predominantly the acceptor is excited, and both blends are able to generate long-lived charges, mainly via hole transfer to the polymer, although the KL blend appears to have more efficient charge generation than the PCBM blend, consistent with a partial contribution from electron transfer to the fullerene due to polymer excitation. On the other hand, when excited at 800 nm (Figure 7.32b), the dynamics of the PCBM blend signal is almost indistinguishable from the polymer, while the KL blend has some longer-lived charges. This suggests that the species generated by 800 nm excitation in the PCBM blend are the same as those generated in the polymer-only blend, so are polymer-only states. Furthermore, the signal decays with a time constant of approximately 20 ps, which is remarkably similar to the decay of bound charges in the pump-push photocurrent experiment, suggesting that these bound states were dominated by polymeric states.

Dr Clarke also acquired microsecond TAS spectra of the two blends, and the spectra of the two blends excited at 450 nm and 709 nm are shown in Figure 7.33. The peak at approximately 1600 nm corresponds to the polymer polaron, while the higher energy peak, which changes position slightly depending on the blend, likely corresponds to the acceptor anion. For the case of the PCBM blend, excitation at 450 nm generates more signal than excitation at 709 nm, corresponding to a higher concentration of long-lived charges. However the situation is reversed for the case of the KL blend, where excitation at 709 nm results in more free charges than excitation at 450 nm.

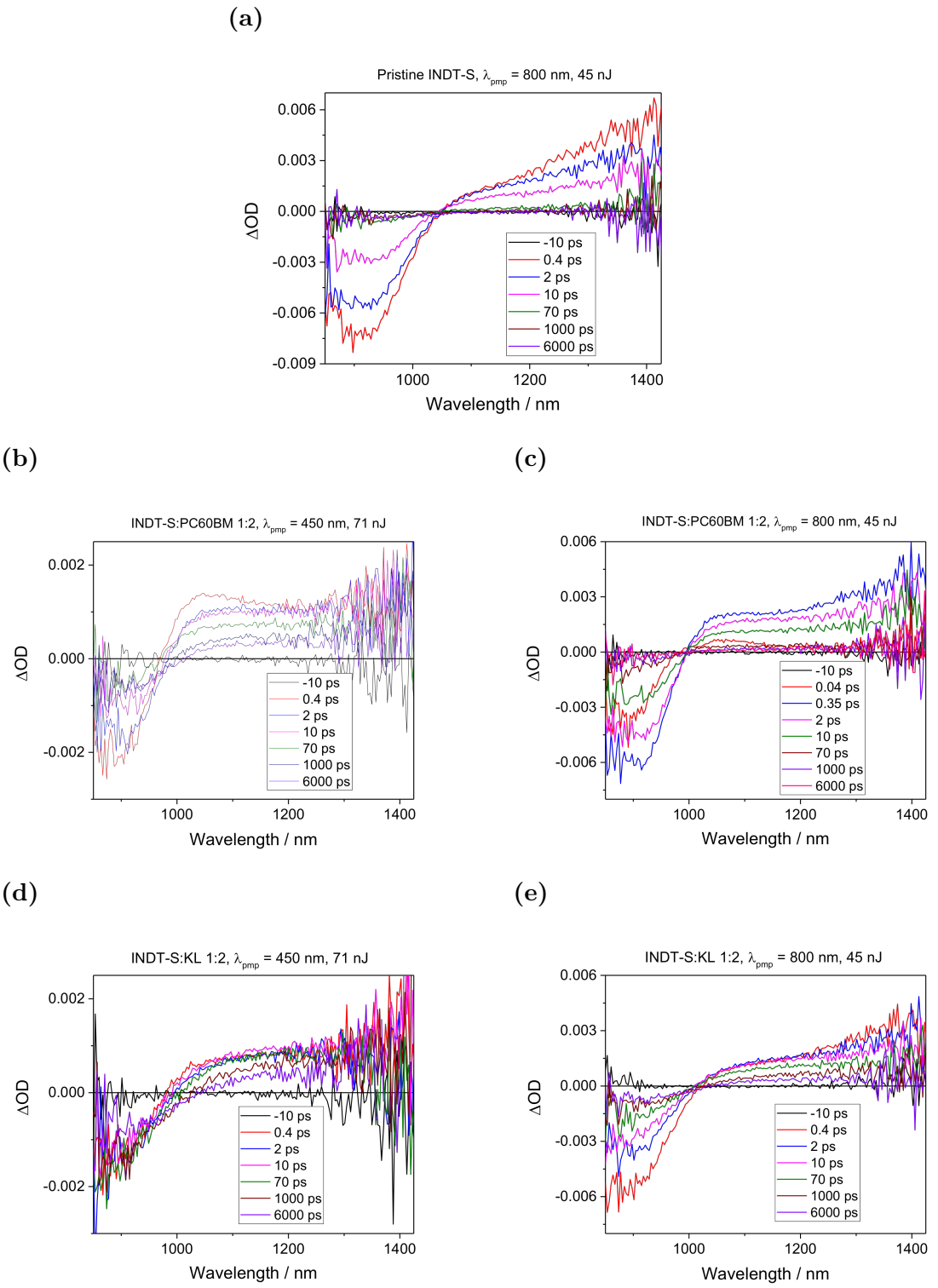


Figure 7.31: Picosecond transient absorption spectroscopy of (a) INDT-S polymer, (b,c) INDT-S:PCBM and (d,e) INDT-S:KL films on spectrosil; both blends are 1:2 w/w. The pump wavelength was either 800 nm (a,c,e) or 450 nm (b,d) in order to selectively probe the polymer or fullerene respectively. The delay times for each spectrum are indicated in the legends. In each case the pump fluence was minimised in order to avoid second-order effects. It is evident from these spectra that there is a long-lived signal in the spectra of INDT-S:KL, irrespective of pump wavelength, and INDT-S:PCBM when pumped at 450 nm only. The corresponding dynamics for a probe wavelength of 1200 nm are shown in Figure 7.32. Figure prepared by Dr Tracey Clarke.

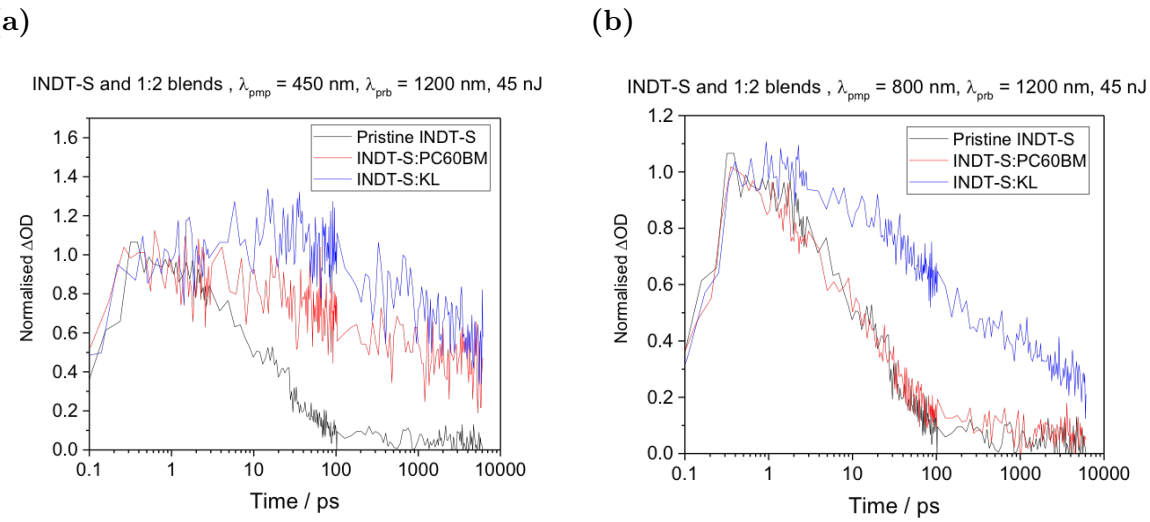


Figure 7.32: ps-TAS data of INDT-S polymer and blend films, pumped at 450 nm (left panel) and 800 nm (right panel). In both panels, the polymer is the black line, INDT-S:PCBM is the red line, and INDT-S:KL is the blue line. Both blends are polymer:acceptor 1:2 (w/w), and all films were deposited on spectrosil. Figure prepared by Dr Tracey Clarke.

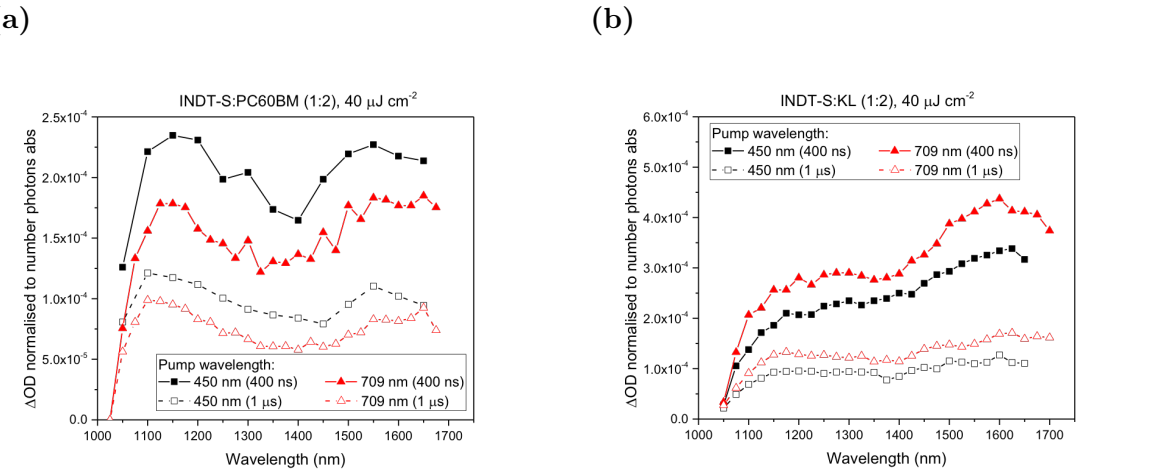


Figure 7.33: μs-TAS data of (a) INDT-S:PCBM and (b) INDT-S:KL blend films; both blends have a 1:2 polymer:acceptor (w/w) composition. In both figures, excitation at 450 nm is shown by black lines, while excitation at 709 nm is shown by red lines. The closed symbols correspond to a delay time of 400 ns, while the open symbols correspond to a delay time of 1 μs. Figure prepared by Dr Tracey Clarke.

7.3.10 Photoluminescence

From the transient absorption spectroscopy data we have proposed that when the polymer is photoexcited in a PCBM blend, the exciton does not dissociate fully to the fullerene but either stays on the polymer or forms an exciton-CT hybrid state. We have determined this by comparing the TA spectra and the dynamics. Another way to track the species present is to look for photoluminescence. Polymer singlets tend to have a strong photoluminescence which is usually strongly quenched in high-performance blends, indicating exciton dissociation from the polymer to the fullerene. Therefore I collaborated with Dr Diego Alonso Alvarez (Imperial College, Physics), who measured the photoluminescence on polymer and blend films, when excited at 785 nm, thereby selectively exciting the polymer.

The results are shown in Figure 7.34, and show that the photoluminescence of the KL blend is significantly more quenched than the PCBM blend. Furthermore, the spectrum does not appear to change relative to the pure polymer film photoluminescence. Therefore we can reasonably conclude that either the luminescing species in each case is the polymer, or a hybrid exciton-CT state at the same energy. The higher photoluminescence flux from the PCBM film relative to the KL film therefore indicates that upon photoexcitation, the polymer exciton indeed does not dissociate very efficiently to the PCBM but can dissociate to the KL.

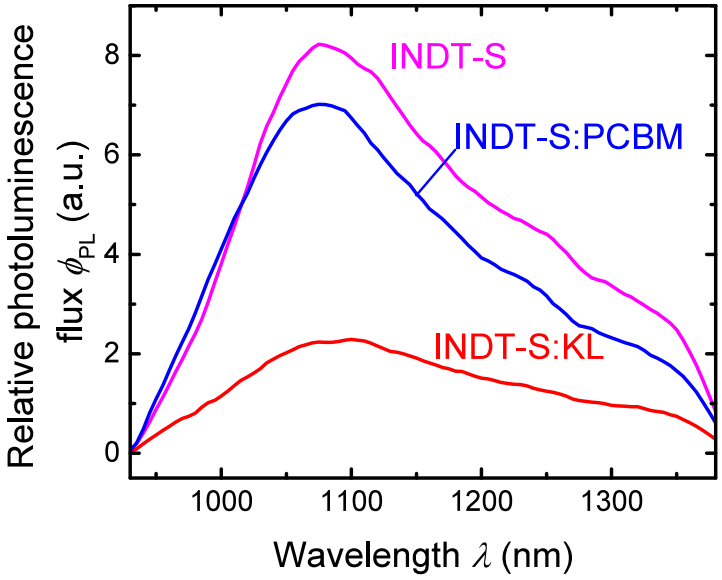


Figure 7.34: Photoluminescence spectra of INDT-S (magenta), INDT-S:PCBM (1:2 w/w) (blue) and INDT-S:KL (1:2 w/w) (red) films on spectrosil. In each case, the film was excited by a continuous wave 785 nm laser with 40 µW power. The photoluminescence was not collected using an integrating sphere and so are not absolute values, nor are they corrected for absorption. For each material three different films were measured, and the data shown above correspond to the greatest PL flux in each case. The INDT-S film was 53 nm thick, INDT-S:PCBM was 187 nm and INDT-S:KL was 134 nm, as measured using a profilometer. PL data was collected by Dr Diego Alonso Alvarez.

7.4 Discussion

This chapter essentially addresses the limit of energetic driving force required for charge separation. Furthermore, the particular species involved in this charge separation are probed, in that we shed light on the various steps from absorption to external current. Once a species in the film has absorbed a photon, the exciton generated can either i) stay on the absorbing species, ii) dissociate but remain on the same species (for example, in a polymer the exciton can dissociate to an adjacent chromophore, to form an intramolecular CT state [247, 248]), iii) charge transfer to an adjacent species forming an intermolecular CT state, iv) form a hybrid exciton-CT state [110], or v) radiatively recombine.

A singlet exciton or an intramolecular CT state itself is unlikely to result in current generation and will most likely radiatively recombine back to the ground state. Intermolecular CT states, especially across heterogeneous species, are spatially more separated and likely to be less strongly coupled to the initial photoexcited state. They can either remain bound at the interface, or the charges can fully charge separate. Free charges can then drift to their respective electrodes resulting in external current, or can meet another charge of opposite polarity and recombine, either radiatively or non-radiatively. If the energy of the absorbing species (i.e. polymer) singlet is degenerate with the lowest CT state, a hybrid exciton-CT state may be generated, which has a greater oscillator strength and lower lifetime than a true interfacial CT state [249]. A hybrid state is characterised by incomplete charge transfer between the species.

The internal quantum efficiency spectra establish that, when a photon is absorbed by the polymer in a PCBM or $PC_{70}BM$ blend where the offset in LUMO energies is approximately zero, this event is unlikely to result in an electron reaching the external circuit. However if the same polymer is blended with KL, with an increased LUMO offset of approximately 170 meV, this event is significantly more likely to result in an electron contributing to current. This finding is similar to a previous study, which instead examined the energy offset required for hole transfer to the polymer [114]. The IQE spectra however do not distinguish between the various sub-processes previously identified in Section 2.5.2. For instance, it is conceivable that free charges generated by higher energy photons are less likely to succumb to non-geminate recombination, in which case the electronic structure of the interfacial states is not relevant. However the IQE spectra do indicate that the charge generation efficiency within the polymer spectral region is not affected by photon energy. This is shown by the flat IQE for wavelengths greater than 650 nm.

The pump-push photocurrent experiment determines that significantly more bound states are formed in the INDT-S:PCBM blend than in the INDT-S:KL blend, at timescales which are too short for non-geminate recombination to be the cause. Therefore, the bound states being probed by this technique are likely geminately-formed intermolecular or intramolecular CT states, or exciton-CT hybrid states, or polymer-only states. The decay time of the bound states is very short (approximately 30 ps) which implies that the states are unlikely to be intermolecular CT states, which tend to have a longer lifetime. However these data cannot be conclusive on this matter. Furthermore, the difference between the number of bound states when the acceptor is excited versus that for polymer excitation indicate that hole transfer can occur comparably efficiently between the two blends. However, electron transfer appears to be severely limited in the INDT-S:PCBM blend.

In the TAS experiments we were able to acquire data from both the polymer and the blend films, which enables us to shed some light on the question of which states are the bottleneck in the charge generation process. The pristine INDT-S and INDT-S:PCBM blend films have almost indistinguishable picosecond dynamics behaviour when pumped at 800 nm and probed at 1200 nm. This suggests that the polaronic state responsible for the ΔOD signal in the PCBM blend is from a polymer-only process. Furthermore, the exponential decay of this state has a time constant of approximately 20 ps, which closely matches the decay time of the bound states responsible for the pump-push photocurrent signal, which implies that this signal is also due to polymer-only states. The INDT-S:KL blend, on the other hand, exhibits a much longer-lived ΔOD signal, corresponding to longer-lived charged states which are likely either intermolecular charge transfer states or free charges. These observations are supported by the photoluminescence data, which show that polymer excitons generated in the PCBM blend do not fully dissociate to the fullerene, but predominantly stay on the polymer and then radiatively recombine, as shown by the limited PL quenching. Meanwhile polymer excitons generated in the KL blend do dissociate to the acceptor much more readily, resulting in a decreased photoluminescence flux.

On the other hand, the blends have much more similar behaviour when excited at 450 nm in the transient absorption experiment, with both blends exhibiting evidence of longer-lived charged states than those causing the polymer signal. However, the KL blend exhibits a slow-rising component at early times, which decreases when the excitation density is increased, suggesting that this is a signature of free charges.

Similarly, the µs-TAS data show the two INDT-S blends behaving differently upon excitation at different wavelengths. Charge generation, embodied by the ΔOD signal at these longer times, is more efficient after 450 nm excitation than after 709 nm excitation in INDT-S:PCBM blends. However the situation is reversed in INDT-S:KL blends, with excitation at 709 nm more efficiently generating free charges. Furthermore, the absolute magnitude of the ΔOD signal for excitation at 450 nm is very similar between the two blends. Therefore the trends observed in the picosecond TAS data, that the KL blend can generate charges from polymer excitation better than the PCBM blend, are corroborated.

It is difficult to conclude decisively the states responsible for the various TAS signals, from those listed at the beginning of this section. There is some evidence that the states observed upon polymer excitation in the PCBM blend are polymeric states, since the dynamics shown in Figure 7.32b are virtually identical between the polymer and PCBM blend case. Furthermore, the PL emission from the PCBM blend is very similar to that from the polymer. However, the TAS spectrum of the PCBM blend is slightly different from the pristine polymer case (Figures 7.31a and 7.31c), with the PCBM blend exhibiting an additional feature at around 1050 nm. In addition, the µs-TAS data (Figure 7.33) shows that the PCBM blend can still form some long-lived charges when excited at the polymer. Furthermore, the IQE value of approximately 10% in the polymer spectral region (Figure 7.21) would be extremely high if there was no contribution from the fullerene. One explanation for these data is that polymer excitation in a PCBM blend results in hybrid exciton-CT states, which behave similarly to excitons, but have some CT state character and so a small percentage can result in separated charges. Another explanation may be that both polymer-only states (intramolecular CT or excitonic), and intermolecular CT states are formed upon excitation, but the behaviour is dominated by the polymer-only states. Quantum chemical calculations could elucidate the energetic landscape and thus help to discern between the possible explanations.

From these data we can propose a model for charge separation from polymer excitons in these systems. When the polymer absorbs a photon, the polymer exciton quickly forms either a polymer-dominated state (a exciton-CT hybrid, or an intramolecular CT exciton), or an intermolecular CT exciton with a fullerene; the branching ratio, i.e. the relative proportion of intermolecular CT excitons formed, depends on the density of states of the fullerene. The deeper the fullerene states, the more likely it is that a distinct intermolecular CT state will be formed, characterised by full electron transfer to the acceptor, which can then fully dissociate into

free charges. The intermolecular CT states have a longer lifetime, and decreased oscillator strength relative to the polymer intramolecular CT state, as evidenced by the decreased PL and EL flux in KL blends, and consistent with a previous study [110]. Meanwhile, if the bottom of the CT state manifold is approximately degenerate with the polymer singlet, a hybrid exciton-CT state may be formed, which may behave very similarly to a polymer exciton, exhibiting a high oscillator strength and short lifetime [249]. This state is characterised by partial electron transfer. Another possibility is the formation of intramolecular CT states. Previous work has generally found that intramolecular CT states may be formed due to variations in the density of states due to polymer microstructure [247, 248]. The similarity in the dynamics between the pristine polymer and the PCBM blend in both the TAS and pump-push experiments support the hypothesis that the states formed are located on the polymer. The various possible states and the proposed mechanism for charge separation, dependent on the acceptor used in the blend, are displayed in Figure 7.35.

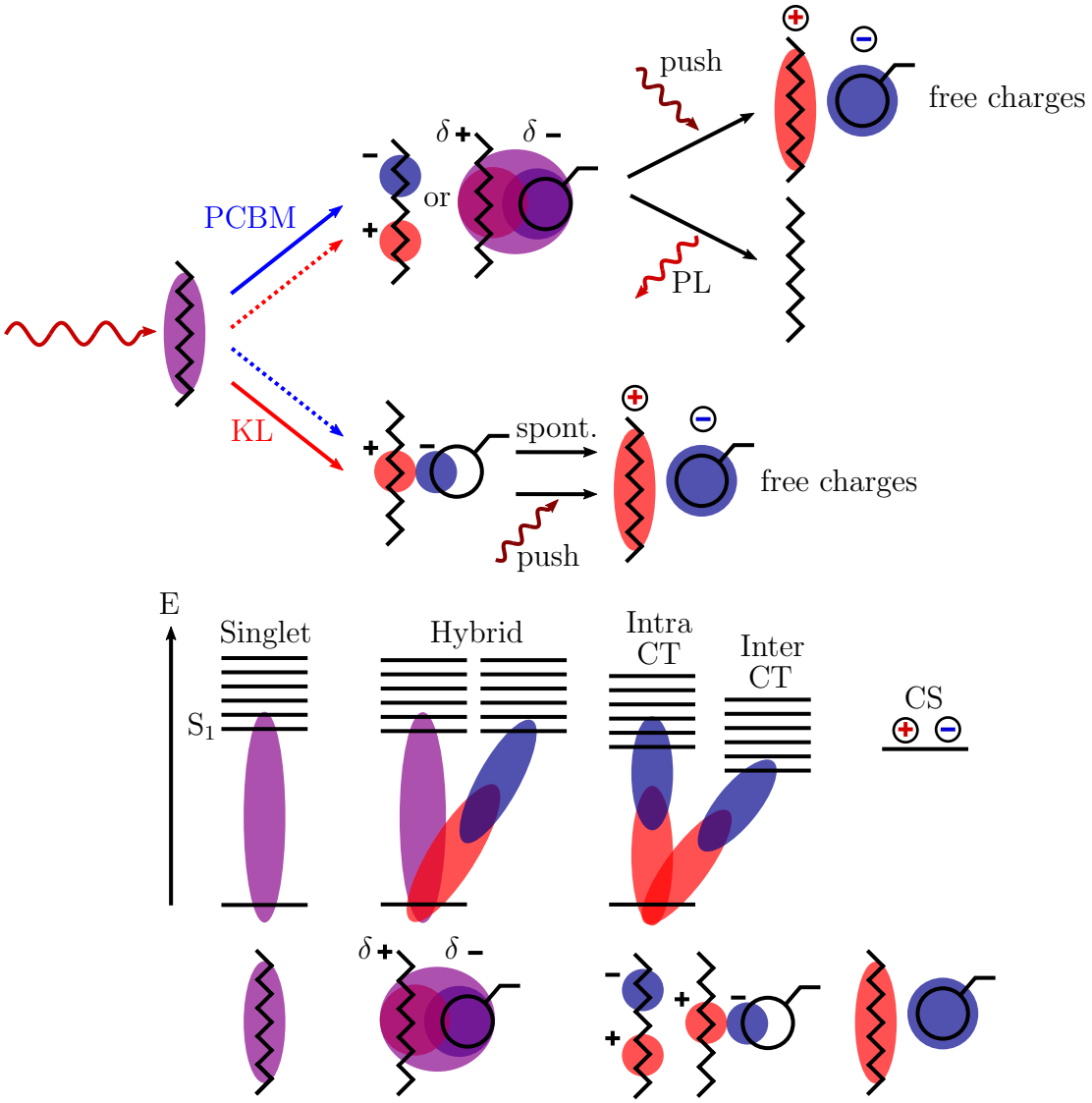


Figure 7.35: Proposed model to explain the INDT-S blend experimental results. In the diagram, the polymer is photoexcited by a low energy pulse, resulting in a polymer singlet exciton (purple). Depending on the particular acceptor the polymer is blended with, the polymer exciton either forms a polymer-only intramolecular CT exciton, or a hybrid exciton-CT state (top branch), or instead forms a heterogeneous intermolecular CT exciton (bottom branch): polymer excitons in the PCBM blend (blue arrows) do not preferentially form an intermolecular CT exciton, while polymer excitons in the KL blend (red arrows) preferentially form the intermolecular CT exciton. The intermolecular CT excitons can dissociate to form separated charges (the CS energy level), either spontaneously or after a push pulse in the pump-push photocurrent experiment. The states in the top branch however either decay radiatively to the ground state, resulting in photoluminescence, or can dissociate into free charges after absorbing a push pulse in the pump-push photocurrent experiment.

7.5 Conclusion

The data presented above provide a remarkably clear picture on the reason behind the differences in charge generation behaviour between blends with very little LUMO level offset, and blends that have a greater LUMO level offset. Insufficient LUMO level offset means that there is an insufficient driving force for the polymer exciton to form a charge transfer state with the acceptor, or that the charge transfer state is not the lowest in energy, meaning that the exciton is trapped on the polymer and eventually recombines. Quantum chemical calculations of the density of states of the donor-acceptor complex, similar to those done in [110], would help elucidate the available states in both blends.

Furthermore, I found that the charge generation efficiency from polymer excitons was not dependent on the photon energy. This resulted in a flat IQE spectrum at wavelengths dominated by polymer absorption.

These findings have implications for design of organic photovoltaic systems more generally as a LUMO-LUMO offset represents an unavoidable energy loss. The rise of power conversion efficiencies of blends using non-fullerene acceptors means that it is now possible to more finely tune relative energy offsets between the donor and acceptor. However the data presented in this chapter suggest that approximately 0.2 eV will inevitably be lost for efficient charge generation to occur. While this study focussed on the LUMO-LUMO offset, since the polymers used were much stronger absorbers than the acceptors, and therefore it is more pertinent to maximise the current generated from polymer excitons, many non-fullerene acceptors exhibit strong light absorption and thus the HOMO-HOMO offset may also prove to be important.

7.6 Experimental Details

The polymers studied in this chapter were made by synthetic chemist collaborators. BTT-DPP was made by Dr Bob Schroeder when he was a member of Prof Iain McCulloch's group in the Chemistry department of Imperial College. Meanwhile INDT-S was made by Kealan Fallon in Dr Hugo Bronstein's group in the Chemistry department of University College London. The ketolactam was kindly provided by Solenne BV, while the PCBM and $PC_{70}BM$ were purchased from Solenne. In general the methods followed in this work are as described previously in Chapter 3.

The BTT-DPP devices used to calculate the IQE spectra had an inverted

architecture and were fabricated using a 25 mg ml^{-1} total concentration solution in a 4:1 chloroform:1,2-dichlorobenzene solvent mixture. The polymer and fullerene were co-dissolved in a 1:2 w/w ratio; this solution was left stirring on a hotplate at 70 °C overnight to ensure full dissolution. After coating of the PEIE layer, the BTT-DPP blend films were bladecoated using a blade speed of 20 mm s^{-1} at a blade height of 200 µm. The bladecoater bed temperature was 30 °C.

On the other hand, the BTT-DPP devices used for the voltage loss analysis had a conventional architecture of ITO/PEDOT:PSS (15 nm)/BTT-DPP:acceptor (1:2, w/w)/Ca (15 nm)/Al (110 nm). The polymer:fullerene solution used to bladecoat the active layer was the same, but the blade speeds used for the BTT-DPP:PCBM, BTT-DPP:$PC_{70}BM$ and BTT-DPP:KL active layers were 20, 25 and 30 mm s^{-1} respectively. In each case the bladecoater bed was held at 30 °C.

The INDT-S blend active layer for devices was coated from a 30 mg ml^{-1} (total) concentration solution in 1,2-dichlorobenzene. The polymer and fullerene were co-dissolved in a 1:2 w/w ratio; this solution was left stirring on a hotplate at 120 °C overnight to ensure full dissolution. After coating of the ZnO layer, the INDT-S blend films were bladecoated using a blade speed of 25 mm s^{-1} at a blade height of 200 µm. The bladecoater bed temperature was 120 °C; the substrates were stored on the bed prior to coating to ensure temperature equilibration.

In each of the device batches used for IQE measurements, a custom evaporation mask was used to evaporate the electrodes, which allowed eight of the sixteen substrates to have very large area electrodes while the remaining eight were the usual configuration of six 0.045 cm^2 devices per substrate.

The BTT-DPP-based films for ellipsometry were coated on spectrosil and silicon; the solutions for the pristine polymer and blend films were all 25 mg ml^{-1} total concentration in 4:1 chloroform:1,2-dichlorobenzene. The ketolactam films for ellipsometry were made using a 40 mg ml^{-1} solution in the same solvent mixture. The films were bladecoated at speeds between 10 and 60 mm s^{-1} to achieve a range of thicknesses. The film UV-Vis spectra were taken on the spectrosil films.

The INDT-S-based films for ellipsometry, transient absorption spectroscopy and photoluminescence were deposited on spectrosil substrates as well. The solutions were prepared in the same way as for devices, except with a concentration of 10 mg ml^{-1} for the polymer-only solution. The films were bladecoated at speeds ranging between 25 and 95 mm s^{-1}.

The INDT-S ellipsometry data were taken on a J.A. Woollam V-VASE ellipsometer, and the data were analysed using the Sopra Winelli II software with the help of Dr Mariano Campoy.

Photoluminecence (PL) was excited using a continuous wave Ti: sapphire laser (Spectra Physics) tuned to 785 nm and 40 µW of absolute power. PL was collected using a 0.5 m focal length spectrometer (Acton 2300i, Princeton Instruments) and an InP/InGaAsP photomultiplier tube for the detection (H12694-45, Hamamatsu). PL intensity was checked at several positions around the centre of the samples to be confident that the spectra taken were representative of the material average properties.

Chapter 8

Conclusions and further work

The focus of this thesis was to examine the factors affecting charge generation and recombination in organic photovoltaics. To this end, I conducted experimental studies of multiple test systems, in order to determine the limiting characteristic(s) in each case. The goal was to use these systematic studies to inform future design of organic photovoltaic devices. Below I therefore first outline the main conclusions I have been able to draw, and then I suggest future work which may build on the work presented here.

8.1 Conclusions

Polymer molecular weight is a critical parameter underlying any study into polymer characteristics. With regard to OPV research, it is a critical parameter to be able to control because the molecular weight distribution can have a profound effect on a myriad of properties. In Chapter 4 I looked to address the source of high non-radiative recombination losses in OPV. I found that devices made from high molecular weight C_2C_6-IDTBT exhibited lower levels of non-radiative recombination, relative to devices made from a non-fractionated batch, which contained a wider range of molecular weight polymer chains. This lower non-radiative recombination coincided with longer charge lifetimes, which outweighed the lower mobility values, resulting in greater mobility-lifetime product values. While determining the cause of the increased non-radiative recombination in non-fractionated polymer blends was beyond the remit of my study, possible explanations include increased concentration of end-groups or impurities, both of which may act as recombination centres. The decreased non-radiative recombination in higher MW material also coincided with increased EL efficiency, as expected from reciprocity relations.

I conducted another study on the influence of polymer molecular weight on OPV performance, but this time focussing on a DPP-TT-T polymer (Chapters 5 and 6). Again I found that the high molecular weight polymer devices exhibited lower non-radiative voltage losses, although this time the charge lifetime was independent of molecular weight while the carrier mobility was greater in high molecular weight polymer devices. This highlights that with polymers, a 'one size fits all' approach is rarely appropriate due to the many inter-related factors. More strikingly however, and in direct contrast to the C_2C_6-IDTBT case, I found a strong dependence of optical absorption on molecular weight, with the high molecular weight polymers absorbing light more strongly than any polymer system we could find in the literature. It appears that stronger optical absorption contributed to better solar cell efficiencies, along with greater electronic quality.

This observation was surprising, since we would expect the chromophores to be unaffected by the overall length of the polymer chains, which were well above the conjugation length, and so we carried out a detailed study to attempt to elucidate the key factors (Chapter 6). Quantum chemical calculations showed that persistence length, or the linearity of the polymer, was the best predictor of optical absorption strength. We found that DPP-TT-T, regardless of its conformation, tended to be very linear. The calculations predicted that two other polymers, DPP3T and IDTBT, would also exhibit very high optical absorption, and indeed we found this was the case. We also found evidence that the molecular weight dependence of absorption in DPP-TT-T was likely the result of differences in polymer conformation, and that the low molecular weight polymer had a higher concentration of curved segments.

Another aspect of current generation is understanding the energetics of exciton dissociation, which generally results in a significant energy loss. Chapter 7 examined this by looking at the effect of pushing the acceptor density of states to lower energy by using a ketolactam fullerene instead of PCBM. Specifically, I looked at the dependence of current collection on the energy of the initial photoexcitation. I found that, when PCBM was the acceptor and there was very little energy offset between the polymer and the acceptor, polymer excitons did not result in collected electrons. Furthermore, I found that the bottleneck process was the formation of interfacial charge transfer states: when PCBM was the acceptor, the polymer excitons stayed on the polymer and eventually recombined. However, when the acceptor density of states was pushed down by using a ketolactam instead, it became favourable for interfacial charge transfer states to be formed, which could dissociate. This study therefore took a step towards quantifying the

precise energy offset required for efficient charge separation, which is ever more important given the recent developments of more tunable non-fullerene acceptors.

The work in this thesis has been presented in the context of organic photovoltaic devices, but can be more widely applied, especially given the rising prominence and bright outlook of plastic electronics in general [250]. For example, the work towards understanding how to maximise light absorption could help inform design for other devices, such as photodetectors, which may require a very thin light-sensitive layer. Understanding the processes which increase non-radiative recombination is also important for improving light-emitting diodes. And the process of charge separation is a question of fundamental understanding of soft matter physics, as well as being important for the development of solar cells.

8.2 Suggestions for further work

Perhaps the most pertinent aspect of further development needed to achieve high-efficiency OPV devices is to further reduce the energy losses if possible. To this end, further work on exploring the origins of non-radiative recombination is needed, as well as decreasing the energy offsets required for efficient charge separation. On the latter point, the advent of non-fullerene acceptors as well as more ordered small-molecule organic solar cells is extremely interesting. With more tunable and ordered systems there is potential to conduct more systematic studies to try and fine-tune the minimisation of energy losses. There are multiple methods to measure recombination, and so a better understanding of how they inter-relate, and more understanding of the losses at a molecular level are needed. For example, greater understanding is needed of how the phase behaviour and molecular packing affects electronic properties. There is also much to be understood with regards to the mechanism of charge separation. Since this is such a multi-scale problem, multi-scale modelling will likely be helpful to try and explain the experimental observations.

There is also much work to be done to understand what limits light absorption in conjugated polymers. The integrated oscillator strength in the visible is an order of magnitude less than the theoretical maximum, so there is a lot of space for potential improvement. Experimental measurement of persistence length in polymers is key to validating our hypothesis, although this is not an easy measurement to do. Neutron scattering can be a very useful method to examine the conformation of molecules in solution, while more classical polymer science methods such as the intrinsic viscosity could also afford a measurement of the

persistence length; both these experiments are underway. Furthermore, the availability of well-controlled oligomers allows for more fundamental assessments of the effect of chain length on the optical absorption. These small systems are also well-suited to complementary quantum chemical calculations as well as molecular dynamics, which could prove very fruitful.

More generally, and unrelated to my research, work is needed to understand and control the mechanisms of degradation in OPV if this technology is going to become commercially viable. In addition, scaling up from lab-scale to industry scale has its hurdles which will need to be overcome. These hurdles are for example materials-related, such as developing cheaper routes of polymer synthesis, or processing-related, such as understanding better the rheology of the printing process and optimising the ink, perhaps moving away from chlorinated solvents. OPV has some particular advantages over the established solar cell technologies so its success will likely rely on targeting specialised applications.

Bibliography

[1] Central Intelligence Agency. *CIA World Factbook*. 2016. URL: https://www.cia.gov/library/publications/the-world-factbook/geos/xx.html (visited on 02/14/2017).

[2] United Nations Sustainable Development. *Sustainable development goals*. 2016. URL: http://www.un.org/sustainabledevelopment/energy/ (visited on 02/14/2017).

[3] US Energy Information Administration. *International Energy Outlook 2016*. 2016. URL: https://www.eia.gov/outlooks/ieo/ (visited on 02/20/2017).

[4] European Environment Agency. *Electric vehicles and the energy sector - impacts on Europe's future emissions*. 2016. URL: http://www.eea.europa.eu/themes/transport/electric-vehicles/electric-vehicles-and-energy (visited on 02/20/2017).

[5] United Nations Development Programme. *World Energy Assessment*. 2000. URL: http://www.undp.org/content/dam/aplaws/publication/en/publications/environment-energy/www-ee-library/sustainable-energy/world-energy-assessment-energy-and-the-challenge-of-sustainability/World%20Energy%20Assessment-2000.pdf/ (visited on 02/20/2017).

[6] World Energy Council. *World Energy Resources 2016*. 2016. URL: https://www.worldenergy.org/wp-content/uploads/2016/10/World-Energy-Resources-Full-report-2016.10.03.pdf (visited on 02/20/2017).

[7] Solargis. *Solargis GHI Solar Map*. 2017. URL: http://solargis.com/products/maps-and-gis-data/free/download/world (visited on 02/20/2017).

[8] Lighting a Billion Lives. *Lighting a Billion Lives*. 2017. URL: http://labl.teriin.org (visited on 02/20/2017).

[9] Mikkel Jørgensen, Jon E. Carlé, Roar R. Søndergaard, Marie Lauritzen, Nikolaj A. Dagnæs-Hansen, Sedi L. Byskov, Thomas R. Andersen, Thue T. Larsen-Olsen, Arvid P. L. Böttiger, Birgitta Andreasen, Lei Fu, Lijian Zuo, Yao Liu, Eva Bundgaard, Xiaowei Zhan, Hongzheng Chen, and Frederik C. Krebs. "The state of organic solar cells - A meta analysis". In: *Solar Energy Materials and Solar Cells* 119 (2013), pp. 84–93.

[10] Jefferson Lab. *Periodic Table of Elements*. URL: `http://education.jlab.org/itselemental/index.html` (visited on 02/20/2017).

[11] Roar R. Søndergaard, Markus Hösel, and Frederik C. Krebs. "Roll-to-Roll fabrication of large area functional organic materials". In: *Journal of Polymer Science Part B: Polymer Physics* 51.1 (2013), pp. 16–34.

[12] United States Department of Energy. *Organic Photovoltaics Research*. 2017. URL: `https://www.energy.gov/eere/sunshot/organic-photovoltaics-research` (visited on 02/20/2017).

[13] Christopher J. M. Emmott, Jason A. Röhr, Mariano Campoy-Quiles, Thomas Kirchartz, Antonio Urbina, Nicholas J. Ekins-Daukes, and Jenny Nelson. "Organic photovoltaic greenhouses: a unique application for semi-transparent PV?" In: *Energy Environ. Sci.* 8 (4 2015), pp. 1317–1328.

[14] National Renewable Energy Laboratory. *Best research-cell efficiencies*. 2017. URL: `https://www.nrel.gov/pv/` (visited on 02/20/2017).

[15] Linyi Bian, Enwei Zhu, Jian Tang, Weihua Tang, and Fujun Zhang. "Recent progress in the design of narrow bandgap conjugated polymers for high-efficiency organic solar cells". In: *Progress in Polymer Science* 37.9 (2012), pp. 1292–1331.

[16] Y. Liu, J. Zhao, Z. Li, C. Mu, W. Ma, H. Hu, K. Jiang, H. Lin, H. Ade, and H. Yan. "Aggregation and morphology control enables multiple cases of high-efficiency polymer solar cells". In: *Nat Commun* 5 (2014), p. 5293.

[17] Shaoqing Zhang, Long Ye, and Jianhui Hou. "Breaking the 10% Efficiency Barrier in Organic Photovoltaics: Morphology and Device Optimization of Well-Known PBDTTT Polymers". In: *Advanced Energy Materials* 6.11 (2016).

[18] Nicola Gasparini, Luca Lucera, Michael Salvador, Mario Prosa, George D. Spyropoulos, Peter Kubis, Hans-Joachim Egelhaaf, Christoph J. Brabec, and Tayebeh Ameri. "High-performance ternary organic solar cells with

thick active layer exceeding 11% efficiency". In: *Energy Environ. Sci.* (2017).

[19] Yuze Lin and Xiaowei Zhan. "Non-fullerene acceptors for organic photovoltaics: an emerging horizon". In: *Mater. Horiz.* 1 (5 2014), pp. 470–488.

[20] Antonio Facchetti. "Polymer donor - polymer acceptor (all-polymer) solar cells". In: *Materials Today* 16.4 (2013), pp. 123–132.

[21] Nanjia Zhou, Alexander S. Dudnik, Ting I. N. G. Li, Eric F. Manley, Thomas J. Aldrich, Peijun Guo, Hsueh-Chung Liao, Zhihua Chen, Lin X. Chen, Robert P. H. Chang, Antonio Facchetti, Monica Olvera de la Cruz, and Tobin J. Marks. "All-Polymer Solar Cell Performance Optimized via Systematic Molecular Weight Tuning of Both Donor and Acceptor Polymers". In: *Journal of the American Chemical Society* 138.4 (2016), pp. 1240–1251.

[22] Qian Zhang, Bin Kan, Feng Liu, Guankui Long, Xiangjian Wan, Xiaoqing Chen, Yi Zuo, Wang Ni, Huijing Zhang, Miaomiao Li, Zhicheng Hu, Fei Huang, Yong Cao, Ziqi Liang, Mingtao Zhang, Thomas P. Russell, and Yongsheng Chen. "Small-molecule solar cells with efficiency over 9%". In: *Nat Photon* 9.1 (Jan. 2015), pp. 35–41.

[23] Bin Kan, Qian Zhang, Miaomiao Li, Xiangjian Wan, Wang Ni, Guankui Long, Yunchuang Wang, Xuan Yang, Huanran Feng, and Yongsheng Chen. "Solution-Processed Organic Solar Cells Based on Dialkylthiol-Substituted Benzodithiophene Unit with Efficiency near 10%". In: *Journal of the American Chemical Society* 136.44 (2014), pp. 15529–15532.

[24] Sachetan M. Tuladhar, Mohammed Azzouzi, Florent Delval, Jizhong Yao, Anne A. Y. Guilbert, Thomas Kirchartz, Nuria F. Montcada, Rocio Dominguez, Fernando Langa, Emilio Palomares, and Jenny Nelson. "Low Open-Circuit Voltage Loss in Solution-Processed Small-Molecule Organic Solar Cells". In: *ACS Energy Letters* 1.1 (2016), pp. 302–308.

[25] Douglas W. Sievers, Vishal Shrotriya, and Yang Yang. "Modeling optical effects and thickness dependent current in polymer bulk-heterojunction solar cells". In: *Journal of Applied Physics* 100.11 (2006), p. 114509.

[26] F. Deledalle, T. Kirchartz, M. S. Vezie, M. Campoy-Quiles, P. S. Tuladhar, J. Nelson, and J. R. Durrant. "Understanding the Effect of Unintentional Doping on Transport Optimization and Analysis in Efficient Organic Bulk-Heterojunction Solar Cells". In: *Physical Review X* 5.1 (2015).

[27] Jizhong Yao, Thomas Kirchartz, Michelle S Vezie, Mark A Faist, Wei Gong, Zhicai He, Hongbin Wu, Joel Troughton, Trystan Watson, Daniel Bryant, and Jenny Nelson. "Quantifying losses in open-circuit voltage in solution-processable solar cells". In: *Physical review applied* 4.1 (2015), p. 014020.

[28] Markus C. Scharber. "On the Efficiency Limit of Conjugated Polymer:Fullerene-Based Bulk Heterojunction Solar Cells". In: *Advanced Materials* 28.10 (2016), pp. 1994–2001.

[29] Dechan Angmo and Frederik C. Krebs. "Over 2 Years of Outdoor Operational and Storage Stability of ITO-Free, Fully Roll-to-Roll Fabricated Polymer Solar Cell Modules". In: *Energy Technology* 3.7 (2015), pp. 774–783.

[30] Christopher J.M. Emmott, Davide Moia, Philip Sandwell, Nicholas Ekins-Daukes, Markus Hösel, Lukas Lukoschek, Charith Amarasinghe, Frederik C. Krebs, and Jenny Nelson. "In-situ, long-term operational stability of organic photovoltaics for off-grid applications in Africa". In: *Solar Energy Materials and Solar Cells* 149 (2016), pp. 284–293.

[31] William R. Mateker and Michael D. McGehee. "Progress in Understanding Degradation Mechanisms and Improving Stability in Organic Photovoltaics". In: *Advanced Materials* (2016).

[32] Marios D. Chatzisideris, Nieves Espinosa, Alexis Laurent, and Frederik C. Krebs. "Ecodesign perspectives of thin-film photovoltaic technologies: A review of life cycle assessment studies". In: *Solar Energy Materials and Solar Cells* 156 (2016), pp. 2–10.

[33] C. J. M. Emmott. "The carbon mitigation potential of emerging photovoltaic technology". Thesis. 2015.

[34] Erin L. Ratcliff, Brian Zacher, and Neal R. Armstrong. "Selective Interlayers and Contacts in Organic Photovoltaic Cells". In: *The Journal of Physical Chemistry Letters* 2.11 (2011), pp. 1337–1350.

[35] A. Katsouras, N. Gasparini, C. Koulogiannis, M. Spanos, T. Ameri, C. J. Brabec, C. L. Chochos, and A. Avgeropoulos. "Systematic Analysis of Polymer Molecular Weight Influence on the Organic Photovoltaic Performance". In: *Macromol Rapid Commun* 36.20 (2015), pp. 1778–97.

[36] Feng Liu, Yu Gu, Jae Woong Jung, Won Ho Jo, and Thomas P. Russell. "On the morphology of polymer-based photovoltaics". In: *Journal of Polymer Science Part B: Polymer Physics* 50.15 (2012), pp. 1018–1044.

[37] C. R. Osterwald and T. J. McMahon. “History of accelerated and qualification testing of terrestrial photovoltaic modules: A literature review”. In: *Progress in Photovoltaics: Research and Applications* 17.1 (2009), pp. 11–33.

[38] Scot Wheeler, Florent Deledalle, Nurlan Tokmoldin, Thomas Kirchartz, Jenny Nelson, and James R. Durrant. “Influence of Surface Recombination on Charge-Carrier Kinetics in Organic Bulk Heterojunction Solar Cells with Nickel Oxide Interlayers”. In: *Phys. Rev. Applied* 4 (2 Aug. 2015), p. 024020.

[39] Mark Fox. *Optical Properties of Solids*. Oxford University Press, 2010.

[40] Donald A. McQuarrie. *Quantum Chemistry*. University Science Books, 2008.

[41] Jenny Nelson and Michael R Tarbutt. Personal communication. 2016.

[42] Jenny Nelson. *Light and Matter Lecture Notes*. 2015.

[43] Frederick Wooten. *Optical Properties of Solids*. Academic Press Inc., 1972.

[44] W. Barford and M. Marcus. “Theory of optical transitions in conjugated polymers. I. Ideal systems”. In: *Journal of Chemical Physics* 141.16 (2014).

[45] M. Marcus, O. R. Tozer, and W. Barford. “Theory of optical transitions in conjugated polymers. II. Real systems”. In: *Journal of Chemical Physics* 141.16 (2014), p. 164102.

[46] Christoph J. Brabec, Martin Heeney, Iain McCulloch, and Jenny Nelson. “Influence of blend microstructure on bulk heterojunction organic photovoltaic performance”. In: *Chemical Society Reviews* 40.3 (2011).

[47] Michael A. Brady, Gregory M. Su, and Michael L. Chabinyc. “Recent progress in the morphology of bulk heterojunction photovoltaics”. In: *Soft Matter* 7.23 (2011), p. 11065.

[48] C. Piliego, T. W. Holcombe, J. D. Douglas, C. H. Woo, P. M. Beaujuge, and J. M. J. Fréchet. “Synthetic Control of Structural Order in N-Alkylthieno[3,4-c]pyrrole-4,6-dione-Based Polymers for Efficient Solar Cells”. In: *Journal of the American Chemical Society* 132.22 (2010), pp. 7595–+.

[49] A. T. Yiu, P. M. Beaujuge, O. P. Lee, C. H. Woo, M. F. Toney, and J. M. Fréchet. “Side-chain tunability of furan-containing low-band-gap polymers provides control of structural order in efficient solar cells”. In: *J Am Chem Soc* 134.4 (2012), pp. 2180–5.

[50] Ergang Wang, Jonas Bergqvist, Koen Vandewal, Zaifei Ma, Lintao Hou, Angelica Lundin, Scott Himmelberger, Alberto Salleo, Christian Müller, Olle Inganäs, Fengling Zhang, and Mats R. Andersson. "Conformational Disorder Enhances Solubility and Photovoltaic Performance of a Thiophene-Quinoxaline Copolymer". In: *Advanced Energy Materials* 3.6 (2013), pp. 806–814.

[51] Ta-Ya Chu, Jianping Lu, Serge Beaupré, Yanguang Zhang, Jean-Rémi Pouliot, Jiayun Zhou, Ahmed Najari, Mario Leclerc, and Ye Tao. "Effects of the Molecular Weight and the Side-Chain Length on the Photovoltaic Performance of Dithienosilole/Thienopyrrolodione Copolymers". In: *Advanced Functional Materials* 22.11 (2012), pp. 2345–2351.

[52] C. Cabanetos, A. El Labban, J. A. Bartelt, J. D. Douglas, W. R. Mateker, J. M. Fréchet, M. D. McGehee, and P. M. Beaujuge. "Linear side chains in benzo[1,2-b:4,5-b']dithiophene-thieno[3,4-c]pyrrole-4,6-dione polymers direct self-assembly and solar cell performance". In: *J Am Chem Soc* 135.12 (2013), pp. 4656–9.

[53] Youngkyoo Kim, Steffan Cook, Sachetan M. Tuladhar, Stelios A. Choulis, Jenny Nelson, James R. Durrant, Donal D. C. Bradley, Mark Giles, Iain McCulloch, Chang-Sik Ha, and Moonhor Ree. "A strong regioregularity effect in self-organizing conjugated polymer films and high-efficiency polythiophene:fullerene solar cells". In: *Nature Materials* 5.3 (2006), pp. 197–203.

[54] James H Bannock, Siva H Krishnadasan, Adrian M Nightingale, Chin Pang Yau, Kevin Khaw, Daniel Burkitt, Jonathan JM Halls, Martin Heeney, and John C de Mello. "Continuous Synthesis of Device-Grade Semiconducting Polymers in Droplet-Based Microreactors". In: *Advanced Functional Materials* 23.17 (2013), pp. 2123–2129.

[55] Steven Holdcroft. "Determination of molecular weights and Mark–Houwink constants for soluble electronically conducting polymers". In: *Journal of Polymer Science Part B: Polymer Physics* 29.13 (1991), pp. 1585–1588.

[56] Paul J. Flory. *Principles of Polymer Chemistry*. Cornell University Press, 1953.

[57] Felix Peter Vinzenz Koch, Jonathan Rivnay, Sam Foster, Christian Müller, Jonathan M. Downing, Ester Buchaca-Domingo, Paul Westacott, Liyang Yu, Mingjian Yuan, Mohammed Baklar, Zhuping Fei, Christine Luscombe,

Martyn A. McLachlan, Martin Heeney, Garry Rumbles, Carlos Silva, Alberto Salleo, Jenny Nelson, Paul Smith, and Natalie Stingelin. "The impact of molecular weight on microstructure and charge transport in semicrystalline polymer semiconductors - poly(3-hexylthiophene), a model study". In: *Progress in Polymer Science* (2013).

[58] Amy M. Ballantyne, Lichun Chen, Justin Dane, Thomas Hammant, Felix M. Braun, Martin Heeney, Warren Duffy, Iain McCulloch, Donal D. C. Bradley, and Jenny Nelson. "The Effect of Poly(3-hexylthiophene) Molecular Weight on Charge Transport and the Performance of Polymer:Fullerene Solar Cells". In: *Advanced Functional Materials* 18.16 (2008), pp. 2373–2380.

[59] Jonathan A. Bartelt, Jessica D. Douglas, William R. Mateker, Abdulrahman El Labban, Christopher J. Tassone, Michael F. Toney, Jean M. J. Fréchet, Pierre M. Beaujuge, and Michael D. McGehee. "Controlling Solution-Phase Polymer Aggregation with Molecular Weight and Solvent Additives to Optimize Polymer-Fullerene Bulk Heterojunction Solar Cells". In: *Advanced Energy Materials* 4.9 (2014), n/a–n/a.

[60] Pascal Wolfer, Ardalan Armin, Almantas Pivrikas, Marappan Velusamy, Paul L. Burn, and Paul Meredith. "Solution structure: defining polymer film morphology and optoelectronic device performance". In: *J. Mater. Chem. C* 2 (1 2014), pp. 71–77.

[61] Nayool Shin, Lee J. Richter, Andrew A. Herzing, R. Joseph Kline, and Dean M. DeLongchamp. "Effect of Processing Additives on the Solidification of Blade-Coated Polymer/Fullerene Blend Films via In-Situ Structure Measurements". In: *Advanced Energy Materials* 3.7 (2013), pp. 938–948.

[62] Tiziano Agostinelli, Samuele Lilliu, John G. Labram, Mariano Campoy-Quiles, Mark Hampton, Ellis Pires, Jonathan Rawle, Oier Bikondoa, Donal D. C. Bradley, Thomas D. Anthopoulos, Jenny Nelson, and J. Emyr Macdonald. "Real-Time Investigation of Crystallization and Phase-Segregation Dynamics in P3HT:PCBM Solar Cells During Thermal Annealing". In: *Advanced Functional Materials* 21.9 (2011), pp. 1701–1708.

[63] E. Buchaca-Domingo, A. J. Ferguson, F. C. Jamieson, T. McCarthy-Ward, S. Shoaee, J. R. Tumbleston, O. G. Reid, L. Yu, M. B. Madec, M. Pfannmöller, F. Hermerschmidt, R. R. Schröder, S. E. Watkins, N. Kopidakis, G. Portale, A. Amassian, M. Heeney, H. Ade, G. Rumbles, J. R. Durrant, and N. Stingelin. "Additive-assisted supramolecular manipulation

of polymer:fullerene blend phase morphologies and its influence on photophysical processes". In: *Mater. Horiz.* 1.2 (2014), pp. 270–279.

[64] Subhrangsu Mukherjee, Christopher M. Proctor, Guillermo C. Bazan, Thuc-Quyen Nguyen, and Harald Ade. "Significance of Average Domain Purity and Mixed Domains on the Photovoltaic Performance of High-Efficiency Solution-Processed Small-Molecule BHJ Solar Cells". In: *Advanced Energy Materials* 5.21 (2015), n/a–n/a.

[65] Mariateresa Scarongella, Arun Aby Paraecattil, Ester Buchaca-Domingo, Jessica D Douglas, Serge Beaupré, Thomas McCarthy-Ward, M Heeney, J-E Moser, Mario Leclerc, JMJ Fréchet, Natalie Stingelin, and Natalie Banerji. "The influence of microstructure on charge separation dynamics in organic bulk heterojunction materials for solar cell applications". In: *Journal of Materials Chemistry A* 2.17 (2014), pp. 6218–6230.

[66] N. D. Treat, A. Varotto, C. J. Takacs, N. Batara, M. Al-Hashimi, M. J. Heeney, A. J. Heeger, F. Wudl, C. J. Hawker, and M. L. Chabinyc. "Polymer-fullerene miscibility: a metric for screening new materials for high-performance organic solar cells". In: *J Am Chem Soc* 134.38 (2012), pp. 15869–79.

[67] Shoji Miyanishi, Keisuke Tajima, and Kazuhito Hashimoto. "Morphological stabilization of polymer photovoltaic cells by using cross-linkable poly (3-(5-hexenyl) thiophene)". In: *Macromolecules* 42.5 (2009), pp. 1610–1618.

[68] Rajeev Dattani, James H Bannock, Zhuping Fei, Roderick CI MacKenzie, Anne AY Guilbert, Michelle S Vezie, Jenny Nelson, John C de Mello, Martin Heeney, João T Cabral, and Alisyn J. Nedoma. "A general mechanism for controlling thin film structures in all-conjugated block copolymer: fullerene blends". In: *Journal of Materials Chemistry A* 2.35 (2014), pp. 14711–14719.

[69] Kenneth R. Graham, Clement Cabanetos, Justin P. Jahnke, Matthew N. Idso, Abdulrahman El Labban, Guy O. Ngongang Ndjawa, Thomas Heumueller, Koen Vandewal, Alberto Salleo, Bradley F. Chmelka, Aram Amassian, Pierre M. Beaujuge, and Michael D. McGehee. "Importance of the Donor: Fullerene Intermolecular Arrangement for High-Efficiency Organic Photovoltaics". In: *Journal of the American Chemical Society* 136.27 (2014), pp. 9608–9618.

[70] M. Campoy-Quiles, T. Ferenczi, T. Agostinelli, P. G. Etchegoin, Y. Kim, T. D. Anthopoulos, P. N. Stavrinou, D. D. Bradley, and J. Nelson. "Morphology evolution via self-organization and lateral and vertical diffusion in polymer:fullerene solar cell blends". In: *Nat Mater* 7.2 (2008), pp. 158–64.

[71] Sean Sweetnam, Kenneth R Graham, Guy O Ngongang Ndjawa, Thomas Heumüller, Jonathan A Bartelt, Timothy M Burke, Wentao Li, Wei You, Aram Amassian, and Michael D McGehee. "Characterization of the polymer energy landscape in polymer: fullerene bulk heterojunctions with pure and mixed phases". In: *Journal of the American Chemical Society* 136.40 (2014), pp. 14078–14088.

[72] Carl Poelking, Max Tietze, Chris Elschner, Selina Olthof, Dirk Hertel, Björn Baumeier, Frank Würthner, Klaus Meerholz, Karl Leo, and Denis Andrienko. "Impact of mesoscale order on open-circuit voltage in organic solar cells". In: *Nat Mater* 14.4 (Apr. 2015), pp. 434–439.

[73] Carl Poelking and Denis Andrienko. "Design Rules for Organic Donor – Acceptor Heterojunctions: Pathway for Charge Splitting and Detrapping". In: *Journal of the American Chemical Society* 137.19 (2015), pp. 6320–6326.

[74] Brian A. Gregg, Si-Guang Chen, and Howard M. Branz. "On the superlinear increase in conductivity with dopant concentration in excitonic semiconductors". In: *Applied Physics Letters* 84.10 (2004), p. 1707.

[75] Duc T. Duong, Chenchen Wang, Erin Antono, Michael F. Toney, and Alberto Salleo. "The chemical and structural origin of efficient p-type doping in P3HT". In: *Organic Electronics* 14.5 (2013), pp. 1330–1336.

[76] K. Walzer, B. Maennig, M. Pfeiffer, and K. Leo. "Highly efficient organic devices based on electrically doped transport layers". In: *Chemical Reviews* 107.4 (2007), pp. 1233–1271.

[77] D Milstein and JK Stille. "A general, selective, and facile method for ketone synthesis from acid chlorides and organotin compounds catalyzed by palladium". In: *Journal of the American Chemical Society* 100.11 (1978), pp. 3636–3638.

[78] Zhenan Bao, Waikin Chan, and Luping Yu. "Synthesis of conjugated polymer by the Stille coupling reaction". In: *Chemistry of materials* 5.1 (1993), pp. 2–3.

[79] Akira Suzuki. “Organoborates in new synthetic reactions”. In: *Accounts of Chemical Research* 15.6 (1982), pp. 178–184.

[80] K. T. Nielsen, K. Bechgaard, and F. C. Krebs. “Removal of palladium nanoparticles from polymer materials”. In: *Macromolecules* 38.3 (2005), pp. 658–659.

[81] F. C. Krebs, R. B. Nyberg, and M. Jorgensen. “Influence of residual catalyst on the properties of conjugated polyphenylenevinylene materials: Palladium nanoparticles and poor electrical performance”. In: *Chemistry of Materials* 16.7 (2004), pp. 1313–1318.

[82] K. Konigsberger, G-P Chen, R. R. Wu, M. J. Girgis, K. Prasad, O. Repic, and T. Blacklock. “A Practical Synthesis of 6-[2-(2,5-Dimethoxyphenyl)ethyl]-4-ethylquinazoline and the Art of Removing Palladium from the Products of Pd-Catalyzed Reactions”. In: *Organic Process Research and Development* 7 (2003), pp. 733–742.

[83] Kim Nielsen, Klaus Bechgaard, and Frederik Krebs. “Effective Removal and Quantitative Analysis of Pd, Cu, Ni, and Pt Catalysts from Small-Molecule Products”. In: *Synthesis* 2006.10 (2006), pp. 1639–1644.

[84] Assunta Marrocchi, Antonio Facchetti, Daniela Lanari, Chiara Petrucci, and Luigi Vaccaro. “Current methodologies for a sustainable approach to π-conjugated organic semiconductors”. In: *Energy & Environmental Science* 9.3 (2016), pp. 763–786.

[85] Nadia Grossiord, Jan M Kroon, Ronn Andriessen, and Paul WM Blom. “Degradation mechanisms in organic photovoltaic devices”. In: *Organic Electronics* 13.3 (2012), pp. 432–456.

[86] Hisao Ishii, Kiyoshi Sugiyama, Eisuke Ito, and Kazuhiko Seki. “Energy Level Alignment and Interfacial Electronic Structures at Organic/Metal and Organic/Organic Interfaces”. In: *Advanced Materials* 11.8 (1999), pp. 605–625.

[87] Thomas Kirchartz, Tiziano Agostinelli, Mariano Campoy-Quiles, Wei Gong, and Jenny Nelson. “Understanding the Thickness-Dependent Performance of Organic Bulk Heterojunction Solar Cells: The Influence of Mobility, Lifetime, and Space Charge”. In: *The Journal of Physical Chemistry Letters* 3.23 (2012), pp. 3470–3475.

[88] George F. A. Dibb, Mathis-Andreas Muth, Thomas Kirchartz, Sebastian Engmann, Harald Hoppe, Gerhard Gobsch, Mukundan Thelakkat, Nicolas Blouin, Steve Tierney, Miguel Carrasco-Orozco, James R. Durrant, and Jenny Nelson. "Influence of doping on charge carrier collection in normal and inverted geometry polymer:fullerene solar cells". In: *Scientific Reports* 3 (2013).

[89] Tracey M Clarke and James R Durrant. "Charge photogeneration in organic solar cells". In: *Chemical reviews* 110.11 (2010), pp. 6736–6767.

[90] Askat E Jailaubekov, Adam P Willard, John R Tritsch, Wai-Lun Chan, Na Sai, Raluca Gearba, Loren G Kaake, Kenrick J Williams, Kevin Leung, Peter J Rossky, and X-Y. Zhu. "Hot charge-transfer excitons set the time limit for charge separation at donor/acceptor interfaces in organic photovoltaics". In: *Nature materials* 12.1 (2013), pp. 66–73.

[91] Christian Schwarz, Steffen Tscheuschner, Johannes Frisch, Stefanie Winkler, Norbert Koch, Heinz Bässler, and Anna Köhler. "Role of the effective mass and interfacial dipoles on exciton dissociation in organic donor-acceptor solar cells". In: *Physical Review B* 87.15 (2013).

[92] Fiona C. Jamieson, Ester Buchaca Domingo, Thomas McCarthy-Ward, Martin Heeney, Natalie Stingelin, and James R. Durrant. "Fullerene crystallisation as a key driver of charge separation in polymer/fullerene bulk heterojunction solar cells". In: *Chemical Science* 3.2 (2012), p. 485.

[93] Francis Paquin, Hajime Yamagata, Nicholas J. Hestand, Maciej Sakowicz, Nicolas Bérubé, Michel Côté, Luke X. Reynolds, Saif A. Haque, Natalie Stingelin, Frank C. Spano, and Carlos Silva. "Two-dimensional spatial coherence of excitons in semicrystalline polymeric semiconductors: Effect of molecular weight". In: *Physical Review B* 88.15 (2013).

[94] W. Barford and O. R. Tozer. "Theory of exciton transfer and diffusion in conjugated polymers". In: *J Chem Phys* 141.16 (2014), p. 164103.

[95] M. Pope and C.E. Swenberg. *Electronic Processes in Organic Crystals and Polymers*. Oxford University Press, 1999.

[96] Yasunari Tamai, Hideo Ohkita, Hiroaki Benten, and Shinzaburo Ito. "Exciton diffusion in conjugated polymers: From fundamental understanding to improvement in photovoltaic conversion efficiency". In: *The journal of physical chemistry letters* 6.17 (2015), pp. 3417–3428.

[97] Yasunari Tamai, Yuu Matsuura, Hideo Ohkita, Hiroaki Benten, and Shinzaburo Ito. "One-dimensional singlet exciton diffusion in poly (3-hexylthiophene) crystalline domains". In: *The journal of physical chemistry letters* 5.2 (2014), pp. 399–403.

[98] Natalie Banerji, Sarah Cowan, Mario Leclerc, Eric Vauthey, and Alan J. Heeger. "Exciton Formation, Relaxation, and Decay in PCDTBT". In: *Journal of the American Chemical Society* 132.49 (2010), pp. 17459–17470.

[99] Simon Gélinas, Akshay Rao, Abhishek Kumar, Samuel L Smith, Alex W Chin, Jenny Clark, Tom S van der Poll, Guillermo C Bazan, and Richard H Friend. "Ultrafast long-range charge separation in organic semiconductor photovoltaic diodes". In: *Science* 343.6170 (2014), pp. 512–516.

[100] Brett M Savoie, Akshay Rao, Artem A Bakulin, Simon Gelinas, Bijan Movaghar, Richard H Friend, Tobin J Marks, and Mark A Ratner. "Unequal partnership: Asymmetric roles of polymeric donor and fullerene acceptor in generating free charge". In: *Journal of the American Chemical Society* 136.7 (2014), pp. 2876–2884.

[101] A. C. Jakowetz, M. L. Böhm, J. Zhang, A. Sadhanala, S. Huettner, A. A. Bakulin, A. Rao, and R. H. Friend. "What Controls the Rate of Ultrafast Charge Transfer and Charge Separation Efficiency in Organic Photovoltaic Blends". In: *J Am Chem Soc* 138.36 (2016), pp. 11672–9.

[102] E. R. Bittner and C. Silva. "Noise-induced quantum coherence drives photocarrier generation dynamics at polymeric semiconductor heterojunctions". In: *Nat Commun* 5 (2014), p. 3119.

[103] E. R. Bittner and A. Kelley. "The role of structural fluctuations and environmental noise in the electron/hole separation kinetics at organic polymer bulk-heterojunction interfaces". In: *Phys Chem Chem Phys* 17.43 (2015), pp. 28853–9.

[104] Sarah Maria Falke, Carlo Andrea Rozzi, Daniele Brida, Margherita Maiuri, Michele Amato, Ephraim Sommer, Antonietta De Sio, Angel Rubio, Giulio Cerullo, Elisa Molinari, and Christoph Lienau. "Coherent ultrafast charge transfer in an organic photovoltaic blend". In: *Science* 344.6187 (2014), pp. 1001–1005.

[105] Juan Aragó and Alessandro Troisi. "Regimes of Exciton Transport in Molecular Crystals in the Presence of Dynamic Disorder". In: *Advanced Functional Materials* 26.14 (2016), pp. 2316–2325.

[106] J. J. Benson-Smith, L. Goris, K. Vandewal, K. Haenen, J. V. Manca, D. Vanderzande, D. D. C. Bradley, and J. Nelson. "Formation of a Ground-State Charge-Transfer Complex in Polyfluorene//[6,6]-Phenyl-C61 Butyric Acid Methyl Ester (PCBM) Blend Films and Its Role in the Function of Polymer/PCBM Solar Cells". In: *Advanced Functional Materials* 17.3 (2007), pp. 451–457.

[107] K. Tvingstedt, K. Vandewal, A. Gadisa, F. L. Zhang, J. Manca, and O. Inganäs. "Electroluminescence from Charge Transfer States in Polymer Solar Cells". In: *Journal of the American Chemical Society* 131.33 (2009), pp. 11819–11824.

[108] M. A. Faist, T. Kirchartz, W. Gong, R. S. Ashraf, I. McCulloch, J. C. de Mello, N. J. Ekins-Daukes, D. D. Bradley, and J. Nelson. "Competition between the charge transfer state and the singlet states of donor or acceptor limiting the efficiency in polymer:fullerene solar cells". In: *J Am Chem Soc* 134.1 (2012), pp. 685–92.

[109] K. Vandewal, K. Tvingstedt, A. Gadisa, O. Ingänas, and J. V. Manca. "On the origin of the open-circuit voltage of polymer-fullerene solar cells". In: *Nature Materials* 8.11 (2009), pp. 904–909.

[110] Sheridan Few, Jarvist M. Frost, James Kirkpatrick, and Jenny Nelson. "Influence of Chemical Structure on the Charge Transfer State Spectrum of a Polymer:Fullerene Complex". In: *The Journal of Physical Chemistry C* 118.16 (2014), pp. 8253–8261.

[111] David C Coffey, Andrew J Ferguson, Nikos Kopidakis, and Garry Rumbles. "Photovoltaic charge generation in organic semiconductors based on long-range energy transfer". In: *ACS nano* 4.9 (2010), pp. 5437–5445.

[112] Patricie Heinrichova, Martin Vala, and Martin Weiter. "Energy versus charge transfer in π-conjugated polymer:fullerene blends". In: *Chemical Physics Letters* 592 (2014), pp. 314–319.

[113] A. R. Kandada, G. Grancini, A. Petrozza, S. Perissinotto, D. Fazzi, S. S. Raavi, and G. Lanzani. "Ultrafast energy transfer in ultrathin organic donor/acceptor blend". In: *Sci Rep* 3 (2013), p. 2073.

[114] Eric T. Hoke, Koen Vandewal, Jonathan A. Bartelt, William R. Mateker, Jessica D. Douglas, Rodrigo Noriega, Kenneth R. Graham, Jean M. J. Fréchet, Alberto Salleo, and Michael D. McGehee. "Recombination in Poly-

mer:Fullerene Solar Cells with Open-Circuit Voltages Approaching and Exceeding 1.0 V". In: *Advanced Energy Materials* 3.2 (2013), pp. 220–230.

[115] Artem A Bakulin, Akshay Rao, Vlad G Pavelyev, Paul HM van Loosdrecht, Maxim S Pshenichnikov, Dorota Niedzialek, Jérôme Cornil, David Beljonne, and Richard H Friend. "The role of driving energy and delocalized states for charge separation in organic semiconductors". In: *Science* 335.6074 (2012), pp. 1340–1344.

[116] Jiye Lee, Koen Vandewal, Shane R Yost, Matthias E Bahlke, Ludwig Goris, Marc A Baldo, Jean V Manca, and Troy Van Voorhis. "Charge transfer state versus hot exciton dissociation in polymer- fullerene blended solar cells". In: *Journal of the American Chemical Society* 132.34 (2010), pp. 11878–11880.

[117] Koen Vandewal, Steve Albrecht, Eric T. Hoke, Kenneth R. Graham, Johannes Widmer, Jessica D. Douglas, Marcel Schubert, William R. Mateker, Jason T. Bloking, George F. Burkhard, Alan Sellinger, Jean M. J. Fréchet, Aram Amassian, Moritz K. Riede, Michael D. McGehee, Dieter Neher, and Alberto Salleo. "Efficient charge generation by relaxed charge-transfer states at organic interfaces". In: *Nat Mater* 13.1 (2014), pp. 63–68.

[118] Tom G. J. van der Hofstad, Daniele Di Nuzzo, Mauricio van den Berg, René A. J. Janssen, and Stefan C. J. Meskers. "Influence of Photon Excess Energy on Charge Carrier Dynamics in a Polymer-Fullerene Solar Cell". In: *Advanced Energy Materials* 2.9 (2012), pp. 1095–1099.

[119] B. Bernardo, D. Cheyns, B. Verreet, R. D. Schaller, B. P. Rand, and N. C. Giebink. "Delocalization and dielectric screening of charge transfer states in organic photovoltaic cells". In: *Nature Communications* 5 (2014), p. 3245.

[120] M. Causa, J. De Jonghe-Risse, M. Scarongella, J. C. Brauer, E. Buchaca-Domingo, J. E. Moser, N. Stingelin, and N. Banerji. "The fate of electron-hole pairs in polymer:fullerene blends for organic photovoltaics". In: *Nat Commun* 7 (2016), p. 12556.

[121] D. Bartesaghi, C. Pérez Idel, J. Kniepert, S. Roland, M. Turbiez, D. Neher, and L. J. Koster. "Competition between recombination and extraction of free charges determines the fill factor of organic solar cells". In: *Nat Commun* 6 (2015), p. 7083.

[122] Pascal Kaienburg, Uwe Rau, and Thomas Kirchartz. “Extracting Information about the Electronic Quality of Organic Solar-Cell Absorbers from Fill Factor and Thickness”. In: *Phys. Rev. Applied* 6 (2 Aug. 2016), p. 024001.

[123] Hsin-Rong Tseng, Hung Phan, Chan Luo, Ming Wang, Louis A. Perez, Shrayesh N. Patel, Lei Ying, Edward J. Kramer, Thuc-Quyen Nguyen, Guillermo C. Bazan, and Alan J. Heeger. “High-Mobility Field-Effect Transistors Fabricated with Macroscopic Aligned Semiconducting Polymers”. In: *Advanced Materials* 26.19 (2014), pp. 2993–2998.

[124] Deepak Venkateshvaran, Mark Nikolka, Aditya Sadhanala, Vincent Lemaur, Mateusz Zelazny, Michal Kepa, Michael Hurhangee, Auke Jisk Kronemeijer, Vincenzo Pecunia, Iyad Nasrallah, Igor Romanov, Katharina Broch, Iain McCulloch, David Emin, Yoann Olivier, Jérôme Cornil, David Beljonne, and Henning Sirringhaus. “Approaching disorder-free transport in high-mobility conjugated polymers”. In: *Nature* 515.7527 (2014), pp. 384–388.

[125] C. B. Nielsen, M. Turbiez, and I. McCulloch. “Recent advances in the development of semiconducting DPP-containing polymers for transistor applications”. In: *Adv Mater* 25.13 (2013), pp. 1859–80.

[126] Iain McCulloch, Alberto Salleo, and Michael Chabinyc. “Avoid the kinks when measuring mobility”. In: *Science* 352.6293 (2016), pp. 1521–1522.

[127] Kwang Hee Cheon, Jangwhan Cho, Byung Tack Lim, Hui-Jun Yun, Soon-Ki Kwon, Yun-Hi Kim, and Dae Sung Chung. “Analysis of charge transport in high-mobility diketopyrrolopyrole polymers by space charge limited current and time of flight methods”. In: *RSC Adv.* 4 (67 2014), pp. 35344–35347.

[128] Veaceslav Coropceanu, Jérôme Cornil, Demetrio A da Silva Filho, Yoann Olivier, Robert Silbey, and Jean-Luc Brédas. “Charge transport in organic semiconductors”. In: *Chemical reviews* 107.4 (2007), pp. 926–952.

[129] Nicholas E Jackson, Lin X Chen, and Mark A Ratner. “Charge transport network dynamics in molecular aggregates”. In: *Proceedings of the National Academy of Sciences* (2016), p. 201601915.

[130] J. L. Brédas, D. Beljonne, V. Coropceanu, and J. Cornil. “Charge-transfer and energy-transfer processes in π-conjugated oligomers and polymers: A molecular picture”. In: *Chemical Reviews* 104.11 (2004), pp. 4971–5003.

[131] Alessandro Troisi. "Charge transport in high mobility molecular semiconductors: classical models and new theories". In: *Chemical Society Reviews* 40.5 (2011), pp. 2347–2358.

[132] Florian Steiner, Samuel Foster, Arthur Losquin, John Labram, Thomas D Anthopoulos, Jarvist M Frost, and Jenny Nelson. "Distinguishing the influence of structural and energetic disorder on electron transport in fullerene multi-adducts". In: *Materials Horizons* 2.1 (2015), pp. 113–119.

[133] Armantas Melianas, Fabian Etzold, Tom J. Savenije, Frédéric Laquai, Olle Inganäs, and Martijn Kemerink. "Photo-generated carriers lose energy during extraction from polymer-fullerene solar cells". In: *Nature Communications* 6 (Nov. 2015).

[134] Christopher G Shuttle, Richard Hamilton, Jenny Nelson, Brian C O'Regan, and James R Durrant. "Measurement of Charge-Density Dependence of Carrier Mobility in an Organic Semiconductor Blend". In: *Advanced Functional Materials* 20.5 (2010), pp. 698–702.

[135] David P McMahon, David L Cheung, Ludwig Goris, Javier Dacuña, Alberto Salleo, and Alessandro Troisi. "Relation between microstructure and charge transport in polymers of different regioregularity". In: *The Journal of Physical Chemistry C* 115.39 (2011), pp. 19386–19393.

[136] Laure Biniek, Bob C. Schroeder, Christian B. Nielsen, and Iain McCulloch. "Recent advances in high mobility donor-acceptor semiconducting polymers". In: *J. Mater. Chem.* 22 (30 2012), pp. 14803–14813.

[137] Rodrigo Noriega, Jonathan Rivnay, Koen Vandewal, Felix PV Koch, Natalie Stingelin, Paul Smith, Michael F Toney, and Alberto Salleo. "A general relationship between disorder, aggregation and charge transport in conjugated polymers". In: *Nature materials* 12.11 (2013), pp. 1038–1044.

[138] Rodrigo Noriega, Alberto Salleo, and Andrew J Spakowitz. "Chain conformations dictate multiscale charge transport phenomena in disordered semiconducting polymers". In: *Proceedings of the National Academy of Sciences* 110.41 (2013), pp. 16315–16320.

[139] Rocco P Fornari and Alessandro Troisi. "Theory of charge hopping along a disordered polymer chain". In: *Physical Chemistry Chemical Physics* 16.21 (2014), pp. 9997–10007.

[140] Scott Himmelberger and Alberto Salleo. “Engineering semiconducting polymers for efficient charge transport”. In: *MRS Communications* 5.03 (2015), pp. 383–395.

[141] Thomas Kirchartz, Bart E Pieters, James Kirkpatrick, Uwe Rau, and Jenny Nelson. “Recombination via tail states in polythiophene: fullerene solar cells”. In: *Physical Review B* 83.11 (2011), p. 115209.

[142] Roderick CI MacKenzie, Christopher G Shuttle, Michael L Chabinyc, and Jenny Nelson. “Extracting microscopic device parameters from transient photocurrent measurements of P3HT: PCBM solar cells”. In: *Advanced Energy Materials* 2.6 (2012), pp. 662–669.

[143] Ruidong Xia, Dong-Seok Leem, Thomas Kirchartz, Steve Spencer, Craig Murphy, Zhicai He, Hongbin Wu, Shijian Su, Yong Cao, Ji Seon Kim, John C. deMello, Donal D.C. Bradley, and Jenny Nelson. “Investigation of a conjugated polyelectrolyte interlayer for inverted polymer: fullerene solar cells”. In: *Advanced Energy Materials* 3.6 (2013), pp. 718–723.

[144] Richard S Crandall. “Transport in hydrogenated amorphous silicon p-i-n solar cells”. In: *Journal of Applied Physics* 53.4 (1982), pp. 3350–3352.

[145] William Shockley and Hans J. Queisser. “Detailed Balance Limit of Efficiency of p-n Junction Solar Cells”. In: *Journal of Applied Physics* 32.3 (1961), p. 510.

[146] Thomas Kirchartz. “Generalized detailed balance theory of solar cells”. Thesis. 2009.

[147] P. Würfel. “The Chemical-Potential of Radiation”. In: *Journal of Physics C-Solid State Physics* 15.18 (1982), pp. 3967–3985.

[148] Uwe Rau. “Reciprocity relation between photovoltaic quantum efficiency and electroluminescent emission of solar cells”. In: *Physical Review B* 76.8 (2007).

[149] Derya Baran, Michelle S Vezie, Nicola Gasparini, Florent Deledalle, Jizhong Yao, Bob C Schroeder, Hugo Bronstein, Tayebeh Ameri, Thomas Kirchartz, Iain McCulloch, Jenny Nelson, and Christopher J Brabec. “Role of Polymer Fractionation in Energetic Losses and Charge Carrier Lifetimes of Polymer: Fullerene Solar Cells”. In: *The Journal of Physical Chemistry C* 119.34 (2015), pp. 19668–19673.

[150] Timothy M Burke, Sean Sweetnam, Koen Vandewal, and Michael D McGehee. "Beyond Langevin Recombination: How Equilibrium Between Free Carriers and Charge Transfer States Determines the Open-Circuit Voltage of Organic Solar Cells". In: *Advanced Energy Materials* 5.11 (2015).

[151] Hiroyuki Fujiwara. *Spectroscopic ellipsometry: principles and applications*. John Wiley & Sons, 2007.

[152] Zdenek Knittl. *Optics of thin films: an optical multilayer theory*. Wiley London: 1976.

[153] Leif A. A. Pettersson, Lucimara S. Roman, and Olle Inganäs. "Modeling photocurrent action spectra of photovoltaic devices based on organic thin films". In: *Journal of Applied Physics* 86.1 (1999), p. 487.

[154] Peter Peumans, Aharon Yakimov, and Stephen R Forrest. "Small molecular weight organic thin-film photodetectors and solar cells". In: *Journal of Applied Physics* 93.7 (2003), pp. 3693–3723.

[155] Stanford University McGehee Group. *Transfer Matrix Optical Modeling*. 2011. URL: `http://web.stanford.edu/group/mcgehee/transfermatrix/` (visited on 11/17/2016).

[156] Yinhua Zhou, Canek Fuentes-Hernandez, Jaewon Shim, Jens Meyer, Anthony J. Giordano, Hong Li, Paul Winget, Theodoros Papadopoulos, Hyeunseok Cheun, Jungbae Kim, Mathieu Fenoll, Amir Dindar, Wojciech Haske, Ehsan Najafabadi, Talha M. Khan, Hossein Sojoudi, Stephen Barlow, Samuel Graham, Jean-Luc Brédas, Seth R. Marder, Antoine Kahn, and Bernard Kippelen. "A Universal Method to Produce Low–Work Function Electrodes for Organic Electronics". In: *Science* 336.6079 (2012), pp. 327–332.

[157] Thomas Kirchartz, Wei Gong, Steven A. Hawks, Tiziano Agostinelli, Roderick C. I. MacKenzie, Yang Yang, and Jenny Nelson. "Sensitivity of the Mott-Schottky Analysis in Organic Solar Cells". In: *The Journal of Physical Chemistry C* 116.14 (2012), pp. 7672–7680.

[158] Thomas Stübinger and Wolfgang Brütting. "Exciton diffusion and optical interference in organic donor-acceptor photovoltaic cells". In: *Journal of Applied Physics* 90.7 (2001), p. 3632.

[159] Ardalan Armin, Marappan Velusamy, Pascal Wolfer, Yuliang Zhang, Paul L. Burn, Paul Meredith, and Almantas Pivrikas. "Quantum Efficiency of Organic Solar Cells: Electro-Optical Cavity Considerations". In: *ACS Photonics* 1.3 (2014), pp. 173–181.

[160] George F Burkhard, Eric T Hoke, and Michael D McGehee. "Accounting for interference, scattering, and electrode absorption to make accurate internal quantum efficiency measurements in organic and other thin solar cells". In: *Advanced Materials* 22.30 (2010), pp. 3293–3297.

[161] CG Shuttle, A Maurano, R Hamilton, B O'Regan, JC De Mello, and JR Durrant. "Charge extraction analysis of charge carrier densities in a polythiophene/fullerene solar cell: Analysis of the origin of the device dark current". In: *Applied Physics Letters* 93.18 (2008), p. 3501.

[162] C. G. Shuttle, B. O'Regan, A. M. Ballantyne, J. Nelson, D. D. C. Bradley, J. de Mello, and J. R. Durrant. "Experimental determination of the rate law for charge carrier decay in a polythiophene: Fullerene solar cell". In: *Applied Physics Letters* 92.9 (2008), p. 093311.

[163] Brian C O'Regan, James R Durrant, Paul M Sommeling, and Nicolaas J Bakker. "Influence of the $TiCl_4$ treatment on nanocrystalline TiO_2 films in dye-sensitized solar cells. 2. Charge density, band edge shifts, and quantification of recombination losses at short circuit". In: *The Journal of Physical Chemistry C* 111.37 (2007), pp. 14001–14010.

[164] Thomas Kirchartz and Jenny Nelson. "Meaning of reaction orders in polymer:fullerene solar cells". In: *Physical Review B* 86.16 (2012).

[165] Andrea Maurano, Chris G Shuttle, Rick Hamilton, Amy M Ballantyne, Jenny Nelson, Weimin Zhang, Martin Heeney, and James R Durrant. "Transient optoelectronic analysis of charge carrier losses in a selenophene/fullerene blend solar cell". In: *The Journal of Physical Chemistry C* 115.13 (2011), pp. 5947–5957.

[166] Andrea Maurano, Rick Hamilton, Chris G Shuttle, Amy M Ballantyne, Jenny Nelson, Brian O'Regan, Weimin Zhang, Iain McCulloch, Hamed Azimi, Mauro Morana, Christopher J Brabec, and James R Durrant. "Recombination dynamics as a key determinant of open-circuit voltage in organic bulk heterojunction solar cells: a comparison of four different donor polymers". In: *Advanced Materials* 22.44 (2010), pp. 4987–4992.

[167] M. Campoy-Quiles, P. G. Etchegoin, and D. D. C. Bradley. "On the optical anisotropy of conjugated polymer thin films". In: *Physical Review B* 72.4 (2005).

[168] M. Losurdo, M. M. Giangregorio, P. Capezzuto, G. Bruno, F. Babudri, D. Colangiuli, G. M. Farinola, and F. Naso. "Spectroscopic ellipsometry for characterization of organic semiconductor polymeric thin films". In: *Synthetic Metals* 138.1-2 (2003), pp. 49–53.

[169] M. Campoy-Quiles, M. I. Alonso, D. D. C. Bradley, and L. J. Richter. "Advanced Ellipsometric Characterization of Conjugated Polymer Films". In: *Advanced Functional Materials* 24.15 (2014), pp. 2116–2134.

[170] A. R. Forouhi and I. Bloomer. "Optical dispersion relations for amorphous semiconductors and amorphous dielectrics". In: *Phys. Rev. B* 34 (10 Nov. 1986), pp. 7018–7026.

[171] G. E. Jellison and F. A. Modine. "Parameterization of the optical functions of amorphous materials in the interband region". In: *Applied Physics Letters* 69.3 (1996), pp. 371–373.

[172] Nadine Ambou and Pierre Boher. *Sopra Winelli II Software Manual*. Version 1.1.

[173] Mariano Campoy-Quiles, Jenny Nelson, Donal Bradley, and Pablo Etchegoin. "Dimensionality of electronic excitations in organic semiconductors: A dielectric function approach". In: *Physical Review B* 76.23 (2007), p. 235206.

[174] Scott Himmelberger, Koen Vandewal, Zhuping Fei, Martin Heeney, and Alberto Salleo. "Role of Molecular Weight Distribution on Charge Transport in Semiconducting Polymers". In: *Macromolecules* 47.20 (2014), pp. 7151–7157.

[175] Sarah Holliday, Jenny E Donaghey, and Iain McCulloch. "Advances in charge carrier mobilities of semiconducting polymers used in organic transistors". In: *Chemistry of Materials* 26.1 (2013), pp. 647–663.

[176] Yun-Xiang Xu, Chu-Chen Chueh, Hin-Lap Yip, Chih-Yu Chang, Po-Wei Liang, Jeremy J Intemann, Wen-Chang Chen, and Alex K-Y Jen. "Indacenodithieno[3, 2-b]thiophene-based broad bandgap polymers for high efficiency polymer solar cells". In: *Polymer Chemistry* 4.20 (2013), pp. 5220–5223.

[177] H. Bronstein, D. S. Leem, R. Hamilton, P. Woebkenberg, S. King, W. M. Zhang, R. S. Ashraf, M. Heeney, T. D. Anthopoulos, J. de Mello, and I. McCulloch. "Indacenodithiophene-co-benzothiadiazole Copolymers for High Performance Solar Cells or Transistors via Alkyl Chain Optimization". In: *Macromolecules* 44.17 (2011), pp. 6649–6652.

[178] X. Zhang, H. Bronstein, A. J. Kronemeijer, J. Smith, Y. Kim, R. J. Kline, L. J. Richter, T. D. Anthopoulos, H. Sirringhaus, K. Song, M. Heeney, W. Zhang, I. McCulloch, and D. M. DeLongchamp. "Molecular origin of high field-effect mobility in an indacenodithiophene-benzothiadiazole copolymer". In: *Nat Commun* 4 (2013), p. 2238.

[179] Iain McCulloch, Raja Shahid Ashraf, Laure Biniek, Hugo Bronstein, Craig Combe, Jenny E Donaghey, David I James, Christian B Nielsen, Bob C Schroeder, and Weimin Zhang. "Design of semiconducting indacenodithiophene polymers for high performance transistors and solar cells". In: *Accounts of chemical research* 45.5 (2012), pp. 714–722.

[180] Yong Zhang, Jingyu Zou, Hin-Lap Yip, Kung-Shih Chen, David F Zeigler, Ying Sun, and Alex K-Y Jen. "Indacenodithiophene and quinoxaline-based conjugated polymers for highly efficient polymer solar cells". In: *Chemistry of Materials* 23.9 (2011), pp. 2289–2291.

[181] R. S. Ashraf, B. C. Schroeder, H. A. Bronstein, Z. Huang, S. Thomas, R. J. Kline, C. J. Brabec, P. Rannou, T. D. Anthopoulos, J. R. Durrant, and I. McCulloch. "The influence of polymer purification on photovoltaic device performance of a series of indacenodithiophene donor polymers". In: *Adv Mater* 25.14 (2013), pp. 2029–34.

[182] Florent Deledalle, Pabitra Shakya Tuladhar, Jenny Nelson, James R. Durrant, and Thomas Kirchartz. "Understanding the Apparent Charge Density Dependence of Mobility and Lifetime in Organic Bulk Heterojunction Solar Cells". In: *The Journal of Physical Chemistry C* 118.17 (2014), pp. 8837–8842.

[183] Weimin Zhang, Jeremy Smith, Scott E. Watkins, Roman Gysel, Michael McGehee, Alberto Salleo, James Kirkpatrick, Shahid Ashraf, Thomas Anthopoulos, Martin Heeney, and Iain McCulloch. "Indacenodithiophene Semiconducting Polymers for High-Performance, Air-Stable Transistors". In: *Journal of the American Chemical Society* 132.33 (2010), pp. 11437–11439.

[184] Yuning Li, Prashant Sonar, Leanne Murphy, and Wei Hong. "High mobility diketopyrrolopyrrole (DPP)-based organic semiconductor materials for organic thin film transistors and photovoltaics". In: *Energy & Environmental Science* 6.6 (2013), p. 1684.

[185] Deepak Chandran and Kwang-Sup Lee. "Diketopyrrolopyrrole: A versatile building block for organic photovoltaic materials". In: *Macromolecular Research* 21.3 (2013), pp. 272–283.

[186] H. Bronstein, Z. Chen, R. S. Ashraf, W. Zhang, J. Du, J. R. Durrant, P. S. Tuladhar, K. Song, S. E. Watkins, Y. Geerts, M. M. Wienk, R. A. Janssen, T. Anthopoulos, H. Sirringhaus, M. Heeney, and I. McCulloch. "Thieno[3,2-b]thiophene-diketopyrrolopyrrole-containing polymers for high-performance organic field-effect transistors and organic photovoltaic devices". In: *J Am Chem Soc* 133.10 (2011), pp. 3272–5.

[187] Sebastian Wood, Jessica Wade, Munazza Shahid, Elisa Collado-Fregoso, Donal D. C. Bradley, James R. Durrant, Martin Heeney, and Ji-Seon Kim. "Natures of optical absorption transitions and excitation energy dependent photostability of diketopyrrolopyrrole (DPP)-based photovoltaic copolymers". In: *Energy & Environmental Science* 8.11 (2015), pp. 3222–3232.

[188] I. Meager, R. S. Ashraf, S. Mollinger, B. C. Schroeder, H. Bronstein, D. Beatrup, M. S. Vezie, T. Kirchartz, A. Salleo, J. Nelson, and I. McCulloch. "Photocurrent Enhancement from Diketopyrrolopyrrole Polymer Solar Cells through Alkyl-Chain Branching Point Manipulation". In: *J Am Chem Soc* 135.31 (2013), pp. 11537–40.

[189] I. Meager, R. S. Ashraf, C. B. Nielsen, J. E. Donaghey, Z. G. Huang, H. Bronstein, J. R. Durrant, and I. McCulloch. "Power conversion efficiency enhancement in diketopyrrolopyrrole based solar cells through polymer fractionation". In: *Journal of Materials Chemistry C* 2.40 (2014), pp. 8593–8598.

[190] Junghwan Kim, Geunjin Kim, Youna Choi, Jongjin Lee, Sung Heum Park, and Kwanghee Lee. "Light-soaking issue in polymer solar cells: Photoinduced energy level alignment at the sol-gel processed metal oxide and indium tin oxide interface". In: *Journal of Applied Physics* 111.11 (2012), p. 114511.

[191] Wei Wei, Chunfu Zhang, Dazheng Chen, Zhizhe Wang, Chunxiang Zhu, Jincheng Zhang, Xiaoli Lu, and Yue Hao. "Efficient "Light-soaking"-free Inverted Organic Solar Cells with Aqueous Solution Processed Low-

Temperature ZnO Electron Extraction Layers". In: *ACS Applied Materials & Interfaces* 5.24 (2013), pp. 13318–13324.

[192] W. M. Prest and D. J. Luca. "Origin of the Optical Anisotropy of Solvent Cast Polymeric Films". In: *Journal of Applied Physics* 50.10 (1979), pp. 6067–6071.

[193] Svante Hedström, Patrik Henriksson, Ergang Wang, Mats R. Andersson, and Petter Persson. "Temperature-Dependent Optical Properties of Flexible Donor-Acceptor Polymers". In: *The Journal of Physical Chemistry C* 119.12 (2015), pp. 6453–6463.

[194] R. J. Kline, M. D. McGehee, E. N. Kadnikova, J. S. Liu, J. M. J. Frechet, and M. F. Toney. "Dependence of regioregular poly(3-hexylthiophene) film morphology and field-effect mobility on molecular weight". In: *Macromolecules* 38.8 (2005), pp. 3312–3319.

[195] Jui-Fen Chang, Jenny Clark, Ni Zhao, Henning Sirringhaus, Dag Breiby, Jens Andreasen, Martin Nielsen, Mark Giles, Martin Heeney, and Iain McCulloch. "Molecular-weight dependence of interchain polaron delocalization and exciton bandwidth in high-mobility conjugated polymers". In: *Physical Review B* 74.11 (2006), p. 115318.

[196] S. Hedström, P. Henriksson, E. Wang, M. R. Andersson, and P. Persson. "Light-harvesting capabilities of low band gap donor-acceptor polymers". In: *Physical Chemistry Chemical Physics* 16.45 (2014), pp. 24853–24865.

[197] F. P. Koch. "Synthesis and Physical Chemistry of a 'Monomer-up Approach'". Thesis. 2013.

[198] F. P. Koch, M. Heeney, and P. Smith. "Thermal and structural characteristics of oligo(3-hexylthiophene)s (3HT)n, n = 4-36". In: *J Am Chem Soc* 135.37 (2013), pp. 13699–709.

[199] R. Dennington, T. Keith, and J. Millam. *GaussView Version 5*. Semichem Inc. Shawnee Mission KS 2009.

[200] MJ Frisch, GW Trucks, HB Schlegel, GE Scuseria, MA Robb, JR Cheeseman, G Scalmani, V Barone, B Mennucci, and GA Petersson. *Gaussian 09, revision A. 1; Gaussian, Inc: Wallingford, CT, 2009*.

[201] Yen-Ju Cheng, Sheng-Hsiung Yang, and Chain-Shu Hsu. "Synthesis of Conjugated Polymers for Organic Solar Cell Applications". In: *Chemical Reviews* 109.11 (2009), pp. 5868–5923.

[202] Pierre M. Beaujuge, Chad M. Amb, and John R. Reynolds. “Spectral Engineering in -Conjugated Polymers with Intramolecular Donor?Acceptor Interactions”. In: *Accounts of Chemical Research* 43.11 (2010), pp. 1396–1407.

[203] Stefan Schumacher, Arvydas Ruseckas, Neil A. Montgomery, Peter J. Skabara, Alexander L. Kanibolotsky, Martin J. Paterson, Ian Galbraith, Graham A. Turnbull, and Ifor D. W. Samuel. “Effect of exciton self-trapping and molecular conformation on photophysical properties of oligofluorenes”. In: *The Journal of Chemical Physics* 131.15, 154906 (2009).

[204] Wei Li, Daojuan Wang, Suhao Wang, Wei Ma, Svante Hedström, David Ian James, Xiaofeng Xu, Petter Persson, Simone Fabiano, Magnus Berggren, Olle Inganäs, Fei Huang, and Ergang Wang. “One-Step Synthesis of Precursor Oligomers for Organic Photovoltaics: A Comparative Study between Polymers and Small Molecules”. In: *ACS Applied Materials & Interfaces* 7.49 (2015), pp. 27106–27114.

[205] M. van Faassen, P. L. de Boeij, R. van Leeuwen, J. A. Berger, and J. G. Snijders. “Ultranonlocality in time-dependent current-density-functional theory: Application to conjugated polymers”. In: *Physical Review Letters* 88.18 (2002), p. 186401.

[206] Z. G. Soos and K. S. Schweizer. “Absorption-Spectrum of Flexible Conjugated Polymers - the Weak-Disorder Limit”. In: *Chemical Physics Letters* 139.2 (1987), pp. 196–200.

[207] G. Rossi, R. R. Chance, and R. Silbey. “Conformational Disorder in Conjugated Polymers”. In: *Journal of Chemical Physics* 90.12 (1989), pp. 7594–7601.

[208] Michelle S. Vezie, Sheridan Few, Iain Meager, Galatia Pieridou, Bernhard Dörling, Raja Shahid Ashraf, Alejandro R. Gonñi, Hugo Bronstein, Iain McCulloch, Sophia C. Hayes, Mariano Campoy-Quiles, and Jenny Nelson. “Exploring the origin of high optical absorption in conjugated polymers”. In: *Nat Mater* 15.7 (2016), pp. 746–753.

[209] N. E. Jackson, K. L. Kohlstedt, B. M. Savoie, M. O. de la Cruz, G. C. Schatz, L. X. Chen, and M. A. Ratner. “Conformational Order in Aggregates of Conjugated Polymers”. In: *Journal of the American Chemical Society* 137.19 (2015), pp. 6254–6262.

[210] W. J. Chung, H. Shibaguchi, K. Terao, M. Fujiki, and M. Naito. "Evaluation of Global Conformation of Polydialkylsilane Using Correlation between Persistence Length and Excitonic Absorption". In: *Macromolecules* 44.16 (2011), pp. 6568–6573.

[211] S. Vanhee, R. Rulkens, U. Lehmann, C. Rosenauer, M. Schulze, W. Köhler, and G. Wegner. "Synthesis and characterization of rigid rod poly(p-phenylenes)". In: *Macromolecules* 29.15 (1996), pp. 5136–5142.

[212] Johan C. Bijleveld, R. A. Melanie Verstrijden, Martijn M. Wienk, and René A. J. Janssen. "Copolymers of diketopyrrolopyrrole and thienothiophene for photovoltaic cells". In: *Journal of Materials Chemistry* 21.25 (2011), p. 9224.

[213] J. P. Aime, F. Bargain, M. Schott, H. Eckhardt, G. G. Miller, and R. L. Elsenbaumer. "Structural study of doped and undoped polythiophene in solution by small-angle neutron scattering". In: *Phys Rev Lett* 62.1 (1989), pp. 55–58.

[214] Dapeng Wang, Yuan Yuan, Yati Mardiyati, Christoph Bubeck, and Kaloian Koynov. "From Single Chains to Aggregates, How Conjugated Polymers Behave in Dilute Solutions". In: *Macromolecules* 46.15 (2013), pp. 6217–6224.

[215] N. J. Hestand and F. C. Spano. "The Effect of Chain Bending on the Photophysical Properties of Conjugated Polymers". In: *Journal of Physical Chemistry B* 118.28 (2014), pp. 8352–8363.

[216] S. C. Hayes and C. Silva. "Analysis of the excited-state absorption spectral bandshape of oligofluorenes". In: *J Chem Phys* 132.21 (2010), p. 214510.

[217] W. Li, K. H. Hendriks, A. Furlan, W. S. Roelofs, S. C. Meskers, M. M. Wienk, and R. A. Janssen. "Effect of the fibrillar microstructure on the efficiency of high molecular weight diketopyrrolopyrrole-based polymer solar cells". In: *Adv Mater* 26.10 (2014), pp. 1565–70.

[218] Thomas J. Fauvell, Tianyue Zheng, Nicholas E. Jackson, Mark A. Ratner, Luping Yu, and Lin X. Chen. "Photophysical and Morphological Implications of Single-Strand Conjugated Polymer Folding in Solution". In: *Chemistry of Materials* 28.8 (2016), pp. 2814–2822.

[219] B. Grimm, C. Risko, J. D. Azoulay, J. L. Brédas, and G. C. Bazan. "Structural dependence of the optical properties of narrow bandgap semiconductors with orthogonal donor-acceptor geometries". In: *Chemical Science* 4.4 (2013), pp. 1807–1819.

[220] J. J. van Franeker, M. Turbiez, W. W. Li, M. M. Wienk, and R. A. J. Janssen. "A real-time study of the benefits of co-solvents in polymer solar cell processing". In: *Nature Communications* 6 (2015), p. 6229.

[221] M. A. Baklar, F. Koch, A. Kumar, E. B. Domingo, M. Campoy-Quiles, K. Feldman, L. Yu, P. Wobkenberg, J. Ball, R. M. Wilson, I. McCulloch, T. Kreouzis, M. Heeney, T. Anthopoulos, P. Smith, and N. Stingelin. "Solid-state processing of organic semiconductors". In: *Adv Mater* 22.35 (2010), pp. 3942–7.

[222] Miloslav Bohdanecký. "New method for estimating the parameters of the wormlike chain model from the intrinsic viscosity of stiff-chain polymers". In: *Macromolecules* 16.9 (1983), pp. 1483–1492.

[223] M. Campoy-Quiles, G. Heliotis, R. D. Xia, M. Ariu, M. Pintani, P. Etchegoin, and D. D. C. Bradley. "Ellipsometric characterization of the optical constants of polyfluorene gain media". In: *Advanced Functional Materials* 15.6 (2005), pp. 925–933.

[224] B. K. Yap, R. D. Xia, M. Campoy-Quiles, P. N. Stavrinou, and D. D. C. Bradley. "Simultaneous optimization of charge-carrier mobility and optical gain in semiconducting polymer films". In: *Nature Materials* 7.5 (2008), pp. 376–380.

[225] C. Müller, J. Bergqvist, K. Vandewal, K. Tvingstedt, A. S. Anselmo, R. Magnusson, M. I. Alonso, E. Moons, H. Arwin, M. Campoy-Quiles, and O. Inganäs. "Phase behaviour of liquid-crystalline polymer/fullerene organic photovoltaic blends: thermal stability and miscibility". In: *Journal of Materials Chemistry* 21.29 (2011), pp. 10676–10684.

[226] C. Müller, L. M. Andersson, O. Peña-Rodriguez, M. Garriga, O. Inganäs, and M. Campoy-Quiles. "Determination of Thermal Transition Depth Profiles in Polymer Semiconductor Films with Ellipsometry". In: *Macromolecules* 46.18 (2013), pp. 7325–7331.

[227] L. T. Hou, E. Wang, J. Bergqvist, B. V. Andersson, Z. Q. Wang, C. Müller, M. Campoy-Quiles, M. R. Andersson, F. L. Zhang, and O. Inganäs. "Lateral Phase Separation Gradients in Spin-Coated Thin Films of

High-Performance Polymer: Fullerene Photovoltaic Blends". In: *Advanced Functional Materials* 21.16 (2011), pp. 3169–3175.

[228] A. Guerrero, B. Dörling, T. Ripolles-Sanchis, M. Aghamohammadi, E. Barrena, M. Campoy-Quiles, and G. Garcia-Belmonte. "Interplay between Fullerene Surface Coverage and Contact Selectivity of Cathode Interfaces in Organic Solar Cells". In: *Acs Nano* 7.5 (2013), pp. 4637–4646.

[229] Kaloian Koynov, Ayi Bahtiar, Taek Ahn, Christoph Bubeck, and Hans-Heinrich Hörhold. "Molecular weight dependence of birefringence of thin films of the conjugated polymer poly[2-methoxy-5-(2'-ethyl-hexyloxy)-1, 4-phenylenevinylene]". In: *Applied Physics Letters* 84.19 (2004), p. 3792.

[230] Uladzimir Zhokhavets, Gerhard Gobsch, Harald Hoppe, and Niyazi Serdar Sariciftci. "A systematic study of the anisotropic optical properties of thin poly(3-octylthiophene)-films in dependence on growth parameters". In: *Thin Solid Films* 451-452 (2004), pp. 69–73.

[231] I. Musa and W. Eccleston. "Determination of the optical constants of thin films of regioregular poly(3-alkylthiophene) on transparent substrates". In: *Synthetic Metals* 97.1 (1998), pp. 69–72.

[232] D. Yang, R. P. Shrestha, T. J. Dingemans, E. T. Samulski, and E. A. Irene. "Optical properties of N,N'-bis(3-phenoxy-3-phenoxy-phenoxy)-1,4,5,8-naphthalene-tetracarboxylic diimide by spectroscopic ellipsometry". In: *Thin Solid Films* 500.1-2 (2006), pp. 9–14.

[233] N. K. Persson, M. Sun, P. Kjellberg, T. Pullerits, and O. Inganäs. "Optical properties of low band gap alternating copolyfluorenes for photovoltaic devices". In: *J Chem Phys* 123.20 (2005), p. 204718.

[234] J. Sturm, S. Tasch, A. Niko, G. Leising, E. Toussaere, J. Zyss, T. C. Kowalczyk, K. D. Singer, U. Scherf, and J. Huber. "Optical anisotropy in thin films of a blue electroluminescent conjugated polymer". In: *Thin Solid Films* 298.1-2 (1997), pp. 138–142.

[235] A. Hinderhofer, U. Heinemeyer, A. Gerlach, S. Kowarik, R. M. J. Jacobs, Y. Sakamoto, T. Suzuki, and F. Schreiber. "Optical properties of pentacene and perfluoropentacene thin films". In: *Journal of Chemical Physics* 127.19 (2007).

[236] M. Losurdo, G. Bruno, and E. A. Irene. "Anisotropy of optical properties of conjugated polymer thin films by spectroscopic ellipsometry". In: *Journal of Applied Physics* 94.8 (2003), pp. 4923–4929.

[237] C. M. Ramsdale and N. C. Greenham. "Ellipsometric determination of anisotropic optical constants in electroluminescent conjugated polymers". In: *Advanced Materials* 14.3 (2002), pp. 212–215.

[238] C. M. Ramsdale and N. C. Greenham. "The optical constants of emitter and electrode materials in polymer light-emitting diodes". In: *Journal of Physics D-Applied Physics* 36.4 (2003), pp. L29–L34.

[239] M. R. Hammond, R. J. Kline, A. A. Herzing, L. J. Richter, D. S. Germack, H. W. Ro, C. L. Soles, D. A. Fischer, T. Xu, L. P. Yu, M. F. Toney, and D. M. DeLongchamp. "Molecular Order in High-Efficiency Polymer/Fullerene Bulk Heterojunction Solar Cells". In: *Acs Nano* 5.10 (2011), pp. 8248–8257.

[240] Dirk Veldman, Stefan CJ Meskers, and René AJ Janssen. "The Energy of Charge-Transfer States in Electron Donor–Acceptor Blends: Insight into the Energy Losses in Organic Solar Cells". In: *Advanced Functional Materials* 19.12 (2009), pp. 1939–1948.

[241] Stoichko D. Dimitrov, Christian B. Nielsen, Safa Shoaee, Pabitra Shakya Tuladhar, Junping Du, Iain McCulloch, and James R. Durrant. "Efficient Charge Photogeneration by the Dissociation of $PC_{70}BM$ Excitons in Polymer/Fullerene Solar Cells". In: *The Journal of Physical Chemistry Letters* 3.1 (2012), pp. 140–144.

[242] S. D. Dimitrov, A. A. Bakulin, C. B. Nielsen, B. C. Schroeder, J. Du, H. Bronstein, I. McCulloch, R. H. Friend, and J. R. Durrant. "On the energetic dependence of charge separation in low-band-gap polymer/fullerene blends". In: *J Am Chem Soc* 134.44 (2012), pp. 18189–92.

[243] Daniele Di Nuzzo, Gert-Jan A. H. Wetzelaer, Ricardo K. M. Bouwer, Veronique S. Gevaerts, Stefan C. J. Meskers, Jan C. Hummelen, Paul W. M. Blom, and René A. J. Janssen. "Simultaneous Open-Circuit Voltage Enhancement and Short-Circuit Current Loss in Polymer: Fullerene Solar Cells Correlated by Reduced Quantum Efficiency for Photoinduced Electron Transfer". In: *Advanced Energy Materials* 3.1 (2013), pp. 85–94.

[244] C. J. Brabec, A. Cravino, D. Meissner, N. S. Sariciftci, T. Fromherz, M. T. Rispens, L. Sanchez, and J. C. Hummelen. "Origin of the Open Circuit Voltage of Plastic Solar Cells". In: *Advanced Functional Materials* 11.5 (2001), pp. 374–380.

[245] Kealan J. Fallon, Nilushi Wijeyasinghe, Eric F. Manley, Stoichko D. Dimitrov, Syeda A. Yousaf, Raja S. Ashraf, Warren Duffy, Anne A. Y. Guilbert, David M. E. Freeman, Mohammed Al-Hashimi, Jenny Nelson, James R. Durrant, Lin X. Chen, Iain McCulloch, Tobin J. Marks, Tracey M. Clarke, Thomas D. Anthopoulos, and Hugo Bronstein. "Indolo-naphthyridine-6,13-dione Thiophene Building Block for Conjugated Polymer Electronics: Molecular Origin of Ultrahigh n-Type Mobility". In: *Chemistry of Materials* 28.22 (2016), pp. 8366–8378.

[246] A. Armin, I. Kassal, P. E. Shaw, M. Hambsch, M. Stolterfoht, D. M. Lyons, J. Li, Z. Shi, P. L. Burn, and P. Meredith. "Spectral dependence of the internal quantum efficiency of organic solar cells: effect of charge generation pathways". In: *J Am Chem Soc* 136.32 (2014), pp. 11465–72.

[247] Francis Paquin, Gianluca Latini, Maciej Sakowicz, Paul-Ludovic Karsenti, Linjun Wang, David Beljonne, Natalie Stingelin, and Carlos Silva. "Charge Separation in Semicrystalline Polymeric Semiconductors by Photoexcitation: Is the Mechanism Intrinsic or Extrinsic?" In: *Phys. Rev. Lett.* 106 (19 May 2011), p. 197401.

[248] Obadiah G. Reid, Jennifer A. Nekuda Malik, Gianluca Latini, Smita Dayal, Nikos Kopidakis, Carlos Silva, Natalie Stingelin, and Garry Rumbles. "The influence of solid-state microstructure on the origin and yield of long-lived photogenerated charge in neat semiconducting polymers". In: *Journal of Polymer Science Part B: Polymer Physics* 50.1 (2012), pp. 27–37.

[249] Ya-shih Huang, Sebastian Westenhoff, Igor Avilov, Paiboon Sreearunothai, Justin M. Hodgkiss, Caroline Deleener, Richard H. Friend, and David Beljonne. "Electronic structures of interfacial states formed at polymeric semiconductor heterojunctions". In: *Nature Materials* 7.6 (June 2008), pp. 483–489.

[250] IDTechEx. *Printed, Organic & Flexible Electronics Forecasts, Players & Opportunities, 2017-2027.* 2017. URL: `http://www.idtechex.com/research/reports/printed-organic-and-flexible-electronics-forecasts-players-and-opportunities-2017-2027-000510.asp?viewopt=desc` (visited on 03/08/2017).